eman ta zabal zazu

Universidad del País Vasco
Euskal Herriko Unibertsitatea

Investigating Lipid and Protein Organization in Cell Membranes

Ling Zhu

Thesis submitted to the Department of Biochemistry and
Molecular Biology, University of the Basque Country
for the degree of doctor of philosophy

Supervisor
Dr. Ilya Reviakine

2013

The Thesis has been performed at:

Surface Interface Biophysics Laboratory

Biosurfaces Unit

CIC biomaGUNE

Donostia-San Sebastian

Spain

Reviakine´s Group

CIC biomaGUNE

Biomaterialetako Ikerkuntza Kooperatiboko Zentroa

Centro de Investigación Cooperativa en Biomateriales

Universidad del País Vasco Euskal Herriko Unibertsitatea

Abstract

Cell membrane encloses the cell, separates intracellular contents from the extracellular environment, and mediates the transport of the solutes and information in and out of the cell. The core structure of the cell membrane is based on a phospholipid bilayer that forms a permeability barrier. Proteins that function as material or information carriers are inserted into the bilayer or are bound to it. In itself, the cell membrane is a self-assembled system, with both lipids and proteins distributed in a non-random manner. This organization is necessary for transport, signal transduction, cell-cell communication and identification.

Lipids in cell membranes are organized laterally and transversely. In the transverse direction, ‘reactive’ lipids like phosphatidyl serine (PS) are enriched in the cytoplasmic leaflet, while ‘non-reactive’ lipids like phosphatidyl choline (PC) are enriched in the extracellular leaflet. This asymmetry is maintained by energy (ATP)-dependent processes. The organization in the lateral direction is less well understood. Heterogeneities in lipid composition—sometimes termed lipid rafts—on the order of a few tens of nanometers are thought to exist. They are also thought to be crucial for various signaling events. Model systems that mimic both the lateral and the transverse organization of lipids in cell membranes are scarce.

Supported phospholipid bilayers (SLBs) are popular cell membrane models. Using SLBs on titania (TiO_2), I developed a model that mimicked physiological lipid compositions as well as the asymmetric transverse organization characteristic of the cell membrane organization. While cells use ATP to sustain lipid asymmetry, in this model system, the lipid-surface adhesion energy supplies the free energy necessary to offset the entropy of mixing between the two leaflets.

During developing this model, the process of SLB formation on TiO_2 surfaces was investigated using a wide variety of lipid compositions and buffer conditions. Lipid diffusion and organization in these SLBs was studied. I was able to demonstrate that the electrostatic interaction between zwitterionic liposomes and negatively charged surface was repulsive, and visualize that the excess lipid leaves the surface during SLB formation in the form of elongated, tubular structures.

Membrane proteins organize into clusters which are involved in cellular processes such as ion transport, signal transduction, and cell-cell adhesion. Common examples of proteins that function as dimers or oligomers include rhodopsin, OmpF porin, and F-type ATPase (ATP synthase). Oligomerization of some other proteins such as Na^+, K^+-ATPase, and H^+, K^+-ATPase, two P-type ATPases, is still under debate. Evidence supporting their oligomerization mainly comes from functional and kinetic studies. Direct evidence visualizing their organization in cell membranes is still lacking. As an example of a transmembrane protein organization, I investigated the supramolecular organization of Na^+, K^+-ATPase in the near-native membrane patches of the outer medulla of rabbit kidney. Using AFM, I showed that this protein is present in the near-native patches as oligomers of various orders, with tetramers $(\alpha\beta)_4$ being the most commonly occurring motif.

This Thesis provides insights into the self-organization of lipids and proteins in cell membranes, and helps to understand the mechanisms underlying cellular behavior.

Resumen

Las células son sistemas complejos, altamente organizados y en no-equilibrio. A lo largo de su ciclo vital, mantienen aspectos dinámicos tales como la polaridad y el transporte direccional, la compartimentalización, y el número y tamaño de varios orgánulos. A pesar de que sabemos mucho a cerca de cómo las células y las subestructuras celulares se organizan, la emergencia y mantenimiento de estos aspectos dinámicos permanece como un área de investigación activa con numerosas cuestiones sin soluciónes.

Esta Tesis se centra en la organización celular. Las membranas celulares envuelven la célula, separan los contenidos celulares del entorno extracelular, y median el transporte de solutos e información dentro y fuera de la célula. El fundamento de su estructura se basa en una bicapa de fosfolípidos que está compuesta por dos capas opuestas, con proteínas insertadas a lo largo de la bicapa o ligadas a cualquiera de las hojas. En sí misma, es por supuesto un sistema auto-ensamblado. El carácter anfipático de los fosfolípidos hace de la membrana celular una barrera para solutos polares y cargados, ayudando a mantener los gradientes electroquímicos a lo largo de la membrana. Por otro lado, la difusión lateral de los lípidos hace de la bicapa una matriz fluida en la que las proteínas de membrana se mueven lateralmente y

experimentan cambios conformacionales, facilitando su rol como transportadoras de material e información a través de la membrana.

Tanto los lípidos como las proteínas están distribuidos de forma no aleatoria en las membranas celulares. Esta organización está supeditada a procesos que requieren energía, y juega roles importantes en muchos procesos celulares tales como el transporte, la transducción de señales, la identificación y la comunicación entre células.

Los lípidos de membrana exhiben una compleja organización transversal y lateral. En la dirección transversal, los lípidos están distribuidos asimétricamente. Concretamente, los fosfolípidos "reactivos" como la fosfatidilserina (PS), la fosfatidiletanolamina (PE), el fosfatidilinositol (PI) se encuentran enriqueciendo la hoja citoplasmática, mientras que los lípidos "no reactivos" como la fosfatidilcolina (PC) y la esfingomielina (SM) son más abundantes en la hoja extracelular de la bicapa. Esta asimetría se mantiene por medio de procesos energéticos ATP-dependientes, y tiene consecuencias fisiológicas y patofisiológicas en procesos como la coagulación sanguínea, las interacciones célula-célula, y la limpieza de células apoptóticas. La organización lateral está peor comprendida. Se piensa que la hetereogeneidad en la composición lipídica existe en el rango de las decenas de nanómetro, con una partición preferencial de las proteínas transmembrana o de anclaje. Se cree que estas heterogeneidades, a veces llamadas balsas lipídicas o rafts lipídicos, juegan un papel crucial en eventos de señalización. Dichas hetereogeneidades han sido difíciles de reproducir en sistemas modelo. Normalmente se observan dominios de fase de tamaño de micrómetros. Asimismo, los sistemas modelo que imitan la organización de los lípidos de la membrana celular en ambas direcciones transversal y lateral utilizando composiciones de lípidos fisiológicas son escasos.

Las bicapas de fosfolípidos soportadas (SLBs) son modelos populares de membranas celulares. Utilizando óxido de titanio (TiO_2) como soporte, he desarrollado un modelo que imita la composición lipídica fisiológica y la asimetría de la distribución lipídica características de las membranas celulares utilizando una mezcla de fosfatidilcolinas de alto y bajo punto de fusión, fosfatidilserina y colesterol. Mientras las células utilizan ATP para mantener la asimetría lipídica, en este sistema la energía de adhesión entre el lípido y la superficie suministra la energía libre necesaria para compensar la entropía de la mezcla entre ambas hojas. La asimetría se verificó a través de estudios de difusión de PS fluorescentemente marcada, a la vez que se investigó la organización lateral por microscopía de fuerza atómica (AFM). No se observó separación de fase lateral macroscópica.

Aunque las SLBs se utilizan de forma rutinaria en estudios biofísicos, así como en investigación biotecnológica y biosensores, el mecanismo de su formación a partir de

liposomas adsorbidos todavía permanece pobremente entendido. Se acepta de forma general que el comportamiento de los liposomas adsorbidos depende le la interacción entre el lípido y la superficie y de los efectos cinéticos que definen su estabilidad. Sin embargo, cómo los distintos factores afectan a la interacción lípido-superficie y a la cinética se desconocen en gran medida. Esta falta de conocimiento limita la aplicación de las SLBs. La preparación de las SLBs imitadoras de membrana me permitió la posibilidad de investigar los efectos que la composición lipídica, las condiciones de las soluciones tampón, la temperatura, la química y la rugosidad de la superficie, tienen sobre el proceso de formación de la SLB. Los resultados de estos estudios arrojaron luz sobre la naturaleza de las interacciones lípido-superficie, el rol de los efectos osmóticos en el proceso de formación de la SLB, y la manera en la que el exceso de lípidos abandona la superficie durante la formación de la SLB.

Se discute si las interacciones electrostáticas entre lípidos zwitteriónicos y superficies cargadas negativamente son atractivas o repulsivas. He investigado las contribuciones osmótica y electrostática a la interacción liposoma-superficie de forma separada comparando soluciones tampón con NaCl con soluciones tampón con sucrosa utilizando microscopía de fluorescencia, recuperación de fluorescencia tras el fotoblanqueo (FRAP), y microbalanza de cristal de cuarzo (QCM). También se utilizó un modelo derivada por los colaboradores para describir las observaciones. Las evidencias mostraron que el efecto de la fuerza iónica sobre la interacción

liposoma-superficie era una combinación de efectos electrostáticos y osmóticos, y que las interacciones electrostáticas entre liposomas zwitteriónicos y la superficie cargada negativamente eran repulsivas.

Se sabe que el exceso de lípidos dejan la superficie durante la formación de la SLB, pero cómo la abandonan, y cómo está relacionado con la cinética general de formación de la SLB todavía se desconoce. Durante la formación de la SLB sobre TiO_2, fui capaz de observar estructuras tubulares coexistiendo con la bicapa y de probar, a través de estudios de fluorescencia, que los lípidos en estas estructuras provenían de los liposomas adsorbidos a la superficie que daban lugar a la SLB. Por tanto, fue posible visualizar el camino por el cual el exceso de lípidos abandonan la superficie durante a formación de SLB. Estudios del tiempo de respuesta del proceso ayudaron a ilustrar la cinética del proceso de formación de la SLB.

Las proteínas de membrana también se organizan—en grupos u oligómeros. Para muchas de ellas, se ha mostrado que la oligomerización es un requisito para su funcionalidad. Los ejemplos más comunes incluyen la rodospina, las porinas OmpF y varios miembros de la familia de las ATPasas. La organización en estructuras de alto orden de otras proteínas de membrana está todavía bajo debate. La evidencia que apoya su oligomerización proviene principalmente de estudios cinéticos y funcionales, pero todavía no hay evidencia visual de su organización en membranas celulares. En esta Tesis, investigué la organización supramolecular de la Na^+, K^+-ATPasa, una proteína transmembrana que transporta Na^+ y K^+ a través de la membana celular para mantener el gradiente electroquímico, en parches de membrana nativos de la médula externa del riñón de conejo. La estructura de esta proteína ha sido determinada por cristalografía de rayos-X. Se compone de subunidades α, β, y en algunos tejidos, subunidades γ. Su oligomerización se ha observado normalmente en cristales bi-dimensionales (2D) y también se ha deducido de estudios cinéticos, pero no ha sido directamente observada. Utilizando AFM, he mostrado que esta proteína está presente en los parches nativos formando oligómeros de varios órdenes, siendo el tretámero $(\alpha\beta)_4$, el motivo más común.

En resumen, construí un modelo de SLB con composición lipídica fisiológica que imita la asimetría lipídica de las membranas celulares, investigué la difusión y organización lipídica de este modelo, y abordé varios interrogantes sobre los mecanismos de la formación de las bicapas de fosfolípidos soportadas. También investigué la organización supramolecular de las proteínas de membrana en parches nativos estudiando la proteína transmembrana Na^+, K^+-ATPasa. Estos resultados revelan información sobre la auto-organización en la membrana celular a nivel tanto de lípidos como de proteínas, y ayudan a explicar los mecanismos fundamentales de muchos comportamientos celulares.

Table of Contents

Chapter 3 How Osmotic Effects and Electrostatic Interactions Control Adsorbed Liposome Behavior..75

Objectives and Outline of This Thesis

The aim of this Thesis is to study lipid and protein organization in cell membranes. In order to study membrane lipid organization, a supported lipid bilayer (SLB) model on titania (TiO_2) surface from the lipid mixture of low-melting and high-melting phosphatidyl cholines (PC), phosphatidyl serine (PS), and cholesterol was developed so as to mimic the physiological lipid composition and the asymmetric lipid distribution found in cell membranes. In developing this model, the mechanistic aspects underlying adsorbed liposome behavior at oxide surfaces were investigated. One of the key findings is the separation of the effect of osmotic pressure from the effect of electrostatic interactions in high ionic strength buffers and the consequent conclusion that the electrostatic interactions between zwitterionic lipids and negatively charged surfaces are repulsive. These results are in Chapter 3. Another one relates to the pathway and kinetics the excess lipids take to leave the surface during SLB formation. These results are in Chapter 4. The evidence of the lipid organization and diffusion in the model SLB, and the effects of varying experimental parameters such as lipid composition, buffer composition, temperature, surface chemistry and roughness on liposome behavior on the surface are shown in Chapter 5. To study membrane protein organization, the supramolecular organization of a particular transmembrane protein Na^+, K^+-ATPase in the near-native membrane fragments purified from the outer medulla of rabbit kidney was investigated by atomic force microscopy (AFM). Evidence showed the oligomerization and common motif of this protein. These results are presented in Chapter 6.

Chapter 1

Introduction

1.1. Self-Organization in Cells

Cells are complex, highly organized, non-equilibrium systems. Throughout their lifecycle, they maintain dynamic aspects such as polarity and directional transport, compartmentalization, number and size of various organelles [3, 4]. Similar complex organization and dynamics are maintained at the level of subcellular organelles such as nuclei and Golgi complexes [5]. These organization and dynamics underlie cellular functions. Even though we know much about how cells and cellular substructures are organized, the emergence and maintenance of these dynamic aspects, and how they are related to cellular functions, remains an area of active research with numerous unanswered questions.

1.2. Cell Membranes and Their Components

This Thesis focuses on cell membrane organization. Cell membranes enclose the cell, separate cell contents from the extracellular environment. They not only serve as barriers to protect the cells from the outside environment, but also play important roles in cell shape maintenance, solute transport and signal transduction in and out of the cell, cell-cell identification and communication [6].

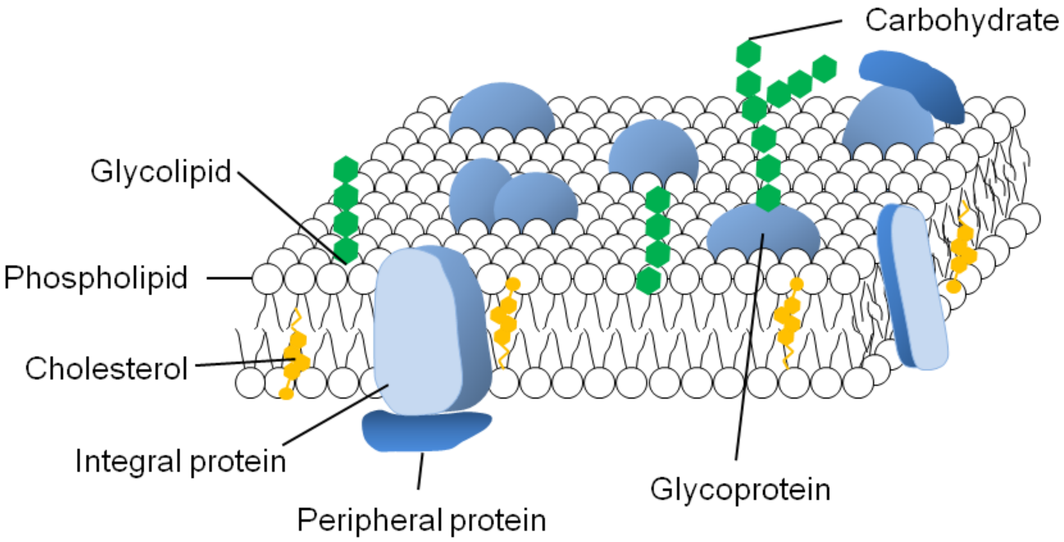

Figure 1.1. Schematic cross-sectional view of cell membrane.

The core structure of cell membranes is based on a lipid bilayer that is composed of two opposing leaflets, with membrane proteins embedded across the bilayer or bound to either side of the leaflets (Figure 1.1). In itself, this is of course a self-assembled system. In mammalian cells, the lipid bilayers are composed of phospholipids, sphingolipids, cholesterol, and glycolipids, among which cholesterol occupies ～30% mol%, glycolipids occupies ～5%, while phospholipids are the most abundant [7]. Membrane lipids have a hydrophilic head group and hydrophobic tails (Figure 1.2). This amphipathic character drives them to self-assemble into a bilayer, with the hydrophilic heads facing outside into the aqueous environment and the hydrophobic tails hidden inside (Figure 1.1). This bilayer serves as a barrier for polar and charged solutes, helping to maintain electrochemical gradients across the membrane.

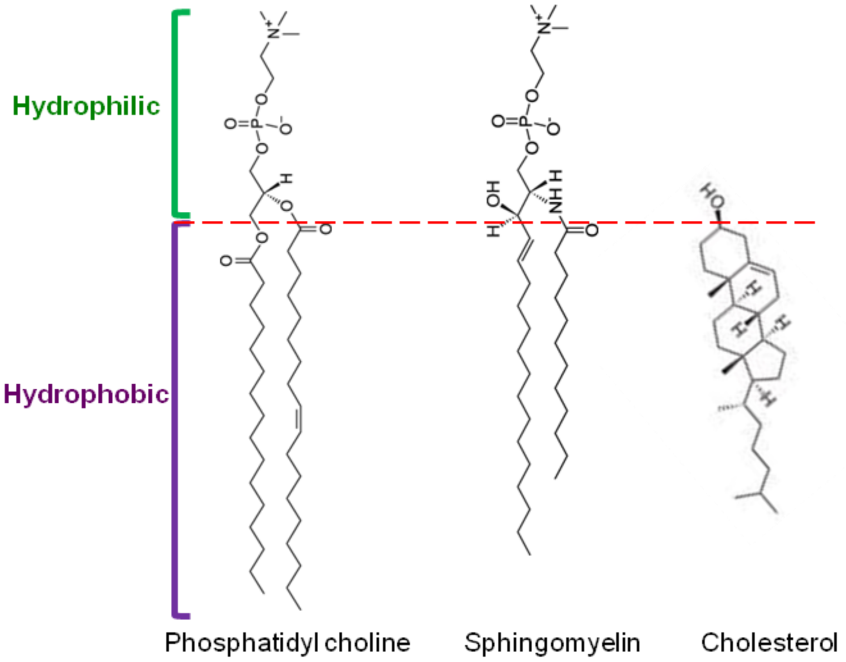

Figure 1.2. The structure of three major lipids in cell membranes: phosphatidylcholine, sphingomyelin, and cholesterol. Their hydrophilic and hydrophobic regions are marked in green and purple, respectively.

Membrane proteins in the bilayer can be classified into two types: integral proteins that span the membrane, and peripheral proteins that are temporarily bound to the membrane [8]. As described by the ‘fluid mosaic model’ of Singer and Nicolson [9], the lateral diffusion of lipids makes the bilayer a fluid matrix for the membrane proteins to move laterally and undergo conformational changes, facilitating their role as transporters of materials and information across the membrane. Further refinement of this model suggested that both lipids and proteins in the cell membranes are distributed in a non-random manner [10, 11]. This organization plays an important role in cell membrane functions such as transport, signal transduction, cell-cell identification and communication [12, 13].

1.3. Self-Organization in Cell Membranes at the Level of Lipids

Lipids in the cell membranes exhibit complex organization in both the transverse (perpendicular to the bilayer) and the lateral (in the plane of the bilayer) directions. This heterogeneous organization is essential for many cellular functions.

1.3.1. Transverse Lipid Asymmetry

In the transverse direction, lipids are asymmetrically distributed. Specifically, ‘reactive’ lipids like phosphatidyl serine (PS), phosphatidyl ethanolamine (PE), and phosphatidyl inositol (PI) are enriched in the cytoplasmic leaflet, while ‘non-reactive’ lipids like phosphatidyl choline (PC) and sphingomyelin (SM) are enriched in the extracellular leaflet [14-20] (Figure 1.3). This transverse lipid asymmetry has been suggested to be regulated by ATP-dependent and -independent lipid transporters [20-22]. Maintenance of this asymmetry is essential for many cellular functions, and vice versa, its loss is involved in various physiological and pathological processes including blood clotting, cell-cell interaction, and clearance of apoptotic cells [15, 23, 24]. For example, activation of platelets following vascular injury leads to PS exposure on the cell surface of platelets. This cell surface PS exposure catalyzes the assembly of prothrombinase complex on platelet surface, and significantly increases the production rate of thrombin, an important coagulation enzyme that cleaves fibrinogen to produce fibrin, which is necessary for clot formation [25, 26]. Cell surface PS exposure in apoptotic cells serves as a marker for the macrophage recognition and phagocytosis of the apoptotic cells [27-30]. Disordered PS exposure at the cell surfaces is related to a number of diseases. For instance, reduced PS exposure at the surface of activated platelets is responsible for Scott syndrome, a

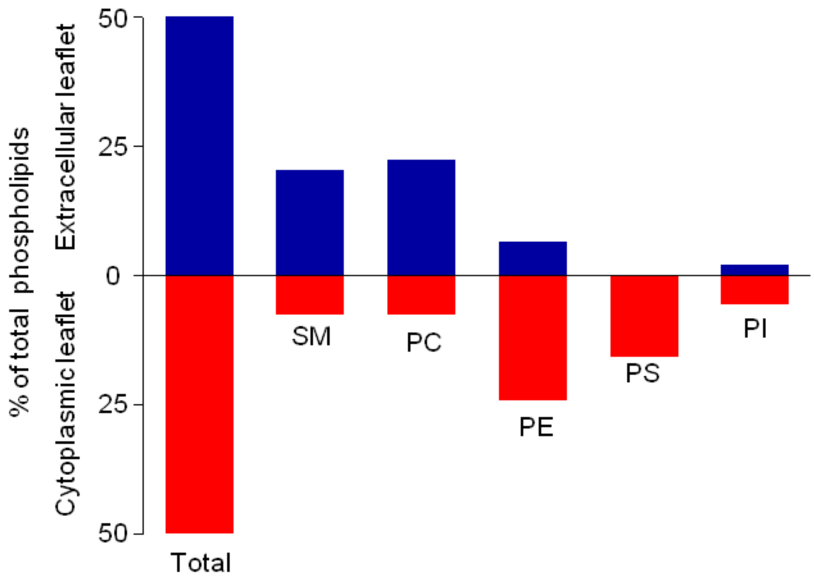

Figure 1.3. Transverse lipid asymmetry in cell membranes. The plot shows the transbilayer distribution of phospholipids across human erythrocyte membranes: total lipids (Total), sphingomyelin (SM), phosphatidyl choline (PC), phosphatidyl ethanolamine (PE), phosphatidyl serine (PS), and phosphatidyl inositol (PI). The blue bars represent the extracellular leaflet of the membrane, the red bars represent the cytoplasmic leaflet. The plot is modified from ref [3].

bleeding disorder [31]. Increased PS exposure on erythrocyte surface is found in sickle-cell anemia [32, 33].

1.3.2. Lateral Organization of Lipids

Compared to transverse asymmetry, lipid organization in the lateral direction is less well understood. Lipid compositional heterogeneities, sometimes referred to as 'lipid rafts' (Figure 1.4) are thought to exist. The 'raft' hypothesis [34] was based on the cholesterol and sphingolipid-enriched detergent-resistance membranes (DRMs) isolated from cell membranes after the treatment of nonionic detergents such as Triton X-100 or CHAPS [35, 36].

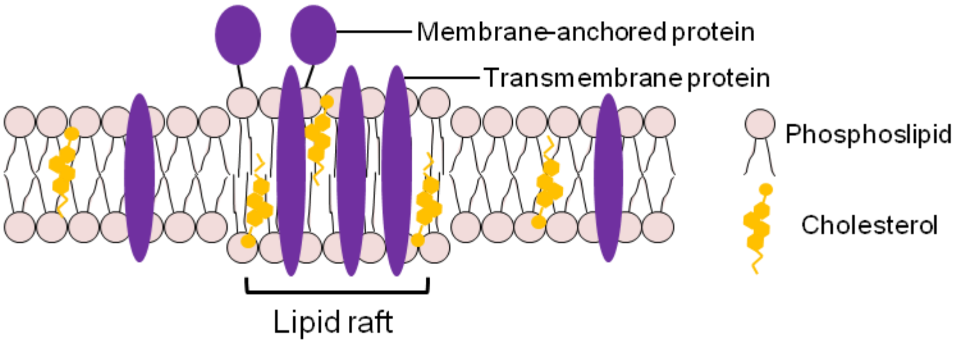

Figure 1.4. Schematic diagram of lipid raft.

Numerous studies have showed that many membrane proteins involved in cell signalling and trafficking were present in these DRMs, such as glycosylphosphatidylinositol (GPI)-anchored proteins and G proteins. [12, 36-43]. Cholesterol depletion from these extracted membranes disrupted the functions of these proteins [44, 45]. These results suggested the important roles of lipid rafts in signal transduction and membrane trafficking.

However, these DRMs were subsequently found to be artifacts of the detergent treatment, and did not exist in cell membranes [46, 47]. Instead, most evidence for the existence of lipid rafts in living cells is based on clustering of transmembrane and membrane-anchored proteins, suggesting the existence of lipid compositional heterogeneities on the order of a few tens of nanometers, with preferential partitioning of these proteins [48-54]. Direct evidence of the lateral heterogeneities of lipids in real cell membranes remains elusive. Only very recently, a stimulated emission depelition (STED) fluorescence nanoscopy study on the diffusion of single lipid showed the two types of diffusion of sphingomyelin in living cell membranes, free and hindered diffusion, the latter one being cholesterol-dependent, and at the scale of < 20 nm. No such heterogeneous diffusion was found with phosphoethanolamine [55]. These results support the existence of lipid rafts in living cells. However, lipid rafts have been difficult to reproduce in model systems. Typically micron-sized phase domains [56, 57] are observed. Critical fluctuations [58] may represent an adequate model of how lipids are organized laterally in cell membrane, but this remains the subject of research. Until now, there is no clear view of how membrane lipids organize into lateral heterogeneities in cell membranes, and how these heterogeneities function in cellular events such as signal transduction and membrane trafficking.

Despite years of research, questions remain about how lipids organize in cell membranes in both the transverse and the lateral directions, and how their dynamic changes participate in cellular functions. Therefore, there is a need for model systems that can mimic cell membrane lipid organization in both the transverse and lateral directions with physiological lipid compositions.

1.4. Self-Organization in Cell Membranes at the Level of Membrane Proteins

As discussed above, cell membranes are heterogeneous rather than homogeneous, with lipid-protein domains being thought to exist in the lateral direction. Accumulating evidence has showed that membrane proteins organize into clusters scaled from tens to hundred of nanometers [52, 53, 59-62]. The mechanism underlying protein clustering is not well understood, but it is generally accepted that it is related to protein-protein and protein-lipid interactions [63]. For many membrane proteins, oligomerization has been shown to be required for functionality such as signal transduction, solute transport, and immune response [64-68]. Common examples of membrane protein oligomers include the G protein-coupled receptor rhodopsin [69, 70], the channel porin OmpF [71], and some members of the ATPase family such as F-type ATPase (ATP synthase) [72]. For some other membrane proteins such as Na^+, K^+-ATPase, and H^+, K^+-ATPase, two P-type ATPases, potential oligomerization is still under debate. Evidence supporting the oligomerization of these proteins mainly comes from functional and kinetic studies. Direct evidence of their organization in cell membranes is still lacking.

Despite studies suggesting that protein-protein interactions [73, 74], and the restricted lateral mobility caused by the surrounding lipid bilayer environment are responsible for the formation and maintenance of the quaternary oligomer structures [63], the mechanisms underlying this organization, and its relevance to the function the proteins perform, are still not clear. Therefore we are studying the supramolecular organization of Na^+, K^+-ATPase, with the aim of understanding how this organization contributes to its function.

1.5. Model System Studies on Lipid Organization in Cell Membranes

1.5.1. Methods to Model Cell Membranes

Various lipid membrane model systems have been developed to study cell membrane organization and properties. These include monolayers [75], giant unilamellar vesicles (GUVs) [76], solid supported lipid bilayers (SLBs) [77], tethered lipid bilayers on the support [78], and bilayers on porous supports [79] (please see reviews [80-82]).

Membranes proteins have also been reconstituted into these free-standing [83-85] and supported lipid bilayers [86-90] to investigate their properties, activities, and interaction with the lipids.

1.5.2. Modeling Transbilayer Lipid Asymmetry

Models for studying transbilayer asymmetry remain scarce. They include bilayers prepared by Langmuir-Blodget and Langmuir-Schaefer methods [91], assembly of asymmetric bilayers across apertures [92], the formation of asymmetric liposomes [93-95], or using cell-derived membrane systems; see review [91], (but note that in that reference it is incorrectly stated that lipid bilayer prepared from liposomes on solid supports are invariably symmetric), as well as ref [95] for an exhaustive discussion of the methods. Each of these methods has its own limitations.

Meanwhile our group [96, 97] and others [98] have previously reported that lipid asymmetries develop spontaneously in bilayers prepared from liposomes composed of mixtures of PC and PS in Ca^{2+}-containing buffers, on TiO_2, a widely used implant biomaterial due to its biocompatibility [99]. In these bilayers, PS, which appears to interact strongly with TiO_2, is enriched in the surface-proximal leaflet and depleted from the surface-distal one. These observations are consistent with the early studies of lipid asymmetries induced by strong electrostatic interactions between cationic lipids and negatively charged oxide surfaces [100, 101]. The effect of support on the spontaneous transverse organization of lipids in supported systems is becoming better understood through the efforts of a number of groups [97, 98, 102-107]. However, this system only has two lipid components. As such, it is inadequate for studying properties of cell membranes and needs to be expanded to include a realistic composition.

1.5.3. Modeling Lateral Lipid Organization

Compared to the limited models for transverse lipid asymmetry, lateral segregation of membrane lipids has been extensively studied in monolayers, GUVs, and SLBs (please see reviews [11, 48, 108, 109]). Single-component lipid bilayers have different phases: subgel (L_c) phase in which the hydrocarbon chains are highly ordered; gel phase in which the lipid head groups are more hydrated, the hydrocarbon chains can be tilted ($L_{\beta'}$ gel phase) or not (L_β gel phase), but they are still ordered; liquid crystalline (L_α) phase (also called liquid-disordered (L_d) phase) in which the hydrocarbon chains are disordered, and bilayers are fluid. The transition between phases can be controlled thermodynamically by temperature. With increasing temperature, lipid bilayers undergo transitions from subgel to gel, and then to liquid phase. Transition from subgel to gel phase is called subtransition. Transition from gel to liquid-disordered phase is called main transition. For some lipids, a pre-transition step is needed from gel to liquid-disordered phase. This intermediate phase is called rippled phase ($P_{\beta'}$) in which the bilayers show ripple like structure [110] (Figure 1.5).

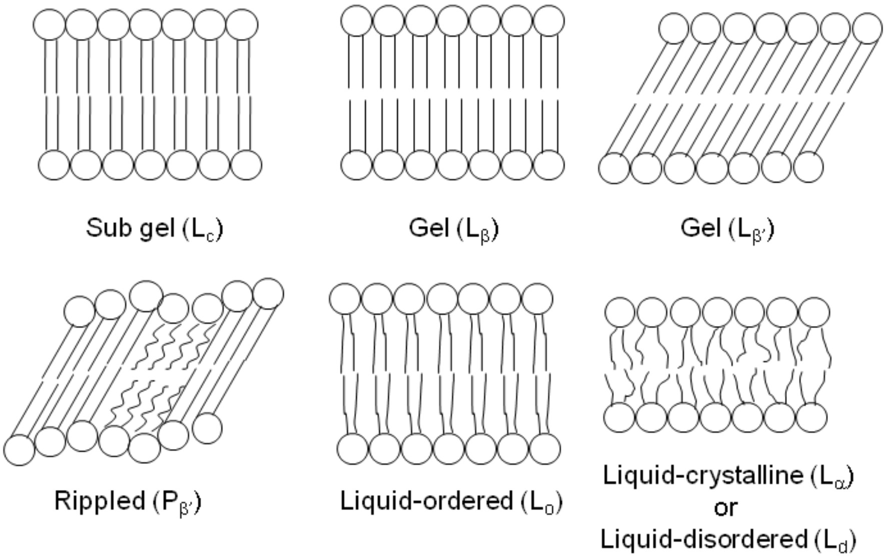

Figure 1.5. Schematic representation of various lipid phases.

The main transition temperature depends on the length and saturation of the lipid chains [111]. Lipids with shorter and unsaturated chains containing double bonds have low transition temperature, while lipids with longer and saturated chains have high transition temperature. The main transition in a single-component bilayer is very sharp, while in multiple-component bilayers, phase separation commonly occurs. Typically, a ternary mixture of unsaturated phospholipids/saturated phospholipids or sphingolipids/cholesterol segregate into liquid ordered (L_o) and liquid disordered (L_d) phases in both free-standing bilayers in GUVs [56, 112-114] and supported lipid bilayers [115-119]. Lipids in the segregated L_o domains are tightly packed and ordered as in gel phase, but laterally diffused as the L_d phase (Figure 1.5).

Treating the model membranes with the non-ionic detergent showed that L_o phase is more detergent resistant than the L_d phase [36, 56, 120]. In addition, DRMs extracted from the cell membranes were found to be enriched in cholesterol and sphingolipids [35]. These results suggested that the DRMs extracted from the cell membranes might also be in L_o phase. However, L_o phase domains observed in these models are micron-sized [56, 57], much bigger than the lipid raft size estimated in real cell membranes which is tens of nanometers [48-54]. Several recent studies showed the critical fluctuations in the L_o-L_d coexistence region at sub-micron scale in giant vesicles with ternary lipid mixture [121] and the giant plasma membrane vesicles isolated from living cells [122], suggesting the existence of nano-sized composition fluctuation in cell membranes. Cells may arrive at the critical point, where such fluctuations are expected, by adjusting lipid composition of the membrane [58]. Possibly this finding can merge the gap between model and real cell membrane systems, but the subject remains under investigation. In addition, most of the multi-component model membranes which mimic the lateral lipid organization of cell membranes are composed of lipids in the extracellular side of the cell membrane. Lipids in the cytoplasmic side of the cell membranes, such as PS and PE, have hardly been included. How lateral organization is coupled with transverse lipid asymmetry is largely unknown. Furthermore, cytoskeleton interacts with cell membranes rapidly and dynamically at micron or submicron scale [123]. Some membrane lipids were found to bind cytoskeleton proteins [124], including PS [125, 126] and phosphatidylinositol 4,5-bisphosphate (PIP2) [127]. Cytoskeleton was also found to be related to clustering of raft-associated protein [128]. However, how this dynamic membrane-cytoskeleton interaction influences the generation and maintenance of transverse and lateral membrane lipid organization is unclear.

Taken together, new model systems containing complex lipid components that can mimic cell membrane lipid organization in both the transverse and the lateral directions with physiological lipid compositions are required, and that is one of the goals of this Thesis.

1.6. Building a New Model System of Lipid Organization in Cell Membranes

A model membrane system is developed in this study based on SLBs on TiO_2 from lipid mixture containing low-melting and high-melting PC, PS, and cholesterol to mimic lipid organization in cell membranes. While in living cells membrane lipids interact with cytoskeleton, and the lipid asymmetry across the membrane is sustained by utilizing energy from ATP, in this model system, lipids interact with surface, and the lipid-surface adhesion energy supplies the free energy necessary to offset the entropy of mixing between the two leaflets. The evidence for the transbilayer PS asymmetry, the lateral organization, and lipid diffusion in these membrane-mimicking SLBs will be discussed in Chapter 5.

1.6.1. Supported Lipid Bilayers (SLBs)

Supported lipid bilayers (SLBs) (Figure 1.6) are popular cell membrane models [77, 81], and are routinely used in biophysical studies, and biosensor and biotechnology research [129-132]. SLBs can be formed by transferring two lipid monolayers onto a surface using the Langmuir-Blodgett (LB) technique [133], or by spreading unilamellar liposomes on hydrophilic surfaces [134]. The latter approach is more commonly used due to its simplicity and reproducibility; it leads to better quality bilayers and is amenable to transmembrane protein incorporation [87, 89, 90, 135, 136].

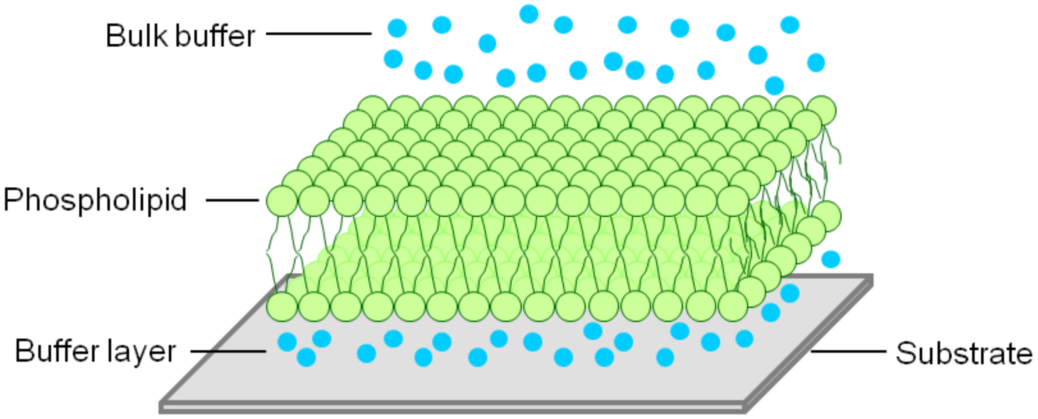

Figure 1.6. Schematic diagram of supported lipid bilayer.

1.6.2. Mechanisms, Pathways, and Driving Force For SLB Formation

There are Numerous studies of liposome behavior on different hydrophilic surfaces including silica [137-139], mica [140, 141], oxidized gold [138], and TiO_2 [96, 97, 139, 142], using various techniques such as quartz crystal microbalance (QCM) [98, 137, 138, 143], atomic force miscroscopy (AFM) [98, 137, 141], surface plasmon resonance (SPR) [144-146]. On some of these surfaces—mica, SiO_2, and TiO_2 at some conditions—SLBs form, on others—oxidized gold, and TiO_2 at some other conditions—they do not. Many factors have been found to influence liposome behavior and whether they rupture on the surface or not, including lipid composition and charge [137, 147], liposome size [138, 141], the presence of Ca^{2+} [137, 141, 148-150], ionic strength and pH [143, 147, 151, 152], and surface chemistry [139, 151, 153, 154]. These experiments together with the theoretical studies [155-158] have provided insights into the mechanisms, pathways and the driving force for SLB formation from fusion of unilamellar vesicles on the surface, but have not yet led to a consistent mechanistic picture.

Empirically, four possibilities have been observed when liposomes interact with a surface, in the order of increasing lipid-surface interactions: no adsorption on the surface due to the repulsion between the liposomes and the surface; formation of a vesicular layer from adsorbed liposomes; formation of an SLB by collective fusion and rupture of the neighboring adsorbed liposomes; formation of an SLB by individual rupture of the adsorbed liposomes [98, 137, 141] (Figure 1.7).

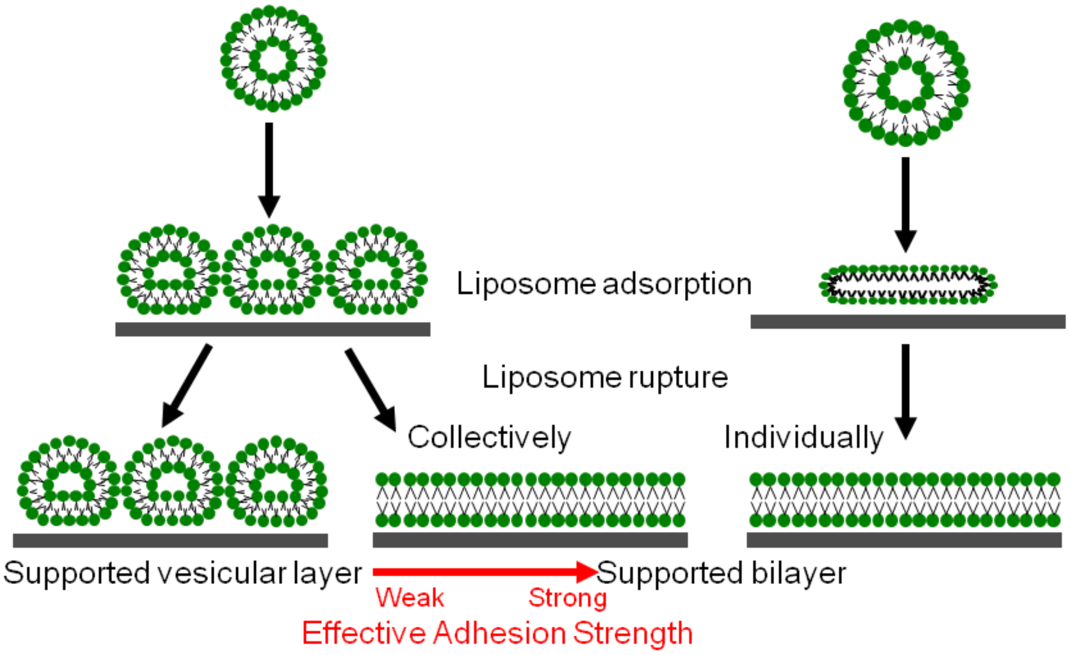

Figure 1.7. Schematic diagram of pathways for SLB formation.

Deformation of liposomes (GUV or SUV) upon adsorption on the surface has been demonstrated theoretically [155, 156, 159] and experimentally [160-162] (Figure 1.8). The driving force for liposome adsorption and deformation, as well as bilayer formation is lipid-surface attraction. Lipid-surface interaction is a combination of electrostatic interactions, van der Waals, and hydration forces [163] (Figure 1.9). Bending energy and membrane tension oppose the driving force. When the membrane-impermeable osmotically active substances (OAS) are included inside or outside the liposomes, osmotic pressure will build up due to the deformation-induced liposome volume change, and the expulsion of water from the liposomes (Figure 1.8), also resisting adhesion. Externally-imposed osmotic stresses by changing the outside buffer composition may work with or against the adhesion energy depending on the direction of the gradient [155], but these are typically minor.

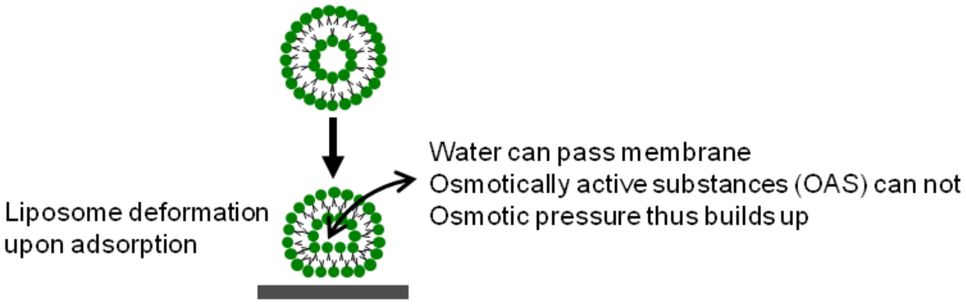

Figure 1.8. Schematic illustration of liposome deformation upon adsorption and the establishment of osmotic pressure

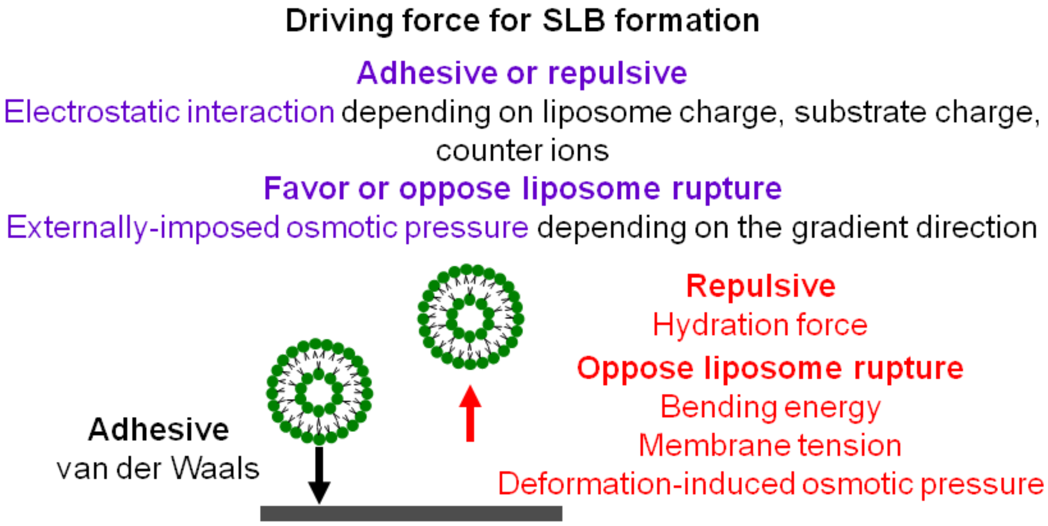

Figure 1.9. Schematic representation of the driving force for SLB formation.

1.7. Questions to be Addressed About the Mechanisms of SLB Formation

Despite more than 20 years of research, questions remain about the mechanisms of SLB formation from adsorbed liposomes. Although it is generally accepted that adsorbed liposome behavior depends on the lipid-surface interaction and the kinetic effects that define their stability, how various factors affect the lipid-surface interaction and the kinetics is largely unknown. This lack of knowledge limits the applicability of the SLBs. During the development of the membrane-mimicking asymmetric SLBs on TiO_2, it was possible to investigate the effects of lipid composition, buffer composition, temperature, surface chemistry and roughness, on the SLB formation process. These results will be discussed in Chapter 3, 4, and 5.

1.7.1. Is the Electrostatic Interaction Between Zwitterionic Liposomes and Oxide Surfaces Attractive or Repulsive?

There has been some controversy in the literature about whether the electrostatic interactions between zwitterionic lipids and negatively charged surfaces are attractive or repulsive. Cremer et al. studied SLB formation from zwitterionic liposomes doped with small amount of negatively or positively charged (fluorescent) lipids on negatively charged glass surface at various pH and ionic strength [147]. The authors of the study found that neutral and positively charged liposomes formed bilayers under all conditions tested, while liposomes containing as little as 1% of negatively charged lipids formed SLBs only under a limited set of conditions of high ionic strength and low pH (reducing pH reduces surface charge on the glass surface). More recently, Richter et al. studied adsorbed liposome behavior as a function of the liposome charge density at a constant pH and ionic strength (a mirror situation to that studied by Cremer et al) [137]. Similarly, they observed SLB formation from positively charged, zwitterionic, and moderately negatively charged liposomes—but not from liposomes that carried too much negative charge. These results fit into the proposal by Cremer et al. that liposome behavior at negatively charged surfaces is governed by van der Waals interactions, which are always attractive, and electrostatic interactions, which can be repulsive (negatively charged liposomes) or attractive (positively charged liposomes). There is a net-attractive interaction between zwitterionic liposomes and negatively charged surfaces, which in this picture is due to the van der Waals interactions.

Building on these earlier studies, Cho et al [151] found that bilayers formed from zwitterionic liposomes on TiO_2 at pH close to, or below, the isoelectric point of the oxide (~ 5.5 [164]). In other words, stronger liposome-surface attraction was observed when surfaces were closer to being neutral (the isoelectric point) or slightly positively charged. Consistent with the above picture, the results of Cho et al. suggest that electrostatic interactions between zwitterionic liposomes and negatively charged oxide surfaces are repulsive, and are weakened by reducing the charge on the oxide surface.

In the studies discussed above, the strength of attraction between liposomes and surfaces was qualitatively evaluated from liposome behavior. Particularly, in the case of Cremer et al.[147], SLB formation corresponds to stronger attraction than mere liposome adsorption. In the later studies [137, 151], the SLB formation pathway—direct or neighbor-induced rupture—could be distinguished as well. In that case, the direct rupture, where each individual liposome ruptures upon adsorption, is thought to correspond to a stronger interaction than the neighbor-induced rupture, where adsorbing liposomes need to interact with their neighbors in order for the SLB to form.

This simple picture of van der Waals and electrostatic interactions governing liposome behavior began to be challenged by results of studies that focused on the effects of ionic strength on the zwitterionic liposome behavior at surfaces. Seantier et al. [152] and Boudard et al. [143] found stronger attraction between zwitterionic liposomes and the negatively charged SiO_2 surface at low NaCl concentrations than at high NaCl concentrations. Interaction strength was inferred qualitatively from the SLB formation pathway: at low ionic strengths, liposomes ruptured upon adsorption (direct rupture, strong attraction), while at high ionic strength, liposomes required neighbors to rupture (neighbor-induced rupture, weaker attraction). These results could be taken to suggest that the electrostatic interactions between zwitterionic lipids and negatively charged surfaces were, perhaps, attractive.

Finally, Anderson et al. [165] measured the adhesion strength of a DMPC bilayer on silica surface with the surface forces apparatus at constant ionic strength in PBS buffer with 150 mM NaCl. They arrived at a range of values for the adhesion energy: 0.5 – 1 mJ/m^2, which is far stronger than the expected van der Waals attraction alone (0.1 mJ/m^2), and the adhesion between two PC bilayers (less than 0.1 mJ/m^2) [166-168]. They explained this strong adhesion in terms of an attractive electrostatic interaction that occurs between a neutral and a charged surface at a constant potential (150 mM NaCl). (In the limit of constant charge, the electrostatic interaction between a neutral and a charged surface is expected to be repulsive). The assumption of a constant potential limit requires a charge regulation mechanism that was not discussed by the authors.

In the previous studies of liposome behavior, the effect of ionic strength on adsorbed liposomes was investigated by varying electrolyte concentration [143, 147, 152]. However, osmotic pressure, which builds up due to liposome deformation and water expulsion upon liposome adsorption, also changes with electrolyte concentration. Our group has shown that this osmotic pressure build-up plays an important role in determining the SLB formation kinetics [169]. Therefore, both electrostatic and osmotic effects should be considered in the effect of electrolyte concentration on liposome behavior on surfaces. As a result, the sign (attractive or repulsive) of the electrostatic interactions between zwitterionic lipids and negatively charged surfaces should also be re-evaluated. Another aim of the Thesis is to separately investigate the osmotic and electrostatic contributions to the zwitterionic liposome-surface interaction in electrolyte buffer. This was achieved by investigating liposome behavior in buffers with varying NaCl concentration but constant tonicity, adjusted with sucrose. A theoretical model was also used to describe the observations, leading to the conclusions that the effect of ionic strength on liposome-surface interactions was a combination of osmotic and electrostatic effects, and the electrostatic interactions between zwitterionic liposomes and negatively charged surface were repulsive. This work is discussed in Chapter 3.

1.7.2. Lipids Leaving the Surface During SLB Formation

SLBs can be prepared from unilamellar liposomes on the hydrophilic surfaces. During the formation process, some of the lipids must leave the surface (Figure 1.10). There are several arguments and lines of evidence for this. A layer of surface-adsorbed liposomes that serves as a precursor for SLB formation may contain more lipids than is needed to form a confluent SLB. The amount of lipid excess depends on the number of liposomes on the surface and the number of lipids per liposome. This last point arises because for small liposomes, the difference between the number of lipids in the inner and the outer leaflet can be quite significant (factor of two) [170], and

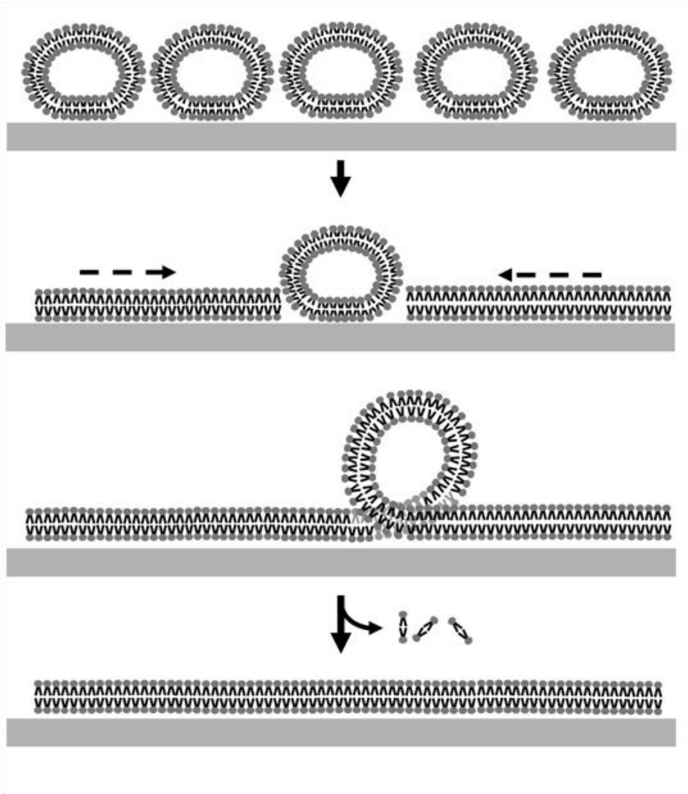

Figure 1.10. Formation of supported lipid bilayers (SLBs) from adsorbed liposomes involves lipid loss from the surface. Liposomes adsorbed on a surface (top) rupture to form supported lipid bilayers (SLBs, bottom). However, a layer of adsorbed liposomes may contain more lipids than can be accommodated in an SLB. Excess of lipids is removed from the surface in some manner during the SLB formation process. Middle images illustrate schematically one possibility, where a rupturing liposome surrounded by the lipid patch locally leads to an excess of lipids. The form, in which lipids are removed, is not clear.

therefore the area covered the surface by a lipid bilayer patch that results from the rupture of a liposome is smaller than expected based on liposome size. This issue is discussed in some detail in ref [171]. For a layer of non-deformed 25 nm liposomes covering the surface at the random close packing limit of ~ 0.55 [172], there are ~ 1.6 × more lipids than needed to cover the surface of the same area with a confluent bilayer. When performing this calculation, the area per lipid was taken as 0.72 nm^2 from ref [173], and the number of lipids in the liposomes was calculated from the areas of the outer and inner leaflets assuming a bilayer thickness of ~ 3.7 nm [170].

This rather simplistic argument does assume a significant concentration of liposomes on the surface required for SLB formation to be initiated, but it is supported by several experimental findings. During their measurements of SLB formation with a QCM – SPR instrument, Reimhult et al. showed loss of lipid mass from the surface [146]. Subsequently, Weirich et al. similarly observed lipid loss in fluorescence microscopy experiments following the SLB formation process [174]. Similar evidence has been provided from ellipsometric measurements [175], leading to the suggestion by Stroumpoulis et al.[175] that the desorption of the excess lipid was the rate-limiting step in the SLB formation under some conditions. What remains unclear is the form in which the lipids depart and the effect this process has on the overall kinetics of the SLB formation.

In the course of my studies, tubular structures coexisting with the bilayer were observed during the formation of SLBs on TiO_2. By visualizing the growth process of the tubular structures through a combination method of time-resolved fluorescence microscopy and fluorescence recovery after photobleaching, it was concluded that late stages of SLB formation involve both desorption of excess lipids from the surface and continued adsorption of liposomes from solution. These results are discussed in Chapter 4.

1.8. Studying Protein Organization in Cell Membranes

Another part of the Thesis is to study protein organization in cell membranes. Membrane protein organization was explored by investigating the supramolecular organization of a particular transmembrane protein, the Na^+, K^+-ATPase, in near-native membrane fragments purified from cell membranes.

1.8.1. Na^+, K^+-ATPase and Its X-Ray Structure

Na^+, K^+-ATPase, a transmembrane protein expressed in almost all the animal cells, is a member of the P-type ATPase family [176]. It utilizes energy from ATP hydrolysis to transport Na^+ out and K^+ into the cell to maintain an electrochemical gradient across the cell membrane which is essential for fundamental cell functions such as solute transport, signal transduction and cell volume regulation [177]. X-ray structures of Na^+, K^+-ATPase from pig kidney [1] and from shark rectal gland [178, 179] revealed that this protein is composed of an α-subunit containing ten transmembrane helixes and a large cytoplasmic domain, a β-subunit containing one transmembrane helix and a small extracellular domain, and in some tissue such as the kidney, a membrane-spanning γ-subunit (Figure 1.11).

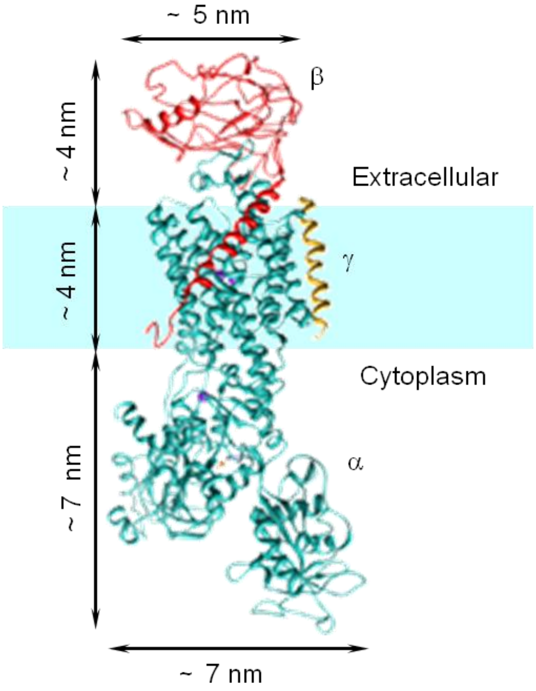

Figure 1.11. X-ray structure of Na^+, K^+-ATPase.

1.8.2. Previous Findings Concerning Supramolecular Organization of the Na^+, K^+-ATPase

Over the past 30 years, there has been a controversy as to whether the minimal functional unit of Na^+, K^+ ATPase is a monomer, (αβ), a dimer, $(\alpha\beta)_2$ [180, 181], or a higher-order oligomer (e.g., a tetramer, $(\alpha\beta)_4$) [182]. For detailed discussion of this subject, please see the reviews by Taniguchi et al., Martin, and Clarke [182-184]. After several structures of P-type ATPases have been solved in different conformations, it has become clear that the $(\alpha\beta)$ monomer is sufficient for ion transport activity with the ion being transported through the channel at the centre of the α subunit [1, 178, 185, 186]. Functional studies using reconstituted shark Na^+, K^+-ATPase in phospholipid vesicles also showed that $(\alpha\beta)$ monomer can transport ions [187]. Kinetic and labeling studies, however, continue to indicate that oligomers of these ATPases are present and functionally relevant [184]. For example, Froehlich et al. reported kinetic evidence of the oligomerization of Na^+, K^+-ATPase and suggested a sequential conformational coupling between the two catalytic subunits in the oligomer [188]. Clarke et al. interpreted the results of their kinetic studies of purified Na^+, K^+-ATPase-containing membrane fragments from pig and rabbit kidneys in terms of a two-gear dimer mechanism. In their model, low ATP concentrations favored formation of dimers while monomers were prevalent at high ATP concentrations [189-191]. They further showed that Na^+, K^+-ATPase is in the monomeric state in shark at both low and high ATP concentration, but is in the dimeric state in mammals at low ATP concentration, and converts into monomeric state when ATP concentration is increased. The authors suggest that the difference in the oligomeric state of the ATPase in shark and in mammals is an adaptation to the different thermal environments under which these organisms exist [192].

Direct evidence of the dimeric or oligomeric state of Na^+, K^+-ATPase in native membranes is however still lacking. Most information is derived from kinetic studies, such as the ones described above, low-resolution electron microscopy (EM) images showing either randomly close-packed assemblies, or rows of the αβ-protomers, or cross-linking studies [193]. Further indirect evidence comes from EM and atomic force microscopy (AFM) studies of 2D crystals, where dimers and higher-order oligomers are often observed [194-198]. However, these crystals do not necessarily reflect the native state of Na^+, K^+-ATPase assembly. The protein in them tends to lose enzyme activity, perhaps due to the stresses or unnatural contacts enforced by the crystallization process.

In this study, high resolution AFM images of Na^+, K^+-ATPase-containing near-native membrane fragments purified from outer medulla of rabbit kidney showed that this protein is present as oligomers of various orders, with the tetramer $(\alpha\beta)_4$, being the most commonly occurring motif. These results are discussed in Chapter 6.

Chapter 2

Experimental

In this chapter, materials, methods, and techniques used in the Thesis are described.

2.1. Materials

Lipids used in this Thesis—dioleoyl phosphatidyl choline (DOPC), dipalmitoyl phosphotidyl choline (DPPC), dioleloyl phosphatidyl serine (DOPS), cholesterol, and chain-labeled 18:1-12:0 NBD-PC and 18:1-12:0 NBD-PS—were purchased from Avanti Polar Lipids (Alabaster, Alabama, USA) in powder form and stored at – 20 ℃. Chloroform (≥99%), methanol (≥99.6%), acetone (≥99.5%), salts (HEPES, Trizma base, imidazole, glycine, NaCl, $CaCl_2$, $MgCl_2$, EDTA) and sucrose, glycerol, bromophenol blue, acrylamide, hydrochloride acid, acetic acid, sodium dodecyl sulfate (SDS), cuvette cleaner, melittin from honey bee venom, were purchased from Sigma-Aldrich (Madrid, Spain). Ethanol (≥99.8) was purchased from Scharlau (Barcelona, Spain). Deuterated chloroform ($CDCl_3$) (≥99.96%) was purchased from Euriso-Top (Paris, France). Cobas cleaner was purchased from Roche (Mannheim, Germany). Ammonium persulfate, β-mercaptoethanol, Coomassie Brilliant Blue R-250 were purchased from Bio-Rad Laboratories (Barcelona, Spain).

Table 2.1 lists the buffers used throughout the Thesis, together with the particular chapters where they were used. All buffers were prepared in Nano-pure water produced with a Diamond UV water purification system (Branstead International, Iowa, USA). All the buffers were filtered through a 0.22 μm syringe filter (Fisher Scientific, Madrid, Spain), and degassed in a water bath (Fisher Scientific, Madrid, Spain) for 30 minutes immediately prior to use.

25 mm and 15 mm thickness #1 (0.13-0.16 mm) glass slides were purchased from Menzel-Glaser (Braunschweig, Germany). Silicon wafers were purchased from University Wafer (South Boston, MA, US). 5 MHz TiO_2-coated crystals were purchased from Biolin Scientific AB (Solna, Sweden). TiO_2-coated glasses, SiO_2-coated glasses were prepared by in-house sputtering. 15 mm diameter mica disks were purchased from SPI Supplies (West Chester, PA, US).

Table 2.1. Buffers used in the Thesis.

Buffers	**Chapter**
5 mM HEPES, pH 7.4	3, 5
10 mM HEPES, 2 mM $CaCl_2$, pH 7.4	4, 5
10 mM HEPES, 150 mM NaCl, 2 mM $CaCl_2$, pH 7.4	5
10 mM HEPES, 150 mM NaCl, pH 7.4	5
10 mM HEPES, 150 mM NaCl, 2 mM EDTA, pH 7.4	5
5 mM HEPES, 25 mM sucrose, pH 7.4	3
5 mM HEPES, 50 mM sucrose, pH 7.4	3
5 mM HEPES, 75 mM sucrose, pH 7.4	3
5 mM HEPES, 150 mM sucrose, pH 7.4	3
5 mM HEPES, 300 mM sucrose, pH 7.4	3
5 mM HEPES, 150 mM NaCl, pH 7.4	3
5 mM HEPES, 75 mM sucrose, 150 mM NaCl, pH 7.4	3
5 mM HEPES, 75 mM sucrose, 112.5 mM NaCl, pH 7.4	3
5 mM HEPES, 150 mM sucrose, 75 mM NaCl, pH 7.4	3
Nano-pure water (18 MΩ resistance)	4, 5
25 mM Imidazole, 1 mM Tris-EDTA pH 7.5, 1% sucrose	6
10 mM Tris-HCl, 2 mM $MgCl_2$, pH 6.8	6
10 mM Tris-HCl, 25 mM $MgCl_2$, pH 6.8	6
10 mM Tris-HCl, 150 mM KCl, pH 6.8	6
10 mM Tris-HCl, 30 mM KCl, 25 mM $MgCl_2$, pH 6.8	6
10 mM Tris-HCl, 75 mM KCl, 25 mM $MgCl_2$, pH 6.8	6
10 mM Tris-HCl, 150 mM KCl, 25 mM $MgCl_2$, pH 6.8	6
10 M Tris-HCl, 150 mM KCl, 1 mM $MgCl_2$, pH 6.8	6

2.2. Liposome Preparation and Characterization

2.2.1. Liposome Preparation: Principles

Liposomes are spherical particles with an inner aqueous core encircled by one or several (phospho)lipid bilayer [199] (Figure 2.1). Since they were first discovered in 1965 [200], they have served as a versatile cell membrane model and have been widely applied in drug delivery and biosensor fields [81, 82, 201-203]. Liposomes can be classified according to their lamellarity and size: multilamellar vesicles (MLV) (500-10,000 nm) which are composed of several concentric lipid bilayers; unilamellar

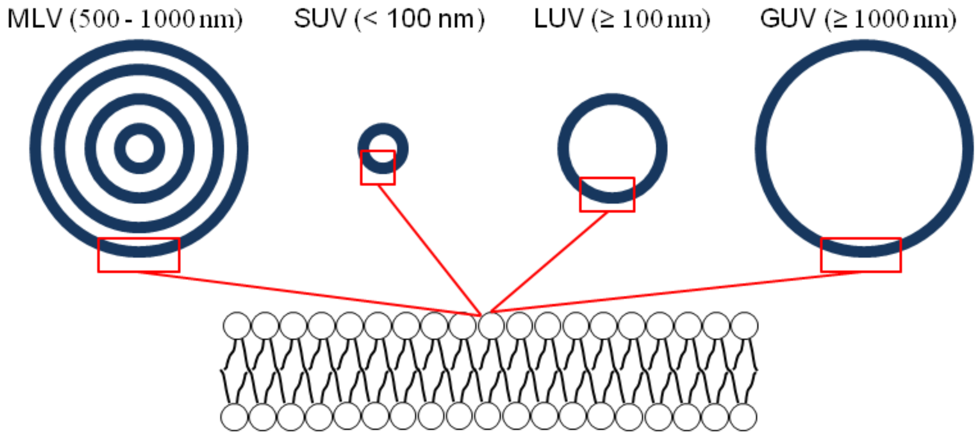

Figure 2.1. Schematic representation of liposome classification. Multilayer vesicles (MLVs) are made of several concentric lipid bilayers, unilamellar vesicles, including small, large and giant unilamellar vesicles (SUVs, LUVs, GUVs) are made of one closed bilayer.

liposomes which are composed of only one bilayer, including small unilamellar vesicles (SUV) (< 100 nm), large unilamellar liposomes (LUV) (≥ 100 nm) and giant unilamellar liposomes (GUV) (≥ 1000 nm) [203] (Figure 2.1).

MLVs form spontaneously upon hydration of lipid films (Figure 2.2) [200]. They can then be broken down into SUVs and LUVs by various mechanical means such as sonication [204], extrusion [205], or freeze-thaw [206], all of which have one thing in common: they entail the formation of an intermediate state, bilayer phospholipid fragments (BPFs) [207]. The thermodynamic instability at the edge of the BPFs causes them to bend and self-close into liposomes [207] (Figure 2.2). The size of the resulting

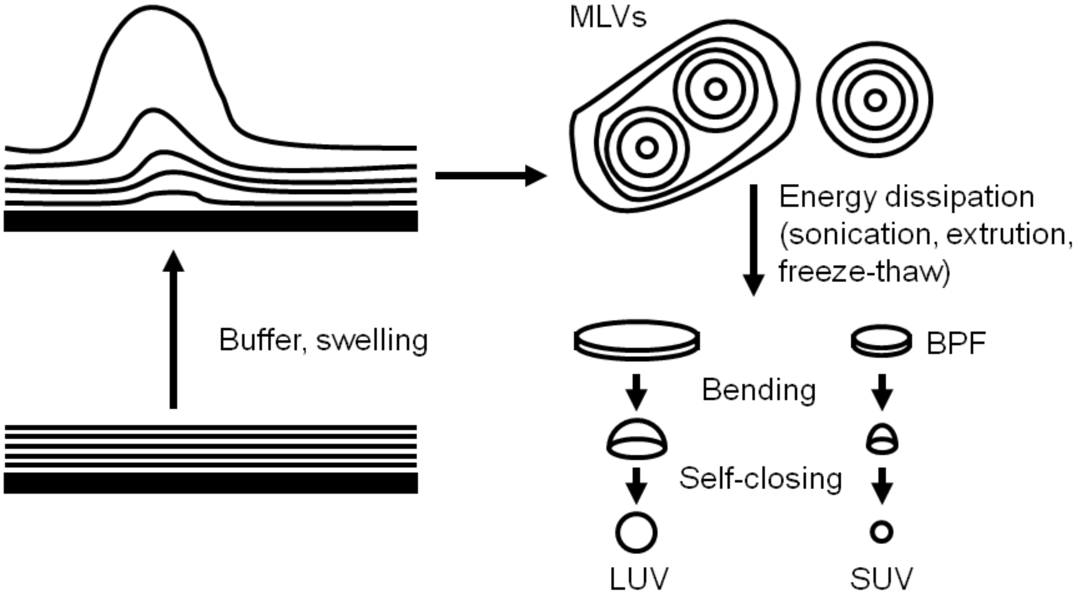

Figure 2.2. Schematic representation of unilamellar liposome preparation. Starting at the bottom left: Dry lipid film is hydrated and swells, shedding MLVs, that can be broken down into LUVs or SUVs by various preparation methods. Unilamellar liposome formation proceeds via bilayer fragments (BPFs).

liposomes is controlled by two factors: the size of the original fragments, which depends on the energy that is applied, and the time the fragments are allowed to equilibrate. As such, sonication produces smaller liposomes than extrusion, because of the higher energies and shorter time between successive bursts. Lipid packing in sonicated liposomes is discussed in Huang et al. [170].

LUVs can also be formed by detergent removal from a solution of micelles composed of lipids and detergents [208]. This process occurs essentially by the same mechanism, with BPFs stabilized by detergent caps.

Freshly prepared liposomes can be characterized with a number of techniques such as dynamic light scattering (DLS), which provides a measure of their size, in combination with the ζ-potential measurements, a measure of surface charge, and transmission electron microscopy (TEM) analysis of frozen-hydrated or negatively stained preparation, which also provides a measure of their size and morphology (lamellarity).

2.2.2. Dynamic Light Scattering and ζ-potential Measurements

Dynamic light scattering (DLS) [209] is a technique used to determine the mean size or size distribution of particles in a solution. It measures the light scattered by the particle suspension. The intensity of the scattered light fluctuates with time due to Brownian motion of the particles [210]. When the intensity of scattered light at certain time is compared with the one at very short time later, they are very similar, which is also called strongly correlated. When compared with the signal intensity at a somewhat later time, they are less correlated. The correlation decays with time until it eventually reaches zero (no correlation, Figure 2.3a). Large particles move slowly, thus correlation decays slowly when compared to small particles which move quickly (Figure 2.3b). By analyzing the time-dependent fluctuation of the scattered light, DLS determines the diffusion coefficient of the particles, and calculates the size of the particles from the diffusion coefficient using Strokes-Einstein equation [210, 211]:

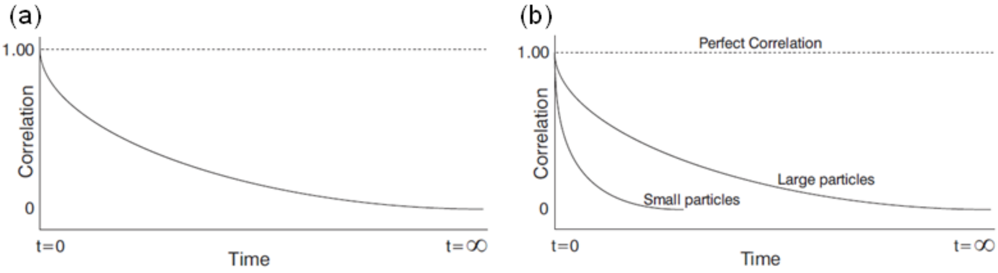

Figure 2.3. Illustration of scattered light intensity correlation function. The correlation is plotted as a function of time. (a) The correlation decays by time until it finally reaches zero. (b) The correlation of large particles decays more slowly than the small particles. Plots taken from the manual of Zetasizer Nano ZS (Malvern, UK).

$$d_H = \frac{\kappa T}{3\pi\eta D}, \text{ (Equation 2.1)}$$

where d_H is the hydrodynamic diameter which is the size of a sphere that has the same diffusion coefficient as the particle, D is the translational diffusion coefficient, k is Boltzmann's constant, T is the absolute temperature and η is the viscosity of the dispersant.

The same system can also be used to study the charge of colloidal particles. Most colloidal dispersions in aqueous media have an electric charge. The net charge at the particle surface attracts the counter ions with the opposite charge in the suspension to form an electrical double layer around the particle. This electrical double layer has two regions. In the inner region (Stern layer), ions with the opposite charge to that of the particle surface are directly adsorbed, or firmly bound to the particle. In the outer region (diffuse layer), the distribution of ions of both charge is decided by the balance

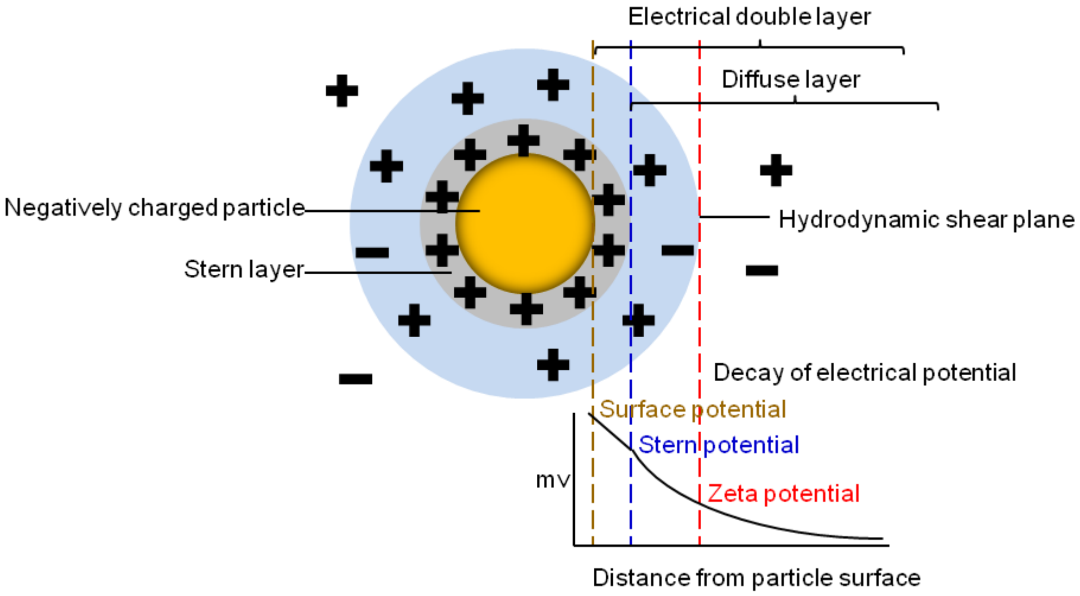

Figure 2.4. Schematic representation of ζ-potential of a negatively charged particle in bulk solution, modified from Ref [2].

between the attractive electrostatic force and random thermal motion, and the electrostatic potential in this region decays with the distance from the particle surface (Figure 2.4). Within the diffuse layer, there is a boundary inside which the ions are more firmly associated with the particle than the ones outside. When the charged particle moves, ions in the Stern layer, together with the ones inside the boundary in the diffuse layer, move with it, while the ions outside the boundary of the diffuse layer stay with the bulk dispersant. The electrical potential at the boundary (hydrodynamic shear plane) is defined as zeta potential (ζ-potential) [2] (Figure 2.4). When an electric field is applied to the particle suspension, the charged particles migrate towards the electrode of the opposite polarity with a velocity related to their ζ-potential. Instead of measuring intensity fluctuation of the scattered laser which is used to decide the particle size, DLS uses Doppler shift of the scattered light from the moving particles in an applied electric field to determine the ζ-potential of the particles. Doppler shift is the frequency shift between the light scattered from the particle and the reference light beam. By measuring the Doppler shift, the electrophoretic mobility (velocity) of the charged particles in the applied electric field can be determined according to the following equation:

$$\upsilon = \frac{\Delta f \lambda}{2\sin(\theta/2)}, \text{ (Equation 2.2)}$$

where υ is the velocity of the particle, Δf is the frequency shift, λ is the wavelength of the laser, θ is the scattering angle. This technique is called laser

Doppler velocimetry (LDV) [2]. ζ-potential of the particles can then be calculated from the electrophoretic mobility (velocity) using Henry's equation [212]:

$$U_E = \frac{2\varepsilon\zeta f(ka)}{3\eta}$$, (Equation 2.3)

where U_E is the electrophoretic mobility, ε is the dielectric constant of the dispersant, ζ is the ζ-potential, $f(ka)$ is Henry's function, η is the viscosity. k is the reciprocal length of the electrical double layer thickness $1/k$. a is the radius of the particle size. When measuring particles in aqueous media at moderate ion concentrations (the electrical double layer is think compared to particle size), $f(ka)$ has the value of 1.5, which is termed as Smoluchowski approximation. When measuring small particles in non-aqueous media, $f(ka)$ has the value of 1, which is termed as Huckel approximation.

2.2.3. Transmission Electron Microscopy (TEM)

The overall working principle of an electron microscope is similar to that of a light microscope except for that it uses an electron beam as a replacement of light source to illuminate the specimen (Figure 2.5). Due to the small wavelength of electron, the electron microscope can provide the resolution down to 0.2 nm, many orders of magnitude higher than can be achieved by light microscopy [213]. A transmission electron microscope (TEM) consists of a high voltage electron source, a set of electromagnetic lenses, a specimen holder, and an imaging system. Briefly, a beam of electrons is generated from the electron source, passes through the electromagnetic lenses to focus into a very thin beam, and then illuminates the specimen. When the electrons are illuminated on the specimen, some of them get scattered due to the repulsion from the electrons surrounding the atom nucleus, while others transmit through the specimen. How much the electrons transmit depends on the electron density of the specimen. Contrast is therefore built up by different scattering and transmission ratio of electrons at different locations in the specimen. Detecting electromagnetic lenses are used to collect the electrons transmitted through the specimen, and generate a magnified two-dimensional ‘shadow’ projection image of the specimen on a fluorescent screen, or charge-coupled device (CCD) camera (Figure 2.5).

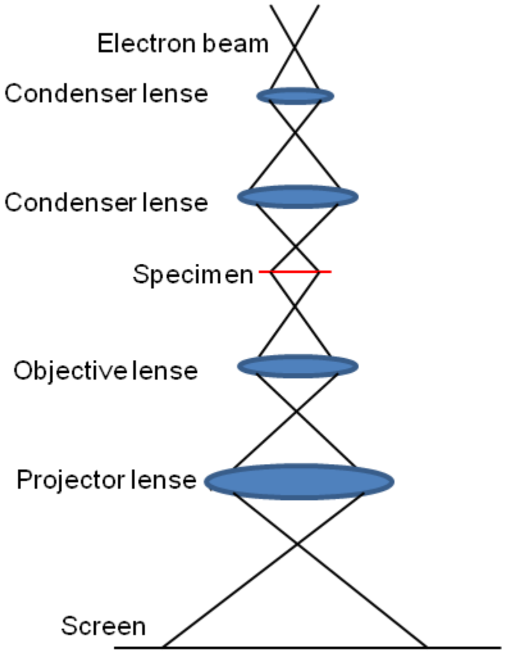

Figure 2.5. Schematic representation of the working principle of TEM

There are generally two factors affecting contrast: specimen thickness and atomic number of the elements making up the specimen. The thinner the specimen is, the easier it is for the electrons to pass through. Similarly, the smaller the atomic number is, the less they scatter with the electrons. Therefore, heavy metal salts such as the ones derived from uranium and molybdenum are commonly used to stain the sample to obtain higher contrast. The specimen itself is not stained, while the surrounding areas are stained. As a result, the electrons get scattered in the stained area, but transmit through the specimen, and the specimen appears light in the dark background in the projection image. For this reason, this staining method is termed negative staining (Figure 2.6 left).

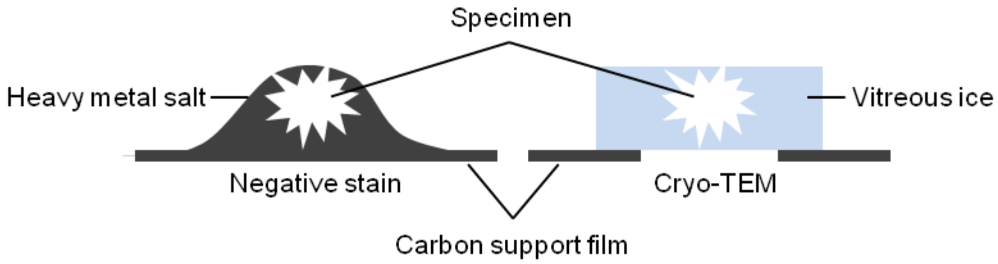

Figure 2.6. Schematic representation of negative staining and sample preparation for cryo-TEM.

Because electron microscopy works in a vacuum, the specimens need to be fixed and dehydrated on a support film. The conventional negative staining method will cause shape change and damage of the specimen. To avoid artifacts associated with drying and staining, cryo preservation methods have been developed for TEM. In cryo-TEM, the specimen suspended in aqueous solution that is rapidly frozen in liquid ethane cooled to liquid nitrogen temperature. This results in a frozen-hydrated specimen embedded in a thin film of vitreous (glass-like) ice (Figure 2.6 right). This allows the observation of aqueous specimens close to their natural, hydrated state. However, sample preparation is complicated, and the contrast is not as high as with the negative staining.

2.2.4. Liposome Preparation and Characterization: Protocols

Lipid stock solutions were prepared by dissolving lipid powder in chloroform in clear glass screw-cap vials with PTFE liners (Sigma-Aldrich, Madrid, Spain), and stored at – 20 °C. Cholesterol was dissolved in a mixture of chloroform : methanol at the volume ratio of 75 : 25 to improve solubility. Lipid concentration of the stock solutions was checked by phosphorous assay following the protocol from Avanti Polar Lipids.

For the preparation of lipid films, appropriate amounts of lipid stock solutions and chloroform were mixed in round bottom glass tubes so that the total amount of lipid was 4.6 mg and the total volume of chloroform was 0.5 ml. 65 μl of this solution (containing 0.6 mg of lipids) was used for analysis of lipid composition in the mixture by proton nuclear magnetic resonance (^{1}H NMR) spectroscopy. The rest of the solution (containing 4 mg of lipids) was used for liposome preparation.

For ^{1}H NMR analysis, NMR sample tubes were cleaned 3 × with chloroform, 3 ×, with ethanol, 3 ×, with acetone and once again 3 × with chloroform, and dried under a stream of nitrogen immediately prior to use. Appropriate lipid solution was transferred into the cleaned NMR sample tubes. Chloroform was evaporated under a stream of argon to form a thin lipid film on the tube walls. Lipid films were further dried under vacuum generated with an oil-free diaphragm pump for one hour. Dry lipid films intended for NMR were dissolved in 0.6 ml of deuterated chloroform ($CDCl_3$) (Euriso-Top, France).

The ^{1}H NMR spectra were recorded at 298K on a Bruker Advance 500 MHz NMR spectrometer (Bruker, Germany) operating at 117.74T using a 5 mm double resonance probe. One pulse experiment was recorded with 15 seconds of recycled delay and 64 transients. The proton spectral width of 8000 Hz and a total of 64K points were used with 90 deg. Pulse of 7.5 us. The data was zero-filled to 128K points, and Fourier transformed. All the spectra were processed with Bruker Topspin 2.0 software and data analysis was made with MestReNova 7.1.1 software. Four replicated measurements were performed for each sample. Pure DOPC, DPPC, DOPS and cholesterol were measured as references to identify them in the mixture. The chemical shift (δ) peak of $CDCl_3$ was set as standard at 7.24 ppm to calibrate the NMR spectra. As illustrated in Figure 2.7, the ratio of the four different lipids was calculated from the integrals of the peaks from the terminal methyl groups in the hydrocarbon chains (0.9 ppm, marked with blue arrows) which are in DOPC, DPPC, and DOPS; the choline methyl groups (3.4 ppm, marked with purple arrows) which are in DOPC and DPPC; the ethenyl groups (5.4 ppm, marked with green arrows) which are in DOPC, DOPS, and cholesterol; and the methyl group located in between the ring system (0.7 ppm, marked with red arrow) which is unique to cholesterol. An NMR spectrum of the lipid mixture is shown in Figure 2.8.

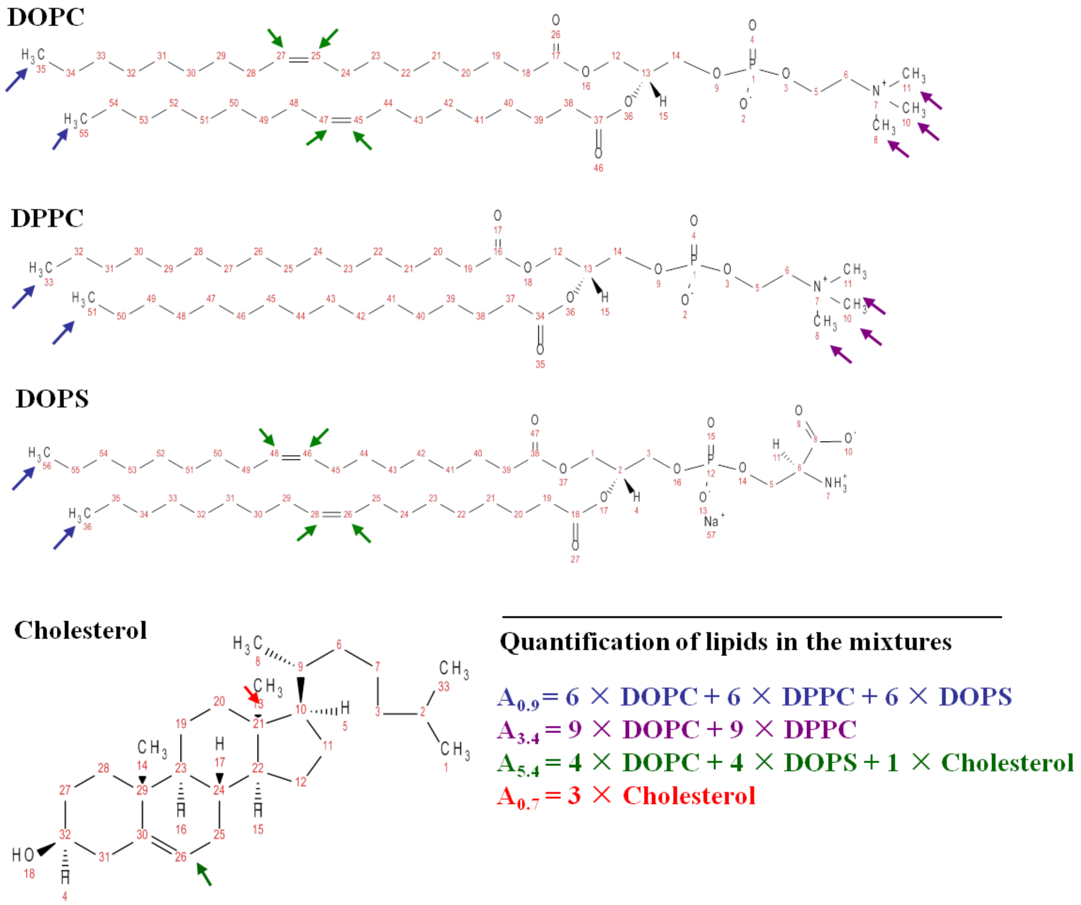

Quantification of lipids in the mixtures

$A_{0.9} = 6 \times \text{DOPC} + 6 \times \text{DPPC} + 6 \times \text{DOPS}$

$A_{3.4} = 9 \times \text{DOPC} + 9 \times \text{DPPC}$

$A_{5.4} = 4 \times \text{DOPC} + 4 \times \text{DOPS} + 1 \times \text{Cholesterol}$

$A_{0.7} = 3 \times \text{Cholesterol}$

Figure 2.7. Assignment of lipid composition in the lipid mixture for liposome preparation from NMR spectrum. The ratio of the four lipids DOPC, DPPC, DOPS, and cholesterol was calculated from the integrals of the peaks from the terminal methyl groups in the hydrocarbon chains (0.9 ppm, marked with blue arrows) which are in DOPC, DPPC, and DOPS; the choline methyl groups (3.4 ppm, marked with purple arrows) which are in DOPC and DPPC; the ethenyl groups (5.4 ppm, marked with green arrows) which are in DOPC, DOPS, and cholesterol; and the methyl group located in between the ring system (0.7 ppm, marked with red arrow) which is unique to cholesterol. The ratio of the four lipids was calculated using the four equations shown in the figure. Figure courtesy of Danijela Gregurec and Marco Marradi, CIC biomaGUNE, Spain.

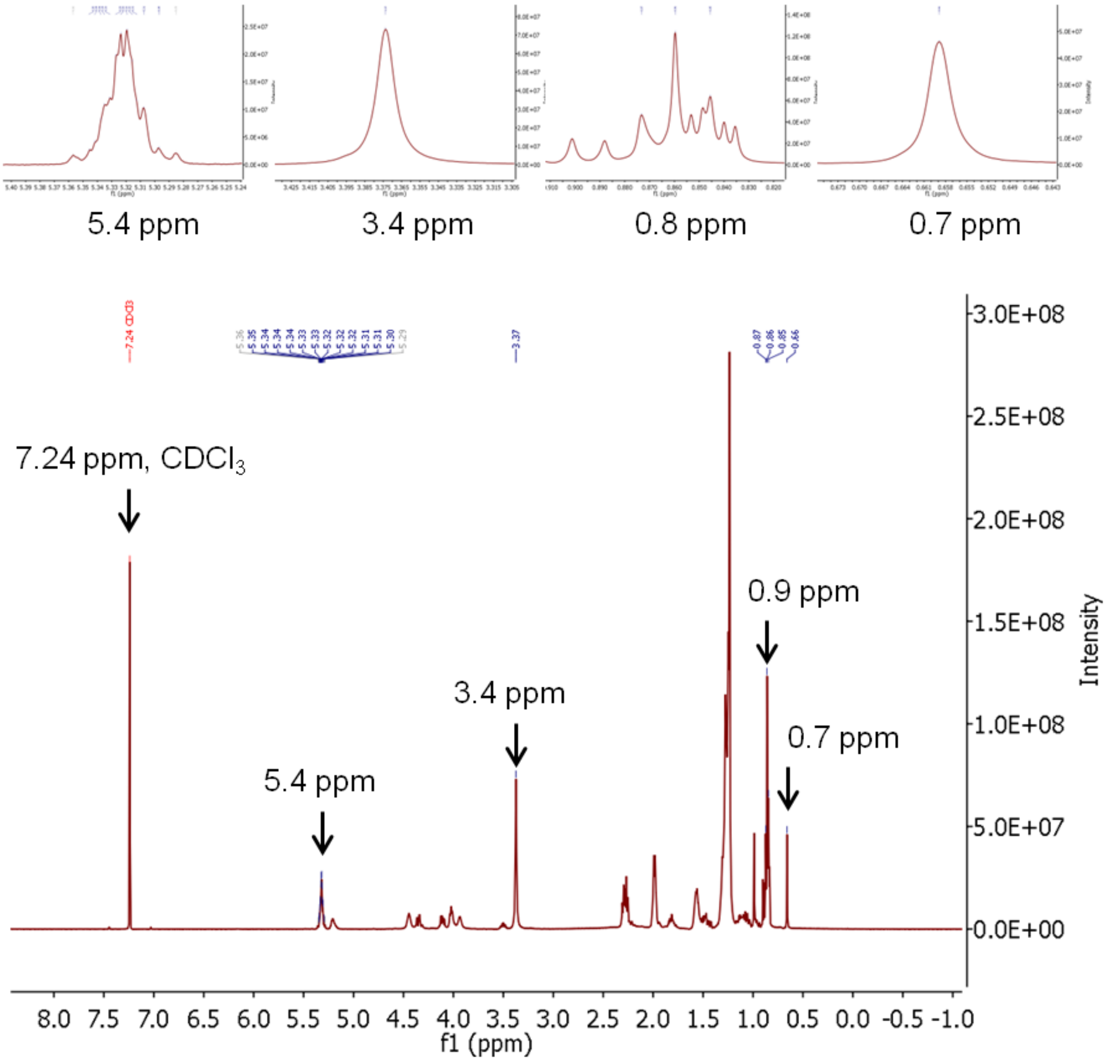

Figure 2.8. An NMR spectrum of the mixture of DOPC : DPPC : DOPS : cholestorl 26 : 26 : 18 : 30 mol-%. Peak 7.24 ppm from $CDCl_3$ is used to calibrate the spectrum. Peaks 5.4 ppm, 3.4 ppm, 0.9 ppm were used to calculate the content of DOPC, DPPC, and DOPS, respectively. Peak 0.7 was used to calculate the content of cholesterol. The zoomed-in spectra of these peaks are shown in the insets.

Lipid compositions used in this Thesis are listed in Table 2.2. 1 mol-% of NBD-PC or NBD-PS, or the mixtures of NBD-PC and NBD-PS at different ratios were used as fluorescence label.

Table 2.2. Lipids compositions used in the Thesis.

Lipids compositions (molar ratio)	**Chapters**
DOPC	3, 4, 5
DPPC	5
DOPC : DPPC 50 : 50	4, 5
DOPC : DPPC: cholesterol 35 : 35 : 30	4, 5
DOPC : DPPC : cholesterol 25 : 25 : 50	5
DOPC : DPPC : DOPS : cholesterol 26 : 26 : 18 : 30	5

Dry lipid films intended for the liposome preparation were also prepared by evaporating chloroform under a stream of argon followed by further drying under vacuum for one hour. The dry lipid films were rehydrated by vigorous vortexing in an appropriate buffer to a final lipid concentration of 2 mg/ml. Unilamellar liposomes were prepared from MLVs by sonication performed with a tip sonicator (Brandson, USA) in pulsed mode at 30% duty cycle under a nitrogen atmosphere [204]. DOPC liposomes were sonicated in an ice-water bath. DPPC-containing liposomes were sonicated at 60ºC (above the transition temperature of DPPC which is 41°C [214]). The sonicated liposome solutions were cleared of titania particles and remaining MLVs by centrifugation at 60,000 × g for 3 hours at 4ºC for DOPC liposomes, and at room temperature for DPPC-containing liposomes. Liposome solutions were stored under an argon atmosphere at 4°C for DPPC-free liposomes or at room temperature for DPPC-containing liposomes, and were used within two weeks.

Size distributions and ζ-potentials of the liposomes were characterized by DLS measurements performed with the Zetasizer Nano ZS (Malvern, UK) equipped with a 4 mW He-Ne laser operating at a wavelength of 633 nm. Size measurements were performed at a detection angle of 173°, and ζ-potential measurements were performed at a detection angle of 13°. For these measurements, liposomes diluted with the appropriate buffer to the final concentration of 0.2 mg/ml were loaded into the clear disposable DTS1060C zeta cells. 3 replicas of size measurements and 50 replicas of the ζ-potential measurements were performed for each sample. Size and ζ-potentials measurements were performed at 25 ℃. ζ-potential measurements were performed at a cell drive voltage of 30 V, using monomodal analysis model. As expected [204], size distributions of the sonicated liposomes were bi-modal, with the sizes of ～ 30 and ～ 150 nm. Liposome morphology was characterized by Cryo-TEM. For this, Quantifoil 200 square mesh grids with round holes (shape R 2/1, size 2 μm and period 3 μm; SPI Supplies, West Chester, USA) were pre-treated in a chloroform atmosphere overnight, vacuum-dried for 1 h, and glow discharged (air plasma) in a EMITECH K100X unit (Emitech Ltd., UK) for 2 min at 15 mA immediately before use. Freshly glow-discharged grids were installed in the VITROBOT Mk IV (FEI Europe, Eindhoven, The Netherlands) operated at 7 ℃ and 100% humidity. 5 μl of the vesicle solution was deposited onto the grid, blotted for 1.5 s and plunge-frozen in liquid ethane. Vitrified grids were mounted in the cryoholder and examined in a JEOL JEM-2100F transmission electron microscope operating at 200 kV. Images were recorded with an Ultrascan 1000, 2k × 2k CCD camera (Gatan UK, Abingdon Oxon, UK) under low-dose conditions and 25 k magnification. Corresponding to DLS measurements, cryo-TEM images show the bi-modal size distribution of the liposomes. Liposomes were found to be unilamellar (Figure 2.9). Liposomes were then used in the bilayer preparation experiments.

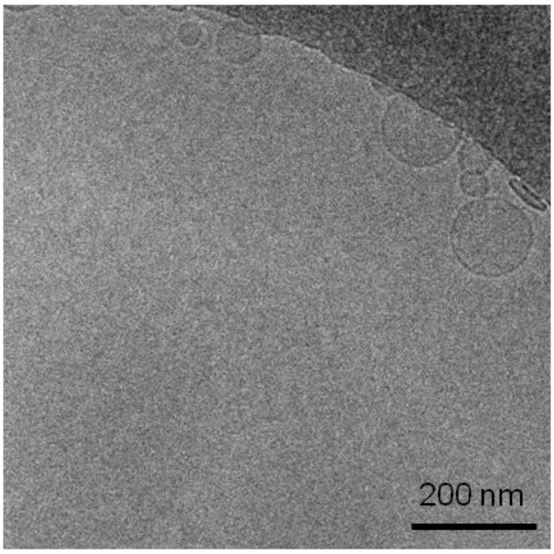

Figure 2.9. An example cryo-TEM image of sonicated liposomes. Liposomes in this image were from the mixture of DOPC : DPPC : cholesterol 35 : 35 : 30 mol-% in 5 mM HEPES. Image courtesy of Marta Gallego, CIC biomaGUNE, Spain.

2.3. Surface Preparation

2.3.1. Preparation of TiO_2- and SiO_2-coated Glass Slides

TiO_2- and SiO_2-coated glass slides were prepared by Danijela Gregurec, CICbiomaGUNE, Spain. 25 mm and 12 mm TiO_2- and SiO_2-coated glass coverslips were prepared by direct current (d.c.) and radio frequency (r.f) magnetron reactive sputtering, respectively in an ATC 1800 UHV sputtering system (AJA International Inc., MA, USA) equipped with a load-lock transfer chamber. The base pressure in the chamber was kept at ~ 1.2×10^{-8} Pa. Prior to the deposition process, glass slides were cleaned for 10 minutes at 50 ℃ in a mixture of H_2O : NH_4OH : H_2O_2 at a volume ratio of 1.5 : 1 : 1, followed by a rinse with nano-pure water, and another 10 minutes at 50 ℃ in a mixture of H_2O : HCl : H_2O_2, also at a volume ratio of 1.5 : 1 : 1. Cleaned slides were rinsed in nano-pure water and dried under a stream of nitrogen. They were then installed in the sputtering plant where they were further cleaned in Ar plasma generated with a negative radio frequency (r.f.) bias of 162 V in a 4 Pa Ar atmosphere for 3 min.

TiO_2 film deposition was carried out by the protocol adapted from ref [215]. Briefly, a 2-inch diameter Ti target (99.99% purity, AJA International Inc., MA, USA) was used, with a power of 228 W, in the Ar/O_2 atmosphere generated by combining 10 sccm of Ar flow with 20 sccm of O_2 flow at 0.4 Pa working pressure. Substrate-to-target distance was kept at 4 cm and the holder with the glass lides was rotated at 80 rpm. Sputtering was performed at room temperature for 120 minutes, resulting in transparent TiO_2 films of ~ 30 nm thickness. Film thickness was calculated based on the sputtering rate of 0.42 nm/sec measured with a built-in QCM sensor under identical conditions and verified by optical ellipsometry.

SiO_2 film deposition was carried out by the protocol adapted from ref [216]. Briefly, 1 nm Ti adhesion layer was deposited from a 2-inch diameter Ti target with a power of 225 W, in the Ar atmosphere generated by 24 sccm of Ar flow at a 0.4 Pa working pressure. Substrate-to-target distance was kept at 3 cm and the holder with the substrates was rotated at 50 rpm. The sputtering was performed at room temperature for 15 seconds. SiO_2 was then deposited on this Ti film from the Si target (99.99% purity, AJA International Inc., MA, USA), with a power of 201 W, no bias, in the Ar/O_2 atmosphere generated by combining 10 sccm of Ar flow with 20 sccm of O_2 flow at 0.8 Pa working pressure. Substrate-to-target distance was kept at 3 cm and the substrates were rotated at 80 rpm. The sputtering was performed at room temperature for 29 minutes, resulting in transparent SiO_2 films of ~ 30 nm thickness.

Surface chemical composition of the films was analyzed by XPS after cleaning. I then characterized surface roughness of the coated glass slides by atomic force microscopy, performed with Nanoscope V Multimode atomic force microscope (AFM) (Santa Barbara, CA, USA) in air, which is discussed in Chapter 5.

2.3.2. Surface Cleaning

All the surfaces used for liposome deposition (uncoated glass slides, TiO_2- and SiO_2-coated glass slides, silicon wafers, TiO_2-coated quartz crystals) were cleaned in the same way immediately prior to the lipid deposition experiments: they were exposed to 2% SDS solution for 30 minutes, thoroughly rinsed with nano-pure water, blow-dried with nitrogen, and treated in a preheated UV-Ozone cleaning chamber (Bioforce, Nanosciences, Ames, AL, USA) for 30 minutes immediately before use. The UV-Ozone treatment cleaned the surface of the organic contaminants , and makes the surface hydrophilic [217].

2.3.3. Surface Chemical Composition Analysis by X-ray Photoelectron Spectroscopy (XPS)

X-ray photoelectron spectroscopy (XPS) is a technique for characterizing the surface chemical composition with a depth resolution of a few nm. The technique is based on photoelectric effect. The surface of a material is irradiated with monoenergetic soft x-rays causing the emission of the photoelectrons. The elements in the sample are identified from the kinetic energies of the emitted photoelectrons, while peak intensities, suitably normalized, are used to calculate their relative contents. The kinetic energy of a photoelectron can be determined from the Einstein equation:

$$KE = hv - BE - e\phi, \text{ (Equation 2.4)}$$

Where KE is the kinetic energy of the emitted photoelectron, hv is the characteristic energy of x-ray photon, BE is the binding energy of the atomic orbital from which the photoelectron originates, $e\phi$ is the spectrometer work function.

Surface chemical composition of the TiO_2-and SiO_2-coated glass slides was analyzed by XPS in a SPECS SAGE HR 100 (SPECS, Berlin, Germany) spectrometer equipped with a Mg Kα (1253.6 eV) non-monochromatic source operated at 12.5 kV and 250 W. The take-off angle was fixed at 90 ° and the analysis was conducted at a pressure of ~10^{-8} Torr. Surfaces were brought into the XPS chamber within 5 min after cleaning/preparation. Survey spectra were obtained with a pass energy of 30 eV. For TiO_2-coated surfaces, detailed spectra were acquired for Ti 2p3/2, Ti 2p1/2, O1s, and C1s regions with the pass energy of 15 eV. For SiO_2-coated surfaces, detailed spectra were acquired for Si 2p, O1s, and C1s regions with the pass energy of 15 eV. Flood gun was used for charge compensation, set at 0.7 mA and 1.0 eV. Spectra were analyzed with the CasaXPS 2.3.15dev87 software. The analysis consisted of satellite removal, Shirley background subtraction, calibration to the C1s peak at 285 eV, and peak fitting with Gaussian-Lorentizan line shapes to determine the atomic percentages of various elements present on the surface. Freshly cleaned TiO_2-coated surfaces typically contained < ~ 13 atomic% of carbon and ~ 95% of the Ti2p peak could be assigned to Ti^{IV}, with ~ 5% corresponding to the lower oxidation states [218-220]. Freshly cleaned SiO_2-coated surfaces typically contained < ~ 4.5 atomic% of carbon and ~ 95% of the Si2p peak could be assigned to Si^{IV}, with ~ 5% corresponding to the lower oxidation states. Samples containing extraneous elements or that contained higher amounts of carbon (contamination) were discarded.

2.4. Liposome Deposition for Fluorescence and Atomic Force Microscopy Measurements

A freshly cleaned 25 mm glass slide (uncoated, TiO_2- or SiO_2-coated) was mounted in a homemade fluid cell consisting of a Teflon ring pressed to the glass slide with a metal clamp. A Viton O-ring was placed between the glass and the Teflon to prevent leakage. Viton O-rings were cleaned in Cobas cleaner for 30 minutes, while the Teflon rings were cleaned for 30 minutes in 2% Cuvette cleaner. Both were washed with copious amounts of Nanopure water immediately before assembly. The assembly was performed in a laminar flow hood to reduce contamination and the fluid cell was filled with the freshly filtered and degassed buffer, to which a small amount of concentrated liposome solution was added to a final concentration of 0.36 mg/ml. Solutions were thoroughly mixed. Samples were incubated at room temperature or 60 ℃ for 1 hour, and rinsed with the appropriate buffer to remove excess vesicles. Subsequently, the samples were either used for fluorescence measurements at 60 ℃, or cooled down to allow fluorescence or atomic force miscroscopy measurements at room temperature. The temperature for sample incubation and fluorescence microscopy measurements was maintained by using a water circulator (Analog model 912, Polyscience, Illinois, USA).

For time-resolved experiments, buffer-filled fluid cells were mounted on the stage of the fluorescence microscope at 60 ℃ and lipids were then added. Otherwise, the procedure remained the same as the above paragraph.

For melittin incubation experiments, melittin was resuspended in Nano-pure water at the concentration of 10 mg/ml and stored at -4°C. Prior to use, the solution was diluted to 1 mg/ml in the appropriate buffer used in the concerned measurement. Melittin was added to the sample such that the final melittin-to-lipid ratio was 0.0035 (mol), either together with the liposomes before incubation for 1 hour, or after liposome deposition and 1 hour incubation. Samples were then rinsed with the appropriate buffer before fluorescence measurements.

2.5. Laser Scanning Confocal Microscopy and Fluorescence Recovery After Photobleaching (FRAP)

2.5.1. Principles of Laser Scanning Confocal Microscopy

Most molecules normally stay in the lowest energy state (ground state). When excited by light, they adsorb the photon of light making the electron jump to the high energy state (excited state). The molecule then dissipates small amount of the energy by collision with the surrounding molecules, and drops to the lower excited state. The rest of energy is lost by emitting light with longer wavelength (Figure 2.10).

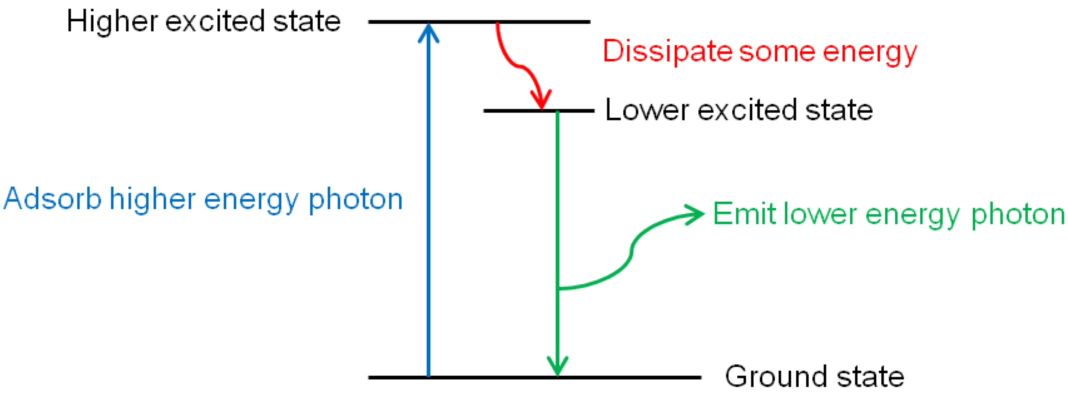

Figure 2.10. Schematic illustration of mechanism of fluorescence.

In a confocal microscope, a pinhole is used to restrict the illumination to a plane a few μm thick, achieving much higher z-resolution than in a conventional microscope (Figure 2.11). Because the pinhole is placed at the focal point of the lens, in other words, they are conjugated, the microscope is named ‘confocal’.

Confocal microscopy can only observe one point at each time. Therefore the scanning mirrors are used after the laser reflected from the diachronic mirror to adjust the excitation light scanning the specimen horizontally and vertically. A computer is linked to the detector to build up the image of the specimen. The schematic set up of a laser scanning confocal microscope is shown in Figure 2.12.

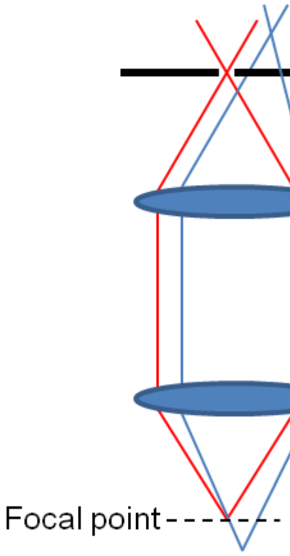

Figure 2.11. Schematic representation of confocal microscope pinhole.

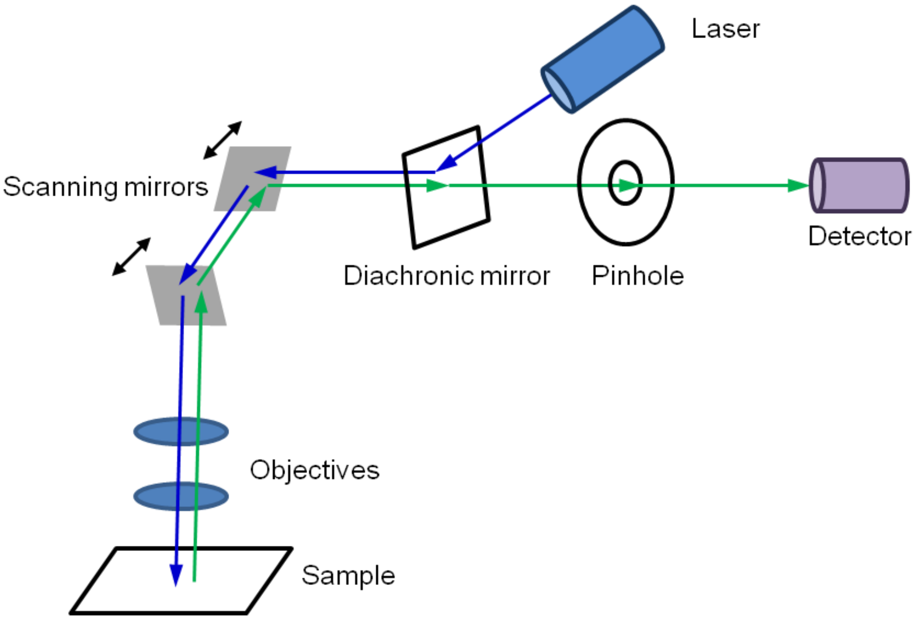

Figure 2.12. Schematic presentation of the laser scanning confocal microscope.

2.5.2. Principles of FRAP

Fluorescence recovery after photobleaching (FRAP) is a technique to measure the lateral diffusion of fluorescent molecules in two dimensions. Basically, one region of the sample is photobleached. Due to the lateral diffusion of molecules in the sample, the bleached molecules exchange with the unbleached molecules outside the bleached area. This will eventually lead to the recovery of fluorescence intensity in the bleached area. Figure 2.13. illustrates the mechanism of FRAP of a bilayer. Due to the long range lateral mobility of lipids in the fluid bilayer, there will be finally full recovery of fluorescence intensity.

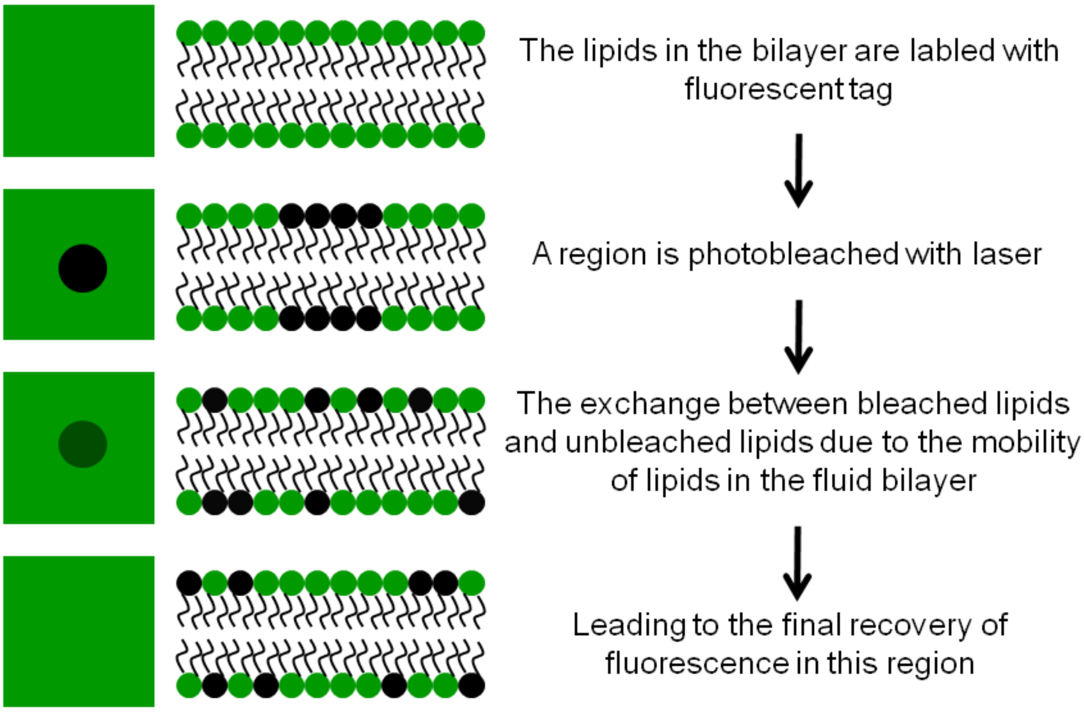

Figure 2.13. Measuring lipid diffusion in a bilayer by FRAP

2.5.3. Protocols for FRAP Measurements

Fluorescence and FRAP experiments were performed with a Zeiss LSM 510 laser scanning confocal microscope (Carl Zeiss, Oberkochen, Germany) equipped with a 25 mV Argon laser (488 nm line was used for the excitation of the NBD fluorophore) and a 63×oil immersion objective. FRAP measurements and analysis to extract mobile fractions and diffusion coefficients were performed after Axelrod et al. [221] and Soumpasis et al. [222] as previously described [97]. Briefly, a round shaped spot with the diameter of 22 μm was photobleached. A non-bleached spot of similar size was used as a reference to account for the focus drift. The bleaching time was kept at less than 5% of the characteristic recovery time. Images after photobleaching were recorded at 5 intervals of 1s, 2s, 5s, 8s, 16s, 32s, 64s, and 128s respectively until the fluorescence intensity was stable.

The fluorescence recovery is defined as $f(t) = \frac{[F(t) - F(0)]}{[F(i) - F(0)]}$, (Equation 2.5) where $F(0)$ is the fluorescence intensity in the bleached spot at $t = 0$ after photobleaching, $F(t)$ is the recovering fluorescence intensity in the bleached spot at time t after photobleaching. $F(i)$ is the normalized fluorescence intensity in the non-bleached reference area, which is calculated from $F(i) = Fr(t) + [Fb(i) - Fr(i)]$ (Equation 2.6) where $Fr(t)$ is the fluorescence intensity in the reference area at time t after photobleaching, $Fb(i)$ is the average fluorescence intensity in the bleached spot before photobleaching, and $Fr(i)$ is the average fluorescence intensity in the reference area before photobleaching. This way, the fluorescence intensity drift of the whole sample due to the photobleaching during the scanning process is normalized.

$f(t)$ is fitted as $f(t)=\exp\left(-2\frac{\tau_D}{t}\right)\left[I_0\left(2\frac{\tau_D}{t}\right)-I_1\left(2\frac{\tau_D}{t}\right)\right]$, (Equation 2.7)

I_0 and I_1 are modified Bessel functions, τ_D is the characteristic diffusion time, and is calculated using $\tau_D=\frac{\omega^2}{4D}$,(Equation 2.8) where D is the diffusion coefficient, ω is the radius of the bleached area at $t=0$. Mobile fraction is calculated using $M=\frac{[F(\infty)-F(0)]}{[F(i)-F(0)]}$ (Equation 2.9).

2.6. Atomic Force Microscopy (AFM)

2.6.1. Principles of AFM

Atomic force microscopy (AFM) invented by Binnig et al. [223] is a development of Scanning tunneling microscope (STM) which was invented by the same group. It uses a sharp probe (tip) mounted on a spring cantilever to scan the sample surface, monitors the interaction between the tip and sample, and generates the image of the topography of the sample surface. As illustrated in Figure 2.14, the sample is mounted on a piezoelectric scanner, and the laser is focused onto the back of the cantilever and is reflected onto a photodiode. As the tip approaches the sample, attractive or repulsive interaction between the tip and the sample will cause bending of the spring cantilever which will result in the moving of the laser on the photodiode. The bending of the cantilever is thus monitored, and a feedback is sent to the piezoelectric scanner to adjust the z-axis position of the sample.

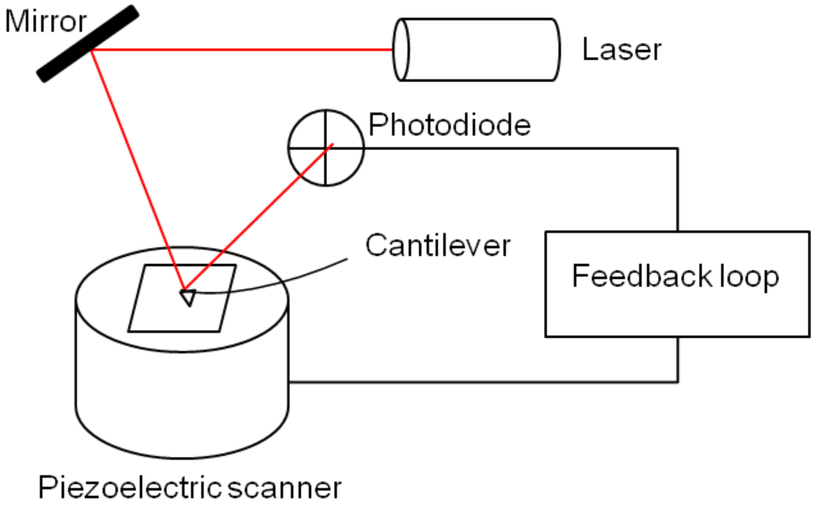

Figure 2.14. Schematic representation of AFM.

Contact and Tapping modes are most usually used to take images. Contact mode keeps the distance or force between the tip and the sample constant. In tapping mode, the cantilever oscillates close to its resonance frequency, and the oscillation amplitude is kept constant so that the interaction between the tip and the sample is constant. PeakForce Tapping mode is a recently introduced AFM technique based on the acquisition of force distance curves with kHz-rate. It allows directly controlling imaging forces down to the pN-range. Since its introduction, it has been proven to be particularly useful for imaging biological specimens in liquid, as it overcomes some of the limitations and difficulties of traditional AFM imaging modes and additionally gives access to quantifitable mechanical information with high resolution [224, 225].

2.6.2. Protocols for AFM

Some of the samples observed in the fluorescence microscope in chapter 4 and 5 were also observed with a JPK Explorer atomic force microscope (JPK Instruments AG, Germany). Other AFM experiments were performed with a Nanoscope V Multimode atomic force microscope (Santa Barbara, CA, USA) equipped with a vertical engage $120 \times 120\ \mu m^2$ ("J") scanner and a tapping mode fluid cell. For these experiments, freshly cleaned 12 mm TiO_2- and SiO_2-coated glass slides were used. They were mounted on the microscope on BYTAC-covered metal disks with double-sided tape as previously described [141]. Lipid solution was added to the fluid cell the same concentration as used for fluorescence measurements that is 0.36 mg/ml, and allowed to incubate at 60^o C or room temperature (depending on the sample) for 1 hour.

In either case (on the JPK or on the Nanoscope), images were acquired in tapping or contact mode, with oxide-sharpened silicon nitride tips mounted on triangular cantilevers with nominal force constants of ~ 0.06 N/m (Veeco, Mannheim, Germany). Images were flattened and plane-fitted as required.

AFM imaging of freshly cleaned bare surfaces was performed in tapping mode in air, at room temperature, using Nanoscope V Multimode atomic force microscope (Santa Barbara, CA, USA) equipped with a vertical engage 120 × 120 μm^2 (“J”) scanner using with antimony doped silicon TESP cantilever with nominal force constants of 20-80 N/m (Veeco, Mannheim, Germany). Images were flattened and plane-fitted as required. Roughness values were root-mean-square (RMS) values determined from the images.

2.7. Quartz Crystal Microbalance (QCM)

2.7.1. Principles of QCM

Quartz Crystal Microbalance (QCM) [226] is a technique that can monitor small mass changes on quartz sensors based on oscillation of the quartz sensors at their resonant frequency in an alternating applied voltage. A quartz sensor is a quartz disc sandwiched between a pair of gold electrodes (Figure 2.15a). Due to the piezoelectric properties of quartz, application of an electric voltage to it results in its deformation (Figure 2.15b), and application of a certain alternating voltage to it results in its oscillation at its resonance frequency (Figure 2.15c). This oscillation decays with the time after the applied voltage is stopped, and dissipation describes the time need for the amplitude to decay. In the case of AT-cut crystal, application of AC current causes it to oscillate in the thickness-shear mode where the two surfaces move in an antiparallel way (Figure 2.15c).

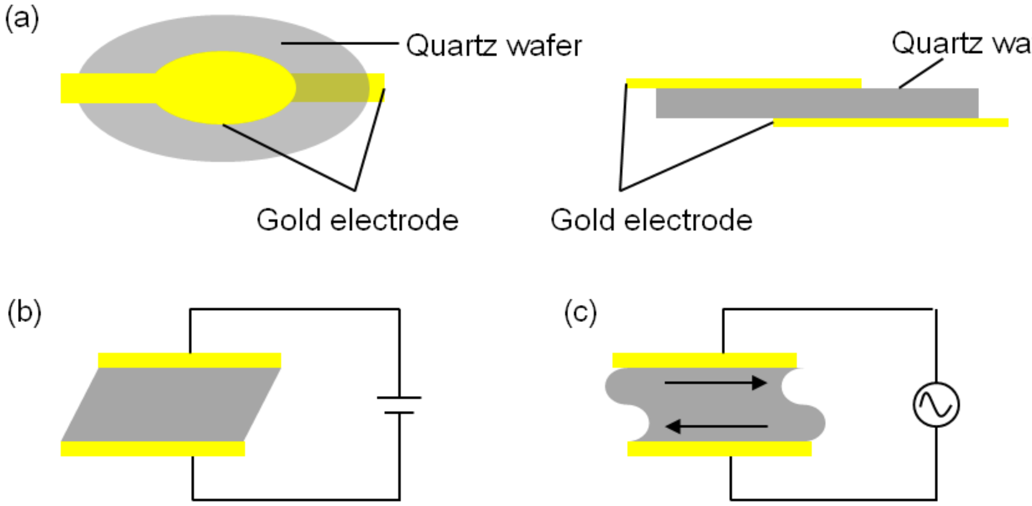

Figure 2.15. Schematic representation of QCM sensing principle.

The value of the resonance frequency, f_n is determined from the following equation: $f_n = nc/2d$, (Equation 2.10), where d is the thickness of the crystal, n is the overtone order, c is the speed of the wave.

QCM measures resonance frequency f_n and half-band half-width of the resonance Γ_n of a quartz crystal as a function of time. The dissipation D is calculated using $D_n = 2\Gamma_n / f_n$ (Equation 2.11). Altering the crystal environment changes frequency and dissipation. The frequency shift Δf_n is inversely related to the areal mass density (mass per unit area) of the adsorbed film, Δm. Sauerbrey showed that for sufficiently thin, homogeneous films that do not dissipate energy, this relationship is linear [227]: $\Delta f_n = -\frac{n\Delta m}{C}$ (Equation 2.12), where n is the overtone number, C is the mass sensitivity constant which has the value of $18\, ng/\left(cm^2 \cdot Hz\right)$ for the 5 MHz crystals used here. In general, it is not. For all other cases, both the frequency shift Δf and the dissipation shift, ΔD_n, depend on thickness, organization, and viscoelastic properties of the adsorbed films. Details can be found in Figure 2 in Ref [226].

2.7.2. Protocols for QCM

QCM measurements were performed using an impedance analysis-based system (IQCM) controlled with QTZ software (Resonant Probes GmbH, Goslar, Germany). QCM flow modules were cleaned by sonicating in Cobas cleaner for 20 minutes at 30 $^{\mathrm{o}}$C, and then sonicating $3\times$ in nano-pure water for 10 minutes at $30^{\mathrm{o}}\mathrm{C}$. Freshly cleaned QCM crystals were mounted in the freshly cleaned flow cells, and tested for oscillations at several overtones (between n = 3 and n = 17, 15 MHz to 85 MHz). If at least six of the overtones were found, the cells were filled with the appropriate buffer to equilibrate. The data was collected for at least 30 minutes until a stable baseline was achieved: frequency shift Δf_n less than 1 Hz within 30 minutes. Following that, temperature-equilibrated liposome suspension or the mixture of liposomes and melittin was injected to the chamber. Liposome and melittin concentrations used in QCM experiments are the same with the ones used in FRAP, which are liposome 0.36 mg/ml, and melittin-to-lipids ratio of 0.0035 (mol). The resonance frequency f and half-band half-width of the resonance Γ were acquired at several overtones (between n = 3 and n = 17, 15 MHz to 85 MHz). Bandwidth Γ is equivalent to the dissipation $D_n = 2\Gamma_n / f_n$ (Equation 2.11), that is recorded by the Q-sense's QCM-D instrument. Temperature was set to 23 ± 1 ℃ using a water circulator (Analog model 912, Polyscience, Illinois, USA). After liposome adsorption was complete, 1 ml of the appropriate buffer was injected into the chamber to rinse away the excess of non-adsorbed liposomes.

2.8. The Source of Na^+, K^+-ATPase-containing Membrane Fragments

Membrane preparations containing Na^+, K^+-ATPase were gifted from the lab of Hans-Jurgen Apell, University of Konstanz, Germany. They were isolated and purified from the outer medulla of rabbit kidney following the procedure of Jørgensen.[228] Briefly, the outer medulla was homogenized, and a microsomal fraction was obtained by differential centrifugation. The fraction was incubated with sodium dodecyl sulfate (SDS) to remove membrane proteins other than Na^+, K^+-ATPase and part of the membrane lipids. The treated membrane fractions were centrifuged in a discontinuous sucrose density gradient. The resulting membrane fragments containing Na^+, K^+-ATPase with the density of up to 10.000 αβ-protomers per μm^2 [229] were resuspended in the buffer containing 25 mM Imidazole, 1 mM Tris-EDTA pH 7.5, 1% sucrose at the concentration of 0.272 mg/ml. The enzyme activity of Na^+, K^+-ATPase in these membrane fragments was verified after purification. The membrane preparations were snap frozen in liquid nitrogen and stored at –80 ℃ until used. Preparations were thawed in hand immediately prior to use.

2.9. Characterization of Membrane Purity by Sodium Dodecylsulfate Polyacrylamide Gel Electrophoresis (SDS-PAGE)

2.9.1. Principles of SDS-PAGE

SDD-PAGE is a commonly used method to separate proteins by size in a polyacrylamide gel matrix in the presence of electric field. SDS is an anionic detergent. It denatures the proteins into linear conformation, binds the polypeptides of the proteins to a constant charge to mass ratio, coating the proteins with negative charge so that they migrate in the gel towards the anode in the applied electric field. The migration rate depends on the molecular weight of the proteins. Smaller proteins migrate faster. A blue dye is usually added to visualize the gel running. Coomassie blue staining is usually used to stain the gel. Molecular weights of the proteins are determined by comparing with a protein marker of known molecular weight run in a different lane in the gel.

2.9.2. Protocols for SDS-PAGE

Purity of the membrane preparations was assessed by SDS-PAGE following the Laemmli method [230]. Specifically, the sample was treated with Laemmli buffer containing 63 mM Tris-HCl, pH 6.8, 25% (v/v) glycerol, 2% (w/v) SDS, 5% (v/v) β-mercaptoethanol, and 0.01% (w/v) Bromophenol Blue at 95 °C for 4 min, loaded onto a discontinuous gel using 4% stacking gel (0.125 M Tris-HCl pH 6.8) and 12% resolving gel (0.375 M Tris-HCl pH 8.8). Electrophoresis was performed by using Mini-PROTEAN® Tetra Cell (Bio-Rad Laboratories) at a constant voltage of 150 V for 1 h in Tris-glycine running buffer (0.025 M Tris pH 8.3, 0.192 M glycine, 0.1% SDS). Upon completion of the electrophoresis, the gel was fixed in the solution of 50% (v/v) methanol and 10% (v/v) of acetic acid for 30 minutes, and stained with 0.1% Coomassie Brilliant Blue R-250 (Bio-Rad Laboratories) in 50% (v/v) methanol and 10% (v/v) acetic acid for 30 minutes based on the method from Meyer and Lambert 1965 [231]. The molecular weights of the bands were determined by comparison with the prestained protein marker Protein Ladder (New England Biolabs).

2.10. Characterization of Purified Membrane Fragments by TEM

TEM was used to characterize membrane fragments. Carbon-coated copper grids (SPI supplies, West Chester, USA) were hydrophilized by glow discharging for 15 seconds in air at low pressure in a EMITECH K100X unit (Emitech Ltd., UK). Freshly thawed membrane fragments were adsorbed onto freshly hydrophilized, carbon-coated grids for 2 minutes and washed with deionized water (18 MΩ resistance) for 30 seconds twice before staining for 30 seconds with 3% (w/v) uranyl acetate. The samples were examined in a JEOL JEM 2100F UHR transmission electron microscope operated at 200 kV. Images were recorded on US 1000 CCD camera (2K × 2K) (Gatan, UK). No further processing of the images was performed.

2.11. AFM Imaging of Purified Membrane Fragments Adsorbed on Mica

To prepare relatively large, flat patches containing the Na^+, K^+-ATPase, the following procedure was adopted. First, 58 μl of ice cold adsorption buffer (10 mM Tris-HCl pH 6.8, 150 mM KCl, 25 mM $MgCl_2$) was added onto freshly cleaved mica placed on ice. Subsequently, 2 μl of 0.272 mg/ml membrane preparation was added to the adsorption buffer drop on mica and allowed to incubate on ice for 15 minutes. It was found to be crucial to rinse the samples after this short incubation step with 15 μl of adsorption buffer 50 times and leave them overnight at 0 ℃. Immediately before imaging, the sample was rinsed with the imaging buffer (10 mM Tris-HCl pH 6.8, 150 mM KCl, 1 mM $MgCl_2$, room temperature). The composition of the adsorption and imaging buffers was optimized to improve sample preparation and imaging as discussed in Chapter 6.

AFM imaging of adsorbed membranes was performed in image buffer at room temperature in PeakForce-Tapping^{TM} mode using Nanoscope V Multimode atomic force microscope (Santa Barbara, CA, USA) equipped with a vertical engage 120 × 120 μm^2 ("J") scanner with oxide-sharpened silicon nitride tips mounted on triangular cantilevers with nominal force constants of ~ 0.32 N/m. Images were flattened and plane-fitted as required, but not otherwise modified.

2.12. AFM Image Analysis for Conserved Motif

High-magnification AFM images (lateral size 314.5 nm, 512 pixels) were analyzed in Groningen Image Processing (GRIP) software package by Fourier analysis and single particle averaging. Fourier analysis was used to reveal the oligomerization state of the protein. Individual non-overlapping motifs (dimers, tetramers, higher-order oligomers) were picked out by hand and subjected to at least four rounds of translational and rotational alignment using one of the motifs as a reference [232-234]. Particles with the highest correlation coefficients were summed, and the obtained average was used as a reference in the next round of alignment. Finally, the average map of the most stable motif is achieved. The location of these motifs was identified in the original images by performing cross-correlation analysis.

2.13. Constructing the Model from X-ray Crystallographic Structure

The model of the tetramer was generated in Chimera (http://www.cgl.ucsf.edu/chimera/) based on the structure of pig kidney Na^+, K^+-ATPase solved by Morth et al. (PDB code 3KDP) [1] by applying appropriate crystallographic symmetry operators. For comparison with the AFM images, a density map of the tetramer was generated using *molmap* command at a resolution of 18 Å with the sigma factor of 0.356 and threshold of 0.0002.

Chapter 3

How Osmotic Effects and Electrostatic Interactions Control Adsorbed Liposome Behavior

---

3.1. Summary

There has been a controversy in the literature about whether the electrostatic interactions between zwitterionic lipids and negatively charged surfaces are attractive [143, 152] or repulsive [137, 147, 151, 165]. In these studies, the effect of ionic strength on adsorbed liposomes was studied by varying the electrolyte concentration in the buffer [143, 147, 152]. However, the osmotic pressure which builds up in the adsorbing liposomes due to their deformation and expulsion of water and which differs with various electrolyte concentrations is expected to affect supported lipid bilayer (SLB) formation [169]. This aspect has, until now, not been taken into account. Here, I examine the role played by the deformation-associated osmotic effects in the liposome behavior at the titanium oxide surface and decouple these effects from those of the ionic strength, thereby evaluate the contribution of the electrostatic interactions.

Sonicated DOPC liposomes were prepared and incubated with TiO_2 in the same buffer so that the buffer inside and outside of liposome is isotonic. The liposome deformation upon adsorption [155, 156, 159-162] results in liposome volume reduction and water expulsion from the adsorbing liposome. Because sucrose can not pass through the membrane, osmotic pressure builds up inside the adsorbing liposome. By comparing different sucrose concentrations, the osmotic effect on liposome-surface interaction was investigated. The sucrose-induced osmotic effect was further confirmed by adding the membrane pore-forming peptide melittin that allows sucrose to pass through the pores in the membrane.

Buffers with increasing NaCl concentrations were kept isotonic by adjusting the osmolarity with sucrose. Liposome behavior on the surface in various buffers was investigated by fluorescence microscopy/fluorescent recovery after photobleaching (FRAP), and quartz crystal microbalance (QCM).

A theoretical model was derived by our collaborators, Gur Fabrikant and Michael Kozlov from the Tel Aviv University to describe the observations. It was possible to conclude that the electrostatic interactions between zwitterionic liposomes and negatively charged TiO_2 surface were repulsive.

3.2. Results and Discussion

3.2.1. Effects of Buffer Osmolarity on Zwitterionic Liposome Behavior on TiO_2

The effect of buffer osmolarity on the behavior of DOPC liposomes on TiO_2 was investigated in buffers with various concentrations of sucrose. These buffers were based on a low ionic strength buffer, 5 mM HEPES, pH 7.4, in which TiO_2 is negatively charged because the buffer pH is above the isoelectric point (～5.5, [164, 235, 236]) of the oxide. In all the cases, sonicated liposomes were prepared in buffers containing various concentrations of sucrose under isotonic conditions, and then allowed to interact with the surface in the same buffer. Size distribution of the sonicated liposomes were checked by dynamic light scattering (DLS), and were bi-modal as expected [204]. No effect of sucrose concentration on liposome size was found (Table 3.1), corresponding to the results from the previous studies [169].

To verify the sucrose-induced osmotic effect, comparison was made in the absence and presence of the membrane pore-forming peptide melittin. The pores made by this peptide are large enough to allow sucrose to pass through. Liposome behavior under different conditions was investigated by fluorescence microscopy, fluorescence recovery after photobleaching (FRAP), and quartz crystal microbalance (QCM).

Table 3.1. DOPC liposome size distribution in different buffers measured by DLS.

Buffer solute concentration	**Peak 1 (nm)**	**Peak 2 (nm)**
0 mM sucrose	41.0 ± 1.0	165.9 ± 7.0
25 mM sucrose	30.0 ± 0.7	109.7 ± 1.0
50 mM sucrose	31.6 ± 0.4	106.8 ± 2.7
50 mM sucrose + melittin	36.1 ± 1.0	151.0 ± 5.6
75 mM sucrose	36.9 ± 0.8	136.9 ± 1.1
150 mM sucrose	33.1 ± 2.0	132.5 ± 5.2
300 mM sucrose	30.8 ± 0.7	108.0 ± 10.8
0 mM sucrose, 150 mM NaCl	44.7 ± 2.5	203.0 ± 7.2
0 mM sucrose, 150 mM NaCl + melittin	49.7 ± 0.6	199.8 ± 9.0
75 mM sucrose, 112.5 mM NaCl	52.6 ± 4.8	151.5 ± 3.3
75 mM sucrose, 112.5 mM NaCl + melittin	41.6 ± 3.8	159.8 ± 2.7
75 mM sucrose, 150 mM NaCl	36.1 ± 3.3	124.3 ± 4.9
150 sucrose, 75 mM NaCl	43.9 ± 2.9	179.0 ± 6.9

3.2.1.1. Diminished Adsorption of Zwitterionic Liposome on TiO_2 with Increasing Sucrose Concentration

Fluorescence results showed that when liposomes were incubated with TiO_2 surface in the absence of sucrose (5 mM HEPES buffer), an SLB formed (Figure 3.1a left side). This could be judged from the homogeneous fluorescence intensity that recovered after photobleaching, yielding a mobile fraction of 1.01 ± 0.06 and a diffusion coefficient of $0.67 \pm 0.11 \times 10^{-8}$ cm^2/s (green curve in Figure 3.1g).

Incubating liposomes with TiO_2 surface in buffers containing various concentrations of sucrose (25 mM, 50 mM, and 75 mM) led to intact liposomes adsorbed on the surface rather than an SLB. This could be judged from the lack of recovery after photobleaching (red, blue, and purple curves, respectively in Figure 3.1g). The fluorescence intensity diminished with increasing sucrose concentration (Figure 3.1b, c, d left side). Finally, almost no fluorescence intensity was observed at 150 mM and 300 mM sucrose. Only several fluorescent dots were visible on the surface (Figure 3.1e, f left side). The mean fluorescence intensity was plotted as a function of sucrose concentration in Figure 3.1h (blue line). Each data point was the mean value from at least three individual samples. Three measurements were taken for each sample. Assuming that the fluorescence intensity correlates with the amount of lipid material, this decrease in the fluorescence intensity shows that liposome adsorption to the surface diminishes with increasing sucrose concentration.

One point is worthy of a special note. The fluorescence intensity in the sucrose-free buffer (5 mM HEPES) is much lower than the one from 25 mM sucrose-containing buffer. This is because in the absence of sucrose, a SLB was formed, while in 25 mM sucrose, a liposome layer was formed. Similar trend was observed in previous fluorescent microscopy experiments showing that the ruptured liposomes have lower fluorescence intensity than the unruptured liposomes on the surface [162, 174]. The fact that the bilayers have lower fluorescence intensity than a supported vesicular layer (SVL) is because a layer of close packed liposomes has more lipids than an SLB. Excess of lipids leave the surface during the transformation from adsorbed liposomes to SLB [146, 175]. Detailed discussion about this issue is in chapter 4.

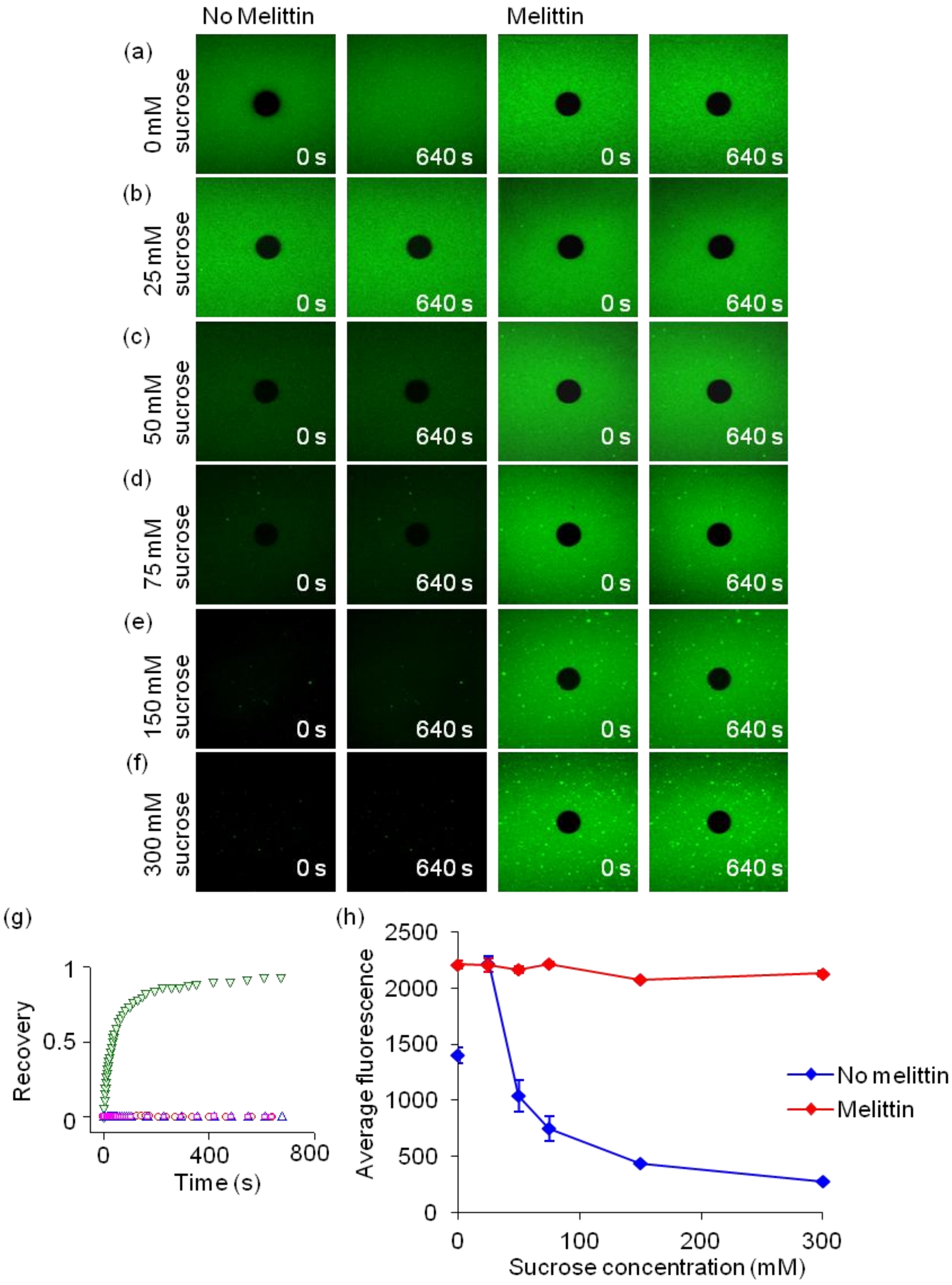

Figure 3.1. Osmotic effects on DOPC liposome behavior on TiO_2 characterized by fluorescence microscopy and FRAP.

(a)-(f) Fluorescence images of DOPC liposomes on TiO_2 in 5 mM HEPES, pH 7.4 buffer containing various concentrations of sucrose (0 mM, 25 mM, 50 mM, 75 mM, 150 mM, and 300 mM) after photobleaching. Left side: liposome incubation on the surface in the absence of melittin; right side: liposome incubation on the surface in the presence of melittin at the melittin-to-lipid molar ratio of 0.0035. The size of the images is 142 × 142 μm^2. The diameter of the bleached spot is 22 μm.

(g) The recovery of the fluorescence intensity in the bleached area of DOPC liposomes on TiO_2 in 5 mM HEPES, pH 7.4 buffers containing various concentrations of sucrose (left side in a-d) is plotted as a function of time after photobleaching. Full recovery in the green curve (corresponding to the 5 mM HEPES buffer without sucrose shown in a) indicates bilayer formation. No recovery in the red, blue and purple curves (corresponding to the buffers with 25 mM, 50 mM, and 75 mM sucrose shown in b-d, respectively) indicates SVL formation.

(h) The average fluorescence intensity of the fluorescence images before photobleaching is plotted as a function of sucrose concentration. Blue curve represents liposome incubation without melittin, and red curve represents liposome incubation with melittin to the melittin-to-lipid molar ratio of 0.0035. The average fluorescence is calculated by using Image J software. Each data point is a mean value from more than three samples at each condition, and three measurements were performed on each sample. The error bars represent the standard deviations.

The effect of sucrose concentration on liposome adsorption was also investigated by QCM, a technique that can monitor small mass changes on quartz crystals by monitoring the shift in the crystal's resonance frequency Δf and the changes in the energy dissipation ΔD of the resonance [226, 237]. A typical experiment consisted of allowing liposomes to interact with the surface of the crystal coated with TiO_2 and monitoring frequency f and bandwidth Γ as a function of time. Dissipation D was calculated using $D = 2\Gamma / f$. Changes in the frequency Δf were inversely, but not linearly, related to the layer thickness. Adsorption of liposomes led to a decrease in Δf and an increase in ΔD; these changes diminished with increasing sucrose concentration in the buffers (Figure 3.2a curves without rhombus, Figure 3.2b blue curves), indicating decreased liposome adsorption on the surface with increasing sucrose concentration. These results were correlated with the fluorescence results.

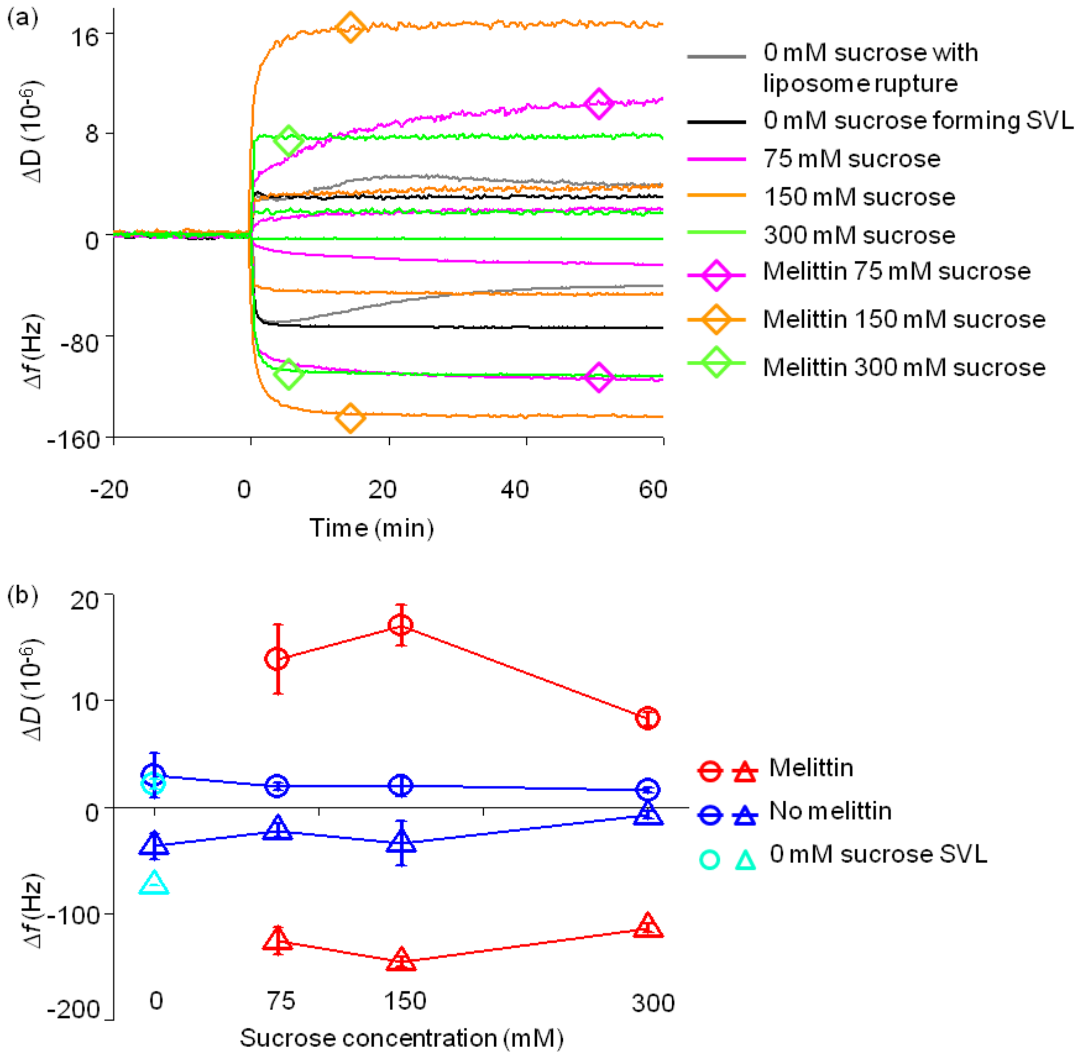

Figure 3.2. Osmotic effects on DOPC liposome behavior on TiO_2 characterized by QCM

(a) Representative frequency shifts, Δ*f*, and dissipation shifts, Δ*D*, obtained from DOPC liposomes in sucrose-containing buffers of various sucrose concentrations on TiO_2-coated QCM crystals. Grey: 0 mM sucrose with liposome rupture; black: 0 mM sucrose forming a vesicular layer; pink: 75 mM sucrose; yellow: 150 mM sucrose; green: 300 mM sucrose. Curves without rhombus are in the absence of melittin; curves with rhombus are in the presence of melittin.

(b) Frequency shifts, Δ*f*, and dissipation shifts, Δ*D*, obtained from DOPC liposomes on TiO_2-coated QCM crystals is plotted as a function of sucrose concentration in the absence (blue curve) and presence (red curve) of melittin.

Triangles represent Δ*f*, circles represent Δ*D*. Light blue triangle and circle represent Δ*f* and Δ*D* in sucrose-free buffer (5 mM HEPES) when SVL formed. Each data point is the mean value from at least three experiments, and the error bars represent the standard deviations.

All the experiments were performed in 5 mM HEPES, pH 7.4 buffer with vaiours concentrations of sucrose. Melittin was added to the melittin-to-lipid molar ratio of 0.0035. The representative Δ*f* and Δ*D* are normalized by /n, where n is 5 representing the 5th overtone.

An important difference between QCM and fluorescence results was observed. In QCM, no bilayer formation was observed in the 5 mM HEPES buffer (Figure 3.2a), while a bilayer was found under this condition (Figure 3.1a) on the TiO_2-coated glass slides examined by fluorescence microscopy. QCM experiments performed under this condition were not very reproducible, as in some cases extrema appeared in the Δ*f*(t) and Δ*D*(t) curves, possibly indicating liposome rupture [153], but in no case was complete SLB formation observed by QCM (grey curve in Figure 3.2a). Complete bilayer formation is characterized by (Δ*f* ~ -25 Hz, and Δ*D* ~ 0) [98, 153], while in 5 mM HEPES Δ*f* ~ -40 Hz, and Δ*D* ~ 4 $\times 10^{-6}$ were typically observed. The origin of this difference between liposome behavior observed in fluorescence and QCM with the same liposomes is not altogether clear, but it is most likely related to the subtle differences in surface chemistry or roughness between TiO_2-coated QCM crystals and TiO_2-coated glass slides.

Taken together, both fluorescence and QCM results showed diminished liposome adsorption with increasing sucrose concentration, indicating a weaker liposome-surface attraction at higher sucrose concentrations. At the lowest sucrose concentration (0 mM sucrose), the liposome-surface interaction strength was at its highest, judging from the liposome rupture on the surface.

Our explanation for these observations is as follows. Liposomes deform upon adsorption to the surface [155, 156, 159-162]. The deformation is caused by liposome-surface attraction which increases the liposome-surface contacting area. This deformation causes membrane bending and tension which cost energy and oppose the deformation. It also causes water to be expelled from the adsorbing liposomes, while the membrane-impermeable osmotically active substance (OAS) sucrose stays inside, and as a result, osmotic pressure builds up inside the adsorbing liposome. It acts against the deformation. Liposome behavior on the surface finally depends on the combination of these effects. The higher the sucrose concentration, the higher the osmotic pressure that develops as a result of the deformation-induced volume change. Therefore liposome-surface adhesion is low, and this explains fewer liposomes adsorbed on the surface at higher sucrose concentration. And vice versa, at low sucrose concentration, the liposome-surface adhesion is high due to the low osmotic pressure, therefore more liposome adsorbed on the surface, and some even ruptured.

3.2.1.2. Melittin Restores Zwitterionic Liposome Adsorption On TiO_2 at High Sucrose Concentrations

To verify that the observed reduction in liposome adsorption at high sucrose concentrations was due to the increased osmotic pressure which built up because of the liposome deformation upon adsorption and the membrane impermeability of sucrose, the pore-forming peptide melittin was added together with the liposome to the surface at different sucrose concentrations to allow sucrose expulsion from liposomes. Melittin is a 26-amino acid pore-forming peptide that allows permeation of molecules trapped in the liposome interior [238, 239]. Concentration of melittin was chosen at a molar ratio of 0.0035 (melittin : lipid), which is above that required for the solute to leak from the liposomes (0.002), but below the ratio of 0.3 at which liposome fusion and aggregation are observed in solution [239].

Fluorescence results showed that melittin restored the adsorption of liposomes on the surface judging from the increased fluorescence intensity (Figure 3.1h, red line; the corresponding fluorescence images and FRAP results are shown in Figure 3.1a-f right side), indicating that the diminished liposome adsorption with increasing sucrose concentration was caused by osmotic pressure, and not, for example, from adsorption of sucrose to the surface and consequent repulsion between liposomes and the surface. The fluorescence intensity at different sucrose concentrations in the presence of melittin was almost the same (Figure 3.1h). This is because once the pores are formed in the presence of melittin, sucrose can freely leave the liposomes, and no osmotic pressure builds up.

Correlated with the fluorescence results, QCM also showed that in the presence of melittin, the frequency and dissipation shifts were much greater than the ones in the absence of melittin. No trend was observed with different sucrose concentrations (Figure 3.2a, Figure 3.2b red curve).

In summary, apart from the difference observed in the 5 mM HEPES buffer, the same trend was observed by fluorescence and QCM methods: diminished liposome adsorption with increasing buffer osmolarity at high sucrose concentration, and the restoration of adsorption by the pore-forming peptide melittin which allowed sucrose expulsion from the liposomes, and therefore vanished buffer osmolarity. Our group previously showed the melittin-induced membrane permeability by including the 5 kDa dextran which was too large to pass through the melittin-induced pores at the same melittin concentration used for sucrose penetrating. Diminished melittin-induced effect was found in the presence of dextran [169]. This again confirms the sucrose-induced osmotic pressure in the absence of melittin.

One would expect that the addition of melittin restored not only liposome adsorption, but also SLB formation. This was not the case. Judging from the lack of recovery, only intact liposome adsorption was observed in melittin-containing buffers (Figure 3.1b-f right side). Moreover, addition of melittin to the sucrose-free condition (5 mM HEPES) inhibited SLB formation (Figure 3.1a right side). Most likely, SLB formation from DOPC on TiO_2 is very sensitive to the conditions. Previous studies from our group showed that on SiO_2, melittin not only did not inhibit SLB formation, but increased the rate of the process [169].

To check if melittin had other influences on liposomes such as liposome aggregation which could inhibit SLB formation on surface, size distribution of the liposomes in the presence of melittin was characterized by DLS. No difference was found in the absence and presence of melittin (Table 3.1). The adsorption of DOPC liposomes on silica particles in the presence or absence of melittin was also investigated by cryo-TEM (Figure 3.3). Melittin was added at the same concentration as was used for sucrose penetration (melittin-to-lipid molar ratio of 0.0035). Cryo-TEM Images showed that liposome adsorbed and deformed on silica particles in both presence and absence of melittin, and no aggregates of liposomes were observed in the presence of melittin, indicating that melittin did not add any artifacts on liposome behavior rather than pore forming in the membrane (Figure 3.3).

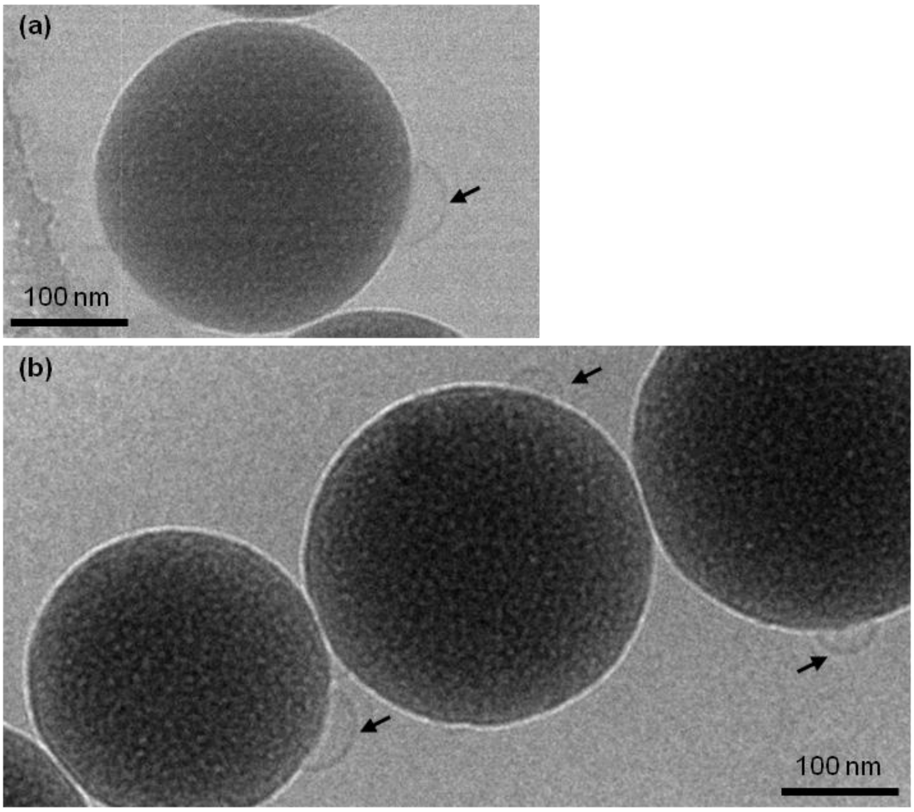

Figure 3.3. Cryo-TEM images of DOPC liposomes adsorbed on SiO_2 particles in the absence (a) and presence (b) of melittin. The adsorbed liposomes are indicated with arrows. Deformation of adsorbed liposomes was found both in the absence and presence of melittin. No aggregation of liposomes was shown in the presence of melittin. Images were taken by Marta Gallego, CICbiomaGUNE, Spain, and the image in (a) was also presented in [161].

It has been demonstrated previously that a range of liposome behavior, from SLB formation, to adsorption of intact liposomes, to no adsorption, could be spanned by varying parameters that control lipid-surface interactions, such as liposome surface charge density [137] or oxide surface charge density (by varying pH) [147, 151]. It is shown here that the same can be achieved by varying buffer osmolarity. This result can be interpreted in terms of diminishing strength of liposome adhesion to the surface with increasing osmolarity.

3.2.2. Effects of Ionic Strength on Zwitterionic Liposome Behavior on TiO_2 under Isotonic Conditions

The results above demonstrate that osmotic pressure which builds in the adsorbing liposomes due to their deformation decreases liposome-surface adhesion strength. In the following section, the effect of ionic strength on the adsorbed liposome behavior is evaluated by varying the ionic strength while keeping the total solution osmolarity constant with sucrose. To this end, liposomes were prepared in buffers of constant osmolarity containing various amounts of NaCl and sucrose. Size distribution of the sonicated liposomes was checked by DLS, and showed bi-modal as expected [204]. No effect of NaCl and sucrose compositions on liposome size was found (Table 3.1). Liposomes were allowed to interact with the surface in the same buffer.

Fluorescence images showed that in buffers with constant osmolarity of 300 mOsm, almost no adsorption of liposomes was observed at low ionic strength (0 mM NaCl, 150 mM sucrose, Figure 3.4a left side). More liposomes adsorbed with increasing ionic strength (75 mM NaCl, 112.5 mM NaCl, Figure 3.4b, c left side) until they covered the surface (150 mM NaCl, Figure 3.4d left side). No recovery was observed in the bleached area in all these buffers, indicating an SVL formed on the surface.

Such SVL formation from zwitterionic liposomes on TiO_2 at high ionic strength was previously shown by Rossetti et al [142].

The mean fluorescence intensity at each condition is plotted as a function of NaCl and sucrose concentrations in Figure 3.4f. It is shown that at a constant osmolarity, fluorescence intensity increases with increasing NaCl concentration (Figure 3.4f blue curve), indicating more liposomes adsorbed on the surface at higher ionic strength. Therefore, higher ionic strength increased liposome-surface adhesion. Since the effect of NaCl is to screen electrostatic interactions, the electrostatic interactions between DOPC liposomes and negatively charged TiO_2 surface must be repulsive.

In the presence of melittin (melittin-to-lipid molar ratio 0.0035), homogenous SVLs were observed in all these buffers (Figure 3.4a-e right side, Figure 3.4f red curve), indicating that melittin-induced pore formation released the osmotic pressure and thus restored liposome adsorption. Apparently, the liposome-surface interactions were strong enough in the low ionic strength (5 mM HEPES, 300 mM sucrose) buffer for a complete SVL to form, because the fluorescence intensities were similar at different ionic strengths when the experiments were performed in the presence of melittin (red curve in Figure 3.4f).

Another measurement was performed in a buffer containing 75 mM sucrose and 150 mM NaCl. As expected, in this buffer the response—fluorescence intensity (Figure 3.4d, e left side, Figure 3.4f)—diminished as compared to that in the 0 mM sucrose : 150 mM NaCl buffer of the same ionic strength, because of the increase in the buffer osmolarity from ~ 300 mOsm/ml to ~ 375 mOsm/ml. Once again, the experiments performed in the presence of melittin showed little difference between the two buffers (Figure 3.4d, e right side, Figure 3.4f).

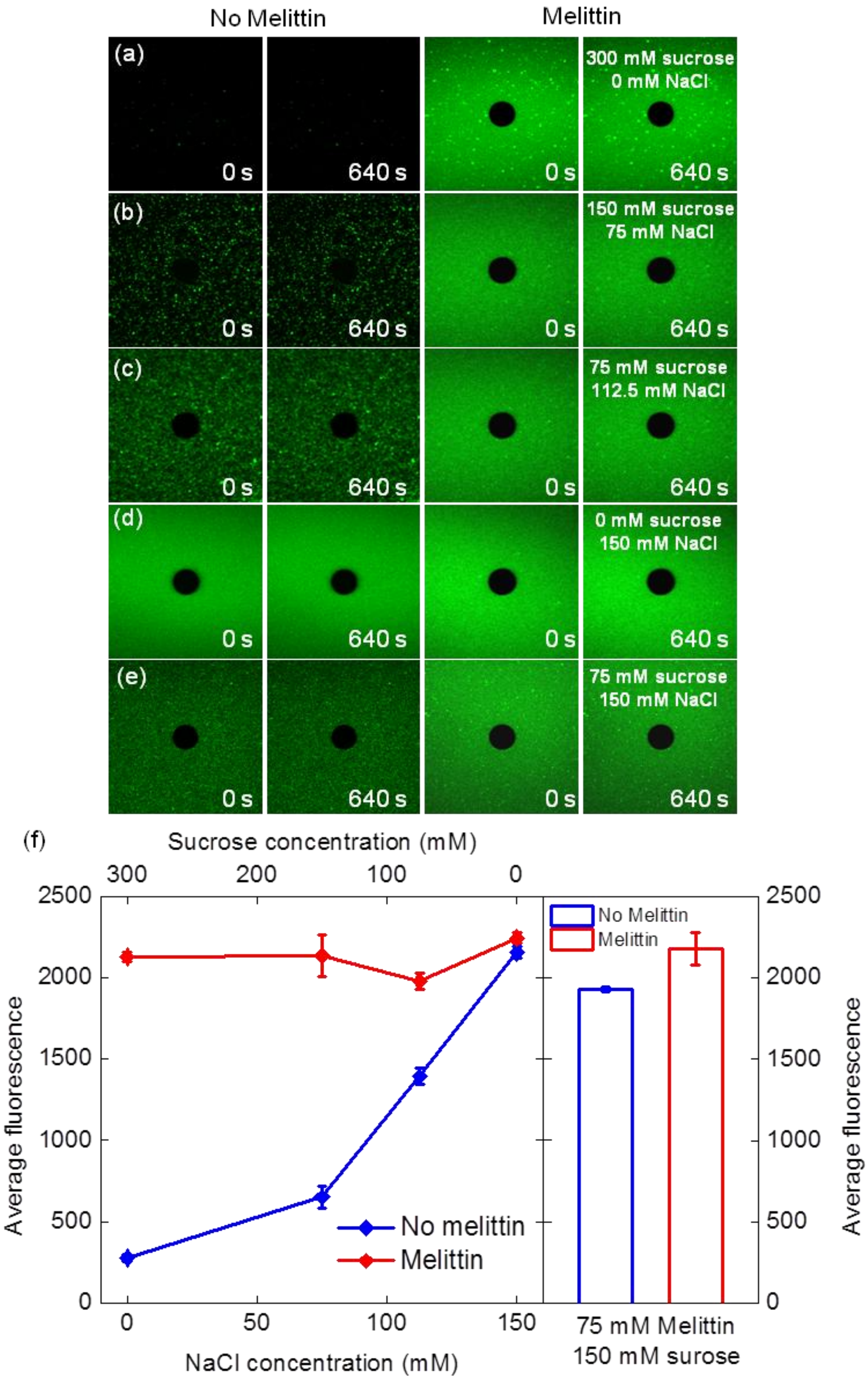

Figure 3.4. Effect of ionic strength on DOPC liposome behavior on TiO_2 at isotonic conditions characterized by FRAP.

(a)-(e) Fluorescence images of DOPC liposomes on TiO_2 in buffers with different sucrose and NaCl concentrations: (a) 300 mM sucrose, 0 mM NaCl; (b) 150 mM sucrose, 75 mM NaCl; (c) 75 mM sucrose, 112.5 mM NaCl; (d) 0 mM sucrose, 150 mM NaCl; (e) 75 mM sucrose, 150 mM NaCl. Left side: liposome incubation in the absence of melittin; right side: liposome incubation in the presence of melittin. The size of the fluorescence images is 142×142 μm^2. The diameter of the bleached spot is 22 μm.

(f) The plot represents the average fluorescence of the fluorescent images before photobleaching in buffers with constant osmolarity but different ionic strength. Blue curve represents liposome incubation in the absence of melittin, and red curve represents liposome incubation in the presence of melittin. The columns represent liposome incubation in 75 mM sucrose and 150 mM NaCl buffer which has different osmolarity than the others, the blue column was in the absence of melittin, the red column was in the presence of melittin.The average fluorescence is calculated by using Image J software. Each data point is the mean values from at least three samples, and three measurements were performed for each sample. The error bars represent the standard deviation.

All the experiments were performed in 5 mM HEPES, pH 7.4 buffer with different compositions of NaCl and sucrose. Melittin was added to the melittin-to-lipid molar ratio of 0.0035. The representative Δf and ΔD are normalized by /n, where n is 5 representing the 5th overtone.

Correlated with the fluorescence results, QCM also showed that an SVL was formed in buffers containing sucrose and NaCl (Figure 3.5a). At constant osmolarity, dissipation and frequency shifts increased with increasing NaCl concentration (green, yellow, pink curves in Figure 3.5a, Figure 3.5b), indicating more liposomes adsorbed on the surface at higher ionic strength.

In the presence of melittin (melittin-to-lipid molar ratio of 0.0035), dissipation and frequency shifts observed at low ionic strength were much greater than in its absence.

The shifts increase with increasing NaCl concentration (curves with rhombi in Figure 3.5a, Figure 3.5b).

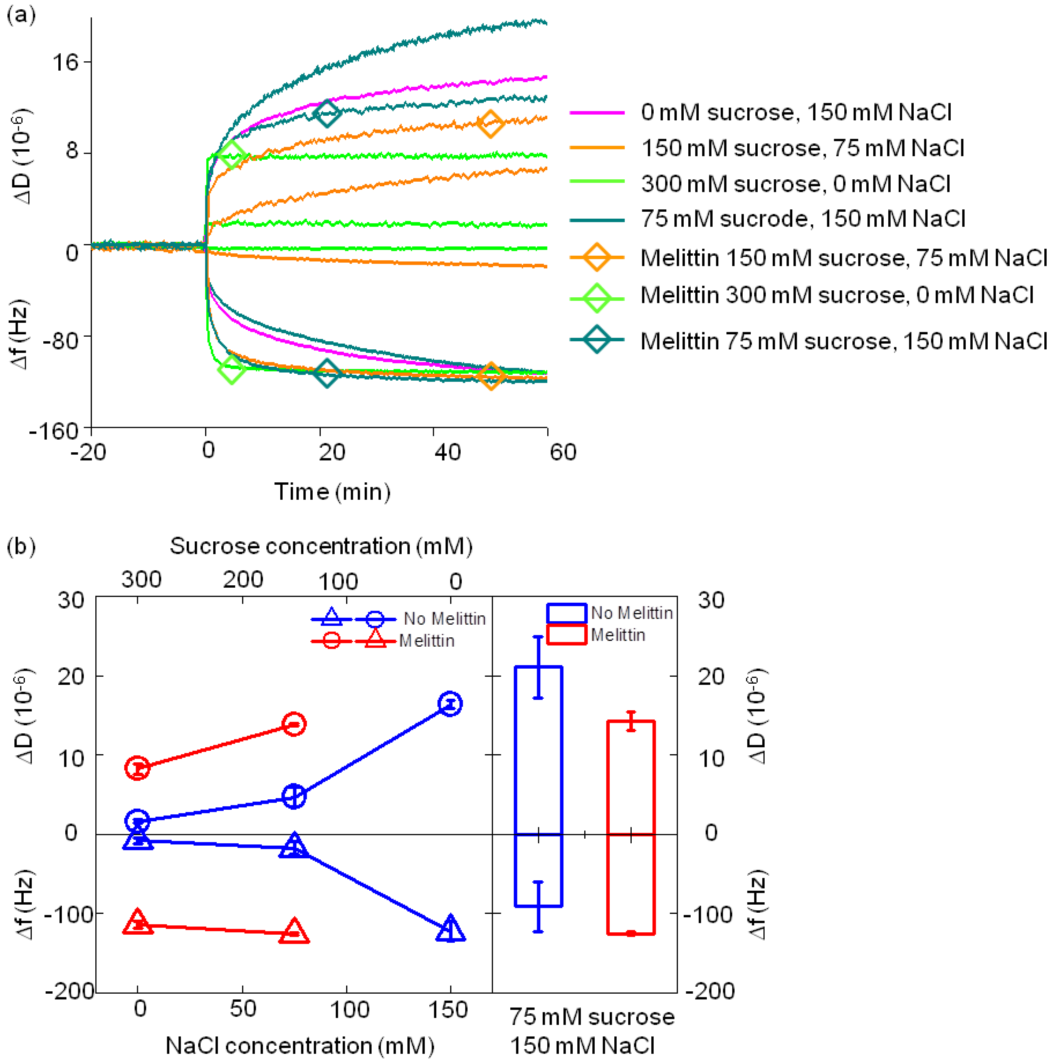

Figure 3.5. Effect of ionic strength on DOPC liposome behavior on TiO_2 at isotonic conditions characterized by QCM.

(a) Representative frequency shifts, Δ*f*, and dissipation shifts, Δ*D*, obtained from DOPC liposomes in 5 mM HEPES, pH 7.4 buffers containing various compositions of sucrose and NaCl on TiO_2-coated QCM crystals. Green: 300 mM sucrose, 0 mM NaCl; yellow: 150 mM sucrose, 75 mM NaCl; pink: 0 mM sucrose, 150 mM NaCl; cyan: 75 mM sucrose, 150 mM NaCl. Curves without rhombus are in the absence of melittin; curves with rhombus are in the presence of melittin. Melittin was added to the melittin-to-lipid molar ratio of 0.0035.

(b) Plots of frequency shifts, Δf, and dissipation shifts, ΔD, obtained from DOPC liposomes on TiO_2-coated QCM crystals at different sucrose and NaCl concentrations in the absence (blue) and presence (red) of melittin to the melittin-to-lipid molar ratio of 0.0035. Triangles represent Δf, circles represent ΔD. The values are mean values from three experiments, and the error bars represent the standard deviations.

In the buffer containing 75 mM sucrose and 150 mM NaCl, there was an increase in the dissipation shift as compared to that in the 0 mM sucrose : 150 mM NaCl buffer of the same ionic strength and a small decrease in the frequency shift (Figure 3.5a cyan and pink curves, Figure 3.5b). The frequency shift decreased, i.e., went in the direction of weaker interaction. This was consistent with the increased buffer osmolarity. The increase in the dissipation shift can in principle be explained by the hydrodynamic effects associated with the lower liposome surface coverage [226, 240].

In summary, both fluorescence and QCM results showed increased liposome adsorption at high ionic strength in isotonic buffers, indicating high ionic strength increased liposome-surface adhesion. It is therefore concluded that the electrostatic interaction between DOPC liposomes and TiO_2 surface is repulsive, and it is screened by counter-ions at high ionic strength.

3.2.3.Comparison with a Theoretical Model

Here, I compare the experimental results with a model that takes adsorbed liposome deformation into account explicitly. It was derived by Gur Fabrikant and Michael Kozlov from the University of Tel Aviv in Israel, and proceeds analogously to that of

Seifert et al. [156], but is considerably simpler. Within the scope of this model an adsorbed liposome is represented as a spherical cap with an area $A = 2\pi r_c^2(1+\cos\theta)$

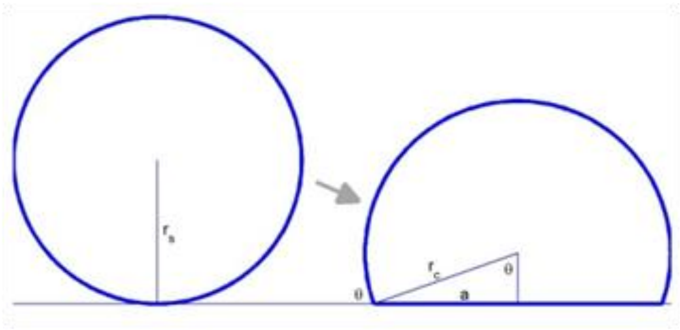

Figure 3.6 System geometry.

(Equation 3.1) and volume $v = \frac{1}{3}\pi r_c^3(2+3\cos\theta-\cos^3\theta)$ (Equation 3.2) where θ is the attachment angle and r_c is the cap radius defined in Figure 3.6. It is further postulated that the area of the liposome doesn't change upon adsorption: $A = A_0$ (Equation 3.3), that is $2\pi r_c^2(1+\cos\theta) = 4\pi r_s^2 - \pi a^2$ (Equation 3.4) where r_s is the radius of liposome in solution, a is the radius of the contact area, and $a = r_c\sin\theta$ (Equation 3.5) (Figure 3.6). The volume of the adsorbing liposome, on the other hand, decreases due to the deformation. As the water is expelled, this leads to an increase in the concentration of osmotically active substances (OAS) inside the liposome, and the build-up of the osmotic pressure $\prod = k_B T c_0\left(\frac{v_0}{v}-1\right)$ (Equation 3.6) where k_B is Boltzmann's constant, T is temperature, c_0 is the OAS concentration in the solution, $v_0 = \frac{4}{3}\pi r_s^3$ (Equation 3.7) is the initial liposome volume before adsorption, and v is the deformed liposome volume defined above. In this model, the free energy of an adsorbed liposome, F, contains two contributions: adhesion and osmotic stress:

$F = -k_B T C_0 V_c \left(\ln\left(\frac{v}{v_0} \right) - \frac{v}{v_0} + 1 \right) - \varepsilon \pi a^2$ (Equation 3.8), where ε is the lipid-surface interaction strength. Bending energy is ignored because it is far smaller than these two.

It is more convenient to write down the free energy in terms of dimensionless parameters. Defining a scaled contact area radius $\xi = \frac{a}{r_s}$ (Equation 3.9) and scaled volume $\bar{v} = \frac{v}{v_0}$ (Equation 3.10), the free energy becomes $F = -k_B T c_0 v_0 \left(\ln \bar{v} - \bar{v} + 1 \right) - \varepsilon \pi \xi^2 r_s^2$ (Equation 3.11). After re-arrangement, this yields $F = k_B T c_0 v_0 \left(-\left(\ln \bar{v} - \bar{v} + 1 \right) - w \xi^2 \right)$ (Equation 3.12), where w is the effective adhesion strength, $w = \frac{3}{4 k_B T} \left(\frac{\varepsilon}{c_0 r_s} \right)$ (Equation 3.13). Equilibrium shapes of adsorbed liposomes are found by minimizing F for different starting values of ε, c_0 and r_s. At constant temperature, $k_B T$ is constant, and Equation 3.13 is simplified as $w = \frac{\varepsilon}{c_0 r_s}$ (Equation 3.14).

A qualitative comparison between my results and the model is shown in Figure 3.7a. Mass of lipids adsorbed on the surface under different conditions was calculated from the fluorescence intensity on the surface based on several assumptions. First, the SVL at 5 mM HEPES : 25 mM sucrose was taken as reference, assuming that under this condition, the surface was fully covered by random closely packed liposomes. This is because apart from the condition without sucrose, at which liposome rupture was observed, among all the conditions forming SVLs, the one with 25 mM sucrose has the lowest sucrose concentration and therefore the lowest osmotic effect. As a result, liposome adsorption and surface coverage should be highest. This is confirmed by the fact that the highest fluorescence intensity was observed under this condition.

Second, the amount of lipids adsorbed on the surface under this condition was calculated as follows. The surface coverage of ~ 0.55 (random close packing limit, [172]) was assumed and the number of liposomes per unit area was calculated from the coverage and from the liposome size assuming that they cover an area πr^2 on the surface, where r is the liposome radius measured with DLS.

The number of lipids per liposome was calculated from the measured liposome size and a bilayer thickness of ~ 3.7 nm according to [170]. The area per lipid in this calculation was taken as ~ 0.72 nm^2 [173]. Only the small vesicles in the distribution (~ 30 nm diameter) were taken into account because they would cover the surface first. Significant adsorption of larger liposomes is unlikely [241]. This calculation further assumes that fluorescence intensity is linearly dependent on the amount of lipids adsorbed on the surface at different conditions. Lipid amounts are indicated in ng/cm^2.

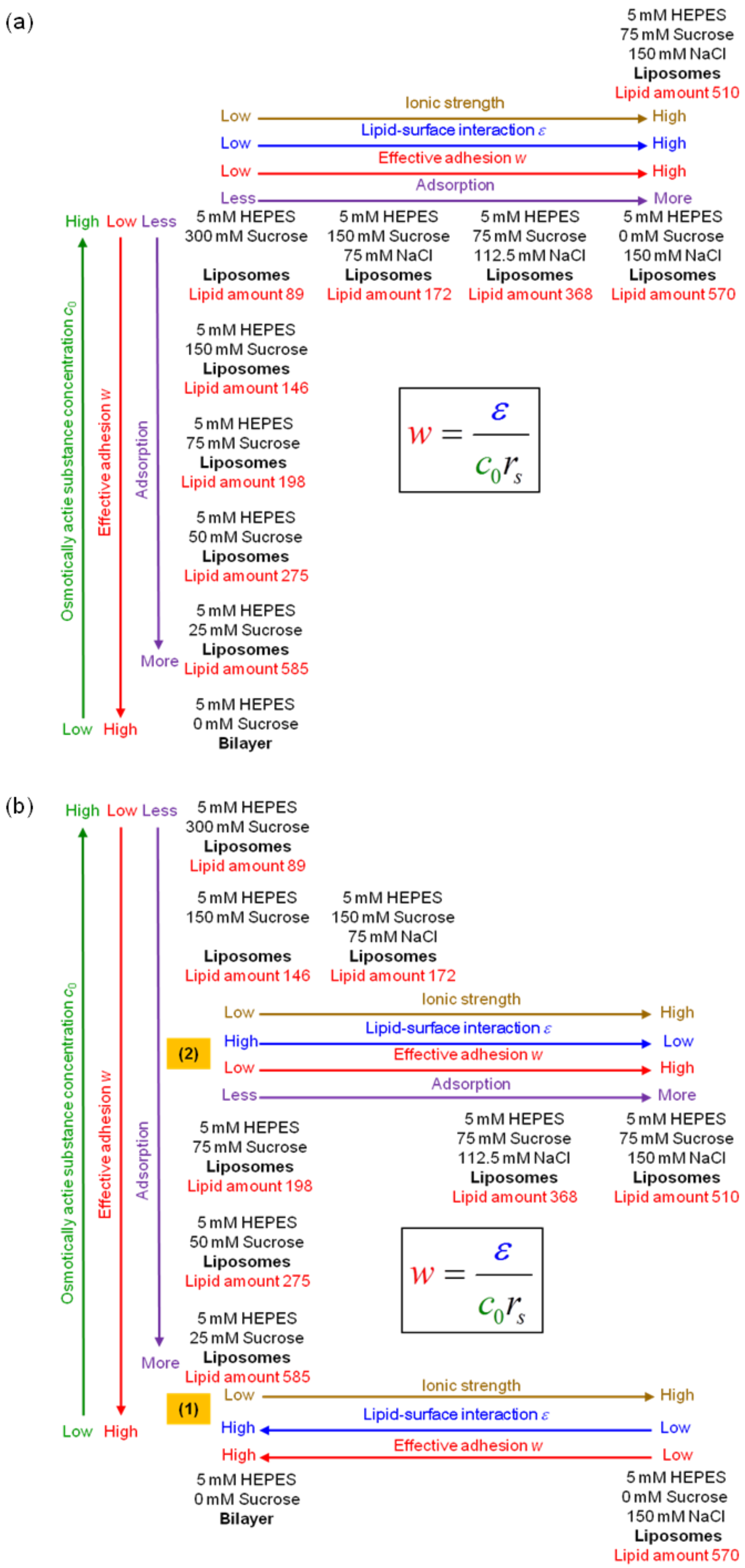
(a)
5 mM HEPES
75 mM Sucrose
150 mM NaCl
Liposomes
Lipid amount 510
Ionic strength
Low
High
Lipid-surface interaction ε
Low
High
Effective adhesion w
Low
High
Adsorption
Less
More
High Low Less
5 mM HEPES
300 mM Sucrose
Liposomes
Lipid amount 89
5 mM HEPES
150 mM Sucrose
75 mM NaCl
Liposomes
Lipid amount 172
5 mM HEPES
75 mM Sucrose
112.5 mM NaCl
Liposomes
Lipid amount 368
5 mM HEPES
0 mM Sucrose
150 mM NaCl
Liposomes
Lipid amount 570
Osmotically actie substance concentration c_0
Effective adhesion w
Adsorption
5 mM HEPES
150 mM Sucrose
Liposomes
Lipid amount 146
$w = \frac{\varepsilon}{c_0 r_s}$
5 mM HEPES
75 mM Sucrose
Liposomes
Lipid amount 198
5 mM HEPES
50 mM Sucrose
Liposomes
Lipid amount 275
5 mM HEPES
25 mM Sucrose
Liposomes
More
Lipid amount 585
Low High
5 mM HEPES
0 mM Sucrose
Bilayer
(b)
High Low Less
5 mM HEPES
300 mM Sucrose
Liposomes
Lipid amount 89
5 mM HEPES
150 mM Sucrose
Liposomes
Lipid amount 146
5 mM HEPES
150 mM Sucrose
75 mM NaCl
Liposomes
Lipid amount 172
Osmotically actie substance concentration c_0
Effective adhesion w
Adsorption
Ionic strength
Low
High
(2)
Lipid-surface interaction ε
High
Low
Effective adhesion w
Low
High
Adsorption
Less
More
5 mM HEPES
75 mM Sucrose
Liposomes
Lipid amount 198
5 mM HEPES
75 mM Sucrose
112.5 mM NaCl
Liposomes
Lipid amount 368
5 mM HEPES
75 mM Sucrose
150 mM NaCl
Liposomes
Lipid amount 510
5 mM HEPES
50 mM Sucrose
Liposomes
Lipid amount 275
$w = \frac{\varepsilon}{c_0 r_s}$
5 mM HEPES
25 mM Sucrose
More
Liposomes
Lipid amount 585
Ionic strength
Low
High
(1)
Lipid-surface interaction ε
High
Low
Low High
Effective adhesion w
High
Low
5 mM HEPES
0 mM Sucrose
Bilayer
5 mM HEPES
0 mM Sucrose
150 mM NaCl
Liposomes
Lipid amount 570

Figure 3.7. Illustration of how osmotic effects and electrostatic interactions conspire to control liposome behavior on surfaces. Lipid amount labeled in the figures was calculated as described in the text above, the unit of lipid amount is ng/cm^2.

(a) Qualitative comparison between the experimental results and the model. The effective adhesion strength w decreases with osmotically active substace (sucrose) concentration c_0 (red and green arrows), and increases with ionic strength (red and brown arrows) at constant osmolarity. In other words, increasing the ionic strength increases the strength of lipid-substrate interactions ε (brown and blue arrows).

(b) This is the same figure as in (a), but drawn with the assumption in mind that while sucrose does have an osmotic effect, NaCl does not. In principle, NaCl is more permeable than sucrose. However, this assumption leads to a contradiction.

Adsorption of more liposomes is taken to indicate stronger effective adhesion strength w. The effective adhesion strength w of bilayer formation (5 mM HEPES, 0 mM sucrose) is higher than the one for vesicular layer formation, because a higher adhesion strength is needed for liposome rupture. The results show that amount of adsorbed lipids, and therefore the effective adhesion strength w, diminishes with sucrose concentration but increases with the ionic strength at a constant osmolarity (illustrated by vertical and horizontal arrows in Figure 3.7a). In other words, in the vertical direction, the denominator of equation $w = \frac{\varepsilon}{c_0 r_s}$ (Equation 3.14) changes while the numerator, that contains the lipid-surface interaction contribution, stays constant (green and red arrows in Figure 3.7a). In the horizontal direction, the denominator stays constant while the numerator changes as the lipid-surface interactions are affected by the ionic strength, qualitatively confirming the model (brown, blue and red arrows in Figure 3.7a).

The lipid-substrate interaction is a combination of all the attractive and repulsive interactions acting between the surface and the lipid headgroup, such as van der Waals, electrostatic, hydration, etc (Figure 1.9 in Chapter 1). In this context, one effect of monovalent salts is to screen electrostatic interactions [242-244]. Therefore, these results suggest that the electrostatic component of the interactions between zwitterionic phospholipid such as DOPC and a negatively charged substrate such as TiO_2 is repulsive, as it becomes stronger at higher ionic strength.

Another two effects of monovalent salts are to weaken the attractive van der Waals force [245, 246], and to increases the repulsive hydration force [247]. The former effect is too weak compared to the effect to screen the electrostatic interaction so that it is negligible [165]. In the latter case, the repulsive hydration force should increase with increasing NaCl concentration, and decrease the lipid-substrate interaction ε. However, the opposite was observed: the effective adhesion strength w, and therefore the lipid-substrate interaction ε, increased with increasing NaCl concentration at constant osmolarity (Figure 3.7a).

In a number of previous studies, zwitterionic liposome behavior on negatively charged surfaces has been investigated at different ionic strength. Note that all these studies discussed below were performed at neutral pH, the same as in the current study. Cho et al. [151] showed intact adsorbed POPC liposomes on TiO_2 at high ionic strength (10 mM Tris, 200 mM NaCl), correlating with what was observed here that DOPC liposomes remained intact on TiO_2 at high ionic strength. They found bilayer formation at the same condition on SiO_2 due to the stronger lipid-surface interaction. Seantier et al. [152] and Boudeard et al. [143] found two-step SLB formation from

DMPC liposomes on SiO_2 at high ionic strength (150 mM NaCl, in both the 20 mM HEPES and 10 mM Tris-HCl buffers) where the critical surface coverage of liposomes on the surface was required, while one-step SLB formation at low ionic strength where the critical surface coverage was not required, indicating stronger effective adhesion between zwitterionic lipids and negatively charged surface at low ionic strength. These results suggested that electrostatic interaction between zwitterionic lipids and negatively charged surfaces was probably attractive. It was also observed in this study that DOPC formed bilayer on TiO_2 at low ionic strength (5 mM HEPES), while vesicular layer at high ionic strength (5 mM HEPES, 150 mM NaCl). Given the results presented above, it appears that the diminished liposome-surface adhesion at higher ionic strength was due to the osmotic effects. In other words, changing the salt concentration changes both the ionic strength and the osmolarity of the buffer, and the overall effective adhesion various in a complex and unpredictable way.

If one assumes, as previous investigators have done that the electrostatic interaction between zwitterionic lipids and negatively charged surfaces is attractive, and electrolyte concentration only has electrostatic effect, but not the osmotic effect, one arrives at the following contradiction. The adhesion strength ω and therefore the lipid-surface interaction ε decrease with increasing salt concentration in sucrose-free buffers (horizontal arrow group (1) in Figure 3.7b), as the electrostatic attraction between zwitterionic liposomes and negatively charged surfaces is screened by salt. However, in buffers with the same concentration of sucrose but different concentrations of NaCl, liposome adsorption increased with increasing NaCl concentration, indicating increased adhesion strength ω and therefore increased lipid-surface interaction ε with increasing salt concentration (horizontal arrow group (2) in Figure 3.7b), which is contradict to the findings in sucrose-free buffers (horizontal arrow group (1) in Figure 3.7b). Therefore, the effect of salt on liposome behavior on the surface is not simply the electrostatic interaction effect, but a combination of electrostatic and osmotic effects (as illustrated in Figure 3.7a).

Recently, Anderson et al. measured the forces between DMPC bilayers and SiO_2 with the surface forces apparatus as well as SLB formation on silica with QCM at different ionic strengths. They found that at high ionic strength, the interaction between the lipids and the surface is attractive and quite strong (0.5-1 mJ/m^2)—much higher than expected from vdW interactions, which they attributed to an attractive electrostatic interaction between a charged and a neutral surface interacting at constant potential. This interpretation implies a non-trivial charge-regulation mechanism on SiO_2 that was not explained [165]. At low ionic strength, they found a repulsive interaction which they attributed to electrostatic repulsion between surfaces interacting at constant charge. These conclusions of Anderson et al. contradict the conclusion I reach from the analysis of adsorbed liposome behavior.

Firstly, both in my experiments and in the experiments reported by Seantier et al. [152] and Boudeard et al. [143], the interactions between zwitterionic lipids and negatively charges substrates (SiO_2 or TiO_2) were attractive, not repulsive, leading to liposome adsorption or bilayer formation. The repulsion reported by Anderson et al. [165] is in this context rather surprising and may be due to the difference of the buffers used: Anderson et al. used PBS, while Seantier et al. and Boudeard et al. and me used

HEPES or Tris-HCl [115, 143, 248]. This buffer effect needs to be investigated further.

Secondly, with their surface forces apparatus measurements, Anderson et al. measured the lipid-surface interactions directly (ε in Equation 3.14), while I infer it from the measurement of the liposome behavior, i.e., effective adhesion *w*. In both cases, it is concluded that the lipid-surface interactions are stronger in the high ionic strength buffers because of the increase in the lipid-surface interactions, which is compensated by the osmotic contribution salt has to the effective adhesion. However, I conclude that the increase in the lipid-surface interactions with the ionic strength is due to the screening of the electrostatic repulsion by the salt, while Anderson et al. asserts that it is due to a change in the charge regulation on the SiO_2 surface that leads to attractive surface-lipid electrostatic interactions at high ionic strength. This difference in interpretations remains to be resolved, for example, by identifying the charge regulation mechanism.

3.3. Conclusions

In this Chapter, how osmotic effects and electrostatic interaction control zwitterionic DOPC liposome behavior on TiO_2 surface was separately investigated in electrolyte-containing buffers. A theoretical model from Gur Fabrikant and Michael Kozlov from the Tel Aviv University was also used to describe these effects. It showed that osmotic pressure induced by liposome deformation and solvent outflow upon liposome adsorption reduced liposome-surface adhesion, and the adhesion decreased with increasing osmotically active substance concentration. The adhesion increased with increasing ionic strength in isotonic buffers. Therefore the electrostatic interaction between zwitterionic DOPC liposomes and negatively charged TiO_2 surface was repulsive, and was screened at high salt concentration.

Chapter 4

Excess Lipid Leaving the Surface During SLB Formation

4.1. Summary

SLBs spontaneously form from the spreading of liposomes of appropriate compositions on hydrophipic surfaces such as glass or silica, mica, silicon nitride, and tinatia. Previous studies have suggested that excess lipid leaves the surface (desorbs) during the transformation from adsorbed liposomes to SLB [146, 175]. However, how excess lipid leaves the surface during SLB formation and how it is related to the overall kinetics of SLB formation is unclear. In this chapter, tubular structures coexisting with the bilayer patches were observed during the formation of SLBs from zwitterionic liposomes (made of pure dioleoyl phosphatidyl choline (DOPC) or the mixture of DOPC, dipalmitoyl phosphatidyl choline (DPPC), and cholesterol) on TiO_2 in the presence of Ca^{2+}. By visualizing the growth process of the tubular structures through a combination method of time-resolved fluorescence microscopy and fluorescence recovery after photobleaching, the form the excess lipid left the surface was observed. These observations also provided the feasibility to analyze bilayer patch growth kinetics during the late stages of SLB formation. It was found that late

stages of SLB formation involved both desorption of excess lipids from the surface and further adsorption of liposomes from solution.

4.2. Results

When preparing bilayers from liposomes containing either DOPC or a mixture of DOPC, DPPC, and cholesterol at the 35 : 35 : 30 molar ratio, on TiO_2 in pH 7.4 buffers containing 2 mM $CaCl_2$ but in the absence of other monovalent salts (except the HEPES buffer itself), I observed the bilayers to co-existed with structures exhibiting tube- or flower-like morphology (Figure 4.1, Figure 4.2). These structures appeared to originate from common centers (indicated with hexagons in Figure 4.1).

SLB formation was evident from the long-range mobility of the lipids evaluated by fluorescence recovery after bleaching. The bleaching sequences and recovery plots for the two systems are shown in Figure 4.1, and the values of the mobile fractions and diffusion coefficients are collected in Table 4.1. The values of the diffusion coefficients are typical of SLBs [97, 249] taking into account that cholesterol slows down lipid diffusion [250, 251]. However, the recovery was not complete, as is evident from relatively low mobile fractions (～0.8, Table 4.1). The elongated tubular or flower-like structures did not recover to the original intensity. This was visible both in the DOPC : DPPC : cholesterol system and in the DOPC system (Figure 4.1d and l). During the recovery process, dark (low-intensity) lines were visible in places where the original tubular structures were present (red arrowheads in Figure 4.1c and k).

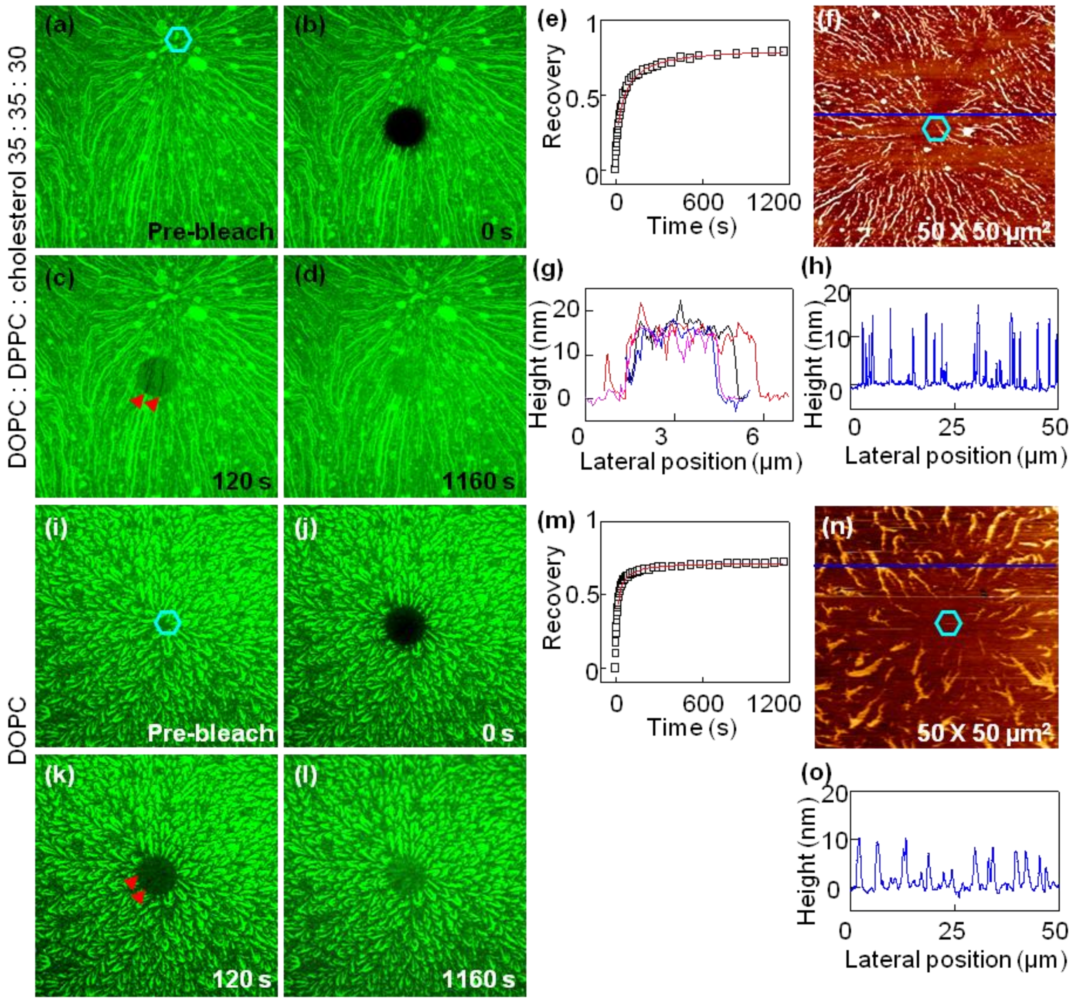

Figure 4.1. Example of an SLB co-existing with tubular structures. These fluorescence and AFM images were obtained with samples prepared from liposomes containing DOPC, DPPC, and cholesterol at the molar ratio of 35 : 35 : 30 (a-h), or pure DOPC (i-o) labeled with 1% NBD-PC prepared and incubated on titania in a buffer containing 10 mM HEPES and 2 mM $CaCl_2$, pH 7.4 at room temperature.(a-d) and (i-l) Fluorescence microscopy images illustrate lipid organization and the photobleaching series. The open hexagons with turquoise borders in (a) and (i) indicate an area devoid of tubular structures, where they appear to originate or terminate. In (b) and (j) the same area can be seen to contain other types of lipid aggregates. The black circle in (b) and (j) is the photobleached area. The fluorescence intensity recovers, as expected for an SLB, but the recovery is never complete. Tubular structures are not visible in the bleached area in (c) and (k), but there are dark lines (red arrowheads) in places where the tubes were located. These dark lines are mostly gone in (d) and (l). The size of the fluorescence images is 142 × 142 μm^2. The

diameter of the bleached spot is 22 μm. (e) and (m) Recovery of the fluorescence intensity in the bleached area fitted with the Soumpasis equation. (f) and (n) Atomic force microscopy image (size 50×50 μm^2, z scale 20 nm) depicting the tubular structures an area relatively devoid of them in the center (open hexagon with turquoise borders). Blue lines indicate where the height profile shown in (h) and (o) were taken. (g) Height profiles along the tubes in the AFM image showed no boundaries or separations indicating that they are not composed of individual liposomes.

The same structures were observed by atomic force microscopy (AFM, Figure 4.1f and n). AFM revealed that the areas where the tubular structures originated were largely devoid of them (see the turquoise hexagons in Figure 4.1f and n). In other words, tubular structures appear at the periphery of smooth SLB regions. The height of these tubular structures was ~ 10 – 15 nm above the surrounding bilayer (Figure 4.1g, h, o). The heights of the isolated liposomes adsorbed on the surface were reported to be range from 10 to 20 nm investigated by AFM [141, 252]. However, along the long axes of the tubular structures, there did not appear to be any boundaries or separations that would indicate that they are composed of individual liposomes (Figure 4.1g). These structures were very loosely attached to the bilayer and could be easily displaced by the tip if the force was not kept to a minimum.

Because the tubular structures appeared at the periphery of the SLB areas, I hypothesized that they might be related to the pathway for lipid desorption from the surface during the SLB formation. To investigate this idea, sequences of time-resolved fluorescence images following the formation of the bilayer from DOPC liposomes were acquired (Figure 4.2, images were selected from two movies). The process of SLB formation began with a layer of adsorbed liposomes. This could be confirmed by bleaching of fluorescence that showed no evidence of recovery (Figure 4.2 b-c, j-k). Subsequently, low-intensity regions began to appear in several places (white arrowheads in Figure 4.2). I interpreted these regions as bilayers. Weirich et al. reached a similar conclusion [174]. These bilayer regions proceeded to expand, covering progressively more area. As they expanded, three events happened: one, flower-like structures formed at the periphery of these low-intensity regions; two, the bilayer regions expanded into the bleached region, where the intensity could be seen to recover to the level of the bilayer regions; and three, there were no flower-like structures in the bleached region even though they were present right next to the bleached region (Figure 4.2e – h, m-p). This indicated that the lipid material in these structures arose from the liposomes adsorbed on the surface. If most of the lipid in these regions had come from solution instead, via adsorption to defects in the bilayer for example, the bleached regions would have been covered by the tubular structures to the similar extent as the regions around them (Figure 4.2h, p). Therefore what was observed was a pathway for excess lipid to leave the surface during the bilayer formation process.

Notably, after some time, some flower-like structures do appear in the bleached region as well (Figure 4.2g, h), indicating that there is a pathway that allows new, fluorescent material from solution to reach the area where fluorescence was previously bleached. However, the fluorescent intensity of these structures reached plateau after some time, but never reached the same level as before bleach, as mentioned above (Figure 4.1). Again, if most of the lipid in these regions came from solution, via adsorption to defects in the bilayer for example, the bleached regions would be covered by the tubular structures just like the regions surrounding them

(Figure 4.2). Therefore what is observed here is a pathway for excess lipid leaving during the bilayer formation process.

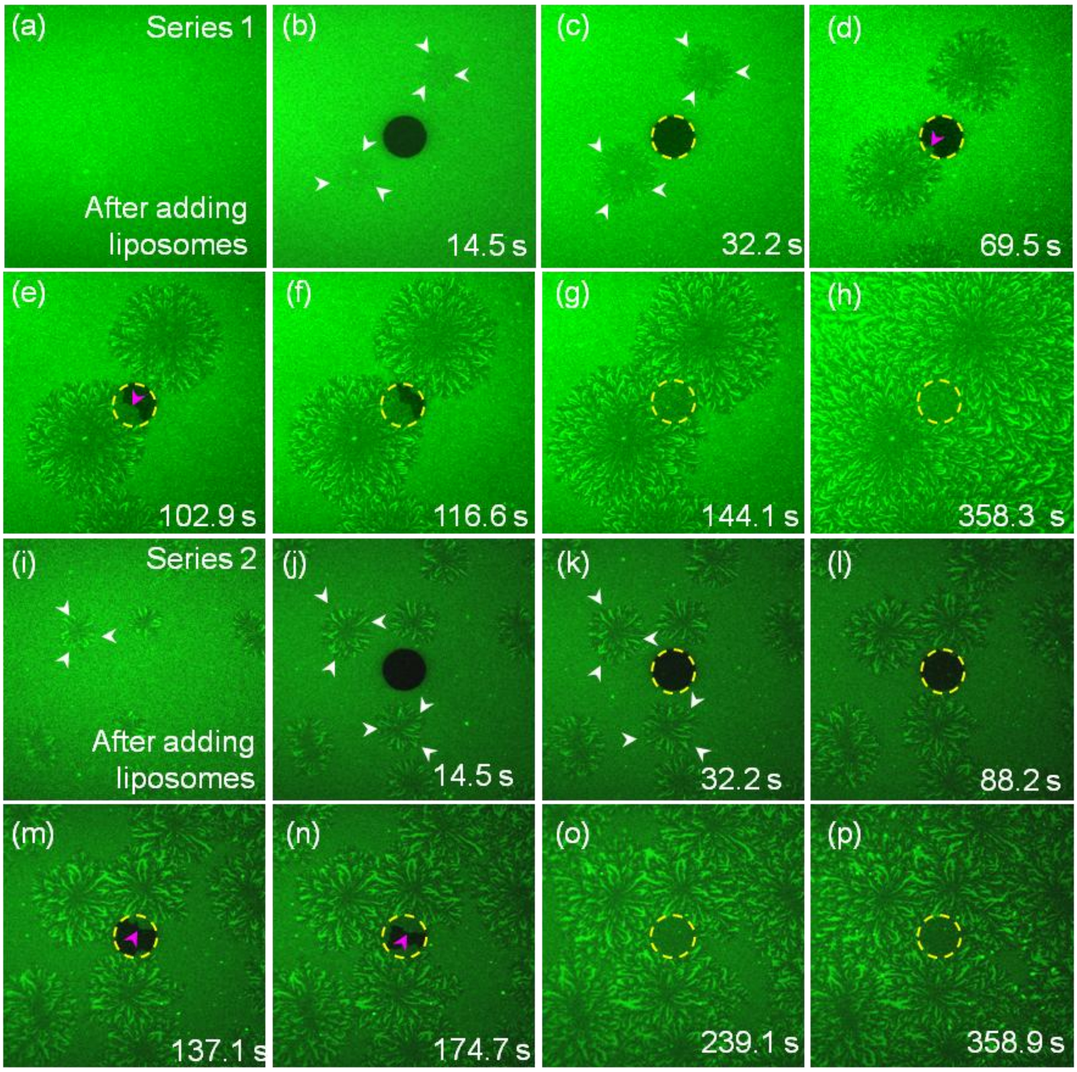

Figure 4.2. Time-resolved fluorescence images of bilayer formation. The fluorescence images were acquired with pure DOPC liposomes in a buffer containing 10 mM HEPES and 2 mM $CaCl_2$ at 60 ℃. Two series were taken: (a)-(h) series 1, (i-p) series 2. A supported vesicular layer is formed after adding liposomes (a) and (i). This can be judged from lack of recovery after photobleaching; the bleached spot is highlighted with dashed yellow circles in (c)-(h) and (k)-(p), and fluorescence intensity within that spot does not recover in images (b)–(c) and (j)-(l). Darker circular domains appear in (b) and (i), highlighted with the white arrowheads, that grow as a function of time until they cover essentially the entire surface (b)–(h), (i)-(p). They are decorated with the flower-like structures at the periphery, but domain

centers are free of these structures. The bleached spot begins to recover once the darker domains extend into it (pink arrowheads in (d)-(e), and (m)-(n)). Based on that, the domains are considered to be bilayers. Note that the flower-like structures are not visible in the bleached area (f)–(h), (n)-(p). Therefore they arise from the lipids present on the surface in the adsorbed liposomes and represent the excess lipid leaving the surface during the bilayer formation. The size of the images is 142 × 142 μm^2. The diameter of the bleached spot is 22 μm.

In the system used here, TiO_2, $CaCl_2$, phosphatidyl cholines with or without cholesterol, there appears to be an energy barrier preventing the complete desorption of these tubular structures, and they remain attached to the SLB. However, they can be removed. After incubating the samples in water for 36 hrs, what was left are SLBs that exhibit normal behavior: homogeneous fluorescence and complete recovery after bleaching (Figure 4.3). Sometimes defects remained in the SLBs after this wash step (Figure 4.3b), but this observation was not reproducible. These defects may heal and are therefore not always observed.

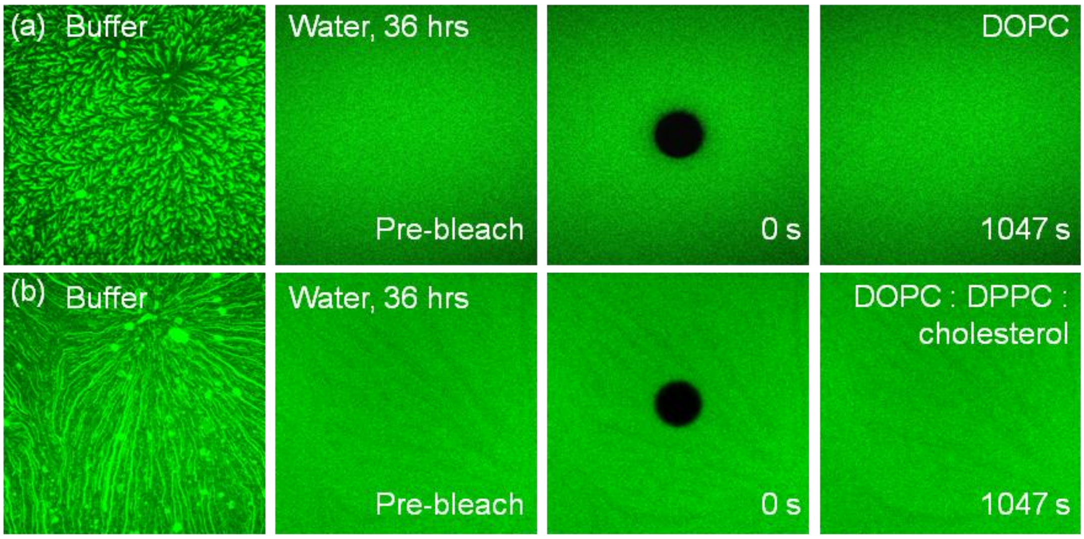

Figure 4.3. Excess lipid can be removed by washing to recover homogeneous SLBs. Fluorescence images of DOPC (a) and DOPC : DPPC : cholesterol 35 : 35 : 30 mol-% (b) systems before (“Buffer”) and after leaving them in water for 36 hrs. The flower- or tube-like structures are seen to disappear, giving way to homogeneous fluorescence

and recovery after bleaching characteristic of supported lipid bilayers. Time (in seconds) refers to the bleaching experiments. Fluorescence intensity recovers after bleaching. The mobile fractions and diffusion coefficient values are presented in Table 4.1, labeled “after wash”. The size of the images is 142 × 142 μm^2. The diameter of the bleached spot is 22 μm.

Table 4.1. Diffusion coefficients and mobile fractions of NBD-PC label determined under various experimental conditions presented in this chapter. For the DOPC : DPPC : cholesterol system, the lipid composition was 35 : 35 : 30 mole-%. For the DPPC : DOPC system, the lipid composition was 50 : 50 mol-%.

Composition	**Temperature**	**M**	**D, × 10^{-8} cm^2/s**	**Figure**
DOPC, before wash	22 ℃	0.80 ± 0.08	1.66 ± 0.45	Figure 4.1
	60 ℃	0.77 ± 0.06	1.83 ± 0.12	
DOPC : DPPC : cholesterol, before wash	22 ℃	0.82 ± 0.06	0.55 ± 0.08	Figure 4.1
	60 ℃	0.73 ± 0.03	1.78 ± 0.18	
DOPC, after wash	22 ℃	1.04 ± 0.05	0.54 ± 0.03	Figure 4.3
	60 ℃	0.99 ± 0.07	0.90 ± 0.07	
DOPC : DPPC : cholesterol, after wash	22 ℃	1.01 ± 0.07	0.31 ± 0.04	Figure 4.3
	60 ℃	0.99 ± 0.07	0.67 ± 0.051	
DOPC : DPPC before wash	60 ℃	1.02 ± 0.07	1.86 ± 0.32	Figure 4.4
DOPC : DPPC after wash	60 ℃	1.01 ± 0.05	1.44 ± 0.78	

4.3. Discussion

There are numerous studies of supported bilayer formation by microscopic techniques under a wide variety of conditions [98, 141, 174, 252-256]. However, tubular structures such as those shown in Figure 4.1 and Figure 4.2, have not been reported in the literature, nor in the majority of conditions that have been investigated in this Thesis (details in Chapter 5). Instead, either lipid bilayers or intact liposome layers are observed. Sometimes isolated liposome inclusions or patches may be visible that may or may not be removed by washing. For example, DOPC : DPPC 50 : 50 mol-% liposomes without cholesterol in the same buffer on TiO_2 gave rise to supported

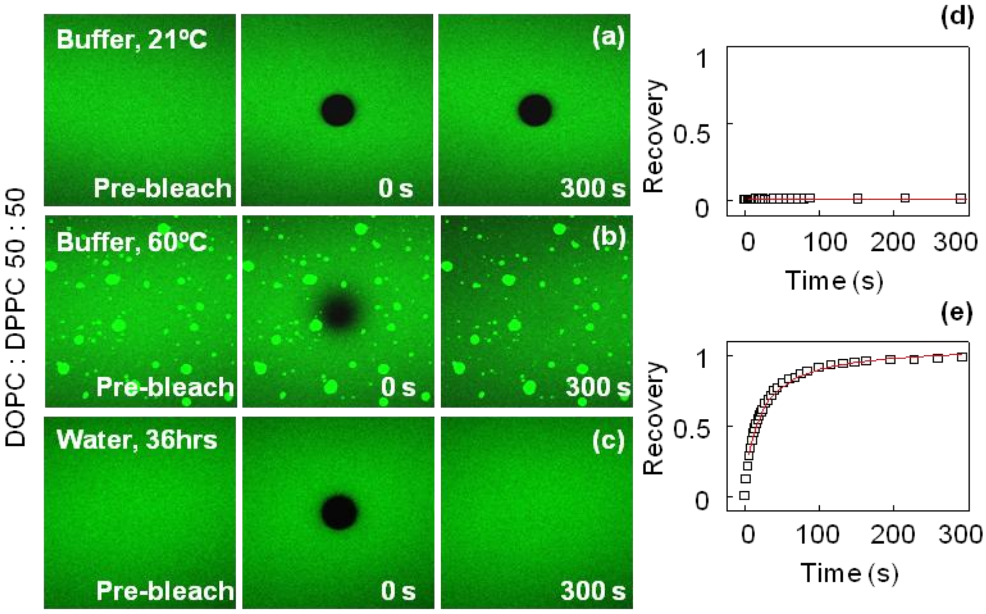

Figure 4.4. DOPC : DPPC liposomes at a molar ratio of 50 : 50 without tubular morphology. (a) Supported vesicular layer was formed at 21° C. Recovery plot (d) showed no recovery. (b) Supported lipid bilayer was formed upon heating to 60° C. No tube-like of flower-like structures were observed. Patches were present. Recovery plot (e) showed full recovery. (C) After leaving the sample in water for 36 hrs, the patches left. Fluorescence images size: 142 × 142 μm^2. Bleached spot diameter: 22 μm.

vesicular layer at room temperature and SLBs upon heating to 60 ℃ without tube-like or flower-like structures (Figure 4.4; SLB formation was judged from the long-range lipid mobility, Table 4.1). DOPC liposomes in high ionic strength buffers with or without Ca^{2+} form bilayer on SiO_2 but supported vesicular layers on TiO_2 [96]. And so on. In total, I have characterized six different lipid compositions in four sets of buffers on TiO_2. Those results will be presented in Chapter 5. Only the two conditions reported here exhibited the kind of behavior shown in Figure 4.1 and Figure 4.2.

On the other hand, the presence and consequent removal of excess lipid material from the surface during bilayer formation is thought to be a general feature of this process, as discussed in the Introduction. I propose that the rate at which excess lipid is removed from the surface varies, depending on the details of lipid-surface and/or lipid-lipid interactions. Under most circumstances, lipid excess is removed faster than can be visualized. For the two systems reported here (TiO_2, $CaCl_2$, phosphatidyl cholines with or without cholesterol), there is a sufficiently high energy barrier that results in a sufficiently slow departure rate, and lipids remain attached to the SLB What supports this idea is that they can be removed by washing with a low ionic strength and Ca^{2+}-free medium (water, Figure 4.3).

It is difficult to speculate on the origin of this energy barrier due to the rather limited set of observations and lack of general knowledge about the liposome-liposome and lipid-surface interactions involved in the SLB formation process. However, two useful deductions can be made from the presented observations. Firstly, the overall appearance of the images is reminiscent of the Saffman-Taylor (fingering) instability that arises when a fluid flows through a porous media or when a less viscous fluid flows into a more viscous one (reviewed in [257]). Such instabilities have been reported for the cases of spreading [258] and rupture [259] of giant unilamellar liposomes, but until now, not in the case of SLB formation. In the two cases shown in Figure 4.1 and Figure 4.2, the fingers appear to be decorated by the excess lipids. Possibly, the significant roughness of the TiO_2-coated glass slides used here contributes to this observation (root mean square roughness ～ 0.6 nm measured from AFM images, details in Chapter 5).

Secondly, the bilayer regions observed in Figure 4.1, 4.2. and 4.3 are roughly circular and well-defined (on the optical scale). Their appearance is rather different from the numerous and irregularly-shaped (also on the optical scale) bilayer patches that are observed on SiO_2 [174]. This indicates that the conditions for nucleation of the bilayer regions are less common in the case of DOPC onTiO_2 than on SiO_2; most likely, the liposome surface coverage required is higher on TiO_2 than on SiO_2. It is also expected that at a higher coverage, the rate of bilayer patch growth would be more isotropic, giving rise to a more circular shape.

The well-defined shape of the bilayer patches makes the analysis of their spreading behavior rather straight-forward. Patch area vs. time plots for the bilayer patches in Figure 4.2 are shown in Figure 4.5 and Figure 4.6. The timescales associated with these experiments are arbitrary, because bilayer formation started at different time relative to when the observations began. The bilayer patches are also of different size: they are much larger in Figure 4.2a-h than i-p. To enable the comparison of these two sets, the area of each patch was scaled by its area at the point when the patches started to merge, and the time axes were aligned by offsetting them relative to each other to bring the scaled patch areas into register. The resulting plot is shown in Figure 4.5, and the log-log version is in Figure 4.6a. After scaling, it becomes apparent that the rate of bilayer patch growth is independent of domain size—i.e., the larger patches in Figure 4.2a-h grow at about the same rate as the smaller ones in Figure 4.2i-p; their size is determined by their number, in other words, by the nucleation rate. On the other hand, the rate at which patches grow increases with time for all of them. This is exemplified by the power law-like behavior where the scaled area grows as $\sim t^{1.3}$ (black solid line in Figure 4.6a).

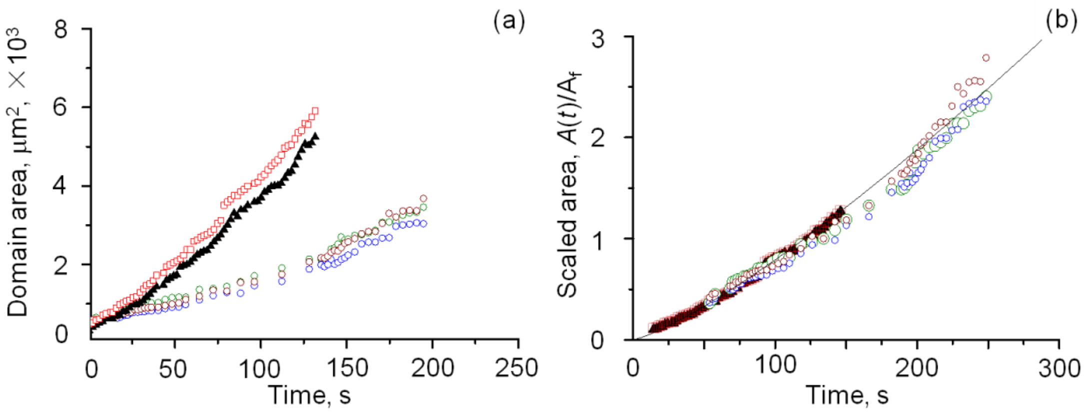

Figure 4.5. Analysis of membrane domain growth rates.

(a) The area vs. time plot for the domains shown in Figure 4.2a-h (black solid triangles and red open squares) and Figure 4.2i-p (brown, green and blue open circles).

(b) The scaled area, $As(t)= A(t)/Af$, was calculated by dividing the area at each time point by the area at the point when domains began to merge, Af, which occurred at $t = 88.23$ s for the domains shown in Figure 4.2 i-p and $t = 124.51$ s for the domains shown in Figure 4.2a-h. Furthermore, the two experiments were started at different times relative to the time when membrane domains nucleated. Therefore, for the domains shown in Figure 4.2i-p, a constant $t_0 = 53.8$ s was added to the time at which images were recorded, such that the scaled area $As(t+t_0)$ for that experiment was similar to the scaled area $A_s(t')$ for the domains shown in Figure 4.2a-h when $t' = t+t_0$. Black solid line: $A(t)/A_f \sim 0.0025t^{1.25}$.

Spreading of lipid bilayers on surfaces has previously been analyzed by Rädler et al [258]. These authors studied the spreading behavior from a central source and found that it was essentially parallel to the Brownian diffusion, with the radius of the patch $r(t)$ proportional to the square root of time, $t^{1/2}$, implying a linear dependence of patch area on time, and front velocity ~ $t^{-1/2}$. This was also observed more recently on nanostructured surfaces [260]. In our system, we are dealing with a nucleation-and growth type phenomenon where new liposomes join the spreading bilayer domains at the periphery. Their rate of growth should, therefore, be controlled by the supply of the material, i.e., by the liposome surface coverage. At a given surface coverage, the rate should be constant. This process is examined in Figure 4.6b.

Figure 4.6b shows a surface with black filled circles representing liposomes placed at random locations at a coverage of ~ 0.38; the coverage is defined as $\Theta = N\pi R^2 / A_{surface}$, where N is the number of liposomes on the surface, R is their radius, and $A_{surface}$ is the surface area. Let's suppose that the two liposomes located in the center of Figure 4.6b rupture, giving rise to a bilayer patch indicated with a red circle (assuming that the area of the patch that arises from liposome rupture simply equals the surface area of the ruptured liposomes, in other words, $A_{patch} = 4n\pi R^2$, where n is the number of liposomes that contributed to the patch). As this red patch comes into contact with more adsorbed liposomes (one to its right and one below), they will also rupture: it is observed experimentally that adsorbed liposomes rupture upon contact with growing bilayer patches [98, 137, 241]. The lipid material from these liposomes will join the patch, giving rise to the green patch comprised of the lipids from the four ruptured liposomes. This process will continue as long as the coverage of the liposomes on the surface is sufficiently high so that the growing patch can reach new liposomes. Simple analysis indicates that for this propagation scenario to work, the surface coverage has to be at least 0.38. At lower coverage, the liposomes are too far apart, and patch growth ceases. For comparison, at a coverage of ∼ 0.25, a layer of adsorbed liposomes contains the same amount of lipid material as a confluent lipid bilayer. This value was obtained by comparing the number of lipid molecules per unit area in an SLB with the number of lipid molecules per unit area in a layer of liposomes. This difference explains lipid excess at the surface during the SLB formation process.

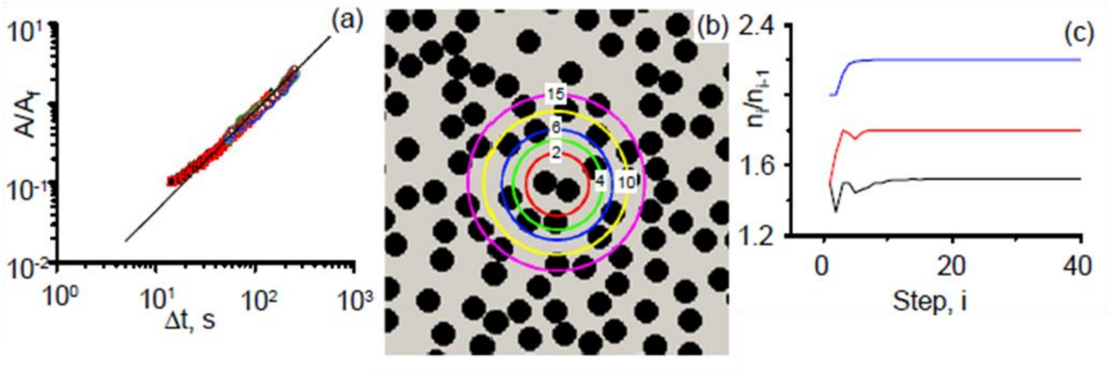

Figure 4.6. Following growth of bilayer patches.

(a) A log-log plot of the scaled bilayer patch area vs. time for the two patches visible in Figure 4.2a-j (black and red) and three of the patches visible in Figure 4.2i-p (brown, green and blue) from the original plot in Figure 4.4.

(b) This illustration shows liposomes (black circles) randomly arranged on the surface at a coverage of 0.38 and circular bilayer domains (colored open circles) that arise from liposome rupture. The red domain corresponds to the area covered by the lipids from the two liposomes present at its center. When formed, this domain will come into contact adsorbed liposomes, which will rupture, contributing to its area and forming the green domain. Numbers indicate the numbers of liposomescontributing to each domain (red – two liposomes, green – four liposomes, etc).

(c) This plot shows how the number of liposomes per bilayer domain evolves as the bilayer domain grows at different liposome surface coverages (0.38, black; 0.45, red; 0.55, blue). In each case, it was assumed that upon rupturing, a liposome contributes an area $4\pi R^2$ to the growing domain (no asymmetry). In each case, the first domain corresponded to two liposomes (nucleation). The number of liposomes, n, contributing to the domain at each subsequent growth step, i, was calculated from the liposome surface coverage as shown in (b).

In the above calculation, we ignored this point: for small liposomes, the area of the patch that arises from liposome rupture is smaller than expected based on the liposome area due to the significant difference in the number of lipids between the inner and outer leaflets of the liposome [170, 171]. If we plug in a realistic number of lipids per liposome for a liposome with a 25 nm outer diameter, 3.7 nm bilayer thickness [170], and area per lipid of 0.72 nm^2 [173], the coverage required for propagation would be ~ 0.51, and the equivalent bilayer coverage ~ 0.33; but now these values depend on the liposome size, because the asymmetry in the number of lipids between the two leaflets decreases with liposome size.

This "propagation coverage" should not be confused with the surface coverage required for nucleation of the bilayer patches, which is not discussed in this work. It is simply an expression of geometrical constraints that operate at the surface: for the bilayer patch to continue growing, it has to be able to reach new liposomes.

Comparison can be made between the number of liposomes contributing to the growing patch at a given step and the number of liposomes contributing to that patch at the preceding step, $\beta = N_i / N_{i-1}$, where i is the step number (i = 0 for the red patch, i = 1 for the green one, and so on, Figure 4.6b). It turns out that for a given coverage, β becomes constant after a few steps. Its value increases with coverage Θ (Figure 4.6c). In other words, as the bilayer patch grows, it will come into contact with progressively greater numbers of liposomes, but that number increases by a constant factor with the size of the patch. The patch should then grow at a constant rate, rather than speed up, as we observe experimentally (Figure 4.6a).

In the preceding analysis, it was assumed that the surface coverage was constant during patch growth. If, on the other hand, liposomes continued to adsorb to the surface as the patches grew, the amount of material available to the growing patch would increase with time. This could explain the behavior of the patch area as a function of time we observe (Figure 4.6a). Supporting this conclusion is the appearance of the fluorescent flower-like structures in the bleached area after some time (Figure 4.2g, h). We conclude that the final stages of the SLB formation—growth and coalescence of bilayer patches—entail an interplay between the departure of excess lipids on one hand and further liposome adsorption on the other. It should be pointed out that Weirich et al. reported an increase in the liposome adsorption rate concurrent with the bilayer patch growth, which they attributed to the affinity of adsorbing liposomes for the bilayer edges [174]. Their observations are consistent with the observation in this chapter, although our interpretations differ somewhat.

4.4. Conclusions

In this chapter, the late stages of SLB formation involving the departure of excess lipid material from the surface were investigated. Excess lipid that remained associated with the bilayer patches in SLBs formed on TiO_2 was observed in a Ca^{2+}-containing buffer in the absence of monovalent ions from pure DOPC or DOPC : DPPC : cholesterol mixtures. This material could be removed by washing with water, leaving behind regular, homogeneous SLBs, indicating that there was an energy barrier preventing desorption. By analyzing bilayer patch growth rate, it can be concluded that the late stages of SLB formation involved both desorption of excess lipid and continued adsorption of liposomes from solution. This is a consequence of the limitations on the long-range transport of lipid material at the surface that arises from poor or non-existent mobility of adsorbed liposomes.

Chapter 5

Cell Membrane Mimics: Phosphatidyl Serine- and Cholesterol-containing Asymmetric Supported Lipid Bilayers on Titania

---

5.1. Summary

Lipid organization in cell membranes is not random. They are organized both in transverse and in lateral directions. In the transverse direction, ‘reactive’ phospholipids like phosphatidyl serine (PS), phosphatidyl ethanolamine (PE), phosphatidyl inositol (PI) are enriched in the cytoplasmic leaflet, while ‘non-reactive’ lipids like phosphatidyl choline (PC) and sphingomyelin (SM) are enriched in the extracellular leaflet [14-20]. This asymmetry is maintained by an energy (ATP)-dependent processes [20-22], and has physiological and pathophysiological significance in blood clotting, cell-cell interactions, and clearance of apoptotic cells [15, 23, 24]. Models for studying transbilayer asymmetry remain scarce. Most of them

only have two components [93, 96-98], which is inadequate for the realistic lipid compositions in the cell membranes.

Lateral lipid organization is less well understood. Lipid compositional heterogeneity is thought to exist on the order of a few tens of nanometers, with preferential partitioning of transmembrane and membrane-anchored proteins [48-55]. These heterogeneities, sometimes referred to as rafts, are thought to play a crucial role in signaling events [12, 45]. Such heterogeneities have been difficult to reproduce in model systems. Instead, micron-sized domains are observed [56, 57], although critical fluctuations at sub-micron scale [121] might represent cell membrane mimics, this subject remains under investigation. Moreover, lipids in the cytoplasmic side of the cell membranes are hardly included in the models mimicking cell membrane lateral lipid organization. How is lateral organization coupled with transverse lipid asymmetry is largely unknown. Model systems that mimic both the transverse and lateral organization of lipids with physiological lipid composition in cell membranes are required but at the moment scarce.

In this Chapter, I describe the development of a model system that mimics both physiological lipid composition as well as the asymmetric lipid distribution. This system is based on titania (TiO_2)-supported lipid bilayers (SLBs) containing mixtures of high-melting and low-melting phosphatidyl cholines, phosphatidyl serine, and cholesterol. I studied lipid diffusion and organization in these SLBs by fluorescence microscopy/fluorescence recovery after photobleaching (FRAP), and atomic force microscopy (AFM) and was able to demonstrate lipid asymmetry in these bilayers but no large-scale phase separation.

While cells use ATP to sustain lipid asymmetry, in this model system, the lipid-surface adhesion energy supplies the free energy necessary to offset the entropy of mixing between the two leaflets. To shed further light on the process of formation of these bilayers, I investigated this process as a function of lipid composition, ionic strength, temperature, as well as surface roughness and chemistry.

5.2. Results and Discussion

5.2.1. Asymmetric Bilayers Containing DOPC, DPPC, DOPS, and Cholesterol Could be Prepared on TiO_2

It has been previously reported that lipid asymmetries develop spontaneously in SLBs prepared from liposomes composed of DOPC : DOPS 80 : 20 mol-% in Ca^{2+}-containing buffers on TiO_2, with DOPS being enriched in the surface-proximal leaflet and depleted from the surface-distal one [97, 98]. These observations are consistent with early studies of lipid asymmetries induced by electrostatic interactions between cationic lipids and negatively charged oxide surfaces [100, 101] if one supposes the strong Ca^{2+}-mediated PS-TiO_2 interaction that drives the asymmetry [96, 97].

Here I further introduced high-melting phosphatidyl choline (DPPC) and cholesterol into the system and showed that SLBs could be formed on TiO_2 from DOPC : DPPC : DOPS : cholesterol 26 : 26 : 18 : 30 mol-% liposomes in Ca^{2+}-containing buffer (10 mM HEPES : 150 mM NaCl : 2 mM $CaCl_2$) independent of incubation temperature (Figure 5.1). As previously, SLB formation was judged from long-range lipid mobility evident from the high recovery fractions ~1 when NBD-PC was used as a label (Figure 5.1a, Table 5.1). In the absence of Ca^{2+} (10 mM HEPES : 150 mM NaCl : 2 mM EDTA, where EDTA is a Ca^{2+}-chelator), this same lipid mixture gave rise to an SVL (Figure 5.1c), judging from no recovery using the combination of 0.5 mol-% NBD-PC and 0.5 mol-% NBD-PS as fluorescent label. These results agree with the previous findings from our group showing that DOPC : DOPS liposomes containing 20% of PS formed SLBs on TiO_2 in the presence of Ca^{2+}, but adsorbed intact in the absence of Ca^{2+} [96].

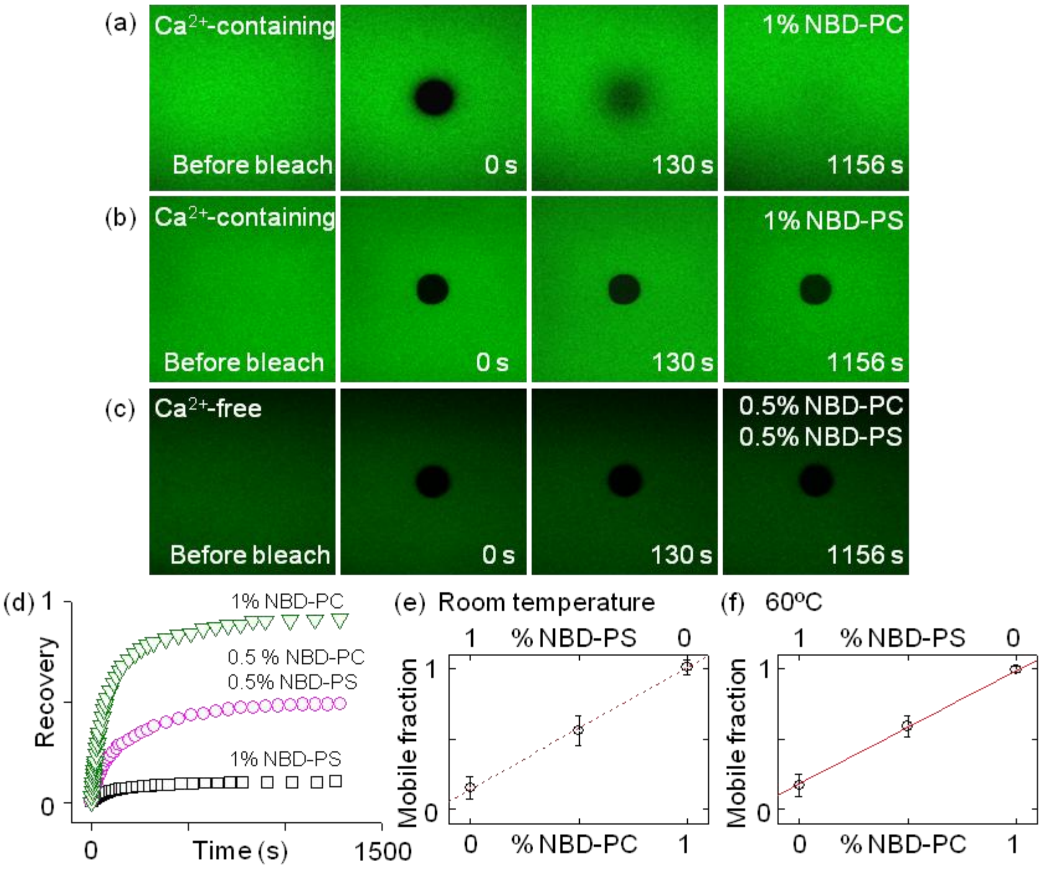

Figure 5.1. DOPC : DPPC : DOPS : cholesterol 26 : 26 : 18 : 30 mol-% liposome behavior on TiO_2 in the presence (a), (b) and absence (c) of Ca^{2+}. (a) and (b) fluorescence images before and after photobleaching in the presence of Ca^{2+} (10 mM HEPES : 150 mM NaCl : 2 mM $CaCl_2$, pH 7.4) showing complete recovery when 1 mol-% NBD-PC was used as label (a), and very little recovery when 1 mol-% NBD-PS was used as label (b). (c) Fluorescence

images before and after photobleaching in the absence of Ca^{2+} (10 mM HEPES : 150 mM NaCl : 2 mM EDTA, pH 7.4) showing no recovery when a combination of 0.5 mol-% NBD-PC and 0.5 mol-% NBD-PS was used as a label. Fluorescence images were taken at room temperature. Image size: 142 × 142 μm^2. The diameter of the bleached spot is 22 μm. (d) Recovery curves in the presence of Ca^{2+} with different compositions of NBD-PC and NBD-PS were used as label. Green triangles: 1 mol-% NBD-PC, corresponding to fluorescence images in (a); purple circles: 0.5 mol-% NBD-PC and 0.5 mol-% NBD-PS; black squares: 1 mol-% NBD-PS, corresponding to fluorescence images in (b). (e) and (f) Mobile fractions, determined from Soumpasis fits [221, 222] to the recovery curves in the presence of Ca^{2+}, when the mixture of NBD-PC and NBD-PS, with different compositions, was used as label. The data shown in (e) were recorded at room temperature, while those shown in (f) – at 60 °C. The mobile fractions increased linearly with increasing NBD-PC content in the label mixture. Each data point was from more than three duplicated samples. At least three measurements were performed for each sample. Error bars represent stand deviations. Dashed lines show the linear fit to the data.

Diffusion of the two different probes, NBD-PC and NBD-PS, was different. While complete recovery was found when NBD-PC was used as a fluorescence label, indicating bilayer formation (Figure 5.1a, Figure 5.1d green curve), almost no recovery was observed when NBD-PS was used as label (Figure 5.1b, Figure 5.1d black curve). Furthermore, the mobile fraction increased linearly with the amount of NBD-PC when mixtures of different ratios of NBD-PC and NBD-PS were used as a label; this trend was independent of incubation temperature (Figure 5.1d-f). The same trend was observed in the previous work in DOPC : DOPS SLBs on TiO_2 in Ca^{2+}-containing buffer [97]. This recovery behavior was shown to be indicative of PS asymmetry in the SLBs, with PS being enriched in the surface-proximal leaflet, consequently restricting its mobility.

No changes were observed when the DOPC : DPPC : DOPS: cholesterol SLBs were rinsed with EDTA-containing buffer (10 mM HEPES : 150 mM NaCl : 2 mM EDTA), and incubated overnight (Figure 5.2). This is considerably different than the behavior of the two component DOPC : DOPS system reported earlier [97]. The reasons for this difference in behavior are not clear and require further investigation, but may be related to the quality or permeability of the cholesterol-containing SLBs.

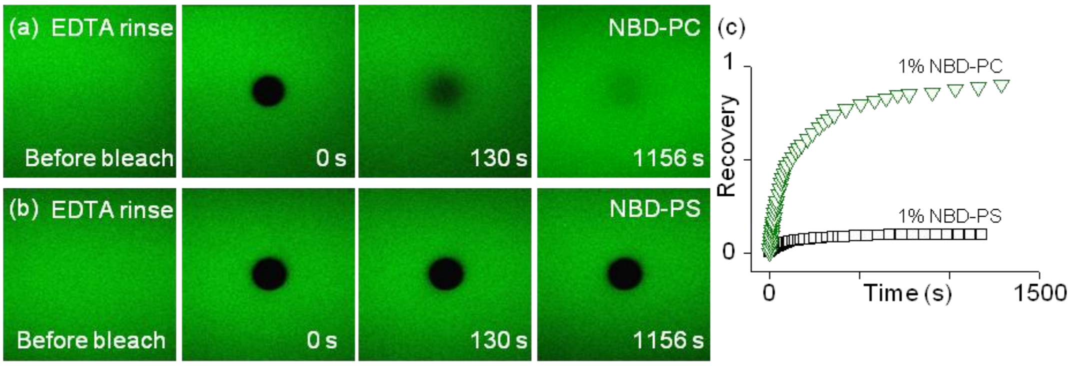

Figure 5.2. EDTA rinsing of DOPC : DPPC : DOPS : cholesterol 26 : 26 : 18 : 30 mol-% SLB on TiO_2 did not change PS asymmetry. SLBs were formed in the presence of Ca^{2+} (10 mM HEPES : 150 mM NaCl : 2 mM Ca^{2+}), following that, the Ca^{2+}-containing buffer was replaced with EDTA-containing buffer (10 mM HEPES : 150 mM NaCl : 2 mM EDTA) to exclude Ca^{2+}. After incubation with EDTA-containing buffer for overnight, no chnages of the recovery of NBD-PC and NBD-PS was observed compared to the one before EDTA rinsing: complete recovery when 1 mol-% NBD-PC was used as label (a); and very little recovery when 1 mol-% NBD-PS was used as label (b). Fluorescence images were taken at room temperature. Image size: 142 × 142 μm^2. The diameter of the bleached spot: 22 μm. (c) Recovery curves: green triangles: 1 mol-% NBD-PC, corresponding to fluorescence images in (a); black squares: 1 mol-% NBD-PS, corresponding to fluorescence images in (b).

One may also think that the recovery with NBD-PC and non-recovery with NBD-PS was due to phase separation in DOPC : DPPC : DOPS : cholesterol system. However, for that to be true, as a label of the low-melting DOPS, NBD-PS would need to be in the liquid disordered phase, and should also completely recover; and the recovery difference should disappear with phase separation at high temperature (60° C). This was not observed.

5.2.2. Asymmetric Bilayers Containing DOPC, DPPC, DOPS, and Cholesterol Do Not Exhibit Macroscopic Phase Separation

The morphology of the resulting bilayers was furthermore examined by atomic force microscopy (AFM). The SLBs appeared smooth and relatively featureless, with individual liposomes occasionally present. The root mean square (RMS) roughness was 0.33 ± 0.03 nm, compared to bare TiO_2-coated class surface which was twice

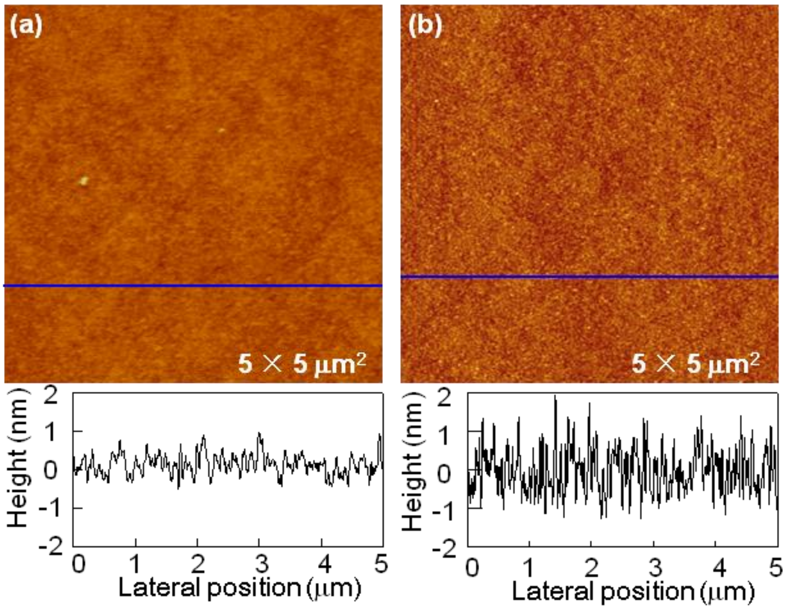

Figure 5.3. Tapping mode AFM images of DOPC : DPPC : DOPS : cholesterol 26 : 26 : 18 : 30 mol-% SLB on TiO_2-coated glass, and the bare TiO_2-coated glass taken at room temperature. Cross section analysis was along the blue line shown in the image. Image size: 5 × 5 μm^2, z-scale: 10 nm.

rougher, with a RMS roughness of 0.6 ± 0.03 nm (Figure 5.3, Table 5.4), correlated with the previous reported results showing decreased RMS roughness of SLBs on SiO_2-coated wafer and SiO_2-coated quartz crystals compared to the bare surfaces [261]. No domains were observed in these DOPC : DPPC : DOPS : cholesterol SLBs, again confirming that the non-recovery from NBD-PS was not due to phase separation, but occurred as a result of PS asymmetry. The reasons why phase separation was not observed in the AFM images will be further discussed below in section 5.2.8.

5.2.3. Bilayers Containing DOPC, DPPC, DOPS, and Cholesterol on Glass

For comparison, the behavior of the identical lipid mixture (DOPC : DPPC : DOPS : cholesterol 26 : 26 : 18 : 30 mol-%) was also examined on glass in the 10 mM HEPES : 150 mM NaCl : 2 mM $CaCl_2$ buffer (Figure 5.4). Bilayers also formed, as evidenced by the long-ranged mobility of the lipids and high recovery fractions of ～1 (Table 5.1). The behavior of the two fluorescent probes was very different on glass than on TiO_2. Firstly, the recovery fraction was independent of the label (NBD-PC or NBD-PS, Figure 5.4a-d). This is consistent with what is known about the interactions between PS and the surfaces of the two materials and the distribution of lipids in SLBs prepared on them [97, 98, 102]. Secondly, when NBD-PC was used as a label, dark (label-excluding) areas were observed in the fluorescence images (Figure 5.4a, b). The number of these areas decreased and their size increased, when the samples were incubated at 60 ℃ rather than room temperature (c.f. Figure 5.4a and Figure 5.4b, Figure 5.4e and Figure 5.4f). No such areas were observed when NBD-PS was used as a label (Figure 5.4c), from which I conclude that these areas are predominantly composed of PS. For this reason, I surmise they correspond to the multilayer structures previously inferred from quartz crystal microbalance measurements with PS-containing lipid mixtures on silica (called “restructuring” in ref [252]). Their origin is most likely related to the cochleates that PS is known for forming [262]. Indeed, AFM (Figure 5.4e – h) revealed the presence of multibilayer structures in these SLBs incubated at both temperatures.

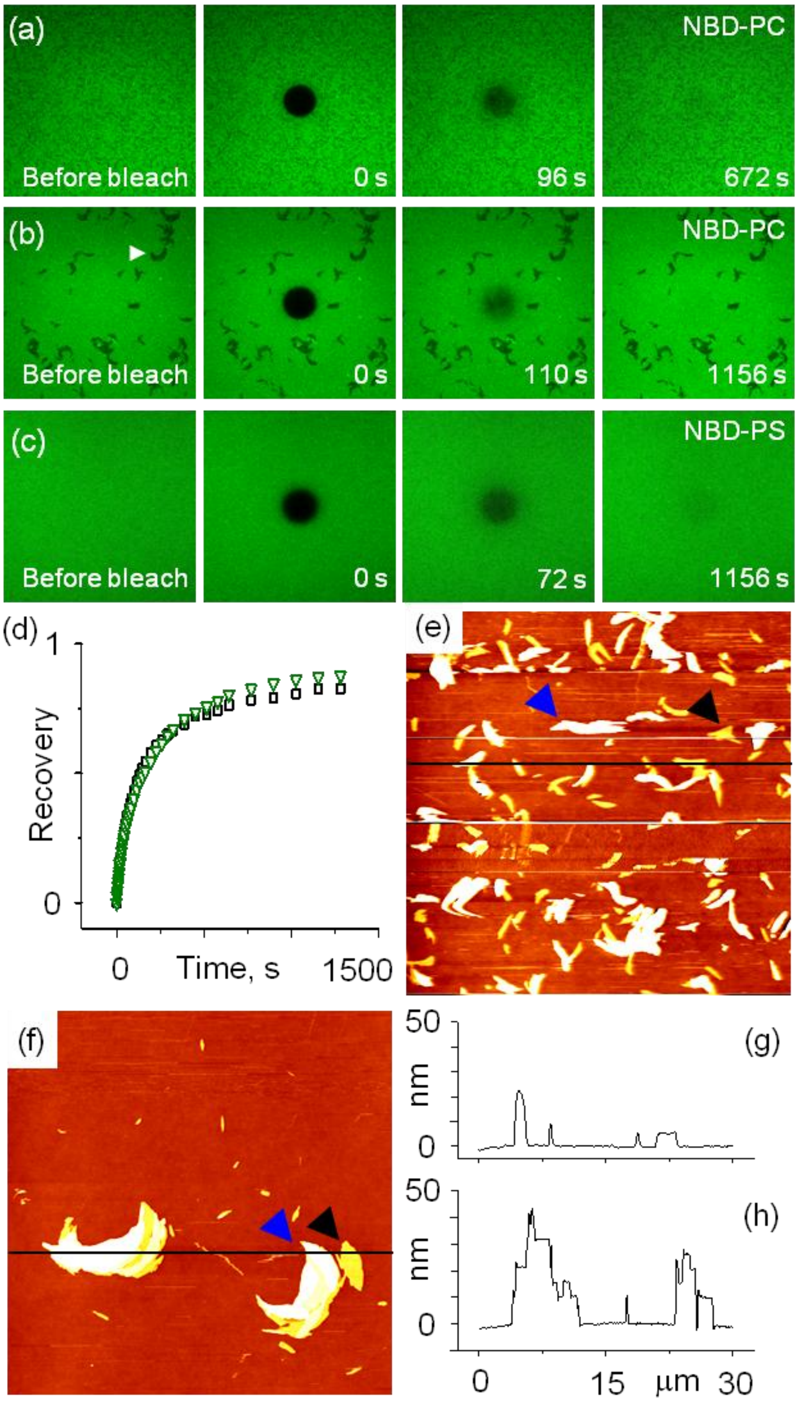

Figure 5.4. DOPC : DPPC : DOPS : cholesterol 26 : 26 : 18 : 30 mol-% supported lipid bilayers (SLBs) on glass. (a)-(c) Fluorescence images before and after photobleaching showing complete recovery when 1 mol-% NBD-PC was used as label (a, b), and no recovery when 1 mol-% NBD-PS was used as label (c). All the images were recorded at room temperature, but the bilayers in (b) and (c) were annealed at 60° C for 1 hour, while the bilayer in (a) was images without the annealing step. White arrowhead in (b) points

to one of the many stain-excluding areas that are visible in the images. The size of the images is 142 × 142 μm^2. The diameter of the bleached spot is 22 μm. (d) Recovery curves for the two probes: NBD-PC, green triangles; NBD-PS, black squares; corresponding to the sequences shown in (b) and (c), respectively. (e) and (f) Tapping mode AFM images of the bilayers shown in (a) and (b), respectively, (e) represents without annealing at 60^o C, (f) represent after annealing. The white aggregates, corresponding to the multilayers, were indicated with the blue arrowheads; the flat domains, with the height of ～5 nm, corresponding to the second layer, are indicated with black arrowheads. The images were taken at room temperature. Image size 30 × 30 μm^2, z-scale 30 nm. (g) and (h) Height profiles along the blue lines in (e) and (f), respectively.

5.2.4. Lipid Diffusion in Bilayers Containing DOPC, DPPC, DOPS, and Cholesterol on TiO_2 and Glass

The diffusion coefficients of the two different labels, NBD-PC and NBD-PS, in DOPC : DPPC : DOPS : cholesterol system measured on TiO_2 and SiO_2 surfaces are shown in Table 5.1, together with the relevant literature values from DOPC : DOPS system.

Table 5.1. Lipids diffusion coefficients and mobile fractions of PS-containing SLBs under different conditions from this study and the literature. All the measurements were taken in 10 mM HEPES : 150 mM NaCl : 2 mM $CaCl_2$, pH 7.4 buffer. Diffusion coefficients and mobile fractions in this study were average values taken from 3 individual samples. Each sample had at least 3 measurements.

Substrate	**Lipid composition (mol-%)**	**Label**	**T, ℃**	***D*, $\times 10^{-8}$cm^2/s**	**M**	**Reference**
TiO_2	DOPC : DPPC : DOPS : chol 26 : 26 : 18 : 30	NBD-PC	22	0.17 ±0.08	1.01 ±0.05	This study
			60	0.61 ±0.02	0.99 ±0.02	
		NBD-PS	22	0.26 ±0.07	0.15 ±0.07	
			60	0.49 ±0.05	0.17 ±0.07	
TiO_2	DOPC : DPPC : DOPS : chol 30 : 30 : 10 : 30	NBD-PC	22	0.17 ±0.01	1.06 ±0.06	
			60	0.66 ±0.09	1.01 ±0.02	
Glass	DOPC : DPPC : DOPS : chol 26 : 26 : 18 : 30	NBD-PC	22	0.19 ±0.02	0.99 ±0.05	
			60	0.25 ±0.06	1.01 ±0.05	
		NBD-PS	22	0.18 ±0.06	0.99 ±0.05	
			60	0.29 ±0.02	0.99 ±0.02	
TiO_2	DOPC : DOPS	NBD-PC	25	2.3 ±0.7	~ 1	Ref [97]
		NBD-PS	25	–	~ 0.04	
SiO_2	DOPC : DOPS	NBD-PC	25	1.1 ±0.2	~ 1	
		NBD-PS	25	2.0 ±0.1	~ 1	

$D_{NBD\text{-}PC}$ and $D_{NBD\text{-}PS}$ in DOPC : DPPC : DOPS : cholesterol system were similar on both TiO_2 and glass (Table 5.1), being ~ 0.2 × 10^{-8} cm^2/s at 22° C. The $D_{NBD\text{-}PS}$ is the diffusion coefficient of the fraction of PS that remains mobile – ~ 6% of the total PS in the SLBs which is presumed to be in the upper leaflet [98]. These diffusion coefficients are considerably slower than the ~ 1 – 2 × 10^{-8} cm^2/s at 25° C previously reported in the literatures [97] in DOPC : DOPS SLBs which do not contain cholesterol. Cholesterol is known to decrease the diffusion coefficient of the lipids in the l_d phase [250].

These diffusion coefficients were slightly dependent of temperature on both TiO_2 and glass, being ~ 0.2 × 10^{-8} and ~ 0.5-0.6 × 10^{-8} cm^2/s at 22 °C and 60 °C, respectively, on TiO_2, and ~ 0.2 × 10^{-8} and ~ 0.3 × 10^{-8} cm^2/s at 22 °C and 60 °C, respectively, on glass, suggesting bilayers in DOPC : DPPC : DOPS : cholesterol mixture here was in the same phase at both temperatures. To further confirm this, $D_{NBD\text{-}PC}$ in SLBs from DOPC : DPPC : DOPS : cholesterol 30 : 30 : 10 : 30 mol-% on TiO_2 was measured as a function of temperature (Figure 5.5). $D_{NBD\text{-}PC}$ was shown to increase smoothly (approximately exponentially) with temperature, $D \sim e^{0.032T}$, where D represents $D_{NBD\text{-}PC}$, and T is the temperature. No abrupt jump in $D_{NBD\text{-}PC}$, characteristic of a phase transition, was observed, again confirming that only one phase was present on the surface in this system. This conclusion correlates well with the AFM observations discussed in section 5.2.2.

The numerical values of the diffusion coefficients are consistent with those of the lipids in l_o phase (Table 5.3, ref [56]). However, the l_o phase that is stable to heating up to 60 °C is more than a little surprising; it would be expected to melt, leading to a significant increase in the diffusion coefficient [251]. We come back to this point below when studying the diffusion in the PS-free systems (Section 5.2.8).

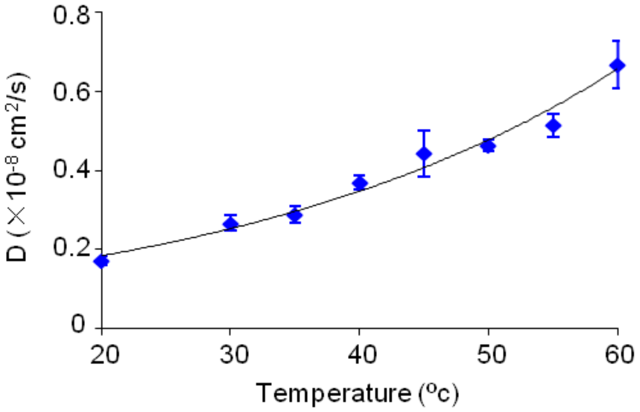

Figure 5.5. Diffusion coefficient of bilayers from DOPC : DPPC : DOPS : cholesterol 30 : 30 : 10 : 30 mol-% on TiO_2 using NBD-PC as label as a function of temperature. The diffusion coefficient increased exponentially with the temperature with $D \sim e^{0.032T}$, where D is the diffusion coefficient, T is the temperature. Each value was the average from at least three measurements. The error bars shows the standard deviation, the black line shows the fitting.

5.2.5. Questions Raised and New Possibilities Opened with the DOPC : DPPC : DOPS : Cholesterol SLB on TiO_2 Model System

Asymmetric SLBs could be formed on TiO_2 from DOPC : DPPC : DOPS : cholesterol 26 : 26 : 18 : 30 mol-% liposomes in Ca^{2+}-containing buffer (10 mM HEPES : 150 mM NaCl : 2 mM $CaCl_2$), with DOPS being enriched in the surface-proximal leaflet. Their formation and behavior raise a number of questions.

Firstly, it has been suggested that the driving force for asymmetric SLB formation from DOPC : DOPS liposomes on TiO_2 is Ca^{2+}-mediated short-range attraction between

TiO_2 surface and PS-containing liposomes [96] based on the evidence showing that Ca^{2+} binds to both TiO_2 [263] and PS [264], and on the effect of EDTA on the mobility of PS in these SLBs [97]. However, this might not be the case in the DOPC : DPPC : DOPS : cholesterol system. It has been reported that low-melting lipids such as DOPC and palmitoyl phosphocholine (POPC) do not form SLBs on TiO_2 at high ionic strength [96, 139, 142], while the mixture of high-melting lipids DPPC and low-melting lipids dipalmitoleoyl phosphatidylcholine (DPoPC) do [265], indicating stronger lipid-surface interaction in the presence of high-melting lipids. Also, DPPC was found to be enriched in surface-proximal leaflet in DOPC : DPPC SLBs on SiO_2, also a negatively charge surface [104], indicating stronger interaction of negatively charged surface with DPPC than with DOPC. Moreover, in the present study, Ca^{2+}-depletion by incubating SLBs with EDTA-containing buffer did not affect PS mobility in DOPC : DPPC : DOPS : cholesterol system. These evidence suggests that the driving force for SLB formation on TiO_2 in DOPC : DPPC : DOPS : cholesterol system may not be the same as in DOPC : DOPS system.

Secondly, no phase separation was observed in the DOPC : DPPC : DOPS : cholesterol system. However, phase separation in SLBs made from the ternary mixtures of low-melting and high-melting lipids with cholesterol on mica or silica have been reported before in the literature [115-119]. There are several possible explanations for the lack of phase separation in the quaternary system studied here. The addition of DOPS, also a low-melting lipid, might shift the phase diagram. Substrate difference (e.g. surface chemistry or roughness) between titania and mica or silica might affect phase separation. The coupling between transbilayer lipid asymmetry and lateral lipid organization might also influence phase separation. These factors need to be examined.

Moreover, these asymmetric SLBs on TiO_2 from quaternary mixture provide an opportunity to study lipid diffusion in an asymmetric, strongly coupled system, which mimics and transmembrane lipid organization and membrane-cytoskeleton interaction in live cells. However, to achieve that, it is required to break this complex mixture into simpler compositions to study the diffusion of each lipid component separately.

Therefore, a range of model systems with various lipid compositions under different buffer conditions on different substrates was prepared and characterized to address these questions. These results are discussed below.

5.2.6. Morphologies of Lipid Assembly on TiO_2 Characterized by Fluorescence Microscopy/Fluorescence Recovery After Photobleaching (FRAP) and AFM

To study the effect of each lipid component separately in the established model system, lipid assemblies on TiO_2 from DOPC : DPPC : cholesterol liposomes with various lipid compositions were investigated at different buffer and temperature conditions. Examples of fluorescence images of various lipid assemblies formed under different conditions on TiO_2 surfaces are shown in Figure 5.6.

When liposomes do not adsorb to the surface, no fluorescence is observed. When liposomes do adsorb, assemblies of lipids on the surfaces can be distinguished by

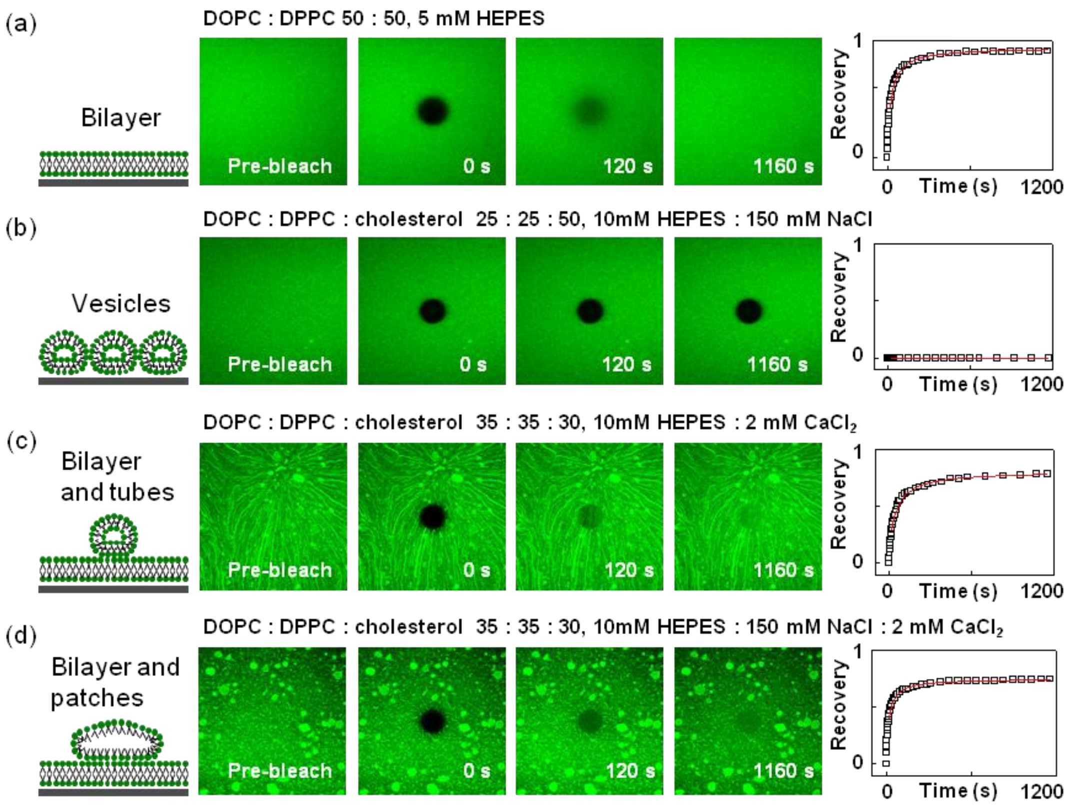

Figure 5.6. Overall characterization of different morphologies by fluorescence microscopy/FRAP. Cartoons on the left illustrated the various morphologies lipids can assume on the surface. Fluorescence images in the middle show the examples of photobleaching series obtained from liposomes labeled with 1 mol-% NBD-PC on TiO_2 in buffers of various compositions indicated in the panels. All the buffers were adjusted to pH 7.4. For these experiments, liposomes were incubated on TiO_2 for 1 hour at 60 ℃. Excess liposomes were rinsed away before cooling down the sample and taking FRAP measurements at room temperature. Image size: 142 × 142 μm^2. The diameter of the bleached spot is 22 μm. (a) Bilayer: full recovery of fluorescence intensity after photobleaching; (b) Vesicles: no recovery of fluorescence intensity; (c)-(d) Coexistence of bilayer and tubes/patches: incomplete recovery of fluorescence intensity.

observing the in-plane distribution of the fluorescence intensity and lipid mobility. Two of the most common cases are supported lipid bilayers (SLBs) (Figure 5.6a) and supported vesicular layers (SVLs) (Figure 5.6b). Both present homogeneous distributions of intensity, but differ in the long-range lipid mobility. Lipids in the bilayer are mobile due to the fluidity of the bilayer, and there is complete recovery (~ 1) of the fluorescence intensity in the bleached area due to the exchange between the lipids inside and outside the bleached area (Figure 5.6a). On the other hand, lipids in the SVLs are confined to within the individual liposomes, and are therefore not mobile at long distances. Therefore, no recovery of the fluorescence intensity in the bleached area is observed (Figure 5.6b). In addition, incomplete recovery (~ 0.8) is observed in the co-existing of tubular morpholoies or patches with SLBs (Figure 5.6c, d). This aspect of work is discussed in detail in Chapter 4.

The assignment of the different morphologies based on the fluorescence results was confirmed by AFM. Representative AFM images are shown in Figure 5.7. Continuous bilayer presented a very smooth aspect (Figure 5.7a, b). Tubular or patch morphologies could be observed under identical conditions as in the fluorescence (c.f. Figure 5.6c, d and Figure 5.7c, d). Cross-section analysis showed that the height of the tubes and patches was 15-20 nm relative to the bilayer (Figure 5.7c, d), and the hole with the depth of ～4 nm confirmed bilayer formation under the tubes and patches (Figure 5.7e). Supported vesicular layer presented a rough aspect (Figure 5.7f, g) which has been previously observed on numerous occasions [141, 252].

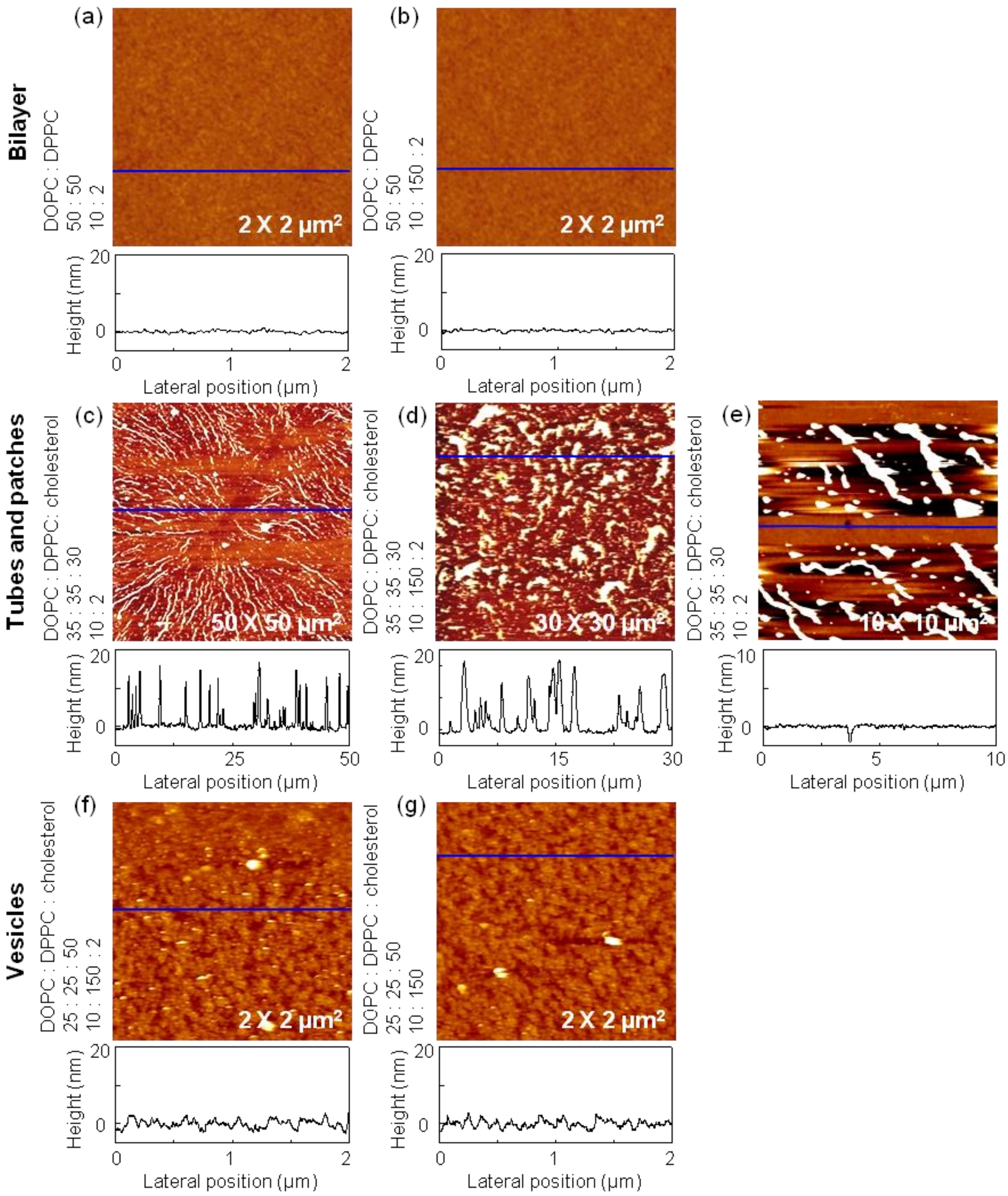

Figure 5.7. Overall characterization of different morphologies by AFM. AFM images show the examples of lipid assembly on TiO_2 in various lipid and buffer compositions as indicated in the panels. Lipid compositions are molar ratio. Buffers are 10 mM HEPES : 2 mM $CaCl_2$ (10 : 2); 10 mM HEPES : 150 mM NaCl : 2 mM $CaCl_2$ (10 : 150 : 2); 10 mM HEPES : 150 mM NaCl (10 : 150). All the buffers were adjusted to pH 7.4. Samples were prepared the same way as for FRAP measurements (in other words, heated to 60 °C and then cooled to room temperature). AFM images were taken at room temperature. (a)-(b) SLBs, (c) coexistence of bilayer and tubes, (d) coexistence of bilayer and flat patches, (e) zoom in image of the coexistence of bilayer and tubes; (f)-(g) SVLs. All the

images have z-scale of 20 nm. Cross section analyses were along the blue lines in the AFM images.

5.2.7. Effects of Preparation Conditions on the Liposome Behavior at the TiO_2 Surface

Having classified different morphologies of lipid assemblies on the surface according to the fluorescence distribution and lipid mobility, and having confirmed this classification by AFM, I proceeded to investigate the effects of varying preparation conditions (lipid and buffer compositions, temperature, surface chemistry and roughness) on the morphology of lipid assemblies. In the same manner as in Chapter 3, SLB formation is assumed to correlate to the stronger adhesion than an SVL formation. Co-existence of SLBs and tubes/patches are considered as SLBs since the tubes/patches are considered to form from the excess lipid leaving the surface during SLB formation. This co-existence morphology is assumed to arise at intermediate adhesion strength between the ones for SLB and SVL formation. This assumption will be discussed below in more detail. The results of this study are shown in Table 5.2 and Figure 5.8. Below, we discuss each set of conditions in turn.

Table 5.2. The resulting lipid assemblies on TiO_2 from different lipid and buffer compositions. Liposomes were deposited on the surface and incubated for 1 hour. Two incubation temperatures were compared: room temperature and 60 ℃. Samples incubated at room temperature were characterized by FRAP and AFM at room temperature (RT). Samples incubated at 60 ℃ were first characterized by FRAP at 60 ℃, and then cooled down and characterized by FRAP and AFM at RT. All the buffers were adjusted to pH 7.4.

		Buffer			
Liposome composition	**Incubating Temperature**	**5 mM HEPES**	**10 mM HEPES 2 mM $CaCl_2$**	**10 mM HEPES 150 mM NaCl 2mM $CaCl_2$**	**10 mM HEPES 150 mM NaCl (2 mM EDTA)[†]**
DOPC	RT	SLB*	SLB + tubes	Vesicles	Vesicles
	60ºC	SLB	SLB + tubes	Vesicles	Vesicles
DPPC*	RT	Vesicles*	Vesicles	Vesicles	Vesicles
	60ºC	Vesicles*	Vesicles	Vesicles	Vesicles
DOPC: DPPC 50: 50	RT	SLB	Vesicles	Vesicles	Vesicles
	60ºC	SLB	SLB + patches	SLB	Vesicles
DOPC: DPPC: cholesterol 35: 35: 30	RT	SLB	SLB + tubes	Vesicles	Vesicles
	60ºC	SLB	SLB + tubes	SLB + patches	Vesicles

DOPC: DPPC: cholesterol 25: 25: 50	RT	Vesicles	SLB + patches	Vesicles	Vesicles
	60ºC	SLB	SLB + patches	Vesicles	Vesicles
DOPC : DPPC : DOPS : chol 26 : 26 : 18 : 30	RT	No adsorption	/	SLB	Vesicles†
	60ºC	No adsorption	/	SLB	Vesicles†

* For FRAP measurements of DPPC which has the transition temperature of 41 ℃ [214], no recovery was found at 60 ℃ at which DPPC was in the liquid phase, indicating the formation of vesicular layer. On the other hand, in other cases, if recovery was observed at 60 ℃, it was also observed after cooling, enabling the vesicular layer to be distinguished from the SLBs.

† Measurements with liposomes from the mixture of DOPC : DPPC : DOPS : Cholesterol (26 : 26 : 18 : 30-mol%) was performed in 10 mM HEPES : 150 mM NaCl : 2 mM EDTA buffer, measurements with the other lipid compositions were performed in 10 mM HEPES : 150 mM NaCl buffer.

(a) Incubation at room temperature

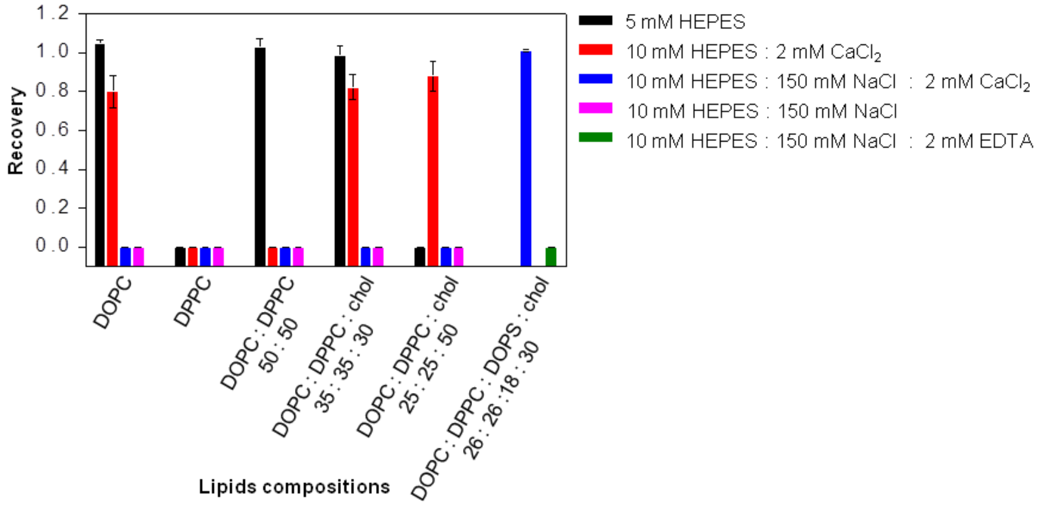

(b) Incubation at 60°C

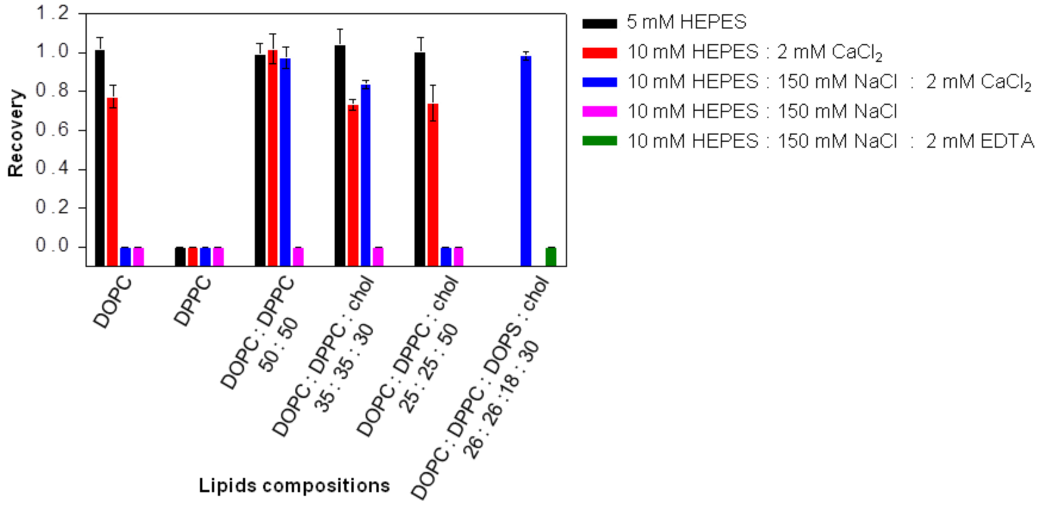

(c) Incubation at 60°C, then cooled down to room temperature

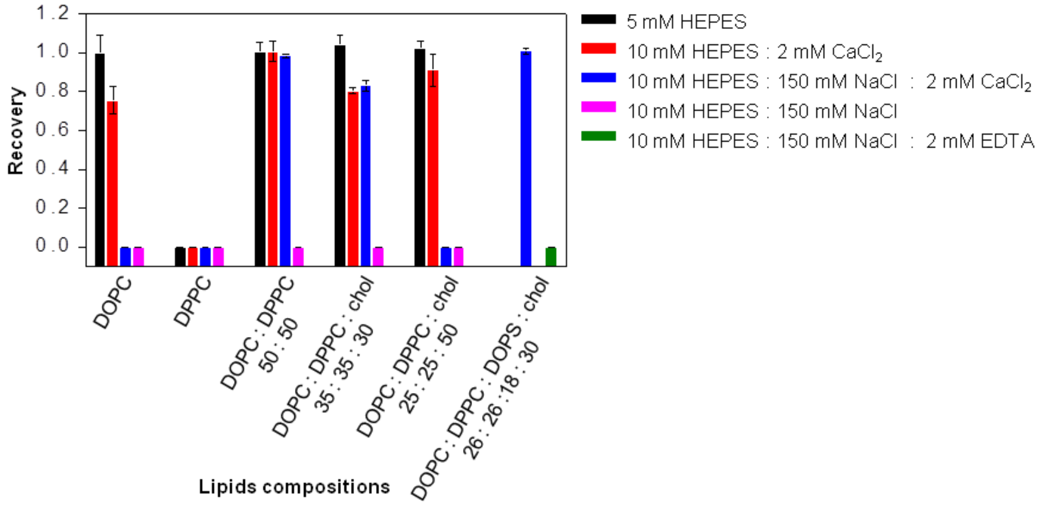

Figure 5.8. Overview of the fluorescence recovery from lipid assemblies on TiO_2 under different conditions. Lipid compositions marked in the plot are molar ratios.

1 mol-% NBD-PC was used as fluorescent label. All the buffers were adjusted to pH 7.4. (a) Sample incubation and FRAP measurements were taken at room temperature; (b) Sample incubation and FRAP measurements were taken at 60 ℃; (c) Sample incubation at 60 ℃, then the samples were cooled down and FRAP measurements were taken at room temperature. All the columns are mean values from at least 3 samples, for each sample more than 3 measurements were taken. The error bars show standard deviation. Recovery of 1 corresponds to SLBs, recovery of 0 corresponds to SVLs, and recovery between 0 ~ 1 corresponds to the coexistence of bilayer and tubes/patches. Recovery was complete for DOPC : DPPC 50 : 50 mol-% in 10 mM HEPES : 2 mM $CaCl_2$ due to the large patches being present at only several random locations, and the bleached area was chosen in the SLB part (Figure 4.11b in Chapter 4).

5.2.7.1. Effect of Incubation Temperature

In the majority of cases, temperature had no effect on SLB formation (Figure 5.8, Table 5.2). However under certain conditions, it increased the propensity of the adsorbed vesicles to rupture. A similar effect has previously been noted [138, 266]. Thus, in the case of DOPC : DPPC 50 : 50 mol-% liposomes in 10 mM HEPES : 2 mM $CaCl_2$, and 10 mM HEPES : 150 mM NaCl : 2 mM $CaCl_2$, heating was required for SLBs to form (Figure 5.8, Table 5.2). A similar effect was observed in the DOPC : DPPC : cholesterol 25 : 25 : 50 mol-% liposomes in the 5 mM HEPES, and DOPC : DPPC : cholesterol 35 : 35 : 30 mol-% liposomes in 10 mM HEPES : 150 mM NaCl : 2 mM $CaCl_2$, though in the latter case patch-like lipid assemblies co-existed with the SLBs (Figure 5.8, Table 5.2). It was also found that if recovery was observed at 60 ℃, it would remained the same after cooling (Figure 5.8 b, c), and vice a versa (Figure 5.8 a, b). It was therefore not possible to interpret lack of recovery in the DPPC samples as being due to the solid-phase bilayers: these would exhibit recovery at 60 ℃.

Studying recovery at different temperatures enabled adsorbed liposomes to be distinguished from the SLBs in all cases investigated in this study.

Liposome behavior on a surface depends on the adhesion strength between them. When liposomes are deposited on the surface, there is an energy barrier preventing them from rupturing. When the adhesion strength is low, the adsorbed liposomes remain intact on the surface, and form a supported vesicular layer. Increasing adhesion strength decreases the height of the energy barrier, therefore aiding the liposome rupture [147, 241, 267]. Lipid and buffer compositions, and surface chemistry, affect the adhesion strength to influence liposome behavior, while temperature increases the probability of overcoming the energy barrier, and consequently promotes liposome rupture. Therefore, the comparison of liposome behavior at various lipid and buffer compositions will be made at 60 ℃ where the kinetic factor has less of an influence.

5.2.7.2. Effect of Varying Buffer Composition

In low salt buffer (5 mM HEPES and 10 mM HEPES : 2 mM $CaCl_2$), apart from DPPC, SLBs could be formed from all of the PS-free liposomes (Table 5.2, black and red bars in Figure 5.8), indicating high adhesion strength between PC liposomes and TiO_2 at low salt. Tubes and patches co-existed with SLBs in the presence of Ca^{2+} (10 mM HEPES : 2 mM $CaCl_2$) (Table 5.2, red bards in Figure 5.8), indicating lower adhesion strength than without Ca^{2+} at low salt. One of these compositions, DOPC : DPPC 50 : 50 mol-%, was tested in water and found to form SLBs (Figure 5.9).

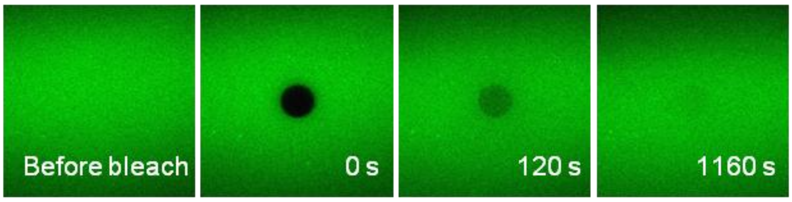

Figure 5.9. Fluorescent series of DOPC : DPPC 50 : 50 mol-% on TiO_2 in nano-pure water. Images were taken at room temperature. Image size: 142 × 142 µm. The diameter of the bleached spot is 22 µm.

In high ionic strength buffer, SVLs was formed from all the PS-free liposomes in the absence of Ca^{2+} (10 mM HEPES : 150 mM NaCl) (Table 5.2, purple bars in Figure 5.8; in the case of PS-containing liposomes, and SLB was formed in this buffer, indicating presence of trace amounts of Ca^{2+}; this is not discussed further). In the presence of Ca^{2+} (10 mM HEPES : 150 mM NaCl : 2 mM $CaCl_2$), coexistence of tubes/patches and SLBs were found with DOPC : DPPC 50 : 50 mol-% and DOPC : DPPC : chol 35 : 35 : 30 mol-%, while SVLs formed with the other PS-free lipid compositions (Table 5.2, blue bars in Figure 5.8). These results indicate lower adhesion strength between PC liposomes and TiO_2 surface at high salt. In the presence of Ca^{2+}, the adhesion was stronger than in the absence of Ca^{2+} at high salt.

Diffusion coefficient in the SLBs on TiO_2 at different lipid and buffer compositions showed that in all the PS-free SLBs, $D_{NBD\text{-}PC}$ was the lowest in the 5 mM HEPES buffer, intermediate in the 10 mM HEPES : 2 mM $CaCl_2$ buffer, and the highest in the 10 mM HEPES : 150 mM NaCl : 2 mM $CaCl_2$ buffer (Figure 5.10, Table 5.3), indicating that lipid-surface interaction is the strongest in 5 mM HEPES, intermediate in 10 mM HEPES : 2 mM $CaCl_2$, and the lowest in 10 mM HEPS : 150 mM NaCl : 2 mM $CaCl_2$ because strong lipid-surface interaction retarded the diffusion of lipids, especially in the surface-proximal leaflet.

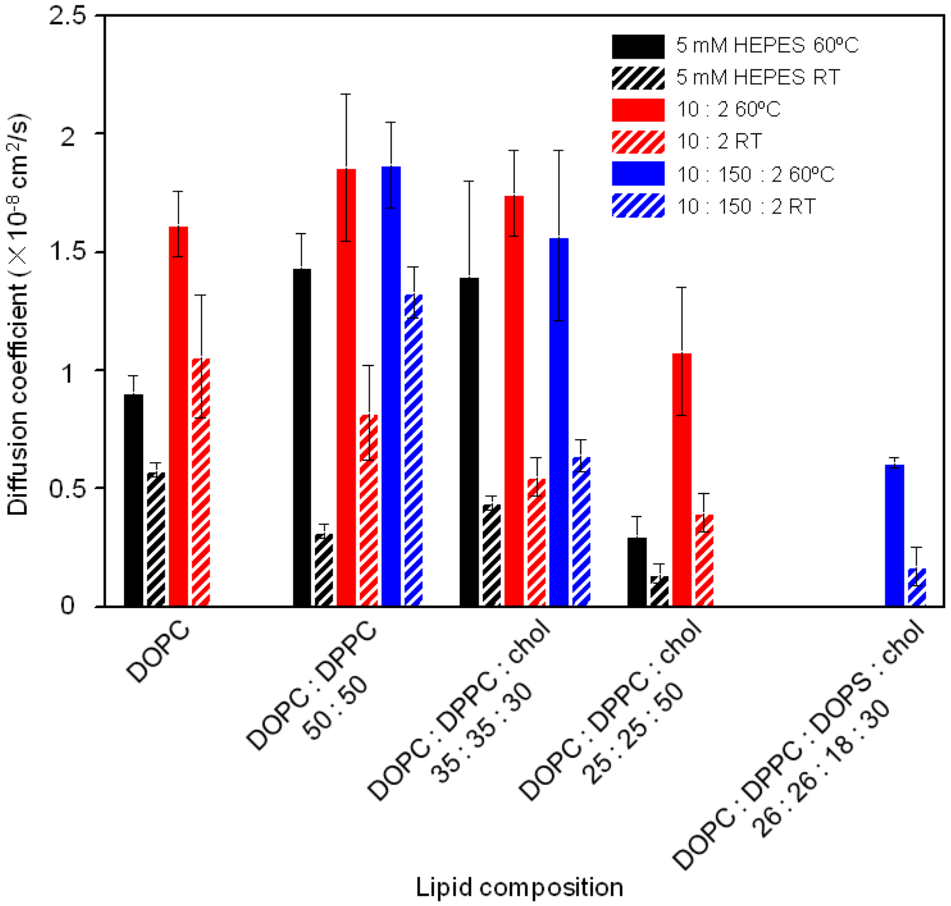

Figure 5.10. Diffusion coefficients in SLBs on TiO_2 at various lipid and buffer compositions using 1 mol-% NBD-PC as the fluorescent label. Solid bars represent D_{NBD-PC} at 60 ℃, while the bars filled with twills represent D_{NBD-PC} at room temperature (RT). Black bars: 5 mM HEPES; red bars: 10 mM HEPES : 2 mM $CaCl_2$; blue bars: 10 mM HEPES : 150 mM NaCl : 2 mM $CaCl_2$. All the buffers were adjusted to pH 7.4.

Table 5.3. Lipids diffusion coefficients and mobile fractions of PS-free bilayers under various conditions from this study and the literature. All the values in this study were averaged from 3 individual samples, and at least 3 measurements were performed for each sample.

Substrate	**Lipid composition (mol-%)**	**Buffer**	**Label**	**T, ℃**	***D*, $\times 10^{-8}$cm^2/s**	**M**	**Reference**
TiO_2	DOPC	5 mM HEPES, pH 7.4	NBD-PC	22	0.58 ±0.03	1.04 ±0.01	This study
				60	0.91 ±0.07	1.02 ±0.06	
		10 mM HEPES: 2 mM $CaCl_2$, pH 7.4	NBD-PC	22	1.06 ±0.26	0.76 ±0.07	
				60	1.62 ±0.14	0.77 ±0.05	
TiO_2	DOPC : DPPC 50 : 50	5 mM HEPES, pH 7.4	NBD-PC	22	0.32 ±0.03	1.03 ±0.04	
				60	1.44 ±0.14	0.99 ±0.05	
		10 mM HEPES: 2 mM $CaCl_2$, pH 7.4	NBD-PC	22*	0.82 ±0.20	1.01 ±0.05	
				60	1.86 ±0.31	1.02 ±0.07	
		10 mM HEPES: 150 mM NaCl : 2 mM $CaCl_2$, pH 7.4	NBD-PC	22*	1.33 ±0.11	0.99 ±0.01	
				60	1.87 ±0.18	0.98 ±0.05	
TiO_2	DOPC : DPPC : chol 35 : 35 : 30	5 mM HEPES, pH 7.4	NBD-PC	22	0.44 ±0.03	1.04 ±0.04	
				60	1.40 ±0.40	1.04 ±0.07	
		10 mM HEPES: 2 mM $CaCl_2$, pH 7.4	NBD-PC	22	0.55 ±0.08	0.80 ±0.01	
				60	1.75 ±0.18	0.73 ±0.03	
		10 mM HEPES: 150 mM NaCl : 2 mM $CaCl_2$, pH 7.4	NBD-PC	22*	0.64 ±0.07	0.83 ±0.03	
				60	1.57 ±0.36	0.84 ±0.02	
TiO_2	DOPC : DPPC : chol 25 : 25 : 50	5 mM HEPES, pH 7.4	NBD-PC	22*	0.14 ±0.04	1.02 ±0.03	
				60	0.30 ±0.08	1.00 ±0.07	
		10 mM HEPES: 2 mM $CaCl_2$, pH 7.4	NBD-PC	22*	0.40 ±0.08	0.91 ±0.08	

				60	1.08 ± 0.27	0.74 ± 0.09	
SiO_2	POPC	10 mM Tris, 150 mM NaCl, pH 7.4	TR-DHPE	25	1.80 ± 0.34		Ref [268]
TiO_2	POPC	10 mM Tris, 150 mM NaCl, pH 7.4	TR-DHPE	25	1.5 ± 0.29		
Mica	DOPC	10 mM HEPES: 150 mM NaCl : 2 mM $CaCl_2$	C8-BODIPY 500/510 C5-HPC	16	3.1 ± 0.3		Ref [249]
Silanized Glass	POPC : chol: SM 1 : 1 : 1	Phosphate buffer saline (PBS)	FL-DPPE	24	l_o: 0.38 l_d: 1.1		Ref [269] (particle tracking)
Free	DOPC (GUVs)	10 mM HEPES: 150 mM NaCl : 2 mM $CaCl_2$	C8-BODIPY 500/510 C5-HPC	16	7.8 ± 0.8		Ref [249]
Free	DOPC : chol (GUVs)	Triple-distilled water	Multiple	23	6.5		Ref [250]; *D* decreases with cholesterol content.
	POPC : chol (GUVs)	Triple-distilled water			5.5		
Free	DOPC	Distilled water	Multiple		~ 10		Ref [95], asymmetric incorporation of SM.
	DOPC : bSM, asymmetric	Distilled water			~ 6		

Free	DOPC : DPPC : chol 35 : 35 : 30	-	DOPC	20	l_o: 0.5	Ref [251] (NMR)
				20	l_d: 4	
				60	l_d: 10	

*SLBs were formed when incubating at 60 ℃, while SVLs formed when incubating at room temperature. Mobile fractions and diffusion coefficients at 22 ℃ were obtained by forming SLBs at 60 ℃, and then cooled down to 22 ℃.

Taken together, the adhesion between PC liposomes and TiO_2 is stronger at low ionic strength than at high ionic strength. In Chapter 3, I discussed that this decrease in adhesion originates from osmotic effects that arise from adsorbed liposome deformation.

On the other hand, it appears that Ca^{2+} decreases the adhesion strength at low salt, but increases it at high salt. Ca^{2+} binds to zwitterionic liposomes, especially to those containing saturated lipids [148, 270]. This is apparent form the reversal of the ζ-potential of DOPC, DOPC : DPPC, and DOPC : DPPC : cholesterol liposomes in 10 mM HEPES: 2 mM $CaCl_2$ (Figure 5.11). Ca^{2+} also binds to TiO_2, and neutralizes its charge [236, 263]. It is possible that this binding and consequent charge reversal

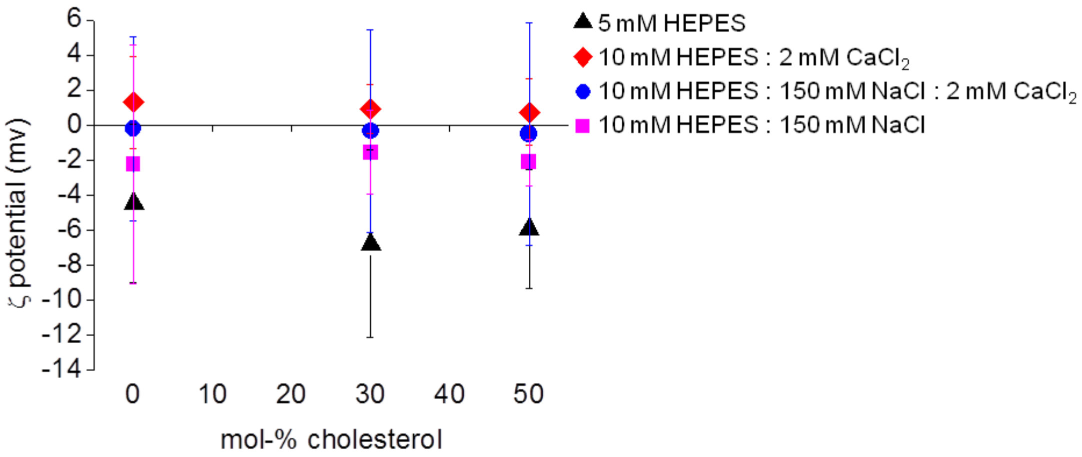

Figure 5.11. ζ-potential of DOPC : DPPC liposomes with different cholesterol content in different buffers. In low salt (5 mM HEPES), ζ-potential was at its most negative, in high salt (10 mM HEPES: 150 mM NaCl, 10 mM HEPES: 150 mM NaCl: 2 mM $CaCl_2$), the negative ζ-potential was reduced, indicating that Na^+ masks the surface charge of PC liposomes. In 10 mM HEPES: 2 mM $CaCl_2$, ζ-potential was reversed to positive. These trends are independent of cholesterol content. All the buffers were adjusted to pH 7.4. ζ-potential was measured by Zetasizer Nano ZS (Malvern, UK).

lead to the reduction of the liposome-surface adhesion strength. It is difficult to understand why the situation would be different in the presence of monovalent salts, except that they compete with Ca^{2+}.

Above arguments about the interaction strength have been inferred from liposome behavior and analysis of the diffusion coefficients. They need to be verified by systematically examining how adsorbed liposome deformation depends on buffer composition. Recent technical developments in our group do make such a study possible [161, 240], while this work provides experimental conditions for performing it.

5.2.7.3. Effect of Varying Lipid Compositions

DOPC liposomes formed bilayers on TiO_2 in low salt buffers (5 mM HEPES and in 10 mM HEPES: 2 mM $CaCl_2$) at pH 7.4, although tube morphologies were found to co-exist with SLBs in the presence of Ca^{2+} (Figure 5.8, Table 5.2). The behavior of fluid-phase zwitterionic liposomes has been extensively studied on TiO_2. SVLs were reported at high salt and neutral pH from DOPC [142, 271], egg PC [138, 139], or POPC [151]. These observations are confirmed in this study for the high ionic strength and neutral pH (10 mM HEPES: 150 mM NaCl and 10 mM HEPES: 150 mM NaCl: 2mM $CaCl_2$ buffers at pH 7.4) conditions where adsorbed DOPC liposomes are found (Figure 5.8, Table 5.2). SLBs were found to form from POPC liposomes on TiO_2 at high salt and low pH [151], or at low salt [154], which was also what was found in this study SLB formation from DOPC liposomes on TiO_2 surface at low salt and neutral pH.

DPPC liposomes did not form bilayers in any of the buffers (Figure 5.8, Table 5.2). This is an unexpected finding because the experiments were done at 60 ℃, where DPPC is in the fluid phase. There is therefore a considerable difference between the behavior of DPPC and DOPC even when both are in the fluid phase and their bending moduli are similar [272, 273].

Liposomes containing a mixture of DOPC and DPPC (DOPC : DPPC 50 : 50 mol-%) formed bilayers in low salt buffers (5 mM HEPES buffer, and 10 mM HEPES : 2 mM $CaCl_2$). No tubes were found in the presence of Ca^{2+} as with pure DOPC. In high salt buffer with Ca^{2+} (10 mM HEPES : 150 NaCl : 2 mM $CaCl_2$), liposomes composed of this mixture also formed SLBs where pure DOPC and DPPC alone did not (Figure 5.8, Table 5.2). These results indicate that the adhesion strength between liposomes and TiO_2 was stronger in the mixture of DOPC : DPPC compared to pure DOPC or DPPC. Similar trend was reported before by Tero et al. that the mixture of high-melting lipids DPPC and low-melting lipids dipalmitoleoyl phosphatidylcholine (DPoPC) formed bilayers on TiO_2(100) at high salt [265]. This may be because in the mixture there is solid-liquid phase separation. Lipids in the solid phase are more densely packed than in the liquid phase, and in the lipid-surface interaction, therefore the adhesion strength is stronger per unit area in the mixture system than in pure lipids. Another explanation may the asymmetric distribution of lipids. It was reported before that DPPC was enriched in surface-proximal leaflet in DOPC : DPPC SLBs on SiO_2, also a negatively charge surface [104], indicating DPPC may have stronger interaction with the negatively charged surface than DOPC does. This suggest that in the DOPC : DPPC system, DPPC might be the driving force for bilayer formation. However, this does not explain why DPPC did not form SLB on TiO_2 at any buffer conditions.

When cholesterol is introduced into the DOPC : DPPC mixture, bilayers could be formed at the 30 mol-% cholesterol (DOPC : DPPC : cholesterol 35 : 35 : 30 mol-%) on TiO_2 in 10 mM HEPES : 2 mM $CaCl_2$ and 10 mM HEPES : 150 mM NaCl : 2 mM $CaCl_2$ buffers, though tubes and patches co-existed with these SLBs. At 50 mol-% cholesterol (DOPC : DPPC : cholesterol 25 : 25 : 50 mol-%) no bilayer formation was found in 10 mM HEPES : 150 mM NaCl : 2 mM $CaCl_2$ (Figure 5.8, Table 5.2). These results indicate that increasing cholesterol content diminishes liposome adhesion on TiO_2.This may be because that cholesterol increases viscoelasticity of the liposomal membrane, thus making the liposomes more difficult to rupture, and also slowing down lipid diffusion [274]. It may also be because cholesterol inserts between lipid headgroups and reduces the headgroup packing density, resulting in reduced interaction strength.

At low salt (5 mM HEPES), the adhesion strength was so strong that the effect of cholesterol content did not show (Figure 5.8, Table 5.2).

PS-containing liposomes (DOPC : DPPC : DOPS : cholesterol 26 : 26 : 18 : 30 mol-%) did not adsorb on TiO_2 in 5 mM HEPES buffer due to the electrostatic repulsion between the negatively charged liposomes and the negatively charged surface (Figure 5.8, Table 5.2). Bilayers formed from these liposomes at high salt in the presence of Ca^{2+} (10 mM HEPES : 150 mM NaCl : 2 mM $CaCl_2$), but liposomes remained intact on the surface in the absence of Ca^{2+} (10 mM HEPES : 150 mM NaCl : 2 mM EDTA) (Figure 5.1), correlated the previous findings in DOPC : DOPS system which was discussed above in Section 5.2.1. [96]. This is also supported by $D_{NBD\text{-}PC}$ and $D_{NBD\text{-}PS}$

in these SLBs which much slower than in the PS-free systems (Figure 5.10, Table 5.1, Table 5.3), indicating strong interaction between lipids and surface.

5.2.8. Phase Separation

SLBs composed of mixtures of lipids with different phase transition temperatures, such as DPPC and DOPC, with and without cholesterol, have previously been studied on substrates other than TiO_2 (silica, mica, glass, etc). Typically, solid-phase domains [57, 275, 276], or in the case of cholesterol-containing mixtures, liquid-ordered domains [115-119], have been reported. It was therefore surprising that domains were not observed in the present study, neither by fluorescence microscopy nor by AFM. To investigate whether the lack of domain formation was a result of surface chemistry (TiO_2 vs. SiO_2), roughness, or both, I compared the morphologies of bilayers from various lipid compositions formed on TiO_2-coated glass, SiO_2-coated glass, and silicon wafers which have naturally oxidized surface [277]. Then I investigated the diffusion coefficients of these SLBs on TiO_2 at different temperatures to further check if there was phase separation.

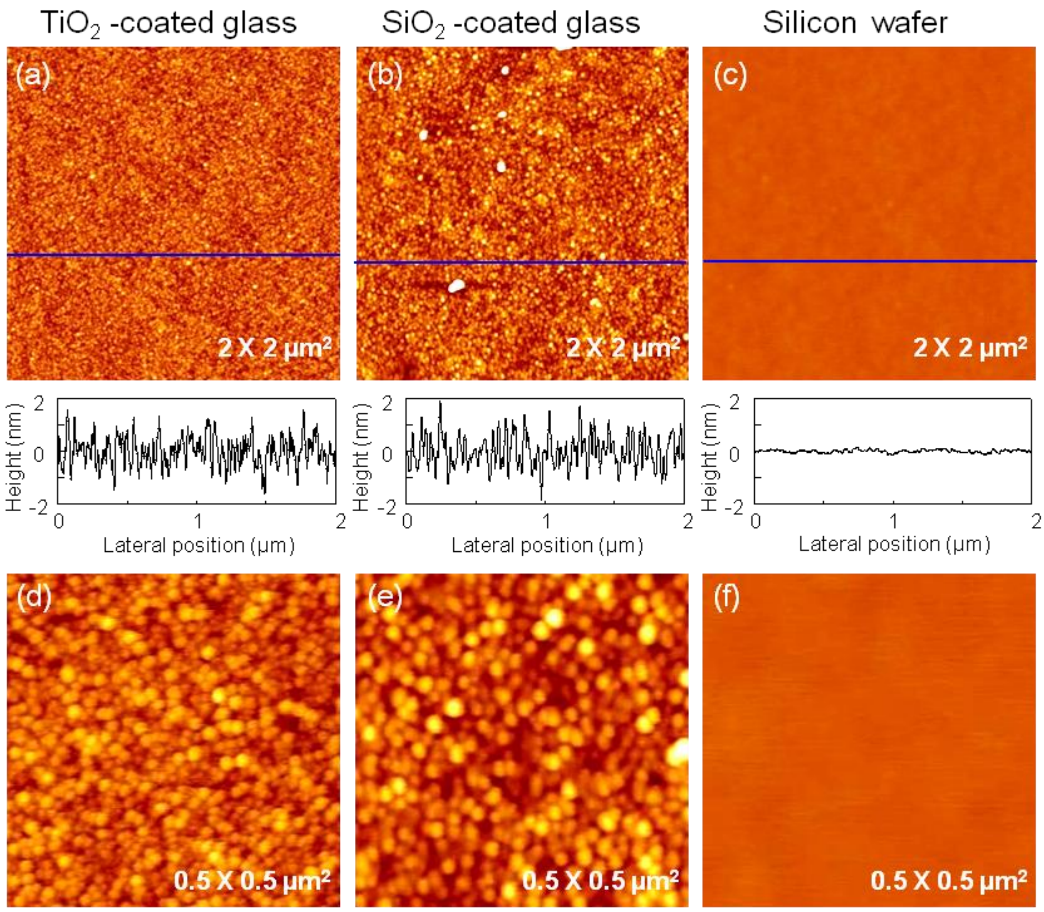

Figure 5.12. Tapping mode AFM images of UV/ozone treated substrates: (a) and (d), TiO_2-coated glass; (b) and (e), SiO_2-coated glass; (c) and (f), silicon wafer. The sizes (z-scales) of images were 2×2 µm^2 (10 nm) in (a-c), and 0.5×0.5 µm^2 (10 nm) in (d-f). Cross section analyses were along the blue lines in the AFM images.

Table 5.4. Roughness of bare surfaces and SLBs on the surfaces. Roughness values are root mean square (RMS) values determined from 2 × 2 μm^2 AFM images.

Liposome compositions	**Surfaces**	**Buffers**	**Morphologies**	**RMS roughness (nm)**
/	TiO_2-coated glass	/	Bare surface	0.60 ± 0.03
/	SiO_2-coated glass	/	Bare surface	0.71 ± 0.08
/	SiO_2 wafer	/	Bare surface	0.06 ± 0.00
DOPC : DPPC 50 : 50	TiO_2-coated glass	5 mM HEPES	SLB	0.33 ± 0.03
	SiO_2-coated glass	5 mM HEPES	SLB	0.34 ± 0.04
	SiO_2 wafer	5 mM HEPES	SLB (domains)	0.37 ± 0.04
DOPC : DPPC : chol 35 : 35 : 30	TiO_2-coated glass	5 mM HEPES	SLB	0.32 ± 0.02
	SiO_2 wafer	5 mM HEPES	SLB (domains)	0.43 ± 0.04
DOPC : DPPC : chol 25 : 25 : 50	TiO_2-coated glass	5 mM HEPES	SLB	0.30 ± 0.04
DOPC : DPPC : DOPS : chol 26 : 26 : 18 : 30	TiO_2-coated glass	10 : 150 : 2	SLB	0.33 ± 0.03
	SiO_2 wafer	10 : 150 : 2	SLB	0.05 ± 0.00

AFM images of bare surfaces showed that TiO_2-coated glass and SiO_2-coated glass had a similar roughness (Figure 5.12a and b; RMS roughness 0.60 ± 0.03 nm and 0.71 ± 0.08 nm, respectively; Table 5.4, corresponding to the previous reported value ranging from 0.2-0.99 nm [278, 279]). High magnification images identified individual grains with the diameter of ～18 and ～20 nm on both TiO_2- and SiO_2-coated glass respectively (Figure 5.12d and e). Silicon wafers were about 10 × smoother compared to the other two surfaces (Figure 5.12c; RMS roughness 0.06 ± 0.00 nm; Table 5.4, corresponding to the previous reported value range from 0.05-0.14 nm [261, 280]). No grains were visible in high magnification AFM images (Figure 5.12f).

AFM images of the SLBs formed on these three surfaces are shown in Figure 5.13. On the smooth silicon wafers, domains were clearly visible in DOPC : DPPC 50 : 50 mol-% and DOPC : DPPC : cholesterol 35 : 35 : 30 mol-% SLBs. The boundaries of the domains were clear and sharp. Height difference between these two phases was ～ 1 nm (Figure 5.13c, e). This indicated that for these compositions solid-liquid or liquid-ordered (l_o)/disordered (l_d) phase separation did exist.

On SiO_2-coated glass slides, which have similar chemical properties as silicon wafers, and similar roughness as TiO_2-coated glass slides, domains were also visible in DOPC : DPPC 50 : 50 mol% SLBs, but the sizes of the liquid domains were much smaller (diameter ～100 nm, compared to the ones on silicon wafers, which are ～ 300 – 500 nm), and the boundaries between the two phases were not as clear or sharp as on the silicon wafers. Cross section analysis showed that the height difference between the two phases was also ～1 nm (Figure 5.13b). These results indicated that surface roughness does indeed affect phase separation in the SLBs, but does not abolish it completely.

On TiO_2-coated glass slides, no domains were visible in DOPC : DPPC 50 : 50 mol% SLBs (Figure 5.13a, d), indicating that the chemical properties of TiO_2 contribute to the behavior of the lipids. It appears, therefore, that the disappearance of the domains on TiO_2 is due to the combination of two factors: surface chemical properties and roughness. The former factor probably affects the lipid composition of the two leaflets. The latter factor may affect the observation of domains by AFM. The liquid domains on SiO_2- coated glass slides have the diameter of ～ 100 nm (Figure 5.13b), five times larger than the grains of the bare surface (diameter ～20 nm, Figure 5.12e). If the domains on TiO_2-coated glass slides are much smaller than the ones on SiO_2-coated glass slides, and are close to the grain size of the bare surfaces (diameter ~ 18 nm Figure 5.12d), they will be difficult to be resolved by AFM.

However, in the DOPC : DPPC : DOPS : cholesterol 26 : 26 : 18 : 30 mol-% system, no domains were observed even on the smooth silica wafer (Figure 5.13g). This may be due to the higher amount of low-melting lipids 44 mol-% compared to 35 mol-% in the DOPC : DPPC : cholesterol system which shifted the phase diagram.

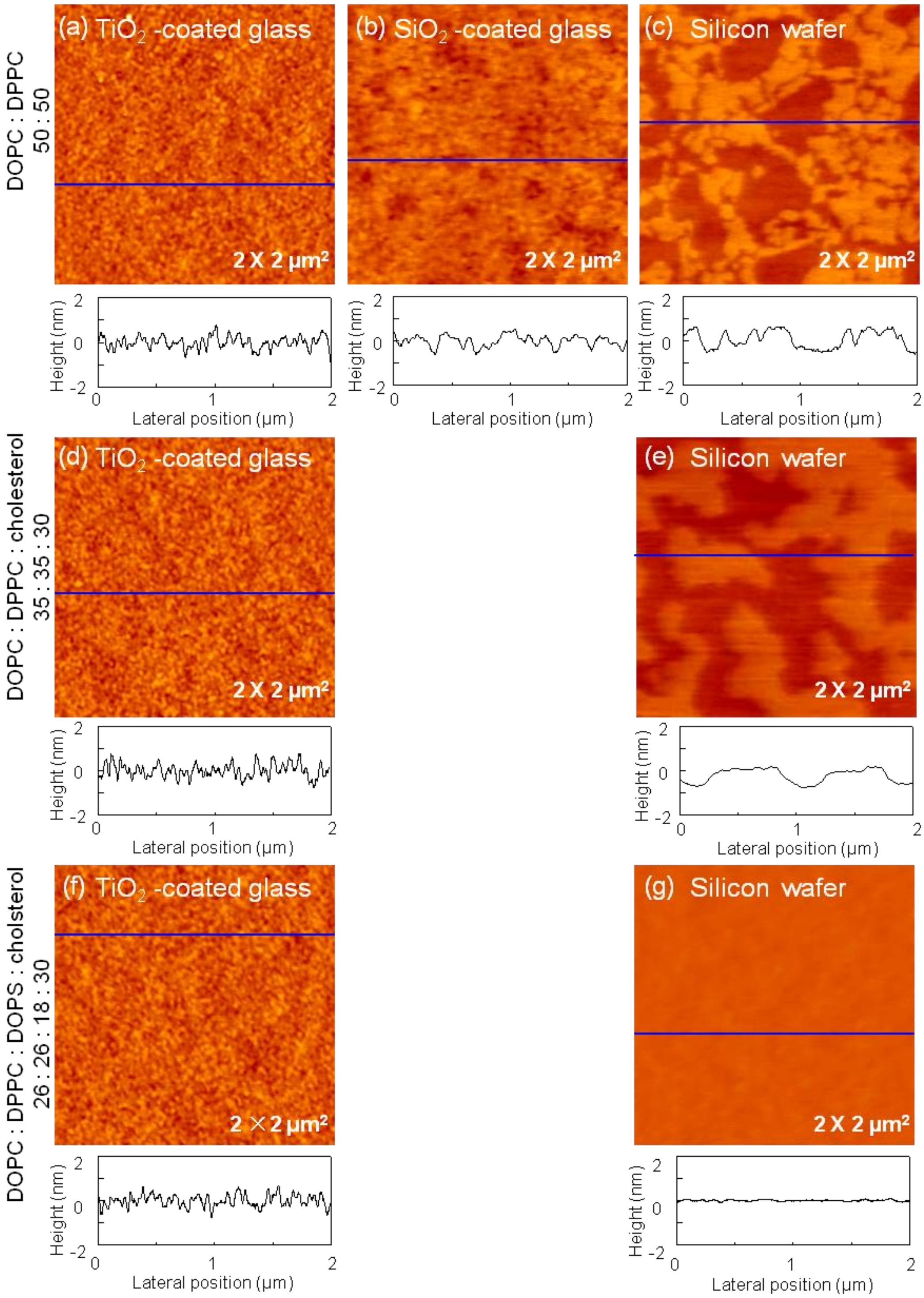

Figure 5.13. Contact mode AFM images of SLBs with different lipid compositions on different surfaces: (a)-(c) DOPC : DPPC 50 : 50 mol-%; (d)-(e) DOPC : DPPC : cholesterol 35 : 35 : 30 mol-%; (f)-(g) DOPC : DPPC : DOPS : cholesterol 26 : 26 : 18 : 30 mo-%. The surfaces used were labeled in the images. The sizes (z-scales) of images were 2 × 2 μm^2 (10 nm). Cross section analyses were along the blue lines in the AFM images. All the images were taken in 5 mM HEPES, pH 7.4 buffer.

To further investigate the phase behavior of lipids in these SLBs, the diffusion coefficients of the NBD-PC probe were investigated on TiO_2 at different temperatures (Table 5.3). Although in all cases, $D_{NBD\text{-}PC}$ increased with temperature, only under two conditions the increase was significant: in the case of DOPC : DPPC 50 : 50 mol-% and DOPC : DPPC : cholesterol 35 : 35 : 30 mol-% systems (Figure 5.10, Table 5.3). In both of these systems, the diffusion coefficient at 22 ℃ is lower than that in the pure DOPC in the same buffer (Table 5.3), but then goes up to a value that is considerably higher than that of DOPC alone at 60 ℃. Such an increase is not observed in the system containing 50 mol-% of cholesterol, where $D_{NBD\text{-}PC}$ is quite a bit slower than that in the pure DOPC, and is of the same order as in the DOPS-containing system, in which the increase with temperature is small (Table 5.1, Table 5.3). In all cases, the NBD-PC probe exhibits long-range mobility—in other words, there may be obstacles in its path reducing the diffusion coefficient, but it can not be organized in isolated, disconnected pockets of a high temperature phase in the low-temperature phase.

The simplest interpretation of the significant increase in the diffusion coefficient in these two systems is a phase transition. The high-temperature phase is certainly l_d, and the diffusion coefficient confirms that (Table 5.3). Two questions arise: what is the identity and the morphology of the low-temperature phase, and why does this transition disappear in the 50 mol-% cholesterol and (30% cholesterol, PS)-containing systems where $D_{NBD\text{-}PC} \sim 0.1 - 0.2\times10^{-9}$ and do not significantly depend on temperature? It essentially appears that we are observing some sort of a high-melting structure, undoubtedly stabilized by the lipid-surface interactions, that forms under these conditions. To shed further light on this issue, studies with different fluorescent probes and analysis of lipid compositions in the two leaflets, need to be performed.

Taken together, AFM images showed phase separation in the DOPC : DPPC 50 : 50 mol-% and DOPC : DPPC : cholesterol 35 : 35 : 30 mol-% SLBs on SiO_2 regardless of surface roughness, but not on TiO_2. Diffusion coefficients of theses SLBs on TiO_2 were temperature-dependent, suggesting a possible phase transition, although further studies are required to confirm that because this conclusion implies an unexpectedly stable lipid organization on the surface.

These results suggest that surface chemistry affects lipid assemblies on the surface. One way in which surface chemistry may affect phase behavior is by altering the composition of the SLB relative to that of the starting liposomes. SiO_2 has stronger interaction with low-melting PC than TiO_2 does, judging from the fact that low-melting PC liposomes can easily form SLBs on SiO_2 in salt buffers [138, 141, 147], but can only form SLBs on TiO_2 at low pH [151], or at low salt ([154], and findings in this study) where the adhesion strength between the lipids and surface is high. It was also found that SLBs can form from the mixture of high-melting lipids DPPC and low-melting lipids dipalmitoleoyl phosphatidylcholine (DPoPC) on TiO_2(100) at high salt [265], indicating increased lipid-surface adhesion in the presence of high-melting PC, though the possible asymmetric distribution of DPPC was not investigated in this system. Actually, DPPC was shown to be enriched in surface-proximal leaflet in DOPC : DPPC SLBs on SiO_2 [104], suggesting stronger interaction between high-melting PC and negatively charged surface. This suggested that DPPC may also be asymmetric in SLBs on TiO_2. Furthermore, PS was shown to be enriched in SLBs on TiO2 from PC : PS mixtures from this study and the previous studies [97, 98]. The transbilayer asymmetry of lipids on different surface influences lipid compositions in different leaflets of the SLBs, and thus influences phase separation.

5.3. Conclusions

SLBs are commonly used models to study cell membranes, and are widely utilized in biointerfaces and biosensors studies. Despite numerous studies, SLBs that can mimic lipid asymmetry and physiological compositions in cell membranes are scarce. Here I have been able to prepare asymmetric SLBs on TiO_2 with PS being enriched in the surface-proximal leaflet from DOPC : DPPC : DOPS : cholesterol mixtures with physiological lipid compositions. Phase separation was not observed in DOPC : DPPC : DOPS : cholesterol SLBs at micro meter scale. However, it was observed in DOPC : DPPC, and DOPC : DPPC : cholesterol systems, at least on silicon wafers and on silica-coated glass slides. Whether this is due to the surface chemistry difference between TiO_2 and SiO_2 which influences transbilayer lipid asymmetry and therefore influences the coupled lateral lipid organization is unknown. Although the distribution of each lipid component is not known in this model system, at least it provides a cell membrane mimics platform to study the diffusion of various components and the coupling of their organization in the membrane.

Furthermore, while there are literally dozens of studies on SLB formation from zwitterionic liposomes on silica or mica, studies on TiO_2 are scarce and none of them explore this parameter space systematically. Here I investigated liposome behaviors on TiO_2 surface as a function of different parameters, and offered some essentially new observations that lead to the interpretation of the SLB formation in terms of lipid-substrate interactions.

Chapter 6

Supramolecular Organization of the Na$^+$, K$^+$-ATPase in Near-Native Membranes

---

6.1. Summary

In this chapter, the supramolecular organization of a transmembrane protein, Na$^+$, K$^+$-ATPase, in membrane fragments purified from the outer medulla of rabbit kidneys is investigated. The structure of this protein was solved by X-ray crystallography revealing that it consists of α, β, and γ subunits [1, 178, 179]. Its oligomerization has been commonly observed in two-dimensional (2D) crystals [194-198], and also suggested by kinetic studies [184, 188-192]. However, direct evidence of the oligomers of this protein is until now lacking. Membrane fragments containing Na$^+$, K$^+$-ATPase obtained from the outer medulla of rabbit kidneys with minimum of purification and manipulation were studied by atomic force microscopy. The findings suggest a particular supramolecular organization of this protein in these membrane fragments.

First these membrane fragments were characterized by sodium dodecylsulfate polyacrylamide gel electrophoresis (SDS-PAGE) and transmission electron microscopy (TEM) to check their purity and morphology. Their adsorption on mica

was then studied to obtain samples suitable for high-resolution atomic force microscopy (AFM). To this end, the composition of the adsorption and imaging buffers was optimized to improve quality of the samples and the AFM images. Finally, suitable high-magnification images were analyzed by Fourier-analysis and correlation averaging to obtain the most commonly occurring motif, which was identified as an $(\alpha\beta)_4$ tetramer. Further comparison was made between the averaged motif and the X-ray crystallographic structure of this protein, and suggested that the tetramer motif corresponded to the extracellular side view of this protein.

6.2. Results

6.2.1. Characterization of the Purified Membrane Fragments by Sodium Dodecylsulfate Polyacrylamide Gel Electrophoresis (SDS-PAGE)

Membrane preparations containing Na^+, K^+-ATPase were gifted from the lab of Hans-Jurgen Apell, University of Konstanz, Germany. They were purified from the outer medulla of rabbit kidneys following the method of Jørgensen [228]. Briefly, microsomal fractions of the homogenized tissue were incubated with SDS in the presence of adenosine triphosphate (ATP), followed by centrifugation steps. In this way, Na^+, K^+-ATPases were kept embedded in the membrane, while the other membrane proteins, together with some lipids, were removed. Protein purity in the resulting membrane fragments was verified by SDS-PAGE (Figure 6.1).

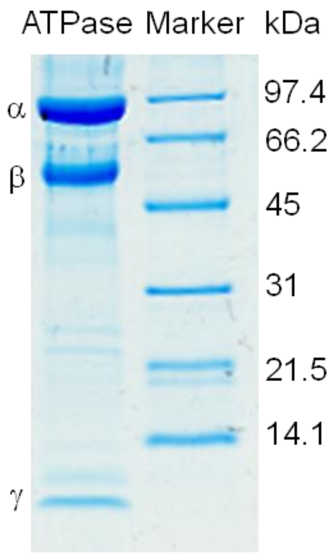

Figure 6.1. Coomassie blue stained SDS-PAGE gel of ATPase samples. The three prominent bands labeled with α, β, and γ correspond to the α, β, and γ subunit of the ATPase [228, 281], respectively. Image courtesy of Hans-Jurgen Apell, University of Konstanz, Germany.

In agreement with the previous results [1, 228, 281] there were three prominent bands corresponding to the three subunits of the protein: the α-subunit (MW ~ 100 kDa), the glycosylated β-subunit (MW ~ 55 kDa), and the γ-subunit (MW ~ 9 kDa), confirming that Na^+, K^+-ATPase is the major protein present in the membrane preparations. Some non-significant bands corresponding to the other protein components were also present in the gel, also in agreement with the previous results that ～80% of the proteins could be removed from the membrane preparations [228]. Electron microscopic studies showed that this purification method provided membrane fragments containing Na^+, K^+-ATPase with the density of up to 10,000 αβ-protomers per μm^2 [229]. This purity and density are good enough for atomic force microscopy imaging of this protein.

6.2.2. Characterization of the Native Membrane Patches by Negative Stain Transmission Electron Microscopy (TEM)

TEM analysis of negatively stained preparations of the membrane fragments showed that the patches consisted of protein-free and protein-containing regions (labeled with white rhombus and white triangle, respectively, in Figure 6.2). These were identified based on their staining pattern: protein-free, lipid regions are stain-excluding and appear light. Protein-containing regions appear darker, presumably because the stain accumulates in the spaces between the protein molecules (light dots visible in the region labeled with the triangle). In some of the TEM images, rows of protein molecules could be identified in the protein-containing regions (Figure 6.2, inset).

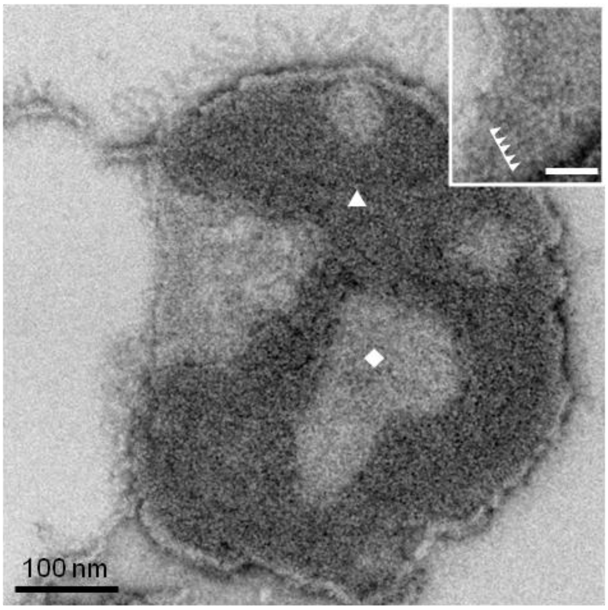

Figure 6.2. Low magnification electron micrograph of the negatively stained ATPase-containing membrane fragment preparations. The staining pattern allows the identification of the protein-free (lipid) and protein-containing parts, labeled with rhombus and triangle, respectively. Inset: high magnification electron micrograph of the protein-containing part. The proteins are aligned in rows, indicated with arrowheads. The scale bar in the inset represents 100 nm.

6.2.3. Optimizing Native Membrane Patches' Adsorption on Mica under Different Buffer Conditions

In order to obtain high-resolution images of proteins by AFM, relatively large, flat, and well-separated protein-containing patches tightly adsorbed to the substrate are needed [69, 282, 283]. The composition of the adsorption buffer ($MgCl_2$ and KCl concentration in 10 mM Tris-HCl pH 6.8) was varied in order to optimize the conditions for arriving at such patches.

Membrane fragments were adsorbed and incubated on freshly cleaved mica placed on ice for 1 hour in buffers containing different KCl and $MgCl_2$ concentrations, rinsed with the respective adsorption buffer to remove the loosely-adsorbed, excess material, and then rinsed with the imaging buffer (10 mM Tris-HCl pH 6.8, 1 mM $MgCl_2$, 150 mM KCl) before taking AFM images in the same imaging buffer at room temperature. In all the buffer compositions, three patterns of the samples were observed: protein-free patches (labeled with blue arrows in Figure 6.3), protein-containing patches (labeled with green arrows in Figure 6.3), and vesicles or aggregates (appear white in the images in Figure 6.3). Treating the sample with phospholipase A_2 (PLA_2), an enzyme that catalyzes lipid hydrolysis [284, 285], and removing the hydrolytic products by dialysis [286] before adsorption resulted in the disappearance of the protein-free patches, but not the protein-containing patches, further confirming the two patterns in the sample (Figure 6.4).

In particular, at low Mg^{2+} concentrations (2 mM, Figure 6.3a), a lot of material was present on the surface, both in the form of protein-containing patches or protein-free lipid patches, and vesicles or aggregates. Significantly less material was present on the surface at high Mg^{2+} concentrations (25 mM, Figure 6.3b). Furthermore, more of this material was in the form of patches. Similar trend was observed when KCl was used as the only electrolyte in the adsorption buffer: at 300 mM KCl, the surface was nearly blank, while some patches were present on the surface when the adsorption buffer contained 150 mM KCl (Figure 6.3c). In mixtures of the two electrolytes, higher concentrations of either of the two electrolytes lead to less material present on the surface (Figure 6.3d, e, f). Finally, the adsorption buffer containing 25 mM $MgCl_2$ and 150 mM KCl was chosen as the good adsorption condition, that is similar to the conditions previously used by Scheuring and co-workers [72] and incubated membrane preparations overnight after adsorption and washing steps to allow the formation of flat patches, such as shown in Figure 6.5.

The pH and electrolyte concentration of the imaging buffer were also screened to optimize the force between the AFM tip and the membranes. The goal was to arrive at a force that is slightly repulsive so that the interaction between the tip and the membranes is minimized [71, 287]. A force that was too strongly attractive would damage the patches during imaging, while a force that was too repulsive would decrease the resolution. The imaging buffer of 10mM Tris-HCl pH 6.8, 1mM $MgCl_2$, 150mM KCl was finally decided as a good imaging condition.

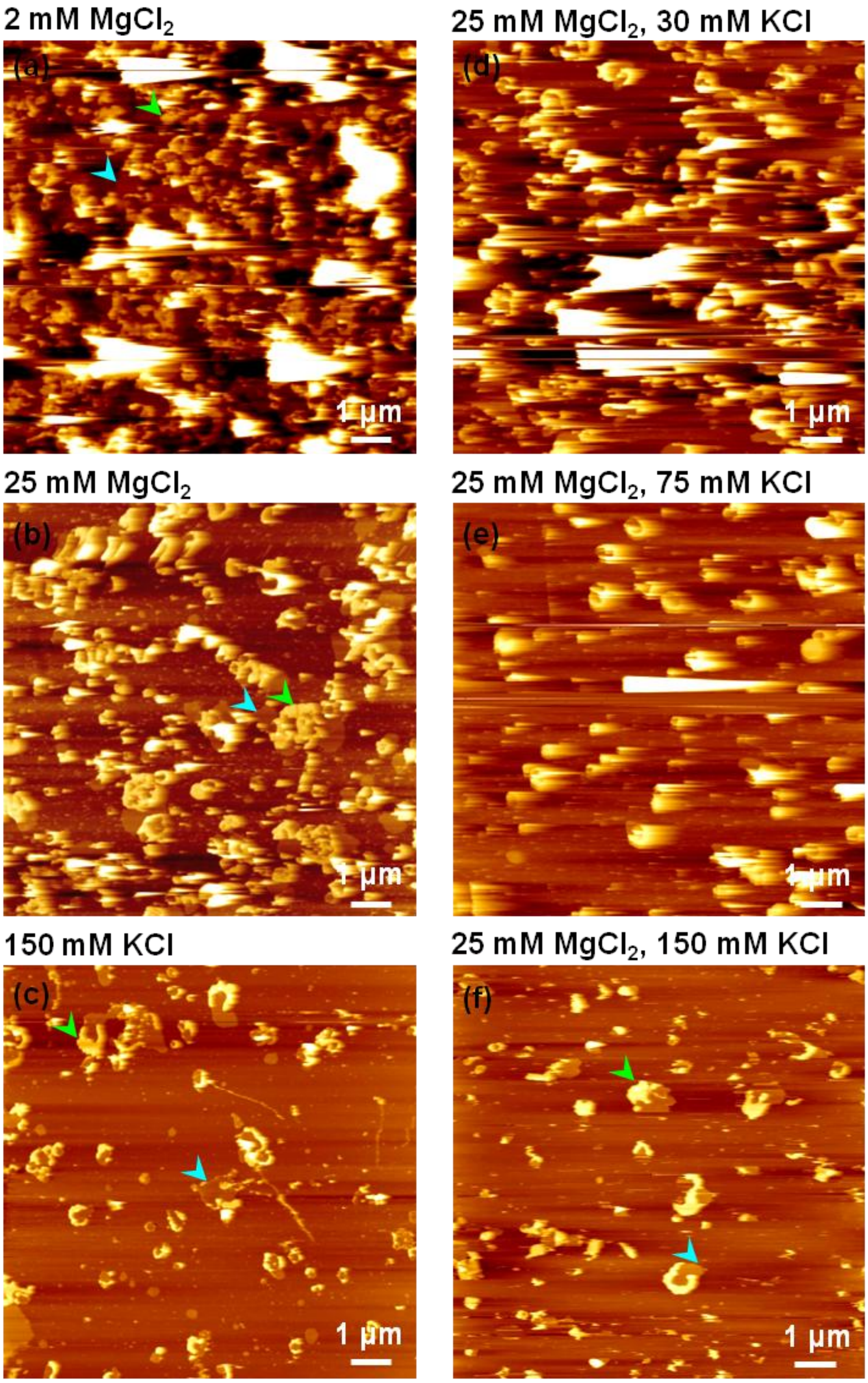

Figure 6.3. The effect of adsorption buffer composition on sample quality examined by AFM. The composition of the adsorption buffer was varied as indicated in the figure; all buffers were based on 10 mM Tris-HCl pH 6.8. The protein-containing patches and protein-free lipid patches are marked with green and blue arrows, respectively. Vesicles or aggregates appear white in the images. The z-scales (black-to-white) of the images are 50 nm.

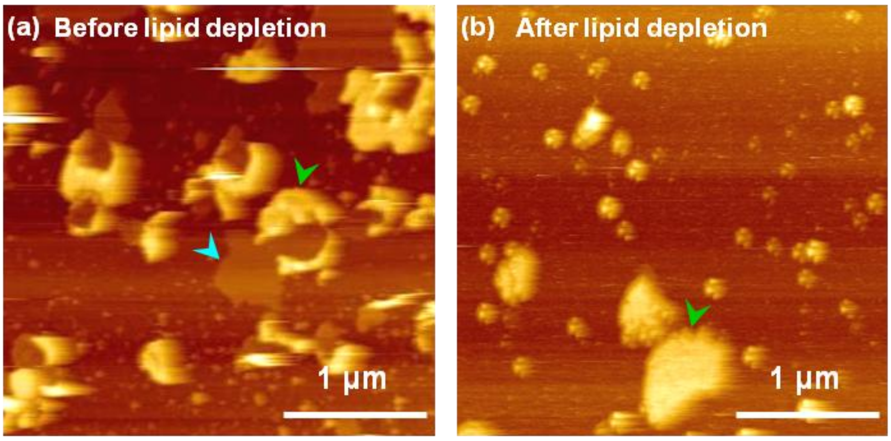

Figure 6.4. Lipid depletion from membrane fragments. Comparison of sample before (a) and after (b) lipid hydrolysis with phospholipase A_2 (PLA_2). Lipid hydrolysis was performed by adding PLA_2 to the membrane fragments containing 0.272 mg/ml ATPase. The final concentration of PLA2 was 16 µg/ml. The sample was dialyzed against 10 mM Tris-HCl, pH 6.8, 25 mM $MgCl_2$, 150 mM KCl through dialysis membrane with a 3.5K molecular weight cut-off (MWCO) pore size for 10 hours to remove the products of hydrolysis. Samples before and after PLA_2 treatment were prepared by adsorbing on freshly cleaved mica in a buffer containing 10 mM Tris-HCl pH 6.8, 25 mM $MgCl_2$, 150mM KCl. AFM images were taken in the 10 mM Tris-HCl pH 6.8, 1 mM $MgCl_2$, 150mM KCl buffer. Blue arrow indicates protein-free lipid patch, green arrow indicates protein-containing patches. After PLA_2 treatment, the protein-free patches left. The z-scale (black-to-while) of the images is 50 nm.

6.2.4. AFM Studies of the Purified Membrane Fragments

AFM images at low magnification showed protein-free and protein-containing areas within the membrane patches (labeled with rhombus and triangle respectively in Figure 6.5a), very similar to that observed in TEM (Figure 6.2). The protein-containing areas appeared higher (lighter) than the protein-free ones. The height of the protein-free patches above mica was ~ 6 nm (Figure 6.5b), correlated with the height of a bilayer [137, 241, 288, 289]. The height of the protein-containing patches above the mica was ~ 16 – 18 nm (Figure 6.5b). This was comparable to the ~ 15 nm expected for the Na^+, K^+-ATPase molecule in the direction perpendicular to the cell membrane based on the X-ray structure (PDB 3KDP, Figure 6.5c) [1]. The height of the protein-containing patches above the protein-free ones was ~ 11 nm (Figure 6.5b), which was consistent with the height difference between the whole protein and the bilayer (Figure 6.5c). Unfortunately this information could not be used to determine protein orientation: the protein could be adsorbed with the extracellular or the cytoplasmic side up (Figure 6.5c).

High-magnification images of the protein-containing patches revealed densely packed arrays of approximately circular protrusions ~ 5 – 6 nm in diameter (Figure 6.5d).

The size of these protrusions was consistent with the lateral size of the extracellular portion of the β-subunit (～5 nm) rather than the cytoplasmic portion of the α-subunit (～8 nm) (Figure 6.5c) [1], suggesting that the patches were adsorbed with the extracellular side facing up. However, further studies are required to confirm this (e.g., experiments with antibodies against particular subunits).

The arrays were disordered in the sense that there was no long-range order. However, most of these protrusions were clearly organized in pairs, which were in turn organized in rods indicated in Figure 6.5d with white arrowheads. Examples of various organizations (tetramers, hexamers, and rods) are shown in the insets of Figure 6.5d. Some rods were bent (Figure 6.5d, right-most inset). It might very well be that these rods were actually pairs of two hexamers, rather than one dodecamer.

There were also areas apparently devoid of protein (marked with green arrows in Figure 6.5d).

The heights of the protrusions were only ～1.5 nm above the gaps in-between them, much lower than the expected height difference of the extracellular side of the protein above the membrane (～4 nm illustrated in Figure 6.5c). These images were required using PeakForce Tapping mode, which is based on the acquisition of force distance curves with kHz-rate, and allows directly controlling imaging forces down to the pN-range [224, 290]. Therefore it is unlikely that this low height was due to the force being too strong during imaging (“hammering”). Instead, this is more likely that because the proteins are densely packed, the height difference between the protrusions and the gap in-between them does not represent the real height of the protrusions above the membrane.

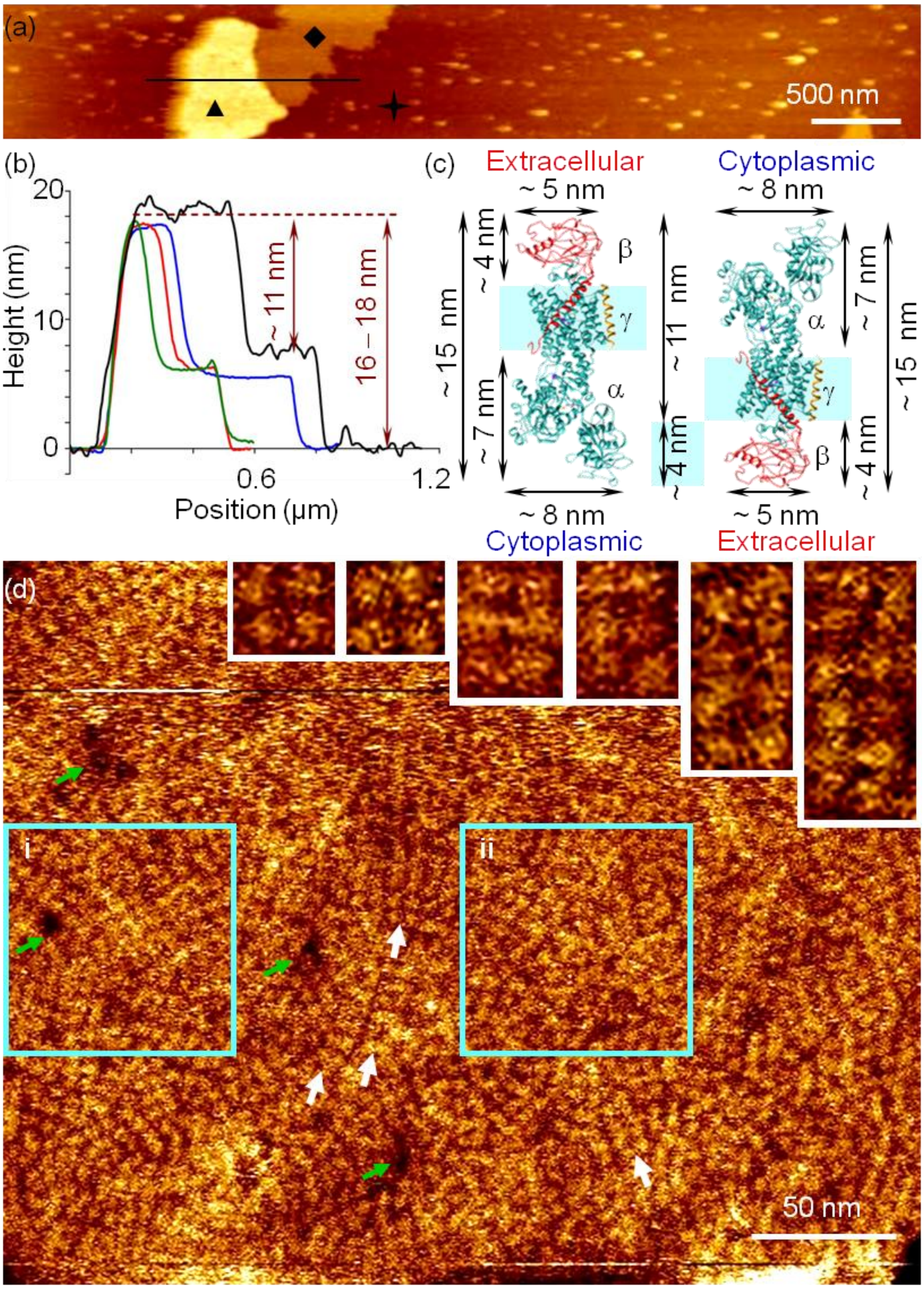

Figure 6.5. Supramolecular organization of ATPase in purified membrane fragments studied by AFM.

(a) AFM height image of native membrane patches containing the Na^+,K^+-ATPase adsorbed on mica (z-scale from black to white is 50 nm). Protein-containing membrane fragments, protein-free lipid membranes, and bare mica surface are labeled with triangle, rhombus, and cross respectively.

The image also reveals many small pieces of material adsorbed on the surface.

(b) Cross-section profiles indicating the observed heights of the protein-containing and protein-free patches in the AFM images. Black line corresponds to the height measured along the black line shown in (a).

(c) Cartoon illustration of the observed height differences between protein-containing patches, protein-free lipid patches, and mica. The α, β, and γ subunits are shown in cyan, red, and yellow, respectively, with the lipid bilayer indicated in aquamarine. The observed difference of ~ 11 nm between the height of the protein-containing and protein-free areas can be explained in terms of the difference between the total height of the protein and the height of the lipid bilayer, independent of the orientation of the protein adsorbed on mica (extracellular side up or cytoplasmic side up). The absolute values of the protein patches and lipid bilayer heights observed in the AFM are somewhat higher than the expected ones.

(d) High magnification AFM height image of the protein-containing patch (z-scale from black to which is 3 nm). Numerous circular protrusions with the diameter of ~ 5 nm are visible. Some of the protrusions aligned in pairs of lines (marked by white arrowheads). Green arrows indicate areas devoid of protein. Insets: examples of proteins organized in the form of tetramers, hexamers, and rods. Fourier transforms of the areas labeled with turquoise squares (i) and (ii) will be discussed below in Figure 6.6a, b.

6.3. Discussion

6.3.1. Adsorption of the Purified Membrane Fragments on Mica in Different Buffer Conditions

The composition of the adsorption buffer ($MgCl_2$ and KCl concentration) was optimized to get good conditions for AFM imaging. It was found that higher concentrations of either of the two electrolytes led to less material present on the surface. The observed trends with respect to the amount of adsorbed material can be explained based on the standard arguments of the Derjaguin, Landau, Verwey, Overbeek (DLVO) theory [244] and goes as follows. At neutral pH, mica is negatively charged [247]. The surface of the membrane fragments is also charged because of the exposed acidic and basic amino acid residues. According to DLVO theory, the force between two charged surfaces in solution is a combination of electrostatic force and the attractive van der Waals force. The electrostatic interaction can be modulated by changing the solution ionic strength. More material was observed on the surface at low salt concentration but less material at high salt concentration. There does not seem to be a significant difference between the effect of KCl and the effect of $MgCl_2$. From these observations it can be concluded that the electrostatic component of the interaction is attractive. This could be either due to a net positive charge on one side of the protein, or due to inhomogeneities in the charge distribution on the protein molecules. Both acidic and basic residues are exposed on the surface of the protein. Charge-mosaic surfaces exposing both positive and negative charges have been shown exhibit an attraction across water. The attraction was modulated by ionic strength in a similar way as an interaction between charged surfaces is [291].

There is another possibility for the observed effect of salt on the amount of material adsorbed. It is possible that two species with different charges are present in solution: for example, positively charged aggregates and weakly charged (positively or negatively) membrane patches. The adsorption of the first is attenuated by salt, and the adsorption of the second is not affected. Qualitatively, this would result in a very similar picture as shown in Figure 6.3.

Concerning the organization of the adsorbed material (aggregates or vesicles vs. patches), the formation of the patches involves two steps: adsorption of the membrane fragments and their spreading. This is similar to the process of supported lipid bilayer formation from vesicles on mica [137, 171, 241, 292, 293]. At low salt concentration, the adsorption of membrane fragments on mica is fast due to the strong attraction, resulting in crowding of the surface. This appeared to have inhibited spreading (Figure 6.3a). On the contrary, the relatively sparse adsorption of material at high salt concentrations left sufficient space for the spreading of the fragments. Indeed, the largest patches were obtained by incubating the surfaces overnight after adsorption was stopped by washing the samples.

6.3.2. Overview of the Morphology of the Purified Membrane Fragments

Both AFM and TEM revealed protein-free and protein-containing areas within the membrane fragments (labeled with rhombus and triangle, respectively, in Figure 6.5a and Figure 6.2). This correlates with what was shown in the AFM images of various isolated membrane fragments adsorbed on mica from the previous studies [69, 70, 294]. There are several possibilities for the separation of protein-containing and protein-free patches. It might exist in the real cell membranes, or might be a result of membrane isolation procedure, or the adsorption procedure, which drove the clustering of the proteins by detergent or protein-surface interaction. Lipid depletion by phospholipase A_2 resulted in the disappearance of the protein-free patches adsorbed on the mica surfaces, but no significant changes were observed with the protein-containing patches, suggesting that these two patterns existed before the adsorption procedure. This was also supported by the observation of protein-free and protein-rich patches with the TEM. Furthermore, protrusions organized in pairs in the form of rods were observed by AFM. This type of specific organization (as opposed to random close-packing) is not likely to result from densification that may accompany adsorption. On the other hand, detergent treatment in the isolation procedure may cause protein organization. Finally, native cell membranes need to be observed to confirm the native origin of the protein patterns identified.

In AFM, the height of the protein-free patches above mica matches the height of a bilayer. The height of the protein-containing patches above the mica matches the expected height of Na^+, K^+-ATPase molecule in the direction perpendicular to the cell membrane. AFM images at high magnification revealed densely packed arrays of pairs of protrusions in the protein-containing area. This correlated with the rows revealed in the protein-containing area in high magnification electron micrograph images (Figure 6.2 inset). The size of the protrusions in the AFM images was consistent with the lateral size of the extracellular portion of the β-subunit (Figure 6.5d), suggesting that the membrane fragments adsorbed on mica with extracellular side up.

6.3.3. Analysis of the Organization of Na$^+$, K$^+$-ATPases from the AFM Images

To further elucidate the state of organization of the ATPase monomers in these patches, the images were analyzed as follows. Firstly, Fourier-analysis was used to reveal characteristic spacings present in the images (Figure 6.6a, b). Secondly, correlation averaging was done to elucidate the most reproducible (therefore the most common) motif (Figure 6.6c inset). Finally, the distribution of motifs in the original images was revealed by cross-correlation between the averaged structure and the original AFM images (Figure 6.6c). These are described in turn below.

6.3.3.1. Do Na$^+$, K$^+$-ATPases Exist as Monomers or Oligomers?

The first question to answer was whether the monomers were the only species present in the membrane fragments. To do so, AFM images were subjected to Fourier-analysis to reveal the presence of conserved spacings and directions that would be indicative of short-range order consistent with oligmerization. In particular, a collection of randomly close-packed monomers would present itself as a diffuse ring corresponding to the average monomer-monomer distance because of the monomer position correlations [295]. The appearance of peaks, on the other hand, would indicate oligomers with preferred packing directions. Randomly close-packed oligomers would present a sharp ring because the monomer-monomer distance is conserved. Examples of the Fourier spectra of the high-magnification AFM image (the two areas labeled with turquoise squares i and ii in Figure 6.5d) are shown in Figure 6.6a, b. The presence of peaks is indicative of the presence of oriented oligomeric structures, whose orientation can be readily identified in the boxed areas shown in Figure 6.5d. The peaks occur at a reciprocal spacing of ~ 6 ± 0.6 nm^{-1}. Furthermore, a nearly complete diffuse circle of intensity is visible in both Figure 6.6a and Figure 6.6b at the same spacing of ~ 6 nm^{-1}, indicating the presence of randomly close-packed monomers, which can also be observed in the two turquoise squares in Figure 6.5d. Interestingly, there were two pairs of peaks in Figure 6.6a (marked with green circles), corresponding to the two orthogonal orientations of the monomer-monomer spacings in an oligomer, while there was only one pair of peaks in Figure 6.6b (marked with green circle), indicating only one orientation, probably corresponding to aligned dimers. The other pair of peaks is very faint (marked with white arrow in Figure 6.6b).

As discussed above, indeed the presence of peaks in the Fourier-transform confirms the presence of oriented oligomeric structures in the AFM image.

6.3.3.2. Tetramers as the Conserved Motifs of Na^+, K^+-ATPases in the AFM Images

Correlation averaging was then performed with the high-magnification AFM images in order to elucidate the most stable motif (dimer, tetramer, or higher-order oligomer). This method is widely used in electron microscopy [232-234]. Briefly, motifs were extracted manually from the AFM images, rotationally and translationally aligned on a manually selected reference and conditionally summed. The most stable average motif was found to be a tetramer (Figure 6.5c inset). This means, that even if hexamers or higher-order structures were selected during the alignment and averaging, a tetramer came out as the most clearly resolved motif. The monomer-monomer distances in the tetramers were ~ 6 nm, corresponding to the observations from the raw AFM images and the reciprocal spacing in Fourier analysis.

The distribution of tetramers was analyzed by cross-correlating the image of the average tetramer (Figure 6.6c inset) with the original AFM images (Figure 6.5d). The result of this analysis is shown in the contour map with peaks indicating the relative position of tetramer (Figure 6.6c). The density of the contour lines in the map indicates the degree of similarity between the motif at a given location and the average tetramer. The higher the signal (the more dense the contour lines), the more similar are the motifs in AFM image to the average tetramer. Several clusters of strong correlation peaks are visible in the contour map (an example is marked with a grey arrow in Figure 6.6c), indicating the presence of tetramers at these locations. There are also several blank areas (green arrowheads in Figure 6.6c) indicating no correlation with the tetramer. Some of these places clearly correspond to the areas in the original high-magnification AFM image where devoid of proteins (green arrowheads in Figure 6.5d). On the other hand, there are areas which contain protein but where the correlation with the average tetramer is rather poor (grey box ii in Figure 6.6c). The areas used in Fourier analysis (Figure 6.6a and b) are outlined with grey boxes i and ii in Figure 6.6c. There were higher signals in the contour map in the area shown in grey box i than grey box ii, corresponding to the observation of two pairs of peaks in the Fourier transform in Figure 6.6a, but only one pair—in Figure 6.6b. This suggests that tetramers are not the only species present in the membrane patches. Randomly distributed correlation peaks, and more often, arrays of correlation peaks are also present, indicating that at least some of the protein is probably present in the form of dimers or monomers that could not be clearly visualized due to relatively low resolution of these images. Based on the Fourier analysis results above, dimers are the more likely candidates. Notwithstanding this point, the tetramer appears to be the most commonly occurring motif of Na^+, K^+-ATPase in native membranes under the conditions used in this study (no ATP, 1 mM $MgCl_2$, 150 mM KCl).

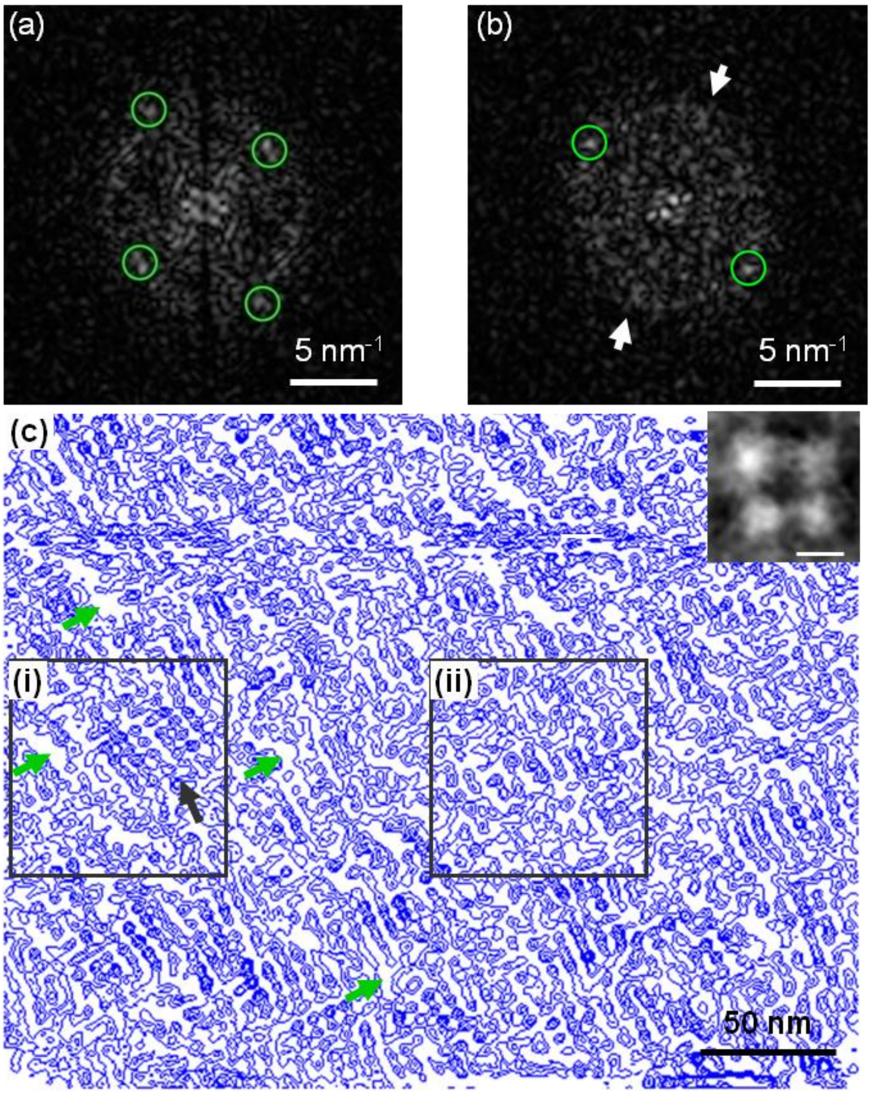

Figure 6.6. Single particle average analysis of AFM images.

(a) and (b) Fourier transforms of the areas labeled with turquoise squares (i) and (ii) in Figure 6.4d. The peaks reflecting the conserved spacings apparent in the AFM images are highlighted with light green circles. The pair of peaks which are very faint is marked with white arrows in (b).

(c) Contour map showing the distribution of tetramers in the AFM image from Figure 6.4d. The map was obtained by cross-correlation analysis between the image of an average tetramer (inset) and the original AFM image. Blank areas where there is no correlation with the tetramer are marked with green arrows. The two grey boxes labeled as (i) and (ii) correspond to the green boxes (i) and (ii) in Figure 6.4d. (i) contains several clusters of strong correlation peaks (grey arrowhead), while (ii) is nearly devoid of such clusters. The average tetramer in the inset was obtained from correlation averaging. Briefly, individual motifs were selected manually in the AFM image, and subjected to sequential alignment using one of them as a reference. Images with the highest cross-correlation coefficients were summed to get an average structure. The process was repeated four times using the resulting sum as a reference in each subsequent step. The scale bar in the inset represents 5 nm.

Tetramer has previously been proposed as the functional unit of Na^+, K^+-ATPase [182, 296, 297]. Studies have shown that only half of the α subunits in the purified membrane-bound Na^+, K^+-ATPases can be phosphorylated [296-298], and half of the α subunits could be cross-linked. The cross-linking is between a phosphorylated and an unphosphorylated α subunit [296]. Moreover, electron microscopy of rotary-shadowed solubilized, membrane-bound and antibody-bound Na^+, K^+-ATPase from dog and pig kidney has demonstrated its tetramerization [196]. Kinetic studies indicate that oligomeric organization of the ATPase is expected under low ATP conditions [189-192].

6.3.4. Comparison of AFM Topographs and X-ray Crystallographic Structure

To compare the tetramer observed in the AFM with the structure of the protein obtained by X-ray diffraction, a model of tetramer was constructed from the dimer in the X-ray crystallographic structure of pig renal Na^+, K^+-ATPase (PDB 3KDP) [1]. This is the structure of the protein in the E2 conformation, the conformation that is expect under the imaging condition used in this study (150 mM KCl, 1 mM $MgCl_2$ buffer) [1]. The views of the cytoplasmic and the extracellular side are shown in Figure 6.7b and c respectively. The tetramer motif obtained from correlation averaging of AFM image (Figure 6.7a**)** is more similar to the extracellular side view. Specifically, there is a prominent depression in the center of the tetramer that is

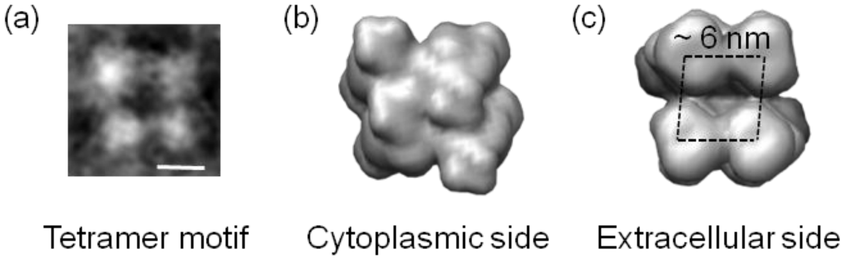

Figure 6.7. Comparison of the conserved tetramer motif with X-ray crystallographic structure. (a) The conserved tetramer motif obtained from correlation averaging of the AFM images. The scale bar represents 5 nm. (b) and (c) cytoplasmic side and extracellular side views of a model of the Na^+, K^+-ATPase tetramer generated from X-ray crystal structure of pig renal Na^+, K^+-ATPase (PDB 3KDP) [1] at a resolution of ~ 1.8 nm. The averaged tetramer motif in (a) corresponds to the extracellular side view. The broken line parallelogram in (c) indicates the monomer-monomer distance of 6 nm within the tetramer.

observed by AFM and evident on the extracellular side of the X-ray structure, but that is entirely absent from the cytoplasmic side. This depression is located in-between the extracellular domains of the individual monomers. This observation confirms the previous assumption from the AFM iamge that the protein is adsorbed with the extracellular side up.

6.4. Conclusions

In conclusion, this chapter shows the oligomerization of Na^+, K^+-ATPase with varies orders in the membrane preparations from outer medulla of the rabbit kidney. Tetramer $(\alpha\beta)_4$ was found to be the most conserved motif. Comparison with the X-ray crystallographic structure suggested that the membrane fragments adsorbed on mica with the extracellular side facing up. This is the first time, to my knowledge, where the supramolecular organization of the Na^+, K^+-ATPase in the native state without the loss of enzyme activity is reported.

References

1. Morth, J.P., et al., *Crystal structure of the sodium-potassium pump.* Nature, 2007. **450**(7172): p. 1043-9.
2. Kaszuba, M., et al., *High-concentration zeta potential measurements using light-scattering techniques.* Philos Transact A Math Phys Eng Sci, 2010. **368**(1927): p. 4439-51.
3. Rafelski, S.M. and W.F. Marshall, *Building the cell: design principles of cellular architecture.* Nat Rev Mol Cell Biol, 2008. **9**(8): p. 593-602.
4. Karsenti, E., *Self-organization in cell biology: a brief history.* Nat Rev Mol Cell Biol, 2008. **9**(3): p. 255-62.
5. Misteli, T., *The concept of self-organization in cellular architecture.* J Cell Biol, 2001. **155**(2): p. 181-5.
6. Yeagle, P.L., *The Membranes of Cells*. 1987, San Francisco, CA, USA: Academic Press, Inc.
7. van Meer, G. and A.I. de Kroon, *Lipid map of the mammalian cell.* J Cell Sci, 2011. **124**(Pt 1): p. 5-8.
8. Lodish, H., et al., *Molecular Cell Bilology, 4th edition*. 4th ed. 2000, New York: W.H. Freeman.
9. Singer, S.J. and G.L. Nicolson, *The fluid mosaic model of the structure of cell membranes.* Science, 1972. **175**(4023): p. 720-31.
10. Jacobson, K., E.D. Sheets, and R. Simson, *REVISITING THE FLUID MOSAIC MODEL OF MEMBRANES.* Science, 1995. **268**(5216): p. 1441-1442.
11. Bagatolli, L.A., et al., *An outlook on organization of lipids in membranes: searching for a realistic connection with the organization of biological membranes.* Prog Lipid Res, 2010. **49**(4): p. 378-89.
12. Simons, K. and D. Toomre, *Lipid rafts and signal transduction.* Nat Rev Mol Cell Biol, 2000. **1**(1): p. 31-9.
13. Laude, A.J. and I.A. Prior, *Plasma membrane microdomains: organization, function and trafficking.* Mol Membr Biol, 2004. **21**(3): p. 193-205.
14. Bretscher, M.S., *Asymmetrical lipid bilayer structure for biological membranes.* Nat New Biol, 1972. **236**(61): p. 11-2.
15. Fadeel, B. and D. Xue, *The ins and outs of phospholipid asymmetry in the plasma membrane: roles in health and disease.* Crit Rev Biochem Mol Biol, 2009. **44**(5): p. 264-77.
16. Op den Kamp, J.A., *Lipid asymmetry in membranes.* Annu Rev Biochem, 1979. **48**: p. 47-71.
17. Balasubramanian, K. and A.J. Schroit, *Aminophospholipid asymmetry: A matter of life and death.* Annual Review of Physiology, 2003. **65**: p. 701-734.
18. Verkleij, A.J., et al., *Asymmetric Distribution of Phospholipids in Human Red-Cell Membrane - Combined Study Using Phospholipases and Freeze-Etch Electron-Microscopy.* Biochimica Et Biophysica Acta, 1973. **323**(2): p. 178-193.
19. Devaux, P.F., *Static and dynamic lipid asymmetry in cell membranes.* Biochemistry, 1991. **30**(5): p. 1163-73.

20. Daleke, D.L., *Regulation of phospholipid asymmetry in the erythrocyte membrane.* Curr Opin Hematol, 2008. **15**(3): p. 191-5.
21. Daleke, D.L., *Regulation of transbilayer plasma membrane phospholipid asymmetry.* Journal of Lipid Research, 2003. **44**(2): p. 233-242.
22. Devaux, P.F., I. Lopez-Montero, and S. Bryde, *Proteins involved in lipid translocation in eukaryotic cells.* Chem Phys Lipids, 2006. **141**(1-2): p. 119-32.
23. Schlegel, R.A. and P. Williamson, *Phosphatidylserine, a death knell.* Cell Death Differ, 2001. **8**(6): p. 551-63.
24. Zwaal, R.F. and A.J. Schroit, *Pathophysiologic implications of membrane phospholipid asymmetry in blood cells.* Blood, 1997. **89**(4): p. 1121-32.
25. Bevers, E.M., et al., *Generation of prothrombin-converting activity and the exposure of phosphatidylserine at the outer surface of platelets.* Eur J Biochem, 1982. **122**(2): p. 429-36.
26. Lentz, B.R., *Exposure of platelet membrane phosphatidylserine regulates blood coagulation.* Prog Lipid Res, 2003. **42**(5): p. 423-38.
27. Fadok, V.A., et al., *Exposure of phosphatidylserine on the surface of apoptotic lymphocytes triggers specific recognition and removal by macrophages.* J Immunol, 1992. **148**(7): p. 2207-16.
28. Savill, J., et al., *Phagocyte recognition of cells undergoing apoptosis.* Immunol Today, 1993. **14**(3): p. 131-6.
29. Utsugi, T., et al., *Elevated expression of phosphatidylserine in the outer membrane leaflet of human tumor cells and recognition by activated human blood monocytes.* Cancer Res, 1991. **51**(11): p. 3062-6.
30. Fadok, V.A., et al., *A receptor for phosphatidylserine-specific clearance of apoptotic cells.* Nature, 2000. **405**(6782): p. 85-90.
31. Rosing, J., et al., *Impaired factor X and prothrombin activation associated with decreased phospholipid exposure in platelets from a patient with a bleeding disorder.* Blood, 1985. **65**(6): p. 1557-61.
32. Wood, B.L., D.F. Gibson, and J.F. Tait, *Increased erythrocyte phosphatidylserine exposure in sickle cell disease: flow-cytometric measurement and clinical associations.* Blood, 1996. **88**(5): p. 1873-80.
33. Zwaal, R.F., P. Comfurius, and E.M. Bevers, *Surface exposure of phosphatidylserine in pathological cells.* Cell Mol Life Sci, 2005. **62**(9): p. 971-88.
34. Simons, K. and E. Ikonen, *Functional rafts in cell membranes.* Nature, 1997. **387**(6633): p. 569-572.
35. Brown, D.A. and J.K. Rose, *Sorting of GPI-anchored proteins to glycolipid-enriched membrane subdomains during transport to the apical cell surface.* Cell, 1992. **68**(3): p. 533-44.
36. Schroeder, R., E. London, and D. Brown, *Interactions between saturated acyl chains confer detergent resistance on lipids and glycosylphosphatidylinositol (GPI)-anchored proteins: GPI-anchored proteins in liposomes and cells show similar behavior.* Proc Natl Acad Sci U S A, 1994. **91**(25): p. 12130-4.
37. Schnitzer, J.E., et al., *Separation of caveolae from associated microdomains of GPI-anchored proteins.* Science, 1995. **269**(5229): p. 1435-9.
38. Sargiacomo, M., et al., *Signal transducing molecules and glycosyl-phosphatidylinositol-linked proteins form a caveolin-rich insoluble complex in MDCK cells.* J Cell Biol, 1993. **122**(4): p. 789-807.

39. Kurzchalia, T.V. and R.G. Parton, *Membrane microdomains and caveolae.* Curr Opin Cell Biol, 1999. **11**(4): p. 424-31.
40. Karpen, H.E., et al., *The sonic hedgehog receptor patched associates with caveolin-1 in cholesterol-rich microdomains of the plasma membrane.* J Biol Chem, 2001. **276**(22): p. 19503-11.
41. Song, K.S., et al., *Co-purification and direct interaction of Ras with caveolin, an integral membrane protein of caveolae microdomains. Detergent-free purification of caveolae microdomains.* J Biol Chem, 1996. **271**(16): p. 9690-7.
42. Moffett, S., D.A. Brown, and M.E. Linder, *Lipid-dependent targeting of G proteins into rafts.* J Biol Chem, 2000. **275**(3): p. 2191-8.
43. Waugh, M.G., D. Lawson, and J.J. Hsuan, *Epidermal growth factor receptor activation is localized within low-buoyant density, non-caveolar membrane domains.* Biochem J, 1999. **337 (Pt 3)**: p. 591-7.
44. Foster, L.J., C.L. De Hoog, and M. Mann, *Unbiased quantitative proteomics of lipid rafts reveals high specificity for signaling factors.* Proc Natl Acad Sci U S A, 2003. **100**(10): p. 5813-8.
45. Pike, L.J., *Lipid rafts: bringing order to chaos.* J Lipid Res, 2003. **44**(4): p. 655-67.
46. Munro, S., *Lipid rafts: elusive or illusive?* Cell, 2003. **115**(4): p. 377-88.
47. Brown, D.A., *Lipid rafts, detergent-resistant membranes, and raft targeting signals.* Physiology (Bethesda), 2006. **21**: p. 430-9.
48. Brown, D.A., *Seeing is believing: visualization of rafts in model membranes.* Proc Natl Acad Sci U S A, 2001. **98**(19): p. 10517-8.
49. Jacobson, K. and C. Dietrich, *Looking at lipid rafts?* Trends Cell Biol, 1999. **9**(3): p. 87-91.
50. Lingwood, D. and K. Simons, *Lipid rafts as a membrane-organizing principle.* Science, 2010. **327**(5961): p. 46-50.
51. Pralle, A., et al., *Sphingolipid-cholesterol rafts diffuse as small entities in the plasma membrane of mammalian cells.* J Cell Biol, 2000. **148**(5): p. 997-1008.
52. Friedrichson, T. and T.V. Kurzchalia, *Microdomains of GPI-anchored proteins in living cells revealed by crosslinking.* Nature, 1998. **394**(6695): p. 802-5.
53. Varma, R. and S. Mayor, *GPI-anchored proteins are organized in submicron domains at the cell surface.* Nature, 1998. **394**(6695): p. 798-801.
54. Jacobson, K., O.G. Mouritsen, and R.G. Anderson, *Lipid rafts: at a crossroad between cell biology and physics.* Nat Cell Biol, 2007. **9**(1): p. 7-14.
55. Eggeling, C., et al., *Direct observation of the nanoscale dynamics of membrane lipids in a living cell.* Nature, 2009. **457**(7233): p. 1159-62.
56. Dietrich, C., et al., *Lipid rafts reconstituted in model membranes.* Biophys J, 2001. **80**(3): p. 1417-28.
57. Giocondi, M.C., et al., *Surface topography of membrane domains.* Biochim Biophys Acta, 2010. **1798**(4): p. 703-18.
58. Honerkamp-Smith, A.R., S.L. Veatch, and S.L. Keller, *An introduction to critical points for biophysicists; observations of compositional heterogeneity in lipid membranes.* Biochim Biophys Acta, 2009. **1788**(1): p. 53-63.
59. Lillemeier, B.F., et al., *Plasma membrane-associated proteins are clustered into islands attached to the cytoskeleton.* Proc Natl Acad Sci U S A, 2006. **103**(50): p. 18992-7.

60. Sieber, J.J., et al., *Anatomy and dynamics of a supramolecular membrane protein cluster.* Science, 2007. **317**(5841): p. 1072-6.
61. Zilly, F.E., et al., *Ca2+ induces clustering of membrane proteins in the plasma membrane via electrostatic interactions.* EMBO J, 2011. **30**(7): p. 1209-20.
62. Nagy, P., et al., *Activation-dependent clustering of the erbB2 receptor tyrosine kinase detected by scanning near-field optical microscopy.* J Cell Sci, 1999. **112 (Pt 11)**: p. 1733-41.
63. Muller, D.J., N. Wu, and K. Palczewski, *Vertebrate membrane proteins: structure, function, and insights from biophysical approaches.* Pharmacol Rev, 2008. **60**(1): p. 43-78.
64. Engelman, D.M., *Membranes are more mosaic than fluid.* Nature, 2005. **438**(7068): p. 578-580.
65. Goodsell, D.S. and A.J. Olson, *Structural symmetry and protein function.* Annu Rev Biophys Biomol Struct, 2000. **29**: p. 105-53.
66. Veenhoff, L.M., E.H. Heuberger, and B. Poolman, *Quaternary structure and function of transport proteins.* Trends Biochem Sci, 2002. **27**(5): p. 242-9.
67. Ullrich, A. and J. Schlessinger, *Signal transduction by receptors with tyrosine kinase activity.* Cell, 1990. **61**(2): p. 203-12.
68. Stock, J., *Receptor signaling: dimerization and beyond.* Curr Biol, 1996. **6**(7): p. 825-7.
69. Fotiadis, D., et al., *Atomic-force microscopy: Rhodopsin dimers in native disc membranes.* Nature, 2003. **421**(6919): p. 127-128.
70. Liang, Y., et al., *Organization of the G protein-coupled receptors rhodopsin and opsin in native membranes.* J Biol Chem, 2003. **278**(24): p. 21655-62.
71. Muller, D.J., et al., *Electrostatically balanced subnanometer imaging of biological specimens by atomic force microscope.* Biophys J, 1999. **76**(2): p. 1101-11.
72. Buzhynskyy, N., et al., *Rows of ATP synthase dimers in native mitochondrial inner membranes.* Biophys J, 2007. **93**(8): p. 2870-6.
73. Brinda, K.V. and S. Vishveshwara, *Oligomeric protein structure networks: insights into protein-protein interactions.* BMC Bioinformatics, 2005. **6**: p. 296.
74. Bahadur, R.P., et al., *Dissecting subunit interfaces in homodimeric proteins.* Proteins, 2003. **53**(3): p. 708-19.
75. Blodgett, K.B., *Films built by depositing successive monomolecular layers on a solid surface.* Journal of the American Chemical Society, 1935. **57**: p. 1007-1022.
76. Angelova, M.I. and D.S. Dimitrov, *Liposome electroformation.* Faraday Discussions of the Chemical Society, 1986. **81**: p. 303-311.
77. Sackmann, E., *Supported membranes: Scientific and practical applications.* Science, 1996. **271**(5245): p. 43-48.
78. Giess, F., et al., *The protein-tethered lipid bilayer: a novel mimic of the biological membrane.* Biophys J, 2004. **87**(5): p. 3213-20.
79. Drexler, J. and C. Steinem, *Pore-Suspending Lipid Bilayers on Porous Alumina Investigated by Electrical Impedance Spectroscopy.* The Journal of Physical Chemistry B, 2003. **107**(40): p. 11245-11245.
80. Janshoff, A. and C. Steinem, *Transport across artificial membranes-an analytical perspective.* Anal Bioanal Chem, 2006. **385**(3): p. 433-51.
81. Chan, Y.H. and S.G. Boxer, *Model membrane systems and their applications.* Curr Opin Chem Biol, 2007. **11**(6): p. 581-7.

82. Peetla, C., A. Stine, and V. Labhasetwar, *Biophysical interactions with model lipid membranes: applications in drug discovery and drug delivery.* Mol Pharm, 2009. **6**(5): p. 1264-76.
83. Girard, P., et al., *A new method for the reconstitution of membrane proteins into giant unilamellar vesicles.* Biophys J, 2004. **87**(1): p. 419-29.
84. Doeven, M.K., et al., *Distribution, lateral mobility and function of membrane proteins incorporated into giant unilamellar vesicles.* Biophys J, 2005. **88**(2): p. 1134-42.
85. Kahya, N., et al., *Reconstitution of membrane proteins into giant unilamellar vesicles via peptide-induced fusion.* Biophys J, 2001. **81**(3): p. 1464-74.
86. Vockenroth, I.K., et al., *Functional incorporation of the pore forming segment of AChR M2 into tethered bilayer lipid membranes.* Biochim Biophys Acta, 2007. **1768**(5): p. 1114-20.
87. Milhiet, P.E., et al., *High-resolution AFM of membrane proteins directly incorporated at high density in planar lipid bilayer.* Biophys J, 2006. **91**(9): p. 3268-75.
88. Wagner, M.L. and L.K. Tamm, *Tethered polymer-supported planar lipid bilayers for reconstitution of integral membrane proteins: silane-polyethyleneglycol-lipid as a cushion and covalent linker.* Biophys J, 2000. **79**(3): p. 1400-14.
89. Heyse, S., et al., *Incorporation of rhodopsin in laterally structured supported membranes: Observation of transducin activation with spatially and time-resolved surface plasmon resonance.* Biochemistry, 1998. **37**(2): p. 507-522.
90. Salafsky, J., J.T. Groves, and S.G. Boxer, *Architecture and function of membrane proteins in planar supported bilayers: a study with photosynthetic reaction centers* Biochemistry, 1996. **35**: p. 14773-14781.
91. Kiessling, V., C. Wan, and L.K. Tamm, *Domain coupling in asymmetric lipid bilayers.* Biochim Biophys Acta, 2009. **1788**(1): p. 64-71.
92. Collins, M.D. and S.L. Keller, *Tuning lipid mixtures to induce or suppress domain formation across leaflets of unsupported asymmetric bilayers.* Proceedings of the National Academy of Sciences of the United States of America, 2008. **105**(1): p. 124-128.
93. Pautot, S., B.J. Frisken, and D.A. Weitz, *Engineering asymmetric vesicles.* Proceedings of the National Academy of Sciences of the United States of America, 2003. **100**(19): p. 10718-10721.
94. Cheng, H.T., Megha, and E. London, *Preparation and properties of asymmetric vesicles that mimic cell membranes: effect upon lipid raft formation and transmembrane helix orientation.* J Biol Chem, 2009. **284**(10): p. 6079-92.
95. Chiantia, S., et al., *Asymmetric GUVs prepared by MbetaCD-mediated lipid exchange: an FCS study.* Biophys J, 2011. **100**(1): p. L1-3.
96. Rossetti, F.F., et al., *Interactions between Titanium Dioxide and Phosphatidyl Serine-containing Liposomes: Formation and Patterning of Supported Phospholipid Bilayers on the Surface of a Medically Relevant Material.* Langmuir, 2005. **21**: p. 6443-6450.
97. Rossetti, F.F., M. Textor, and I. Reviakine, *Asymmetric distribution of phosphatidyl serine in supported phospholipid bilayers on titanium dioxide.* Langmuir, 2006. **22**(8): p. 3467-3473.

98. Richter, R.P., R. Berat, and A.R. Brisson, *Formation of solid-supported lipid bilayers: An integrated view.* Langmuir, 2006. **22**(8): p. 3497-3505.
99. Brunette, D.M., et al., *Titanium in Medicine*. 2001, Berlin: Springer-Verlag.
100. Kasbauer, M., M. Junglas, and T.M. Bayerl, *Effect of cationic lipids in the formation of asymmetries in supported bilayers.* Biophysical Journal, 1999. **76**(5): p. 2600-2605.
101. Hetzer, M., et al., *Asymmetric molecular friction in supported phospholipid bilayers revealed by NMR measurements of lipid diffusion.* Langmuir, 1998. **14**(5): p. 982-984.
102. Richter, R.P., N. Maury, and A.R. Brisson, *On the effect of the solid support on the interleaflet distribution of lipids in supported lipid bilayers.* Langmuir, 2005. **21**(1): p. 299-304.
103. Lin, W.C., et al., *Lipid asymmetry in DLPC/DSPC-supported lipid bilayers: A combined AFM and fluorescence microscopy study.* Biophysical Journal, 2006. **90**(1): p. 228-237.
104. Wacklin, H.P. and R.K. Thomas, *Spontaneous formation of asymmetric lipid bilayers by adsorption of vesicles.* Langmuir, 2007. **23**(14): p. 7644-7651.
105. Wacklin, H.P., *Composition and Asymmetry in Supported Membranes Formed by Vesicle Fusion.* Langmuir, 2011. **27**(12): p. 7698-7707.
106. Akesson, A., et al., *Composition and structure of mixed phospholipid supported bilayers formed by POPC and DPPC.* Soft Matter, 2012. **8**: p. 5658-5665.
107. Fritz, K., et al., *Arrangement of Annexin A2 tetramer and its impact on the structure and diffusivity of supported lipid bilayers.* Soft Matter, 2010. **6**(17): p. 4084-4094.
108. London, E., *Insights into lipid raft structure and formation from experiments in model membranes.* Curr Opin Struct Biol, 2002. **12**(4): p. 480-6.
109. London, E., *How principles of domain formation in model membranes may explain ambiguities concerning lipid raft formation in cells.* Biochim Biophys Acta, 2005. **1746**(3): p. 203-20.
110. Koynova, R. and M. Caffrey, *Phases and phase transitions of the phosphatidylcholines.* Biochim Biophys Acta, 1998. **1376**(1): p. 91-145.
111. Rawicz, W., et al., *Effect of chain length and unsaturation on elasticity of lipid bilayers.* Biophys J, 2000. **79**(1): p. 328-39.
112. Veatch, S.L. and S.L. Keller, *Separation of liquid phases in giant vesicles of ternary mixtures of phospholipids and cholesterol.* Biophys J, 2003. **85**(5): p. 3074-83.
113. Veatch, S.L. and S.L. Keller, *Organization in lipid membranes containing cholesterol.* Phys Rev Lett, 2002. **89**(26): p. 268101.
114. Veatch, S.L. and S.L. Keller, *Seeing spots: complex phase behavior in simple membranes.* Biochim Biophys Acta, 2005. **1746**(3): p. 172-85.
115. Weerachatyanukul, W., et al., *Visualizing the localization of sulfoglycolipids in lipid raft domains in model membranes and sperm membrane extracts.* Biochim Biophys Acta, 2007. **1768**(2): p. 299-310.
116. Goksu, E.I. and M.L. Longo, *Ternary Lipid Bilayers Containing Cholesterol in a High Curvature Silica Xerogel Environment.* Langmuir, 2010. **26**(11): p. 8614-8624.
117. Sullan, R.M., et al., *Cholesterol-dependent nanomechanical stability of phase-segregated multicomponent lipid bilayers.* Biophys J, 2010. **99**(2): p. 507-16.

118. Marques, J.T., A.S. Viana, and R.F. De Almeida, *Ethanol effects on binary and ternary supported lipid bilayers with gel/fluid domains and lipid rafts.* Biochim Biophys Acta, 2011. **1808**(1): p. 405-14.
119. Garcia-Saez, A.J., et al., *Pore formation by a Bax-derived peptide: effect on the line tension of the membrane probed by AFM.* Biophys J, 2007. **93**(1): p. 103-12.
120. Ahmed, S.N., D.A. Brown, and E. London, *On the origin of sphingolipid/cholesterol-rich detergent-insoluble cell membranes: physiological concentrations of cholesterol and sphingolipid induce formation of a detergent-insoluble, liquid-ordered lipid phase in model membranes.* Biochemistry, 1997. **36**(36): p. 10944-53.
121. Honerkamp-Smith, A.R., et al., *Line tensions, correlation lengths, and critical exponents in lipid membranes near critical points.* Biophys J, 2008. **95**(1): p. 236-46.
122. Veatch, S.L., et al., *Critical fluctuations in plasma membrane vesicles.* ACS Chem Biol, 2008. **3**(5): p. 287-93.
123. Sheetz, M.P., *Cell control by membrane-cytoskeleton adhesion.* Nat Rev Mol Cell Biol, 2001. **2**(5): p. 392-6.
124. Janmey, P.A., W. Xian, and L.A. Flanagan, *Controlling cytoskeleton structure by phosphoinositide-protein interactions: phosphoinositide binding protein domains and effects of lipid packing.* Chem Phys Lipids, 1999. **101**(1): p. 93-107.
125. Middelkoop, E., et al., *Studies on sickled erythrocytes provide evidence that the asymmetric distribution of phosphatidylserine in the red cell membrane is maintained by both ATP-dependent translocation and interaction with membrane skeletal proteins.* Biochim Biophys Acta, 1988. **937**(2): p. 281-8.
126. Manno, S., Y. Takakuwa, and N. Mohandas, *Identification of a functional role for lipid asymmetry in biological membranes: Phosphatidylserine-skeletal protein interactions modulate membrane stability.* Proc Natl Acad Sci U S A, 2002. **99**(4): p. 1943-8.
127. Logan, M.R. and C.A. Mandato, *Regulation of the actin cytoskeleton by PIP2 in cytokinesis.* Biol Cell, 2006. **98**(6): p. 377-88.
128. Chichili, G.R. and W. Rodgers, *Clustering of membrane raft proteins by the actin cytoskeleton.* J Biol Chem, 2007. **282**(50): p. 36682-91.
129. Castellana, E.T. and P.S. Cremer, *Solid supported lipid bilayers: From biophysical studies to sensor design.* 2006. **61**(10): p. 429-444.
130. Stelzle, M., G. Weissmüller, and E. Sackmann, *On the application of supported bilayers as receptive layers for biosensors with electrical detection.* J. Phys. Chem., 1993. **97**(12): p. 2974-2981.
131. Groves, J.T. and M.L. Dustin, *Supported planar bilayers in studies on immune cell adhesion and communication.* Journal of Immunological Methods, 2003. **278**(1-2): p. 19-32.
132. Tanaka, M. and E. Sackmann, *Supported membranes as biofunctional interfaces and smart biosensor platforms.* Physica Status Solidi a-Applications and Materials Science, 2006. **203**(14): p. 3452-3462.
133. Mueller, P., et al., *Reconstitution of cell membrane structure in vitro and its transformation into an excitable system.* Nature, 1962. **194**: p. 979-80.
134. McConnell, H.M., et al., *Supported planar membranes in studies of cell-cell recognition in the immune system.* Biochim Biophys Acta, 1986. **864**(1): p. 95-106.

135. Trepout, S., et al., *Membrane protein selectively oriented on solid support and reconstituted into a lipid membrane.* Langmuir, 2007. **23**(5): p. 2647-2654.
136. Hussain, M.A., A. Agnihotri, and C.A. Siedlecki, *AFM imaging of ligand binding to platelet integrin alpha(IIb)beta(3) receptors reconstituted into planar lipid bilayers.* Langmuir, 2005. **21**(15): p. 6979-6986.
137. Richter, R., A. Mukhopadhyay, and A. Brisson, *Pathways of lipid vesicle deposition on solid surfaces: a combined QCM-D and AFM study.* Biophys J, 2003. **85**(5): p. 3035-47.
138. Reimhult, E., F. Hook, and B. Kasemo, *Intact vesicle adsorption and supported biomembrane formation from vesicles in solution: Influence of surface chemistry, vesicle size, temperature, and osmotic pressure.* Langmuir, 2003. **19**(5): p. 1681-1691.
139. Reimhult, E., F. Hook, and B. Kasemo, *Vesicle adsorption on SiO2 and TiO2: Dependence on vesicle size.* Journal of Chemical Physics, 2002. **117**(16): p. 7401-7404.
140. Egawa, H. and K. Furusawa, *Liposome Adhesion on Mica Surface Studies by Atomic Force Microscopy.* Langmuir, 1999. **15**: p. 1660-1666.
141. Reviakine, I. and A. Brisson, *Formation of supported phospholipid bilayers from unilamellar vesicles investigated by atomic force microscopy.* Langmuir, 2000. **16**(4): p. 1806-1815.
142. Reviakine, I., et al., *Investigating the properties of supported vesicular layers on titanium dioxide by quartz crystal microbalance with dissipation measurements.* J Chem Phys, 2005. **122**(20): p. 204711.
143. Boudard, S., et al., *Controlling the pathway of formation of supported lipid bilayers of DMPC by varying the sodium chloride concentration.* Thin Solid Films, 2006. **495**(1-2): p. 246-251.
144. Tawa, K. and K. Morigaki, *Substrate-supported phospholipid membranes studied by surface plasmon resonance and surface plasmon fluorescence spectroscopy.* Biophysical Journal, 2005. **89**(4): p. 2750-2758.
145. Hubbard, J.B., V. Silin, and A.L. Plant, *Self assembly driven by hydrophobic interactions at alkanethiol monolayers: mechanism of formation of hybrid bilayer membranes.* Biophysical Chemistry, 1998. **75**(3): p. 163-176.
146. Reimhult, E., et al., *Simultaneous surface plasmon resonance and quartz crystal microbalance with dissipation monitoring measurements of biomolecular adsorption events involving structural transformations and variations in coupled water.* Analytical Chemistry, 2004. **76**(24): p. 7211-7220.
147. Cremer, P.S. and S.G. Boxer, *Formation and spreading of lipid bilayers on planar glass supports.* Journal of Physical Chemistry B, 1999. **103**(13): p. 2554-2559.
148. McLaughlin, A., C. Grathwohl, and S. McLaughlin, *The adsorption of divalent cations to phosphatidylcholine bilayer membranes.* Biochim.Biophys.Acta, 1978. **513**(3): p. 338-357.
149. Leckband, D.E., C.A. Helm, and J. Israelachvili, *Role of Clacium in Adhesion and Fusion of Bilayers.* Biochemistry, 1993. **32**: p. 1127-1140.
150. Gregory, D.P. and L. Ginsberg, *Calcium association with phosphatidylserine. Modification by cholesterol and phosphatidylcholine in monolayers and bilayers.* Biochim Biophys Acta, 1984. **769**(1): p. 238-44.

151. Cho, N.J., et al., *pH-Driven Assembly of Various Supported Lipid Platforms: A Comparative Study on Silicon Oxide and Titanium Oxide.* Langmuir, 2011. **27**(7): p. 3739-3748.
152. Seantier, B., et al., *Dissipation-enhanced quartz crystal microbalance studies on the experimental parameters controlling the formation of supported lipid bilayers.* Journal of Physical Chemistry B, 2005. **109**(46): p. 21755-21765.
153. Keller, C.A. and B. Kasemo, *Surface specific kinetics of lipid vesicle adsorption measured with a quartz crystal microbalance.* Biophysical Journal, 1998. **75**(3): p. 1397-1402.
154. Starr, T.E. and N.L. Thompson, *Formation and characterization of planar phospholipid bilayers supported on TiO2 and SrTiO3 single crystals.* Langmuir, 2000. **16**(26): p. 10301-10308.
155. Seifert, U., *Configurations of fluid membranes and vesicles.* Advances in Physics, 1997. **46**(1): p. 13-137.
156. Seifert, U. and R. Lipowsky, *Adhesion of Vesicles.* Physical Review A, 1990. **42**(8): p. 4768-4771.
157. Zhdanov, V.P., et al., *Simulation of adsorption kinetics of lipid vesicles.* Journal of Chemical Physics, 2000. **112**(2): p. 900-909.
158. Zhdanov, V.P. and B. Kasemo, *Comments on rupture of absorbed vesicles.* Langmuir, 2001. **17**(12): p. 3518-3521.
159. Smith, A.S., E. Sackmann, and U. Seifert, *Effects of a pulling force on the shape of a bound vesicle.* Europhysics Letters, 2003. **64**(2): p. 281-287.
160. Mornet, S., et al., *The formation of supported lipid bilayers on silica nanoparticles revealed by cryoelectron microscopy.* Nano Letters, 2005. **5**(2): p. 281-285.
161. Reviakine, I., et al., *Adsorbed liposome deformation studied with quartz crystal microbalance.* J Chem Phys, 2012. **136**(8): p. 084702 - 084705.
162. Hamai, C., P.S. Cremer, and S.M. Musser, *Single giant vesicle rupture events reveal multiple mechanisms of glass-supported bilayer formation.* Biophys J, 2007. **92**(6): p. 1988-99.
163. Israelachvili, J., *Intermolecular and Surface Forces, 2nd Edition.* 1992, London: Academic Press.
164. Kosmulski, M., *The significance of the difference in the point of zero charge between rutile and anatase.* Advances in Colloid and Interface Science, 2002. **99**(3): p. 255-264.
165. Anderson, T.H., et al., *Formation of Supported Bilayers on Silica Substrates.* Langmuir, 2009. **25**(12): p. 6997-7005.
166. Marra, J. and J. Israelachvili, *Direct measurements of forces between phosphatidylcholine and phosphatidylethanolamine bilayers in aqueous electrolyte solutions.* Biochemistry, 1985. **24**(17): p. 4608-4618.
167. Helm, C.A., J.N. Israelachvilli, and P.M. McGuiggan, *Molecuar Mechanisms and Forces Involved in the Adhesion and Fusion of Amphiphilic Bilayers.* Science, 1989. **246**: p. 919-922.
168. Evans, E. and M. Metcalfe, *Freee Energy Potential for Aggregation of Giant, Neutral Lipid Bilayers by van der Waals Attraction.* Biophysical Journal, 1984. **46**: p. 423-426.
169. Hain, N., M. Gallego, and I. Reviakine, *Unraveling Supported Lipid Bilayer Formation Kinetics: Osmotic Effects.* Langmuir, 2013.

170. Huang, C. and J.T. Mason, *Geometric Packing Constraints in Egg Phosphatidylcholine Vesicles.* Proceedings of the National Academy of Sciences of the United States of America, 1978. **75**(1): p. 308-310.
171. Richter, R.P. and A.R. Brisson, *Following the formation of supported lipid bilayers on mica: a study combining AFM, QCM-D, and ellipsometry.* Biophys J, 2005. **88**(5): p. 3422-33.
172. Hinrichsen, E.L., J. Feder, and T. Jossang, *RANDOM PACKING OF DISKS IN 2 DIMENSIONS.* Physical Review A, 1990. **41**(8): p. 4199-4209.
173. Nagle, J.F. and S. Tristram-Nagle, *Structure of lipid bilayers.* Biochimica et Biophysica Acta-Reviews on Biomembranes, 2000. **1469**(3): p. 159-195.
174. Weirich, K.L., J.N. Israelachvili, and D.K. Fygenson, *Bilayer Edges Catalyze Supported Lipid Bilayer Formation.* Biophysical Journal, 2010. **98**(1): p. 85-92.
175. Stroumpoulis, D., A. Parra, and M. Tirrell, *A kinetic study of vesicle fusion on silicon dioxide surfaces by ellipsometry.* Aiche Journal, 2006. **52**(8): p. 2931-2937.
176. Moller, J.V., B. Juul, and M. le Maire, *Structural organization, ion transport, and energy transduction of P-type ATPases.* Biochim Biophys Acta, 1996. **1286**(1): p. 1-51.
177. Kaplan, J.H., *Biochemistry of Na,K-ATPase.* Annu Rev Biochem, 2002. **71**: p. 511-35.
178. Shinoda, T., et al., *Crystal structure of the sodium-potassium pump at 2.4 A resolution.* Nature, 2009. **459**(7245): p. 446-50.
179. Ogawa, H., et al., *Crystal structure of the sodium-potassium pump (Na+,K+-ATPase) with bound potassium and ouabain.* Proc Natl Acad Sci U S A, 2009. **106**(33): p. 13742-7.
180. Stein, W.D., et al., *A modle for active transport of sodium and potassium ions as mediated by a tetrameric enzyme.* Proc Natl Acad Sci U S A, 1973. **70**(1): p. 275-8.
181. Repke, K.R. and R. Schon, *Flip-flop model of (NaK)-ATPase function.* Acta Biol Med Ger, 1973. **31**(4): p. Suppl:K19-30.
182. Taniguchi, K., et al., *The oligomeric nature of Na/K-transport ATPase.* J Biochem, 2001. **129**(3): p. 335-42.
183. Martin, D.W., *Structure-function relationships in the NA+,K+-pump.* Semin Nephrol, 2005. **25**(5): p. 282-91.
184. Clarke, R.J., *Mechanism of allosteric effects of ATP on the kinetics of P-type ATPases.* Eur Biophys J, 2009. **39**(1): p. 3-17.
185. Toyoshima, C., et al., *Crystal structure of the calcium pump of sarcoplasmic reticulum at 2.6 A resolution.* Nature, 2000. **405**(6787): p. 647-55.
186. Olesen, C., et al., *The structural basis of calcium transport by the calcium pump.* Nature, 2007. **450**(7172): p. 1036-42.
187. Cornelius, F., *Phosphorylation/dephosphorylation of reconstituted shark Na+,K(+)-ATPase: one phosphorylation site per alpha beta protomer.* Biochim Biophys Acta, 1995. **1235**(2): p. 197-204.
188. Froehlich, J.P., et al., *Complex kinetic behavior in the Na,K- and Ca-ATPases. Evidence for subunit-subunit interactions and energy conservation during catalysis.* Ann N Y Acad Sci, 1997. **834**: p. 280-96.
189. Clarke, R.J. and D.J. Kane, *Two gears of pumping by the sodium pump.* Biophys J, 2007. **93**(12): p. 4187-96.

190. Khalid, M., et al., *Interaction of ATP with the phosphoenzyme of the Na+,K+-ATPase.* Biochemistry, 2010. **49**(6): p. 1248-58.
191. Clarke, R.J. and X. Fan, *Pumping ions.* Clin Exp Pharmacol Physiol, 2011. **38**(11): p. 726-33.
192. Khalid, M., F. Cornelius, and R.J. Clarke, *Dual mechanisms of allosteric acceleration of the Na(+),K(+)-ATPase by ATP.* Biophys J, 2010. **98**(10): p. 2290-8.
193. Martin, D.W., et al., *Alphabeta protomers of Na+,K+-ATPase from microsomes of duck salt gland are mostly monomeric: formation of higher oligomers does not modify molecular activity.* Proc Natl Acad Sci U S A, 2000. **97**(7): p. 3195-200.
194. Herbert, H., E. Skriver, and A.B. Maunsbach, *Three-dimensional structure of renal Na,K-ATPase determined by electron microscopy of membrane crystals.* FEBS Lett, 1985. **187**(1): p. 182-6.
195. Soderholm, M., et al., *Assembly of two-dimensional membrane crystals of Na,K-ATPase.* J Ultrastruct Mol Struct Res, 1988. **99**(3): p. 234-43.
196. Yokoyama, T., et al., *Acid-labile ATP and/or ADP/P(i) binding to the tetraprotomeric form of Na/K-ATPase accompanying catalytic phosphorylation-dephosphorylation cycle.* J Biol Chem, 1999. **274**(45): p. 31792-6.
197. Apell, H.J., et al., *Na,K-ATPase in crystalline form investigated by scanning force microscopy.* Ultramicroscopy, 1992. **42-44 (Pt B)**: p. 1133-40.
198. Apell, H.J., Colchero,J., Linder, A., Marti, O., *Investigation of the Na,K-ATPase by Scanning Force Microscopy.*, in *STM and SFM in Biology*, O. Marti, Amrein, M., Editor. 1993, Academic Press: Orlando. p. 275-308.
199. Sessa, G. and G. Weissmann, *Phospholipid spherules (liposomes) as a model for biological membranes.* J Lipid Res, 1968. **9**(3): p. 310-8.
200. Bangham, A.D., M.M. Standish, and J.C. Watkins, *Diffusion of univalent ions across the lamellae of swollen phospholipids.* J Mol Biol, 1965. **13**(1): p. 238-52.
201. Maurer, N., D.B. Fenske, and P.R. Cullis, *Developments in liposomal drug delivery systems.* Expert Opin Biol Ther, 2001. **1**(6): p. 923-47.
202. Liu, Q. and B.J. Boyd, *Liposomes in biosensors.* Analyst, 2013. **138**(2): p. 391-409.
203. Jesorka, A. and O. Orwar, *Liposomes: technologies and analytical applications.* Annu Rev Anal Chem (Palo Alto Calif), 2008. **1**: p. 801-32.
204. Huang, C.H., *Studies on Phosphatidylcholine Vesicles . Formation and Physical Characteristics.* Biochemistry, 1969. **8**(1): p. 344-&.
205. MacDonald, R.C., et al., *Small-volume extrusion apparatus for preparation of large, unilamellar vesicles.* Biochim Biophys Acta, 1991. **1061**(2): p. 297-303.
206. MacDonald, R.C., F.D. Jones, and R. Qiu, *Fragmentation into small vesicles of dioleoylphosphatidylcholine bilayers during freezing and thawing.* Biochim Biophys Acta, 1994. **1191**(2): p. 362-70.
207. Lasic, D.D., *The mechanism of vesicle formation.* Biochemical Journal, 1988. **256**(1): p. 1-11.
208. Brunner, J., P. Skrabal, and H. Hauser, *Single bilayer vesicles prepared without sonication. Physico-chemical properties.* Biochim Biophys Acta, 1976. **455**(2): p. 322-31.
209. Pecora, R., *Dynamic light scattering: applications of photon correlation spectroscopy*. 1985, New York: Plenum Press.

210. Einstein, A., *On the motion of small particles suspended in liquids at rest required by the molecular-kinetic theory of heat.* Annalen der Physik, 1905. **17**: p. 549-560.
211. Sutherland, W., *A dynamical theory of diffusino for non-electrolytes and the molecular mass of albumin.* Philosophical Magazine, 1905. **9**(54): p. 781-785.
212. Hunter, R.J., *Zeta potential in colloid science: principles and applications*. 1988, London, UK: Academic Press.
213. Egerton, R.F., *Physical Principles of Electron Microscopy: An Introduction to TEM, SEM, and AEM*. 2005, New York, US: Springer Science + Business Media, Inc.
214. Blume, A., *Biological Calorimetry: Membranes.* Thermochimica Acta, 1991. **193**: p. 299-347.
215. Kurrat, R., et al., *Instrumental improvements in optical waveguide light mode spectroscopy for the study of biomolecule adsorption.* Review of Scientific Instruments, 1997. **68**(5): p. 2172-2176.
216. Jun, S.-I., et al., *Characterisation of reactively sputtered silicon oxide for thin-film transistor fabrication.* Electronics Letters, 2005. **41**(14): p. 822-823.
217. Keller, C.A. and B. Kasemo, *Surface specific kinetics of lipid vesicle adsorption measured with a quartz crystal microbalance.* Biophys J, 1998. **75**(3): p. 1397-1402.
218. Tejero, R., et al., *Implant surfaces activated with plasma rich in growth factors: time of flight secondary ion mass spectrometry and principal component analysis study.* Langmuir, 2013. **29**: p. 902 - 912.
219. Sittig, C.E., *Charakterisierung der Oxidschichten auf Titan und Titanlegierungen sowie deren Reaktionen in Kontakt mit biologisch relevanten Modelllösungen*, in *Materials*. 1998, ETH Zurich: Zurich.
220. Rossetti, F.F., I. Reviakine, and M. Textor, *Characterization of titanium oxide films prepared by the template-stripping method.* Langmuir, 2003. **19**(24): p. 10116-10123.
221. Axelrod, D., et al., *Mobility Measurement by Analysis of Fluorescence Photobleaching Recovery Kinetics.* Biophysical Journal, 1976. **16**(9): p. 1055-1069.
222. Soumpasis, D.M., *Theoretical analysis of fluorescence photobleaching recovery experiments.* Biophys J, 1983. **41**(1): p. 95-7.
223. Binnig, G., C.F. Quate, and C. Gerber, *Atomic force microscope.* Phys Rev Lett, 1986. **56**(9): p. 930-933.
224. Rico, F., C. Su, and S. Scheuring, *Mechanical mapping of single membrane proteins at submolecular resolution.* Nano Lett, 2011. **11**(9): p. 3983-6.
225. Adamcik, J., A. Berquand, and R. Mezzenga, *Single-step direct measurement of amyloid fibrils stiffness by peak force quantitative nanomechanical atomic force microscopy.* Applied Physics Letters, 2011. **98**(19).
226. Reviakine, I., D. Johannsmann, and R.P. Richter, *Hearing what you can't see and visualizing what you hear: interpreting quartz crystal microbalance data from solvated interfaces.* Analytical Chemistry, 2011. **83**(23): p. 8838-8848.
227. Sauerbrey, G., *Use of quartz vibrator for weighring thin films on a microbalance.* Z.Phys., 1959. **155**: p. 206-222.
228. Jorgensen, P.L., *Purification and characterization of (Na+ plus K+)-ATPase. 3. Purification from the outer medulla of mammalian kidney after selective removal of membrane components by sodium dodecylsulphate.* Biochim Biophys Acta, 1974. **356**(1): p. 36-52.

229. Deguchi, N., P.L. Jorgensen, and A.B. Maunsbach, *Ultrastructure of the sodium pump. Comparison of thin sectioning, negative staining, and freeze-fracture of purified, membrane-bound (Na+,K+)-ATPase.* J Cell Biol, 1977. **75**(3): p. 619-34.
230. Laemmli, U.K., *Cleavage of structural proteins during the assembly of the head of bacteriophage T4.* Nature, 1970. **227**(5259): p. 680-5.
231. Meyer, T.S. and B.L. Lamberts, *Use of coomassie brilliant blue R250 for the electrophoresis of microgram quantities of parotid saliva proteins on acrylamide-gel strips.* Biochim Biophys Acta, 1965. **107**(1): p. 144-5.
232. Frank, J., *Classification of macromolecular assemblies studied as 'single particles'.* Q Rev Biophys, 1990. **23**(3): p. 281-329.
233. Boekema, E.J., M. Folea, and R. Kouril, *Single particle electron microscopy.* Photosynth Res, 2009. **102**(2-3): p. 189-96.
234. van Heel, M., et al., *Single-particle electron cryo-microscopy: towards atomic resolution.* Q Rev Biophys, 2000. **33**(4): p. 307-69.
235. Kosmulski, M., J. Gustafsson, and J.B. Rosenholm, *Ion specificity and viscosity of rutile dispersions.* Colloid and Polymer Science, 1999. **277**(6): p. 550-556.
236. Kosmulski, M. and E. Matijevic, *ZETA-POTENTIAL OF ANATASE (TIO2) IN MIXED-SOLVENTS.* Colloids and Surfaces, 1992. **64**(1): p. 57-65.
237. Rodahl, M., et al., *Quartz-Crystal Microbalance Setup for Frequency and Q-Factor Measurements in Gaseous and Liquid Environments.* Review of Scientific Instruments, 1995. **66**(7): p. 3924-3930.
238. Haberman.E, *Bee Wasp Venoms.* Science, 1972. **177**(4046): p. 314-&.
239. van den Bogaart, G., et al., *The lipid dependence of melittin action investigated by dual-color fluorescence burst analysis.* Biophysical Journal, 2007. **93**(1): p. 154-163.
240. Tellechea, E., et al., *Model-Independent Analysis of QCM Data on Colloidal Particle Adsorption.* Langmuir, 2009. **25**(9): p. 5177-5184.
241. Reviakine, I., Brisson, A., *Formation of supported phospholipid bilayers from unilamellar vesicles investigated by atomic force microscopy.* Langmuir, 2000. **16**(4): p. 1806-1815.
242. Derjaguin, B., Landau, L., *Theory of the stability of strongly charged lyophobic sols and of the adhesion of strongly charged particles in solutions of electrolytes.* Acta Physico Chemica URSS, 1941. **14**: p. 633-662.
243. Verwey, E.J.W., Overbeek, J. Th. G., *Theory of the stability of lyophobi colloids*. 1948: Amsterdam: Elsevier.
244. Israelachvili, J., *Intermolecular and Surface Forces*. 1991: Academic Press, London.
245. Loosley-Millman, M.E., R.P. Rand, and V.A. Parsegian, *Effects of monovalent ion binding and screening on measured electrostatic forces between charged phospholipid bilayers.* Biophys J, 1982. **40**(3): p. 221-32.
246. Petrache, H.I., et al., *Swelling of phospholipids by monovalent salt.* J Lipid Res, 2006. **47**(2): p. 302-9.
247. Pashley, R.M., *DLVO and hydration forces between mica surfaces in Li+, Na+, K+, and Cs+ electrolyte solutions: A correlation of double-layer and hydration forces with surface cation exchange properties.* Journal of Colloid and Interface Science, 1981. **83**(2): p. 531-546.
248. Rapuano, R. and A.M. Carmona-Ribeiro, *Supported Bilayers on Silica.* Journal of Colloid and Interface Science, 2000. **226**(2): p. 299-307.

249. Przybylo, M., et al., *Lipid diffusion in giant unilamellar vesicles is more than 2 times faster than in supported phospholipid bilayers under identical conditions.* Langmuir, 2006. **22**(22): p. 9096-9.

250. Kahya, N. and P. Schwille, *How phospholipid-cholesterol interactions modulate lipid lateral diffusion, as revealed by fluorescence correlation spectroscopy.* J Fluoresc, 2006. **16**(5): p. 671-8.

251. Oradd, G., P.W. Westerman, and G. Lindblom, *Lateral diffusion coefficients of separate lipid species in a ternary raft-forming bilayer: a Pfg-NMR multinuclear study.* Biophys J, 2005. **89**(1): p. 315-20.

252. Richter, R., A. Mukhopadhyay, and A. Brisson, *Pathways of lipid vesicle deposition on solid surfaces: A combined QCM-D and AFM study.* Biophysical Journal, 2003. **85**(5): p. 3035-3047.

253. Muresan, A.S. and K.Y.C. Lee, *Shape evolution of lipid bilayer patches adsorbed on mica: An atomic force microscopy study.* Journal of Physical Chemistry B, 2001. **105**(4): p. 852-855.

254. Richter, R.P. and A.R. Brisson, *Following the formation of supported lipid bilayers on mica: A study combining AFM, QCM-D, and ellipsometry.* Biophysical Journal, 2005. **88**(5): p. 3422-3433.

255. Reimhult, E., et al., *A multitechnique study of liposome adsorption on Au and lipid bilayer formation on SiO2.* Langmuir, 2006. **22**(7): p. 3313-3319.

256. Jass, J., T. Tjarnhage, and G. Puu, *From liposomes to supported, planar bilayer structures on hydrophilic and hydrophobic surfaces: An atomic force microscopy study.* Biophysical Journal, 2000. **79**(6): p. 3153-3163.

257. Homsy, G.M., *Viscous fingering in porous media.* Annual review of Fluid Mechanics, 1987. **19**: p. 271-311.

258. Radler, J., H. Strey, and E. Sackmann, *Phenomenology And Kinetics Of Lipid Bilayer Spreading On Hydrophilic Surfaces.* Langmuir, 1995. **11**(11): p. 4539-4548.

259. Gozen, I., et al., *Fractal avalanche ruptures in biological membranes.* Nat Mater, 2010. **9**(11): p. 908-12.

260. Furukawa, K., et al., *Supported lipid bilayer self-spreading on a nanostructured silicon surface.* Langmuir, 2007. **23**(2): p. 367-371.

261. Richter, R.P. and A. Brisson, *Characterization of lipid bilayers and protein assemblies supported on rough surfaces by atomic force microscopy.* Langmuir, 2003. **19**(5): p. 1632-1640.

262. Papahadjopoulos, D., et al., *Cochleate Lipid Cylinders - Formation by Fusion of Unilamellar Lipid Vesicles.* Biochimica Et Biophysica Acta, 1975. **394**(3): p. 483-491.

263. Rossetti, F.F., *Interaction of lipidic assemblies with metal oxides and brush-like polylectrolytes*, in *Swiss Federal Institute of Technology*. 2005.

264. Wilschut, J., N. Duzgunes, and Papahadjopoulos, *Calcium/Magnesium Specificity in Membrane Fusion: Kinetics of Aggregation and Fusion of Phosphatidylserine Vesicles and the role ob Bilayer Curvature.* Biochemistry, 1981. **20**: p. 3126-3133.

265. Tero, R., T. Ujihara, and T. Urisu, *Lipid bilayer membrane with atomic step structure: supported bilayer on a step-and-terrace TiO2(100) surface.* Langmuir, 2008. **24**(20): p. 11567-76.

266. Reimhult, E., F. Hook, and B. Kasemo, *Temperature dependence of formation of a supported phospholipid bilayer from vesicles on SiO2.* Physical Review e, 2002. **66**(5): p. art-051905.

267. Keller, C.A., et al., *Formation of supported membranes from vesicles.* Physical Review Letters, 2000. **84**(23): p. 5443-5446.
268. Cho, N.J. and C.W. Frank, *Fabrication of a Planar Zwitterionic Lipid Bilayer on Titanium Oxide.* Langmuir, 2010. **26**(20): p. 15706-15710.
269. Dietrich, C., et al., *Lipid rafts reconstituted in model membranes.* Biophysical Journal, 2001. **80**(3): p. 1417-1428.
270. McLaughlin, S., et al., *Adsorption of Divalent-Cations to Bilayer-Membranes Containing Phosphatidylserine.* Journal of General Physiology, 1981. **77**(4): p. 445-473.
271. Rossetti, F.F., et al., *Interactions between titanium dioxide and phosphatidyl serine-containing liposomes: formation and patterning of supported phospholipid bilayers on the surface of a medically relevant material.* Langmuir, 2005. **21**(14): p. 6443-50.
272. Rawicz, W., et al., *Effect of chain length and unsaturation on elasticity of lipid bilayers.* Biophysical Journal, 2000. **79**(1): p. 328-339.
273. Pan, J., et al., *Temperature dependence of structure, bending rigidity, and bilayer interactions of dioleoylphosphatidylcholine bilayers.* Biophys J, 2008. **94**(1): p. 117-24.
274. el-Sayed, M.Y., T.A. Guion, and M.D. Fayer, *Effect of cholesterol on viscoelastic properties of dipalmitoylphosphatidylcholine multibilayers as measured by a laser-induced ultrasonic probe.* Biochemistry, 1986. **25**(17): p. 4825-32.
275. Lin, W.C., et al., *Lipid asymmetry in DLPC/DSPC-supported lipid bilayers: a combined AFM and fluorescence microscopy study.* Biophys J, 2006. **90**(1): p. 228-37.
276. Reviakine, I., A. Simon, and A. Brisson, *Effect of Ca2+ on the morphology of mixed DPPC-DOPS supported phospholipid bilayers.* Langmuir, 2000. **16**(4): p. 1473-1477.
277. Tsunoda, K., E. Ohashi, and S. Adachi, *Spectroscopic characterization of naturally and chemically oxidized silicon surfaces.* Journal of Applied Physics, 2003. **94**: p. 5613-5616.
278. Kumar, A., *Fabrication of Low-Roughness Au/Ti/SiO2/Si substrates for Nanopatterning of 16-Mercapto Hexadecanoic Acid (MHA) by Dip-Pen-Nanolithography.* Journal of Nano and Electronic Physics, 2012. **4**: p. 02022.
279. Tero, R., H. Watanabe, and T. Urisu, *Supported phospholipid bilayer formation on hydrophilicity-controlled silicon dioxide surfaces.* Phys Chem Chem Phys, 2006. **8**(33): p. 3885-94.
280. Udupa, G. and B.K.A. Ngoi. *Surface Topography Analysis of Silicon Wafers by a Chromameter.* in *American Society for Precision Engineering. 2000 Annual Proceedings*. 2000.
281. Minor, N.T., et al., *The gamma subunit of the Na,K-ATPase induces cation channel activity.* Proc Natl Acad Sci U S A, 1998. **95**(11): p. 6521-5.
282. Scheuring, S., et al., *Nanodissection and high-resolution imaging of the Rhodopseudomonas viridis photosynthetic core complex in native membranes by AFM. Atomic force microscopy.* Proc Natl Acad Sci U S A, 2003. **100**(4): p. 1690-3.
283. Schabert, F.A. and A. Engel, *Reproducible acquisition of Escherichia coli porin surface topographs by atomic force microscopy.* Biophys J, 1994. **67**(6): p. 2394-403.

284. Six, D.A. and E.A. Dennis, *The expanding superfamily of phospholipase A(2) enzymes: classification and characterization.* Biochim Biophys Acta, 2000. **1488**(1-2): p. 1-19.

285. Jorgensen, K., J. Davidsen, and O.G. Mouritsen, *Biophysical mechanisms of phospholipase A2 activation and their use in liposome-based drug delivery.* FEBS Lett, 2002. **531**(1): p. 23-7.

286. Parmar, M.M., K. Edwards, and T.D. Madden, *Incorporation of bacterial membrane proteins into liposomes: factors influencing protein reconstitution.* Biochim Biophys Acta, 1999. **1421**(1): p. 77-90.

287. Muller, D.J., M. Amrein, and A. Engel, *Adsorption of biological molecules to a solid support for scanning probe microscopy.* J Struct Biol, 1997. **119**(2): p. 172-88.

288. Muller, D.J. and A. Engel, *The height of biomolecules measured with the atomic force microscope depends on electrostatic interactions.* Biophys J, 1997. **73**(3): p. 1633-44.

289. Orsini, F., et al., *Intermittent contact mode AFM investigation of native plasma membrane of Xenopus laevis oocyte.* Eur Biophys J, 2009. **38**(7): p. 903-10.

290. Adamcik, J., *Single-step direct measurement of amyloid fibrils stiffness by peak force quantitative nanomechanical atomic force microscopy.* Applied Physics Letters, 2011. **98**(19): p. 193701.

291. Perkin, S., N. Kampf, and J. Klein, *Long-range attraction between charge-mosaic surfaces across water.* Phys Rev Lett, 2006. **96**(3): p. 038301.

292. Jass, J., T. Tjarnhage, and G. Puu, *From liposomes to supported, planar bilayer structures on hydrophilic and hydrophobic surfaces: an atomic force microscopy study.* Biophys J, 2000. **79**(6): p. 3153-63.

293. Richter, R.P. and A. Brisson, *QCM-D on mica for parallel QCM-D-AFM studies.* Langmuir, 2004. **20**(11): p. 4609-4613.

294. Buzhynskyy, N., et al., *The supramolecular architecture of junctional microdomains in native lens membranes.* EMBO Rep, 2007. **8**(1): p. 51-5.

295. Adamczyk, M., et al., *Characterization of protein-hapten conjugates. 1. Matrix-assisted laser desorption ionization mass spectrometry of immuno BSA-hapten conjugates and comparison with other characterization methods.* Bioconjug Chem, 1994. **5**(6): p. 631-5.

296. Askari, A. and W. Huang, *Na+,K+-ATPase: half-of-the-subunits cross-linking reactivity suggests an oligomeric structure containing a minimum of four catalytic subunits.* Biochem Biophys Res Commun, 1980. **93**(2): p. 448-53.

297. Tsuda, T., et al., *Half-site modification of Lys-480 of the Na+,K+-ATPase alpha-chain with pyridoxal 5'-diphospho-5'-adenosine reduces ATP-dependent phosphorylation stoichiometry from half to a quarter.* J Biol Chem, 1998. **273**(38): p. 24334-8.

298. Taniguchi, K., K. Suzuki, and S. Iida, *Conformational change accompanying transition of ADP-sensitive phosphoenzyme to potassium-sensitive phosphoenzyme of (Na+,K+)-ATPase modified with N-[p-(2-benzimidazolyl)phenyl]maleimide.* J Biol Chem, 1982. **257**(18): p. 10659-67.

Acknowledgements

I would like to express my deepest gratitude to my supervisor Dr. Ilya Reviakine for his excellent guidance and support throughout my education and research. Without his encouragement and effort, this thesis would not have been possible.

I would like to thank Dr. Gur Fabrikant and Prof. Michael Kozlov for providing me with the theoretical model to help explaining my experimental results.

I would like to thank Prof. Hans-Jurgen Apell for providing me with the Na^+, K^+-ATPase-containing membrane fragments to give me the opportunity for this study.

I would like to thank Dr. Daniel Padro and Dr. Marco Marradi for help with the NMR, and Dr. Marco Moller for help with the TEM.

I would also like to thank my lab mates Miss Danijela Gregurec, Ms Marta Gallego Gonzalez, and Miss Swati Gupta for their technical and emotional support and helpful discussion.

Last but not the least, I am grateful for my family for their support, sacrifice, and patience.

Publications

Nanoscale Departures: Excess Lipid Leaving the Surface During Supported Lipid Bilayer Formation

Ling Zhu, Danijela Gregurec, Ilya Reviakine

Submitted to Langmuir, 2013

It's a Conspiracy: How Osmotic Effects and Electrostatic Interactions Control Adsorbed Liposome Behavior

Ling Zhu, Marta Gallego, Danijela Gregurec, Ilya Reviakine

Manuscript in preparation

Towards Better Cell Membrane Mimics: Phosphatidyl Serine- and Cholesterol-Containing Asymmetric Supported Lipid Bilayers on Titania

Ling Zhu, Marta Gallego, Danijela Gregurec, Ilya Reviakine

Manuscript in preparation

Conferences

Towards Better Cell Membrane Mimics: Cholesterol-Containing Supported Lipid Bilayer on TiO_2

Poster

FEBES International Physical Chemistry of Biointerfaces Workshop, 9-14th, July, 2012, San Sebastian, Spain

Towards Better Cell Membrane Mimics: Cholesterol-Containing Supported Lipid Bilayer on TiO_2

Oral presentation

COST/LIST Symposium: Bioinspired Nanotechnologies for Distributed Diagnostics, 26-27th, April, 2012, Linköping University, Sweden

Towards Better Cell Membrane Mimics: Cholesterol-Containing Supported Lipid Bilayer on TiO_2

Poster

International Workshop ‘Membranes in Health and Disease’, 12-14th, March, 2012, German Biophysical Society, Gomadingen, Germany

Towards Better Cell Membrane Mimics: Cholesterol-Containing Supported Lipid Bilayer on TiO_2

Oral presentation
Neutrons in Biology and Biotechnology, 19-20th, October, 2011, Grenoble, France

Native membrane patches containing Na^+, K^+-ATPase studied by AFM
Poster
Membrane Proteins: Structure and Function Conference, 06-08th, April, 2011, University of Oxford, UK

Native membrane patches containing Na^+, K^+-ATPase studied by AFM
Poster
Electron Crystallography Workshop, 01-07th, August, 2010, University Basel, Switzerland

Native membrane patches containing Na^+, K^+-ATPase studied by AFM
Poster
IV Spanish Portuguese Biophysical Congress, 01-07th, July, 20101, Zaragoza,Spain

Native membrane patches containing Na^+, K^+-ATPase studied by AFM
Poster
Physical Chemistry of Biointerfaces workshop, 19-24th, July, 2010, San Sebastian, Spain